



저작자표시-비영리-변경금지 2.0 대한민국

이용자는 아래의 조건을 따르는 경우에 한하여 자유롭게

- 이 저작물을 복제, 배포, 전송, 전시, 공연 및 방송할 수 있습니다.

다음과 같은 조건을 따라야 합니다:



저작자표시. 귀하는 원저작자를 표시하여야 합니다.



비영리. 귀하는 이 저작물을 영리 목적으로 이용할 수 없습니다.



변경금지. 귀하는 이 저작물을 개작, 변형 또는 가공할 수 없습니다.

- 귀하는, 이 저작물의 재이용이나 배포의 경우, 이 저작물에 적용된 이용허락조건을 명확하게 나타내어야 합니다.
- 저작권자로부터 별도의 허가를 받으면 이러한 조건들은 적용되지 않습니다.

저작권법에 따른 이용자의 권리는 위의 내용에 의하여 영향을 받지 않습니다.

이것은 [이용허락규약\(Legal Code\)](#)을 이해하기 쉽게 요약한 것입니다.

[Disclaimer](#)

Doctoral Thesis

Theoretical Study for Adsorption Behaviors in
Catalysis and Energy Applications via Multi-Scale
Simulation

Gwan Yeong Jung

Department of Chemical Engineering

Graduate School of UNIST

2020

Theoretical Study for Adsorption Behaviors in
Catalysis and Energy Applications via Multi-Scale
Simulation

Gwan Yeong Jung

Department of Chemical Engineering

Graduate School of UNIST

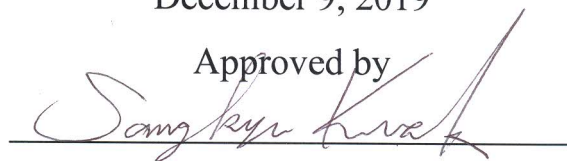
Theoretical Study for Adsorption Behaviors in
Catalysis and Energy Applications via Multi-Scale
Simulation

A thesis/dissertation
submitted to the Graduate School of UNIST
in partial fulfillment of the
requirements for the degree of
Doctor of Philosophy

Gwan Yeong Jung

December 9, 2019

Approved by



Advisor

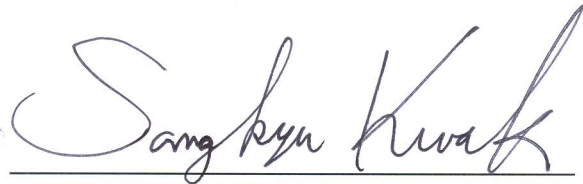
Sang Kyu Kwak

Theoretical Study for Adsorption Behaviors in
Catalysis and Energy Applications via Multi-Scale
Simulation

Gwan Yeong Jung

This certifies that the thesis of Gwan Yeong Jung is approved.

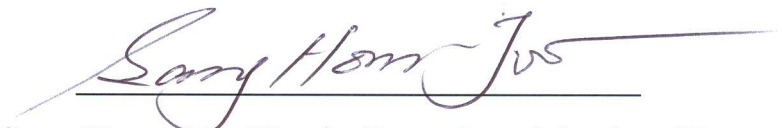
December 9, 2019



Advisor: Sang Kyu Kwak



Sang-Young Lee: Thesis Committee Member #1



Sang Hoon Joo: Thesis Committee Member #2



Hyun-Kon Song: Thesis Committee Member #3



Jun Hee Lee: Thesis Committee Member #4

Abstract

With increasing energy demands and environmental concerns related to the greenhouse effect, one of the most central themes of research society is the development of sustainable and environmental-friendly energy system. In this regard, catalysts play a pivotal role in producing the fossil-free industrial chemicals (*e.g.*, ammonia, hydrogen, and hydrocarbon) from earth-abundant substances (*e.g.*, nitrogen, water) through (electro-)chemical conversion process. Moreover, energy storage technologies, such as lithium-ion batteries and fuel cells, are equally important for practical applications. However, the current levels of energy conversion and storage technologies are inadequate; that is, more advanced design and fundamental understanding of these processes is now pursued.

Adsorption has an important meaning in the (electro-)chemical process in that the energy states of adsorbed reaction intermediates in the mechanistic pathways can determine the reaction mechanisms. Many studies have focused on the adsorption behaviors and corresponding energetics to predict the catalytic activity or battery performance. In this context, molecular simulation approach can be a suitable tool to investigate the adsorption behaviors in the atomistic and molecular level. Particularly, multi-scale molecular simulation methods are useful to properly elucidate the physicochemical phenomena in experimental (or realistic) systems crossing over different temporal and spatial scales. In this dissertation, theoretical studies on adsorption behaviors in catalysis and energy applications have been conducted *via* multi-scale molecular simulation approach.

In Chapter 2, we theoretically demonstrated that atomically dispersed Pt catalysts on carbon nanotube (Pt₁/CNT) could catalyze the chlorine evolution reaction (CER) with excellent activity and selectivity. From *ab initio* Pourbaix diagram, the active adsorbate structures for the Pt₁/CNT were initially found. Subsequently, the mechanistic pathways for the CER were thoroughly investigated by combining the experimental (for kinetics) and theoretical data (for thermodynamics). Among Pt–N₄ sites, PtN₄C₁₂ was identified as the most plausible active site structure for the CER. Moreover, the excellent selectivity of Pt₁/CNT was evidenced by the large differences in thermodynamic overpotentials for respective CER and oxygen evolution reaction, which can be determined from the adsorption free energies of the reaction intermediates. We envision that this type of catalysts may be exploited as an alternative CER catalyst instead of precious metal-based mixed metal oxides (MMOs), which have suffered from concomitant generation of oxygen.

In Chapter 3, we investigated the thermodynamics of ion adsorption on the amorphous intermediate phases of calcium carbonates. Amorphous calcium carbonate (ACC) have received enormous attentions because their local order in the short-range can affect the subsequent pathways for phase transformation. Using molecular dynamic simulation, we theoretically elucidated the precise role

of ion adsorption in controlling the local structures and stability of ACC phases. Starting from the nucleation clusters in aqueous solution, the hydrated and anhydrous forms of ACC were systematically examined by varying the hydration levels and molar composition of additive ions (*e.g.* Mg²⁺, Fe²⁺, Sr²⁺, and Ba²⁺). Our results revealed that each ion can exert promoting or inhibiting effect by tuning the local order and stability of ACC phases depending on their hydrophilicity and ionic radii. More importantly, our findings suggested that the thermodynamic spontaneity of the overall phase transition process can be determined by the balance between two opposing factors – endothermic dehydration and exothermic crystallization.

Chapters 4 and 5 commonly describe the investigation of adsorption phenomena, related to the next-generation rechargeable batteries such as lithium-sulfur (Li-S) and lithium-oxygen (Li-O₂) battery. The adsorption of reaction intermediates for Li-S and Li-O₂ battery, which are polysulfides (*i.e.*, Li₂S_{*x*}, 1 ≤ *x* ≤ 8) and superoxide species (*i.e.*, O₂^{•-} or LiO₂), respectively, is a decisive step for these systems because these floating reaction intermediates can hamper the cell performance by triggering the unwanted side reactions such as shuttle phenomena of Li₂S_{*x*}, and electrolyte degradation by O₂^{•-} species.

In Chapter 4, we investigated the polysulfide adsorption on molecularly designed chemical trap in Li-S battery. A microporous covalent organic framework (COF) net on mesoporous carbon nanotube (CNT) net hybrid architecture was introduced as a new class of chemical trap for polysulfides. Two COFs with different micropore sizes (COF-1 and COF-5) were selected as model systems. Using density functional theory calculation and grand canonical Monte Carlo simulation, the pore-size-enabled selective adsorption of Li₂S in COF-1 was theoretically demonstrated. The results also revealed that COF-1 possesses a well-designed micropore size and (boron-mediated) chemical affinity suitable for selective adsorption of Li₂S, which can significantly improve the electrochemical performance of Li-S battery.

In Chapter 5, we investigated the superoxide adsorption and subsequent disproportionation mechanism in Li-O₂ battery. Reactive O₂^{•-} species can trigger the side reactions, which are serious hurdles hampering the performance of Li-O₂ battery. To resolve this issue, malonic-acid-decorated fullerene (MA-C₆₀) was employed as a superoxide disproportionation chemo-catalyst. Using multi-scale molecular simulation methods including density functional theory and molecular dynamics, we theoretically evidenced the preference to solution mechanism over surface mechanism in the presence of MA-C₆₀ catalyst. Additionally, from the free energy diagram along reaction pathway of the solution mechanism, we identified the beneficial role of MA-C₆₀ to significantly reduce the thermodynamic barrier of the disproportionation step.

Contents

Abstract	i
Contents	iii
List of Tables	vi
List of Figures	vii
Chapter 1. Introduction	1
1.1 General Introduction.....	1
1.2 Adsorption in Electrocatalysis.....	2
1.3 Adsorption in Catalytic Biomineralization.....	5
1.4 Adsorption in Next-Generation Rechargeable Batteries.....	6
1.4.1 Lithium-Sulfur Battery.....	7
1.4.2 Lithium-Oxygen Battery.....	8
1.5 Multi-Scale Molecular Simulation.....	9
1.5.1 Density Functional Theory.....	10
1.5.2 Molecular Dynamics.....	11
1.5.3 Grand Canonical Monte Carlo.....	12
1.6 Outline of Dissertation.....	12
1.7 References.....	13
Chapter 2. Atomically Dispersed Pt Catalyst for Highly Efficient and Selective Chlorine Evolution Reaction	17
2.1 Introduction.....	17
2.2 Methods.....	18
2.2.1 Calculation Details.....	18
2.2.2 Model Systems for Calculation.....	18
2.3 Results and Discussion.....	19
2.3.1 Experimental Measurements of CER Activity and Selectivity.....	19
2.3.2 <i>Ab Initio</i> Pourbaix Diagrams.....	21
2.3.3 Theoretical Evaluations on the CER Activity.....	31
2.3.4 Stability Against Pt Dissolution.....	33
2.3.5 Full Free Energy Diagram of CER over Pt ₁ /CNT.....	35
2.3.6 CER Selectivity Compared to the OER.....	39
2.4 Conclusion.....	42

2.5 References	43
----------------------	----

Chapter 3. Thermodynamic Control of Amorphous Calcium Carbonate Phases *via* Ion Adsorption in Catalytic Biomineralization 48

3.1 Introduction	48
3.2 Methods	49
3.2.1 Simulation Details	49
3.2.2 Forcefield Parameterization	50
3.2.3 Mean Square Displacement Analysis	52
3.3 Results and Discussion	53
3.3.1 Overview of Dehydration Process.....	53
3.3.2 Structural Analysis Based on CN Environment	56
3.3.3 Thermodynamic Analysis for Dehydration and Crystallization Processes	62
3.3.4 TDF Analysis for ACC Structure Involving Additive Ions	72
3.4 Conclusion.....	77
3.5 References	78

Chapter 4. Molecularly Designed Chemical Trap for Polysulfide Adsorption in Lithium-Sulfur Battery 83

4.1 Introduction	83
4.2 Methods	85
4.2.1 Model Systems for Calculation	85
4.2.2 Simulation Details	85
4.2.3 Energy Calculations	87
4.3 Results and Discussion	88
4.3.1 Pore-Size Dependent Adsorption of Polysulfides	88
4.3.2 Chemical Affinity of Polysulfide Adsorption.....	90
4.3.3 Electrochemical Performance of Li-S Battery	97
4.4 Conclusion.....	100
4.5 References	101

Chapter 5. Biomimetic Catalyst for Superoxide Adsorption and Disproportionation in Lithium-Oxygen Battery..... 104

5.1 Introduction	104
5.2 Methods	107
5.2.1 DFT Calculations	107

5.2.2 MD Simulations	107
5.3 Results and Discussion	108
5.3.1 Effect of MA-C ₆₀ on LOB Performance	108
5.3.2 Solution Mechanism of Li ₂ O ₂ Formation Induced by MA-C ₆₀	111
5.3.3 MA-C ₆₀ <i>versus</i> Malonic Acid	115
5.4 Conclusion	117
5.5 References	118
Chapter 6. Summary and Future Perspectives	121
6.1 Summary	121
6.2 Future Perspectives	122
6.3 References	124
Appendix	
List of Publications	125

List of Tables

- Table 1.1** Multi-scale simulation methods, applications and simulation packages.
- Table 2.1** Adsorption free energies (ΔG° 's) of OH^* , O^* , and OOH^* on Pt-N₄ sites (*i.e.*, PtN₄C₁₂, PtN₄C₁₀, and PtN₂₊₂C₄₊₄) and thermodynamic overpotentials for OER ($\eta_{\text{TD(OER)}}$) at the overpotential (η_{OER}) of 0 and 0.13 V.
- Table 3.1** Interaction parameters of Fe²⁺-water (O_w in H₂O) and Fe²⁺-CO₃²⁻ (O_c in CO₃²⁻) and comparison of physical properties [*i.e.*, lattice parameters, bulk modulus (K), linear and volume thermal expansion coefficients (α_a , α_c , and V)], obtained from experiment and calculation.
- Table 3.2** Summary of model systems for Ca_{1-x}M_xCO₃· n H₂O used in MD simulations
- Table 3.3** First minimum of radial distribution function for M-O_c and M-O_w pairs (*i.e.*, M = Ca, Mg, Fe, Sr, and Ba).
- Table 3.4** Ionic radius and hydration free energy (ΔG_{hyd}) of divalent cations in the comparison of experiments and calculations.
- Table 4.1** Total adsorption energies (ΔE_{ads}), chemical bond formation energies (ΔE_{bond}), and reconstruction energies (ΔE_{recon}) of various lithium polysulfide (Li₂S _{x}) species on the CNT surface and in the bulk and layer of COF-1 and COF-5.

List of Figures

Chapter 1

- Figure 1.1** Global energy consumption in 2018. Taken from BP statistical review of world energy.¹
- Figure 1.2** Schematic of a sustainable energy conversion and storage systems. Reprinted from ref. 5. Copyright © 2017, American Association for the Advancement of Science.
- Figure 1.3** Catalytic *versus* non-catalytic pathway for electrochemical reactions. ‘*R*’, ‘*RI*’, and ‘*P*’ represents the reactant, reaction intermediate, and product, respectively. * denotes the adsorbed state.
- Figure 1.4** Volcano plot of exchange current density (j_0) as a function of Gibbs free energy of adsorbed hydrogen on pure metals. Reprinted from ref. 9, Copyright © 2005, the Electrochemical Society.
- Figure 1.5** Schematic illustration of *d*-band center theory describing a chemical bond formation between an adsorbate and surface. Reprinted from ref. 10, Copyright © 2011, National Academy of Sciences.
- Figure 1.6** Schematic illustration of catalytic biomineralization *via* adsorption of additive ions.
- Figure 1.7** Practical specific energies for rechargeable batteries. Light blue represents the range of expected specific energy under development. Reprinted from ref. 32 Copyright © 2016, Springer Nature.
- Figure 1.8** Schematic illustration of the electrochemical cycle of lithium polysulfides in Li-S battery. Reprinted from ref. 40. Copyright © 2019, Elsevier B.V.
- Figure 1.9** Schematic illustration of a rechargeable Li-O₂ battery. Reprinted from ref. 44 Copyright © 2011, Royal Society of Chemistry.
- Figure 1.10** Time *versus* Length (size) of simulation methods. DFT, GCMC, and MD stand for density functional theory, grand canonical Monte Carlo, and molecular dynamics.
- Figure 1.11** Schematic illustration for density functional theory calculation. Reprinted from ref. 51. Copyright © 2011, Materials Research Society.

Chapter 2

Figure 2.1 CER polarization curves of Pt₁/CNT, PtNP/CNT, DSA, and CNT catalysts obtained in 0.1 M HClO₄ + 1.0 M NaCl at an electrode rotation speed of 1600 rpm and a scan rate of 10 mV s⁻¹. The polarization curve of Pt₁/CNT catalyst measured in 0.1 M HClO₄ is also shown. The DSA catalyst (1 cm × 1 cm) was measured without electrode rotation.

Figure 2.2 Chronoamperograms of Pt₁/CNT and PtNP/CNT catalysts deposited on a carbon paper (1 cm × 1 cm) and DSA catalyst (1 cm × 1 cm) measured in 0.1 M HClO₄ + 1.0 M NaCl for 12 h with a stirring speed of 300 rpm.

Figure 2.3 Tafel plots of Pt₁/CNT, PtNP/CNT, and DSA catalysts.

Figure 2.4 Model systems for plausible Pt–N₄ sites including PtN₄C₁₂, PtN₄C₁₀, and PtN₂₊₂C₄₊₄. Six plausible adsorbates (*i.e.*, ClO*, Cl*, H*, OOH*, O*, and OH*) were considered. Coordination numbers (CNs) of Pt atoms in the PtN₂₊₂C₄₊₄ are labelled below. The white, black, pink, dark-blue, purple, and yellow-green coloured spheres represent the hydrogen, carbon, nitrogen, platinum, oxygen, and chlorine atoms, respectively.

Figure 2.5 Model systems for PtO₂ (110) surface including four plausible adsorption sites in top view. Among four plausible adsorption sites, including two bridged oxygen and two coordinatively unsaturated (cus) sites, a total of 18 combinations of adsorbate species (*i.e.*, O_b, OH_b at bridge sites as well as OH_c, Cl_c, O_c, OOH_c, O_{2(c)}, ClO_c at cus sites, respectively) were considered. Black dotted circles represent the adsorbate structures. Topmost layers are magnified with ball-and-stick style for visualization. The dark-blue and red spheres represent the platinum and oxygen atoms at the surface. The white, yellow-green, and purple spheres represent the hydrogen, chlorine, and oxygen atoms for the adsorbates, respectively.

Figure 2.6 The adsorption free energy for plausible adsorbates on three Pt–N₄ sites. Seven plausible adsorbates (*i.e.*, bare (*), Cl*, O*, ClO*, OH*, H*, and OOH*) on Pt–N₄ sites were considered as a function of the theoretical standard hydrogen electrode potential (U_{SHE}) at pH = 0: **a**, PtN₄C₁₂, **b**, PtN₄C₁₀, and **c**, PtN₂₊₂C₄₊₄.

Figure 2.7 The adsorption free energy (ΔG) for plausible adsorbates on PtO₂ (110) surface. A total 18 plausible combinations of adsorbate species (*i.e.*, O_b, OH_b at bridge sites as well as OH_c, Cl_c, O_c, OOH_c, O_{2(c)}, ClO_c at cus sites, respectively) were considered as a function of the theoretical standard hydrogen electrode potential (U_{SHE}) at pH = 0. Black dotted lines represent the phase boundary where two adsorbate species exist in equilibrium. The

most stable adsorbate species at each area (divided by black dotted line) are labelled below.

- Figure 2.8** Pourbaix diagram of theoretical standard hydrogen electrode potential (U_{SHE}) vs. pH for three Pt–N₄ sites in equilibrium with H⁺, Cl⁻ and H₂O at room temperature. **a**, PtN₄C₁₂, **b**, PtN₄C₁₀, and **c**, PtN₂₊₂C₄₊₄. Blue dashed line and red dashed line represent the equilibrium potential for CER in the SHE scale ($U_{\text{eq}} = 1.36$ V) and for OER ($U_{\text{eq}} = 1.23$ V – 0.059 pH), respectively. Black solid lines represent the phase boundary where two adsorbate species exist in equilibrium.
- Figure 2.9** Pourbaix diagram of theoretical standard hydrogen electrode potential (U_{SHE}) vs. pH for PtO₂ (110) surface. Red dashed line and blue dashed line represent the equilibrium potential for CER ($U_{\text{SHE}} = 1.36$ V) and that for OER, respectively. Black solid lines represent the phase boundary where two adsorbate species exist in equilibrium.
- Figure 2.10** Free energy diagrams for CER over Pt–N₄ clusters and PtO₂ (110) surface at zero overpotential ($\eta_{\text{CER}} = 0$ V).
- Figure 2.11** Model systems for PtO₂ (110) surface for CER (top view). Two plausible intermediate structures including 2O_b2Cl_c and 2O_b2ClO_c were considered. Black dotted circles represent reaction sites. Topmost layers are magnified with ball-and-stick style for visualization. Dark-blue and red spheres represent the platinum and oxygen atoms at the surface, while the yellow-green and purple spheres represent chlorine and oxygen atoms for the adsorbates, respectively.
- Figure 2.12** **a**, The difference between adsorption energy of Pt²⁺ ion in the Pt–N₄ sites (ΔE_{ads}) and the chlorination energy of Pt²⁺ ion in the [PtCl₄]²⁻ complex (ΔE_{Cl}). **b**, Optimized structure of [PtCl₄]²⁻ complex, used for ΔE_{Cl} calculation. Color legends – Pt: dark-blue; Cl: yellow-green.
- Figure 2.13** Experimental Tafel plot exhibiting two linear Tafel regions with Tafel slopes of 38 and 79 mV dec⁻¹. The fitting ranges of overpotential for CER (η_{CER}) are indicated. The exchange current density j_0 is given by the extrapolation.
- Figure 2.14** Full free energy diagram along the reaction coordinate of CER over the Pt₁/CNT at respective overpotential for CER (η_{CER}) of 0 V (black thick lines) and 0.09 V (red thick lines). #₁ and #₂ represent the transfer coefficients at each transition state (TS), which are determined as 0.83 and 0.58 from experimental Tafel plot, respectively. The TS with

higher free energy at the respective η_{CER} is indicated by purple line. Orange arrows represent the decreased amounts of free energies by applied η_{CER} for each state (*i.e.*, first TS (denoted as ‘#1’), intermediate state, second TS (denoted as ‘#2’), and final state, respectively). The free energy change for reaction intermediate at zero overpotential ($\Delta G_{\text{TD}(\text{CER})}$) is indicated by blue arrow.

Figure 2.15 Transition state (TS) free energy corresponding to the step # i ($G_{\#i}(\eta_{\text{CER}})$) as a function of applied overpotential η_{CER} in the Pt₁/CNT. The first step (#1) corresponds to the Heyrovsky step, while the second step (#2) corresponds to the Volmer step, respectively. The black dotted line indicates the thermodynamic optimum of PtN₄C₁₂ species, where the η_{CER} equals to the thermodynamic overpotential for CER [*i.e.*, $\eta_{\text{CER}} = \eta_{\text{TD}(\text{CER})}$ (= 0.09 V)].

Figure 2.16 Transition state (TS) free energy corresponding to the step # i ($G_{\#i}(\eta_{\text{CER}})$) as a function of applied overpotential η_{CER} in the Pt₁/CNT. The first step (#1) corresponds to the Heyrovsky step, while the second step (#2) corresponds to the Volmer step, respectively. The black dotted line indicates the thermodynamic optimum of PtN₄C₁₂ species, where the η_{CER} equals to the thermodynamic overpotential for CER [*i.e.*, $\eta_{\text{CER}} = \eta_{\text{TD}(\text{CER})}$ (= 0.09 V)].

Figure 2.17 Free energy diagrams for the OER on Pt–N₄ sites at zero overpotential ($\eta_{\text{OER}} = 0$ V); **a**, PtN₄C₁₂, PtN₄C₁₀ and **b**, PtN₂₊₂C₄₊₄. The active adsorbate structures for each model were employed as initial steps (*i.e.*, bare structure (*) for PtN₄C₁₂ and PtN₄C₁₀, and O* for PtN₂₊₂C₄₊₄, respectively). The black dotted line represents the thermoneutral state (*i.e.*, $\Delta G = 0$).

Chapter 3

- Figure 3.1** Mean square displacement analysis for water and ions (*i.e.*, Ca^{2+} and CO_3^{2-}) in the $\text{CaCO}_3 \cdot n\text{H}_2\text{O}$ system with different hydration levels **a-c**, at $n = 9$, and **d-f**, at $n = 1$. The black lines represent the fitting lines used for estimation of the self-diffusion coefficients.
- Figure 3.2** Dehydration scheme of the $\text{Ca}_{1-x}\text{M}_x\text{CO}_3 \cdot n\text{H}_2\text{O}$ system (*i.e.*, $x = 0 \sim 1$, $n = 0 \sim 9$), where $\text{M} = \text{Mg}^{2+}$, Fe^{2+} , Sr^{2+} , and Ba^{2+} . Color legends – C: gray; O: red; Ca: green; M: yellow; water: cyan.
- Figure 3.3** **a**, MD simulation snapshots for dehydration process of $\text{CaCO}_3 \cdot n\text{H}_2\text{O}$ system (*i.e.*, $n = 9, 6, 3, 1$, and 0). Color legends – C: gray; O: red; Ca: green; H: white. **b**, CN of Ca–O_c pairs in the $\text{CaCO}_3 \cdot n\text{H}_2\text{O}$ system (*i.e.*, $n = 0 \sim 9$). Left: fraction of the local structures corresponding to each CN; right: average CN of Ca–O_c pairs as a function of n . **c**, Self-diffusion coefficients (D) for ions and water in $\text{CaCO}_3 \cdot n\text{H}_2\text{O}$ system and reported values for bulk water and ion pairs in calcite.^{65,66} The black and red dotted lines are guidance for the eye.
- Figure 3.4** CN environment for divalent cations (M_{total} , including Ca^{2+} and M^{2+}) with oxygen atoms in the $\text{Ca}_{1-x}\text{M}_x\text{CO}_3 \cdot n\text{H}_2\text{O}$ systems. Molar composition (x) for M^{2+} were set to 0.5. **a** and **b**, Average CN for **a**, $\text{M}_{\text{total}}\text{--O}_c$ (O in CO_3^{2-}), **b**, $\text{M}_{\text{total}}\text{--O}_w$ (O in water) pairs. **c** and **d**, Relative CN (ΔCN) from the system without M^{2+} for **c**, $\text{M}_{\text{total}}\text{--O}_c$ and **d**, $\text{M}_{\text{total}}\text{--O}_w$ pairs.
- Figure 3.5** Relative CN (ΔCN) environment of O_c (O in CO_3^{2-}) around divalent cations [M_{total} , including Ca^{2+} and additive ions (*i.e.*, Mg^{2+} , Fe^{2+} , Sr^{2+} , and Ba^{2+})] in the $\text{Ca}_{1-x}\text{M}_x\text{CO}_3 \cdot n\text{H}_2\text{O}$ systems, where $\text{M} =$ **a**, Mg, **b**, Fe, **c**, Sr, and **d**, Ba [*i.e.*, $\Delta\text{CN} = \text{CN}(\text{Ca}_{1-x}\text{M}_x\text{CO}_3 \cdot n\text{H}_2\text{O}) - \text{CN}(\text{CaCO}_3 \cdot n\text{H}_2\text{O})$].
- Figure 3.6** Relative CN (ΔCN) environment of O_w (O in water) around divalent cations [M_{total} , including Ca^{2+} and additive ions (*i.e.*, Mg^{2+} , Fe^{2+} , Sr^{2+} , and Ba^{2+})] in the $\text{Ca}_{1-x}\text{M}_x\text{CO}_3 \cdot n\text{H}_2\text{O}$ systems, where $\text{M} =$ **a**, Mg, **b**, Fe, **c**, Sr, and **d**, Ba [*i.e.*, $\Delta\text{CN} = \text{CN}(\text{Ca}_{1-x}\text{M}_x\text{CO}_3 \cdot n\text{H}_2\text{O}) - \text{CN}(\text{CaCO}_3 \cdot n\text{H}_2\text{O})$].
- Figure 3.7** Molar volume change (ΔV_m) for $\text{Ca}_{1-x}\text{M}_x\text{CO}_3 \cdot n\text{H}_2\text{O}$ systems in the range of $n = 0 \sim 9$, where $\text{M} =$ **a**, Mg, **b**, Fe, **c**, Sr, and **d**, Ba.
- Figure 3.8** Enthalpy of formation (ΔH_f) for $\text{Ca}_{1-x}\text{M}_x\text{CO}_3 \cdot n\text{H}_2\text{O}$ systems in the range of $n = 0 \sim 9$, where $\text{M} =$ **a**, Mg, **b**, Fe, **c**, Sr, and **d**, Ba. The black circles represent the actual simulation

points used for constructing the contour plot. The black dotted lines represent the base line for the thermo-neutral state (*i.e.*, $\Delta H_f = 0$). The gray dotted lines represent the line for guidance of the location at $n = 3$.

Figure 3.9 Enthalpy of formation (ΔH_f) for $\text{Ca}_{1-x}\text{M}_x\text{CO}_3 \cdot n\text{H}_2\text{O}$ systems in the range of $n = \sim 3-9$, where $\text{M} = \mathbf{a}$, Mg, \mathbf{b} , Fe, \mathbf{c} , Sr, and \mathbf{d} , Ba. The black circles represent the actual simulation points used for constructing the contour plot. The black dotted lines represent the base line for the thermo-neutral state (*i.e.*, $\Delta H_f = 0$).

Figure 3.10 Enthalpy of formation (ΔH_f) for $\text{Ca}_{1-x}\text{M}_x\text{CO}_3 \cdot n\text{H}_2\text{O}$ systems in the range of $n = \sim 0-3$, where $\text{M} = \mathbf{a}$, Mg, \mathbf{b} , Fe, \mathbf{c} , Sr, and \mathbf{d} , Ba. The black circles represent the actual simulation points used for constructing the contour plot. The black dotted lines represent the base line for the thermo-neutral state (*i.e.*, $\Delta H_f = 0$).

Figure 3.11 Enthalpy of formation (ΔH_f) and its decomposed energy contributions including dehydration (ΔH_{dehyd}) and crystallization (ΔH_{cryst}) for $\text{Ca}_{1-x}\text{M}_x\text{CO}_3 \cdot n\text{H}_2\text{O}$ systems (*i.e.*, $\text{M} = \text{Mg, Fe}$ and $x = 0, 0.25, 0.5, 0.75$ and 1) in the range of $n = 0-3$. The red (or blue) shaded arrows represent the direction of increasing the endothermicity (or exothermicity). The red dotted lines represent the base line for the thermo-neutral state (*i.e.*, $\Delta H_f = 0$).

Figure 3.12 Enthalpy of formation (ΔH_f) and its decomposed energy contributions including dehydration (ΔH_{dehyd}) and crystallization (ΔH_{cryst}) for $\text{Ca}_{1-x}\text{M}_x\text{CO}_3 \cdot n\text{H}_2\text{O}$ systems (*i.e.*, $\text{M} = \text{Sr, Ba}$ and $x = 0, 0.25, 0.5, 0.75$ and 1) in the range of $n = 0-3$. The blue shaded arrows represent the direction of increasing the endothermicity (or exothermicity). The red dotted lines represent the base line for the thermo-neutral state (*i.e.*, $\Delta H_f = 0$).

Figure 3.13 Enthalpy of formation (ΔH_f) and its decomposed enthalpic contributions including electrostatic ($\Delta H_{\text{f(ES)}}$) and van der Waals interactions ($\Delta H_{\text{f(vdW)}}$) for $\text{Ca}_{1-x}\text{M}_x\text{CO}_3 \cdot n\text{H}_2\text{O}$ systems (*i.e.*, $\text{M} = \text{Mg, Fe}$ and $x = 0, 0.25, 0.5, 0.75$ and 1) in the range of $n = 0-9$. The red (or blue) shaded arrows represent the direction of increasing the endothermicity (or exothermicity). The red dotted lines represent the base line for the thermo-neutral state (*i.e.*, $\Delta H_f = 0$).

Figure 3.14 Enthalpy of formation (ΔH_f) and its decomposed enthalpic contributions including electrostatic ($\Delta H_{\text{f(ES)}}$) and van der Waals interactions ($\Delta H_{\text{f(vdW)}}$) for $\text{Ca}_{1-x}\text{M}_x\text{CO}_3 \cdot n\text{H}_2\text{O}$ systems (*i.e.*, $\text{M} = \text{Sr, Ba}$ and $x = 0, 0.25, 0.5, 0.75$ and 1) in the range of $n = 0-9$. The

red (or blue) shaded arrows represent the direction of increasing the endothermicity (or exothermicity). The red dotted lines represent the base line for the thermo-neutral state (*i.e.*, $\Delta H_f = 0$).

Figure 3.15 **a** and **b**, Schematics for the relationships of two opposing factors (*i.e.*, dehydration and crystallization) acting on the ΔH_f as a function of water content (n) and mole fraction of additive ions (x) in the $\text{Ca}_{1-x}\text{M}_x\text{CO}_3 \cdot n\text{H}_2\text{O}$ systems, where **a**, $\text{M} = \text{Mg}$ or Fe and **b**, $\text{M} = \text{Sr}$ or Ba , respectively.

Figure 3.16 Schematics for dehydration and crystallization process from amorphous precursor phases (*i.e.*, $\text{Ca}_{1-x}\text{M}_x\text{CO}_3 \cdot n\text{H}_2\text{O}$) to phase-separated crystalline structures (*i.e.*, $(1-x)\text{CaCO}_3$ and $x\text{MCO}_3$) and liquid water ($n\text{H}_2\text{O}$).

Figure 3.17 Comparison of total distribution function (TDF, $D(r)$) between experiment⁷⁰ and calculated model system for hydrated ACC ($\text{CaCO}_3 \cdot n\text{H}_2\text{O}$, $n = 1$), obtained from our simulation.

Figure 3.18 **a** and **b**, Total distribution functions (TDFs, $D(r)$) for $\text{Ca}_{1-x}\text{M}_x\text{CO}_3 \cdot n\text{H}_2\text{O}$ systems with $n = 1$, where $\text{M} = \mathbf{a}$, Mg and **b**, Fe . The pink, brown, and sky-blue dashed lines represent the $\text{M}-\text{O}_w$, $\text{M}-\text{O}_c$, and $\text{M}-\text{M}$ pairs of each ACC system, respectively.

Figure 3.19 **a** and **b**, Total distribution functions (TDFs, $D(r)$) for $\text{Ca}_{1-x}\text{M}_x\text{CO}_3 \cdot n\text{H}_2\text{O}$ systems with $n = 1$, where $\text{M} = \mathbf{a}$, Sr and **b**, Ba . The pink, brown, and sky-blue dashed lines represent the $\text{M}-\text{O}_w$, $\text{M}-\text{O}_c$, and $\text{M}-\text{M}$ pairs of each ACC system, respectively.

Figure 3.20 Pair-distribution function (PDF, $g(r)$) of $\text{Ca}_{1-x}\text{M}_x\text{CO}_3 \cdot n\text{H}_2\text{O}$ systems for $\text{M}-\text{O}_w$ (O in water) pairs with $n = 1$, where $\text{M} = \mathbf{a}$, Mg , **b**, Fe , **c**, Sr , and **d**, Ba . Note that PDF were scaled by a factor $(4\pi\rho_0 r \left[c_i c_j \cdot z_i z_j / \left(\sum_{k=1}^n c_k z_k \right)^2 \right])$ for each pair in the $D(r)$.

Figure 3.21 Pair-distribution function (PDF, $g(r)$) of $\text{Ca}_{1-x}\text{M}_x\text{CO}_3 \cdot n\text{H}_2\text{O}$ systems for $\text{M}-\text{M}$ pairs with $n = 1$, where $\text{M} = \mathbf{a}$, Mg , **b**, Fe , **c**, Sr , and **d**, Ba . Note that PDF were scaled by a factor $(4\pi\rho_0 r \left[c_i c_j \cdot z_i z_j / \left(\sum_{k=1}^n c_k z_k \right)^2 \right])$ for each pair in the $D(r)$.

Chapter 4

Figure 4.1 Model systems of Li_2S_x and COFs. **a**, Optimized geometries of Li_2S_x ($x = 1, 4, 6,$ and 8) molecules identified by DFT calculations. Purple and yellow colored atoms represent the lithium and sulfur, respectively. **b**, Optimized unit cell model of COF-1 by full relaxation including both atomic positions and lattice parameters. The $1 \times 1 \times 2$ supercell was built for representing the bulk state. For layer models, the vacuum was sufficiently applied in the z -direction (*i.e.*, $\sim 20 \text{ \AA}$) for the $1 \times 1 \times 3$ supercell with fixed two bottom layers. **c**, Optimized unit cell model of the COF-5. The $1 \times 1 \times 2$ and $1 \times 1 \times 3$ supercells were built for the bulk state and layer model, respectively.

Figure 4.2 Synthetic scheme and chemical structures of COF-1 and COF-5.

Figure 4.3 **a**, Pore size and of COFs (COF-1 and COF-5) and molecular size of Li_2S_x species ($x = 1, 4, 6,$ and 8). Pore volume (PV) and molecular volume (estimated by Connolly surface method³⁷) are labelled below. Color legends – C: gray; O: red; H: white; B: pink; Li: purple; S: yellow. **b**, Snapshots depicting the binding configurations of polysulfides in COF-1 (blue box, left) and COF-5 (green box, right), and averaged loading amounts of Li_2S_x species ($x = 1, 4, 6,$ and 8), calculated through GCMC simulation. Blue, red, orange, and green circles represent Li_2S , Li_2S_4 , Li_2S_6 , and Li_2S_8 , respectively.

Figure 4.4 Binding configurations of Li_2S_x molecules on partially cleaved CNT surface; **a**, Li_2S , **b**, Li_2S_4 , **c**, Li_2S_6 , and **d**, Li_2S_8 . $\Delta q(\text{CT})$ values indicate the transferred charges of molecules. Gray, purple, and yellow balls represent C, Li, and S atoms, respectively. Red balls signify the fixed hydrogen-terminated sites.

Figure 4.5 Binding configurations of Li_2S_x ($x = 1, 4, 6,$ and 8) molecules in the bulk state of COF-5; **a**, Li_2S , **b**, Li_2S_4 , **c**, Li_2S_6 , and **d**, Li_2S_8 . $\Delta q(\text{CT})$ values indicate the transferred charges of molecules. Purple and yellow balls represent the Li and S atoms of the Li_2S_x , respectively. Alternate multi-plices between green and orange layers represent the AA-eclipsed stacking arrangement.

Figure 4.6 Binding configurations of Li_2S_x ($x = 1, 4, 6,$ and 8) molecules in the layer models of COF-5; **a**, Li_2S , **b**, Li_2S_4 , **c**, Li_2S_6 , and **d**, Li_2S_8 . $\Delta q(\text{CT})$ values indicate the transferred charges of molecules. Purple and yellow balls represent the Li and S atoms of the Li_2S_x , respectively. Alternate multi-plices between green and orange layers represent the AA-eclipsed stacking arrangement.

- Figure 4.7** Binding configurations of Li_2S in the bulk state of COF-1, in which $\Delta q(\text{CT})$ values indicate the transferred charges of molecules. Purple and yellow balls represent the Li and S atoms of the Li_2S , respectively. Alternate multi-ply layers between green and orange layers represent the AB-staggered stacking arrangement.
- Figure 4.8** Binding configurations of Li_2S_x ($x = 1, 4, 6,$ and 8) molecules in the layer models of COF-1; **a**, Li_2S , **b**, Li_2S_4 , **c**, Li_2S_6 , and **d**, Li_2S_8 . $\Delta q(\text{CT})$ values indicate the transferred charges of molecules. Purple and yellow balls represent the Li and S atoms of the Li_2S_x , respectively. Alternate multi-ply layers between green and orange layers with fixed two bottom layers (red) represent the AB-staggered stacking arrangement.
- Figure 4.9** Change in the local density of states (LDOS) of Li_2S (red line) and boron of COF-1 (black line), before (dotted line) and after Li_2S adsorption (solid line). Electronic structures of Li_2S -adsorbed COF-1 [*i.e.*, HOMO-2 (green box, left) and HOMO-1 (blue box, right)] are shown, along with those of pristine Li_2S [*i.e.*, HOMO-2 (black box, left) and HOMO-1 (black box, right)]. The overlapped peaks in the LDOSs and obvious orbital mixing in both HOMO-2 and HOMO-1 verify the electrostatic stabilization-driven formation of chemical bonds between sulfur and boron.
- Figure 4.10** Effect of NN interlayers on the electrochemical performance of Li-S cells. Cycling performance (at charge/discharge current density = 2.0 C/2.0 C).
- Figure 4.11** **a-c**, SEM images (top) of **a**, CNT, **b**, COF-1 NN interlayer, **c**, COF-5 NN interlayers after the 300th cycle (at charge/discharge current density = 2 C/2 C). The yellow arrows and circles indicate the Li_2S aggregates and clogged pores, respectively. Schematic illustrations (bottom) represent the deposition/dissolution behavior of Li_2S on CNT, the COF-1 NN interlayer, and the COF-5 NN interlayer.
- Figure 4.12** Binding configurations, total adsorption energies (ΔE_{ads}) and chemical bond formation energies (ΔE_{bond}) of Li_2S on CNT surface (left) and in the bulk of COF-5 (center) and COF-1 (right). Gray, purple, yellow, red, pink, and white balls represent the carbon, lithium, sulfur, oxygen, boron, and hydrogen atoms, respectively. The $\Delta q(\text{CT})$ values represent the transferred amount of Mulliken charges of respective systems. Atomic charges of Li_2S and Li_2S -adsorbed COF atoms are indicated on the balls.

Chapter 5

- Figure 5.1** **a** and **b**, Discharge process of oxygen to Li_2O_2 on air cathode of LOBs. **a**, Two dominant mechanisms of the discharge process of oxygen to Li_2O_2 : surface mechanism *versus* solution mechanism. Superoxide radicals ($\text{O}_2^{\cdot-}$) generated from electrochemical reduction of oxygen are deposited on electrode surface and/or dissolved in electrolyte. Two molecules of the dissolved $\text{O}_2^{\cdot-}$ are *chemically* disproportionated to oxygen and peroxide in the solution mechanism while the lithium superoxide deposit on electrode surface is *electrochemically* reduced to lithium peroxide. **b**, Superoxide-triggered side reactions decomposing carbon constituents of electrodes and electrolytes. The solution mechanism encouraged by a SOD-mimetic superoxide disproportionation catalyst, MA-C₆₀. Two superoxide molecules adsorbed on MA-C₆₀ are *chemically* disproportionated by: $2 \text{O}_2^{\cdot-} \rightarrow \text{O}_2 + \text{O}_2^{2-}$. The peroxide (O_2^{2-}) is combined with Li^+ captured by MA-C₆₀ to form toroidal Li_2O_2 on electrode surface.
- Figure 5.2** MA-C₆₀ for LOB cells. Potential profiles of LOBs at galvanostatic discharge in three different ether solvents having low donor and acceptor numbers. MA-C₆₀-free (dashed) and MA-C₆₀-containing (solid) LOB cells were compared. TEGDME = tetraethylene glycol dimethyl ether; DME = dimethoxyethane. The current densities in mA cm^{-2} are indicated in the top; 0.1 mA cm^{-2} was used for the middle and bottom.
- Figure 5.3** **a**, The optimized structures of $[\text{Li}(\text{DEGDME})]^+$ and $[\text{Li}(\text{TEGDME})]^+$ complexes: yellow = lithium, gray = carbon, red = oxygen, hydrogen = white. The binding energies (ΔE_{bind}) and the coordination number of the solvent molecule to a lithium ion (CN) were indicated. **b** and **c**, Molecular dynamics model systems of MA-C₆₀ dispersed in **b**, DEGDME and **c**, TEGDME in the presence of LiTFSI: sky blue = DEGDME, cyan = $[\text{Li}(\text{DEGDME})]^+$, red = TEGDME, light pink = $[\text{Li}(\text{TEGDME})]^+$, gray = TFSI. **d**, The average number of lithium ions captured by MA-C₆₀'s (n_{Li}) in DEGDME *versus* TEGDME.
- Figure 5.4** Model systems of MA-C₆₀'s for $\text{O}_2^{\cdot-}$ adsorption energy (ΔE_{ads}) calculation. Carbon, hydrogen, and oxygen atoms of MA-C₆₀ are colored in gray, white, and red, respectively. Oxygen atoms of superoxide are colored in orange.
- Figure 5.5** Model systems of MA-C₆₀'s for LiO_2 adsorption energy (ΔE_{ads}) calculation. Carbon, hydrogen, and oxygen atoms of MA-C₆₀ are colored in gray, white, and red, respectively. Lithium and oxygen atoms of LiO_2 are colored in yellow and orange, respectively.

- Figure 5.6** Superoxide ($\text{O}_2^{\bullet-}$) adsorption energy (ΔE_{ads}) on MA-C₆₀ *versus* on the (100) surface of Li₂O₂. C = gray; H = white; O = orange only for superoxide and yellow for the rest; Li = yellow.
- Figure 5.7** Free energy diagrams for Li₂O₂ formation through reaction pathways of the solution mechanism in the presence of MA-C₆₀ *versus* in the absence of MA-C₆₀. The pin-colored region indicates the disproportionation step from LiO₂ dimers into Li₂O₂ and solvated oxygen.
- Figure 5.8** Model systems used for calculating the free energy diagram of Li₂O₂ formation *via* solution mechanism in the presence of MA-C₆₀ (denoted as ‘MA-C₆₀’ in **Figure 5.7**). Carbon, hydrogen, and oxygen atoms of MA-C₆₀ are colored in gray, white and red, respectively. Lithium and oxygen atoms of O₂^{•-}, LiO₂ and Li₂O₂ species are colored in yellow and orange, respectively.
- Figure 5.9** Voltage profiles of LOB cells containing MA-C₆₀ or malonic acid (MA) as an additive. 2 mM MA-C₆₀ was used while 6 mM or 50 mM malonic acid was used. The LOB cells were galvanostatically discharged at 0.1 mA cm⁻² as indicated. Lab-made Swagelok-type LOB cells were constructed with a binder-free carbon-fibre gas diffusion layer (GDL, P50, AvCarb) as a cathode and lithium metal disk of 12 mm in diameter as an anode. 1 M LiTFSI in DEGDME was used as electrolyte.
- Figure 5.10** **a**, Electrostatic potential maps around the electron density isosurfaces of the optimized structure of MA-C₆₀ and MA. The 5-mer cluster configuration based on hydrogen bonding was used for representing the MAs in an aprotic solvent. **b**, The adsorption energy (ΔE_{ads}) of superoxide to MA and MA-C₆₀. ΔE_{ads} changed with the number of superoxide adsorbed on the indicated fraction of molecules.

Chapter 1. Introduction

1.1 General Introduction

A secure energy future is threatened by increasing energy demands and global population. To date, the vast majority of the world's energy resources have been derived from fossil fuels. In 2018, the use of hydrocarbon resources including coal, oil, and natural gas reached ~85% of world energy consumption (**Figure 1.1**), while hydro-electricity and renewables only accounted for 6.8% and 4.0%, respectively. The rising energy demand from rapid industrial development is causing a global challenge to find alternative energy sources before fossil fuels are depleted. In addition to resource depletion, combustion of fossil fuels emits carbon dioxide, a cause of serious environmental problems such as global warming.²⁻⁴ In this regard, our goal is to develop a sustainable, environmentally-friendly energy system that can meet rising energy demands and reduce dependency on hydrocarbons (**Figure 1.2**).⁵ This goal should be preceded by the development of renewable energy conversion processes that can produce important fuels and chemicals (*e.g.*, hydrogen, oxygen, and hydrocarbons) from earth-abundant molecules (*e.g.*, nitrogen, carbon dioxide, and water).⁵ Catalysts play a central role in these energy conversion technologies since they enhance the rate of chemical reactions. Moreover, the development of efficient energy storage systems such as lithium-ion batteries, lithium-metal batteries, and metal-air batteries is equally important for practical applications of renewable energy sources. However, current energy conversion and storage technologies are inadequate. Therefore, the design and development of advanced catalysts and battery materials is of great importance for the widespread deployment of clean energy technologies.

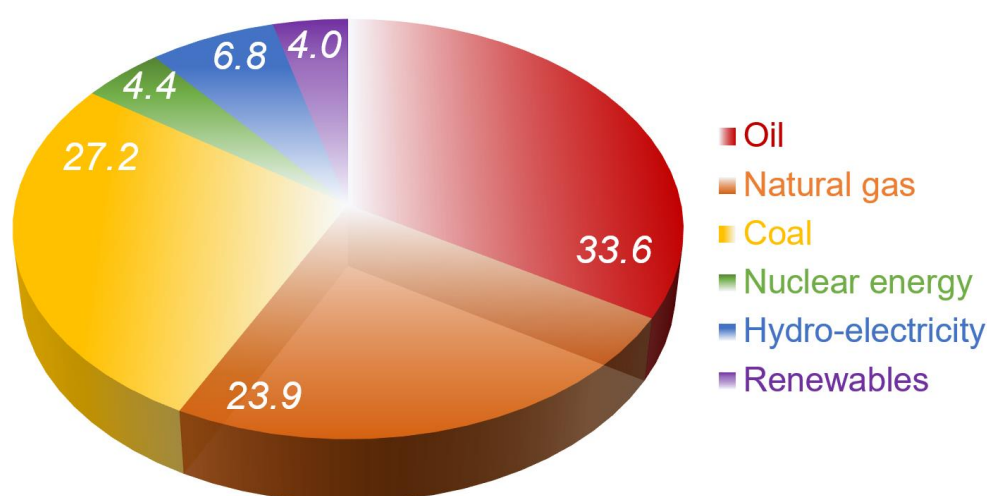


Figure 1.1 Global energy consumption in 2018. Taken from BP statistical review of world energy.¹

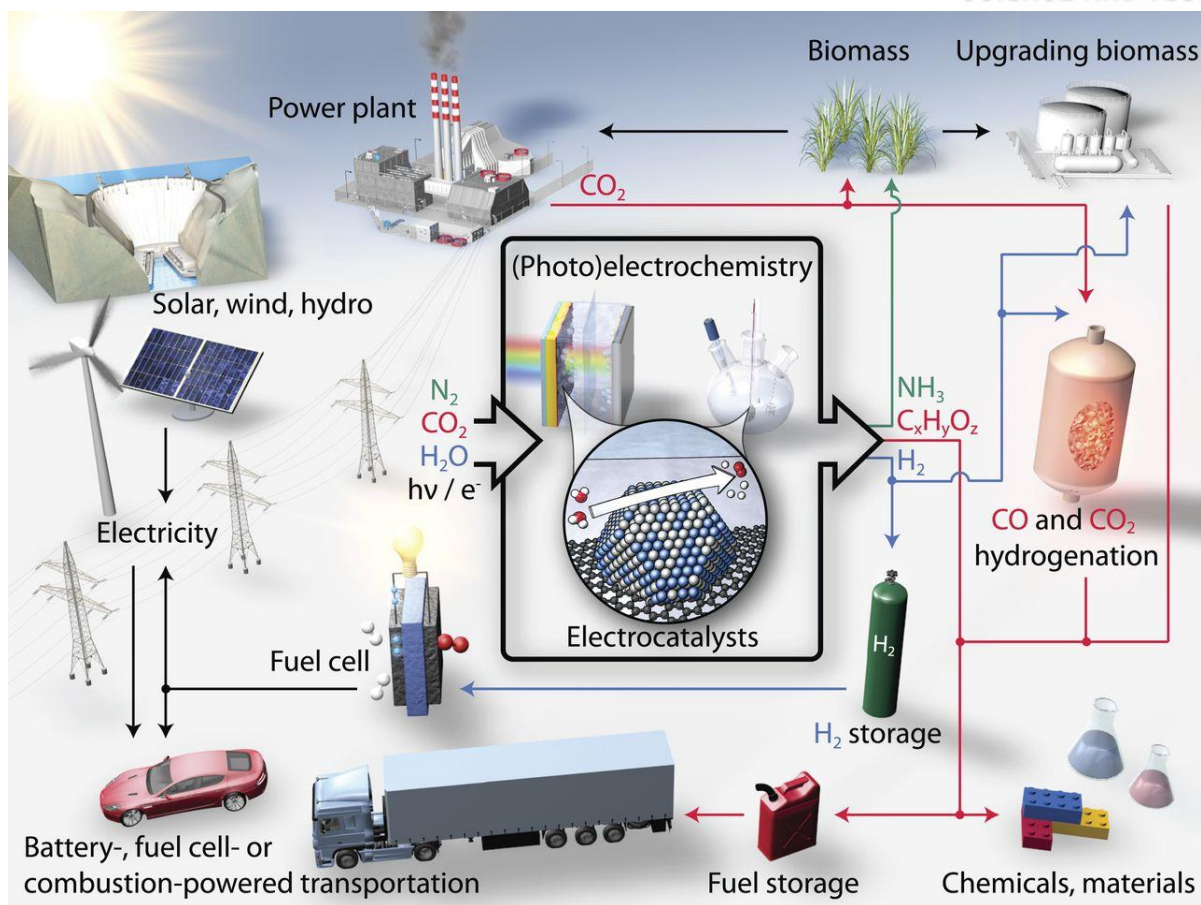


Figure 1.2 Schematic of a sustainable energy conversion and storage systems. Reprinted from ref. 5. Copyright © 2017, American Association for the Advancement of Science.

1.2 Adsorption in Electrocatalysis

In order to develop advanced electrocatalysts for practical uses, the overpotential of reactions should be minimized to enhance the rate of these chemical reactions. Electrocatalytic processes usually involve the adsorption of reactants on the catalyst, and the subsequent generation of active intermediates by forming chemical bonds between the catalyst and adsorbates. Therefore, the energetics of active reaction intermediates enables the prediction of the overall pathway of an electrocatalytic reaction (Figure 1.3).

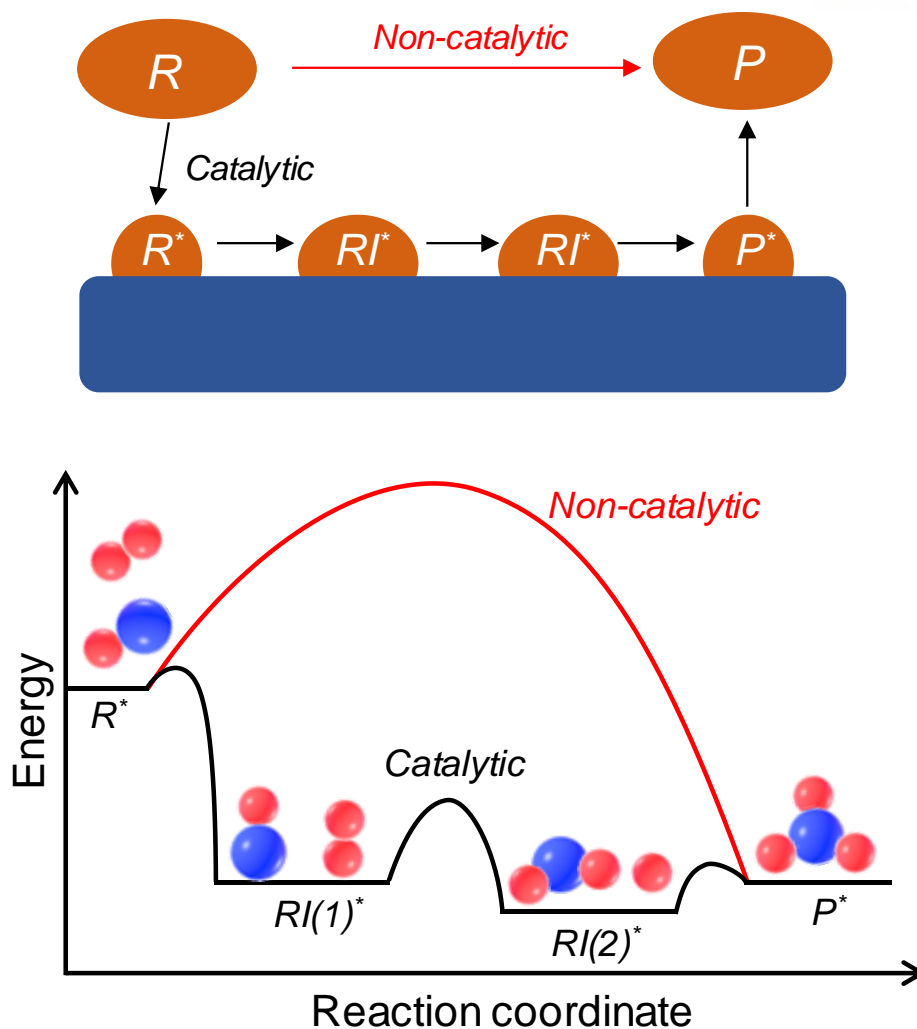


Figure 1.3 Catalytic *versus* non-catalytic pathway for electrochemical reactions. ‘*R*’, ‘*RI*’, and ‘*P*’ represents the reactant, reaction intermediate, and product, respectively. * denotes the adsorbed state.

This concept can also be explained by the “Sabatier principle” that ideal catalysts should bind intermediates neither too strongly nor too weakly.⁶ Moreover, the concept of “Bronsted-Evans-Polanyi” (BEP) relation indicates that an energetic change in transition states (*i.e.*, kinetics) is linearly related to the free energy of reaction (*i.e.*, thermodynamics).⁷ By combining the Sabatier principle and BEP relation, the adsorption free energy of reaction intermediates can be used as the activity descriptor in the form of volcano plot, which was invented by Nørskov and co-workers (**Figure 1.4**).^{8,9} Over the past decade, volcano relations have been accepted as a useful guide to predict the catalytic activity. As an associated approach, description of the relationship between the catalytic activity and intrinsic electronic properties of a catalyst, such as *d*-band center theory (**Figure 1.5**),¹⁰ has also been developed

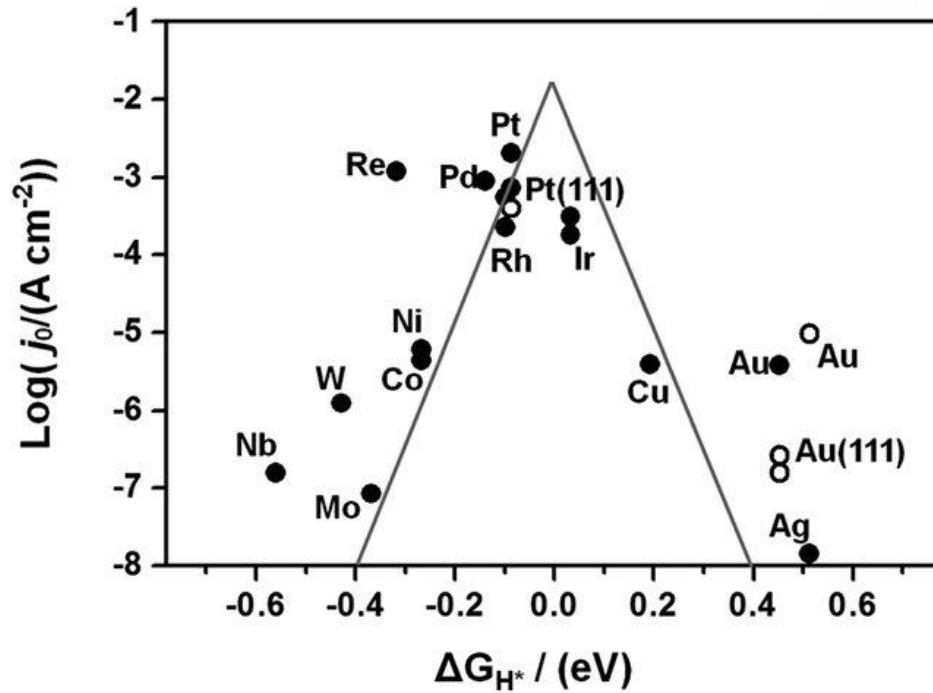


Figure 1.4 Volcano plot of exchange current density (j_0) versus adsorption free energy of hydrogen atoms (ΔG_{H^*}) on pure metals. Reprinted from ref. 9. Copyright © 2005, the Electrochemical Society.

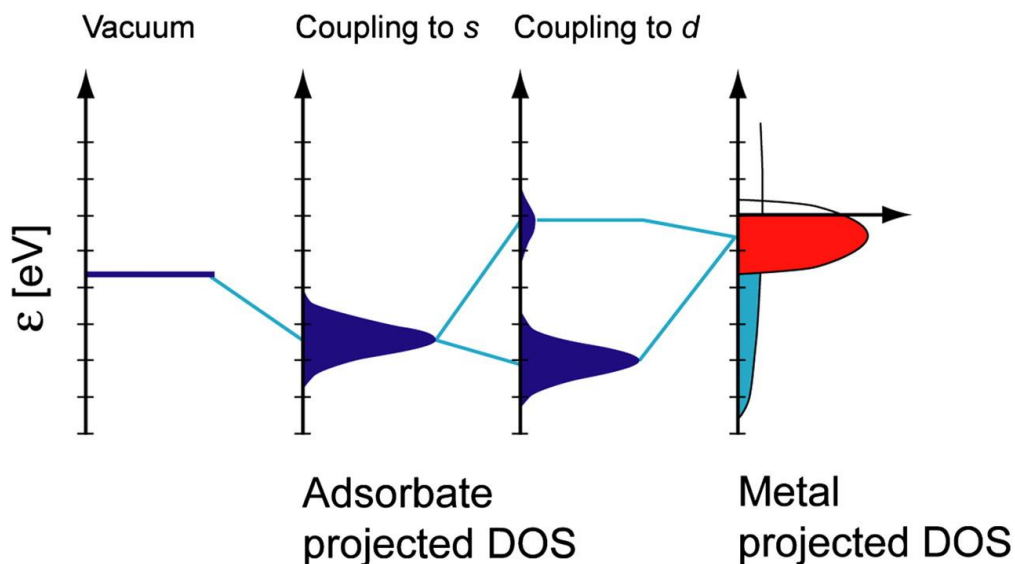


Figure 1.5 Schematic illustration of d -band center theory describing a chemical bond formation between an adsorbate and surface. Reprinted from ref. 10. Copyright © 2011, National Academy of Sciences.

to broaden the fundamental understanding of catalytic activity. Therefore, understanding the adsorption behaviors in electrocatalytic reactions is crucial for predicting the activity and designing the advanced electrocatalysts.

1.3 Adsorption in Catalytic Biomineralization

Biomineralization is a process that living organism produce minerals. One of the most abundant biomineral in nature is calcium carbonate, which exists in a variety of marine environments including corals, shells of mollusks, etc.^{11,12} In particular, amorphous calcium carbonate (ACC) has received considerable attentions as an important intermediate for biomineralization process.¹³⁻¹⁸ In general, ACC exists in a hydrated state and subsequently transitioned into crystalline counterparts *via* a stepwise phase transition process (**Figure 1.6**).^{19,20} In this context, various kinds of additives have been used to facilitate the biomineralization process, which can be referred to the ‘catalytic biomineralization’.²¹ It has been reported for several inorganic ions that their adsorption onto carbonate surface can induce the different morphologies, or affect the lifetime of ACC phases.²²⁻²⁵ However, the precise role of ion adsorption in controlling the local structures and stability of amorphous intermediate phases still remains unclear; that is, it is the first step that should be examined to achieve a comprehensive understanding of catalytic biomineralization process.

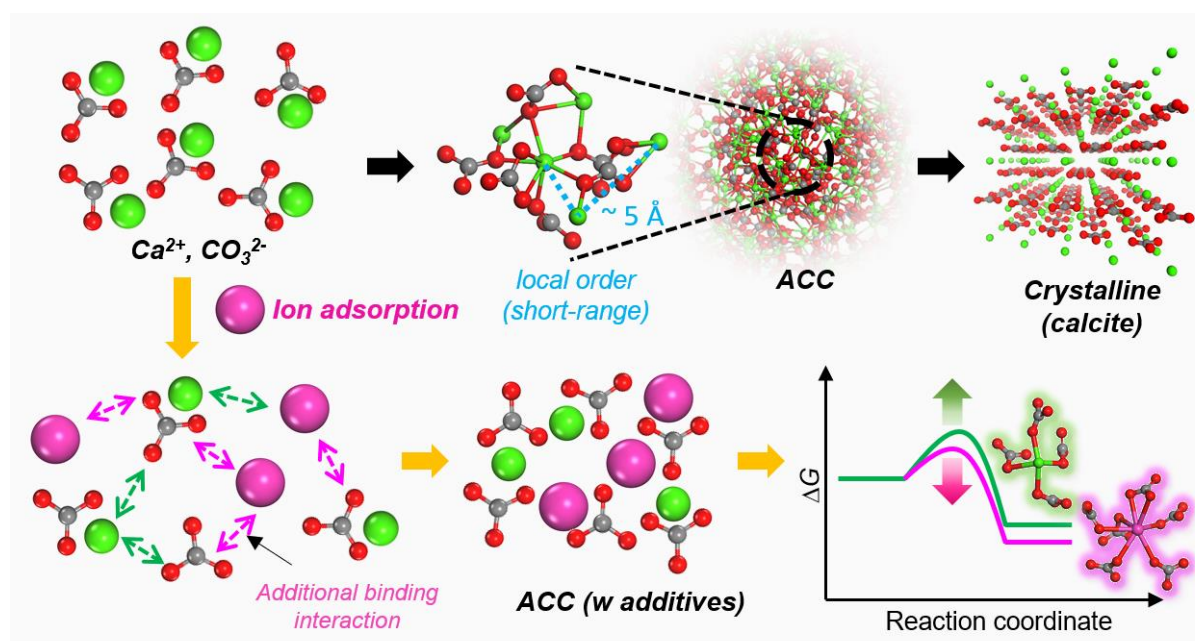


Figure 1.6 Schematic illustration of catalytic biomineralization *via* adsorption of additive ions.

1.4 Adsorption in Next-Generation Rechargeable Batteries

Lithium-ion (Li-ion) battery is considered as one of the most energy efficient storage technologies in a wide variety of applications, spanning from portable electronics to electric vehicles.²⁶⁻²⁹ However, the current state of Li-ion battery technology cannot satisfy future energy demands stemming from large-scale commercialization. In this context, a variety of next-generation rechargeable batteries have been developed to respond to these ever-growing energy demands. At present, two Li-based technologies are receiving enormous attentions as viable options for next-generation battery systems – lithium-sulfur (Li-S) and lithium-air (hereafter denoted as ‘Li-O₂’, using O₂ as fuels) batteries.^{30,31} Both of these technologies have large practical specific energies (> 400 Wh kg⁻¹) that are promising for long-term applications in transport systems (**Figure 1.7**).³² These batteries commonly employ Li metal as the anode, but they have different active cathode materials (S or O₂) that leads to different electrochemical cell chemistries. Common challenges associated with Li-S and Li-O₂ batteries include the effective adsorption of floating reaction intermediates (*i.e.*, lithium polysulfides for Li-S battery and superoxide for Li-O₂ battery) that causes serious problems affecting the cell performance, such as short cycle life, cell polarization, and shuttle reactions.³³⁻³⁷

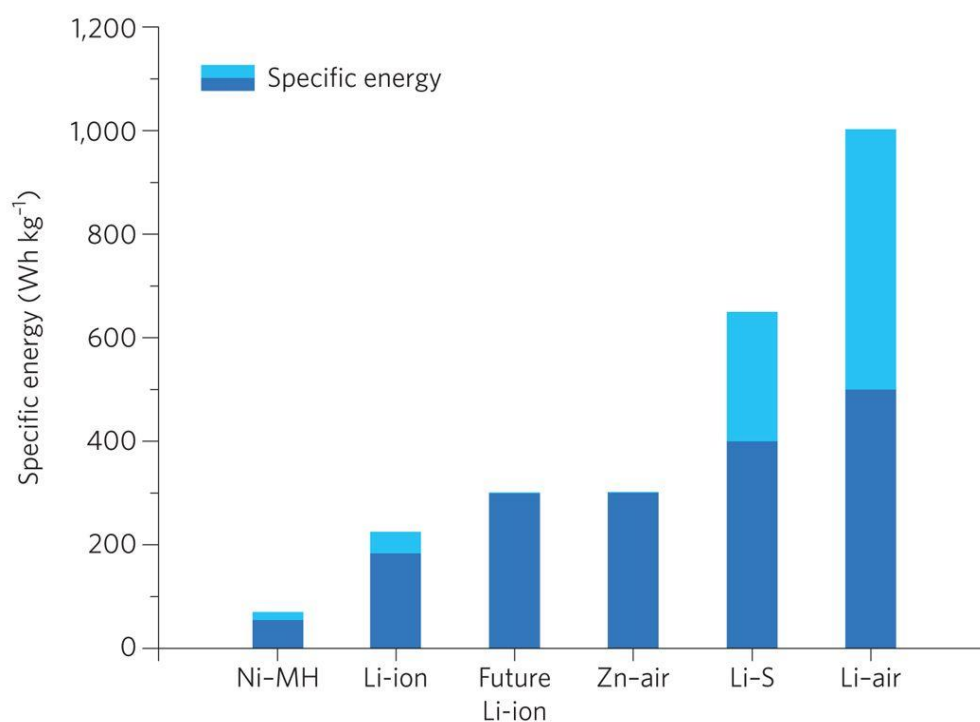


Figure 1.7 Specific energies for rechargeable battery systems. Light blue represents the range of expected specific energy under development. Reprinted from ref. 32. Copyright © 2016, Springer Nature.

1.4.1 Lithium-Sulfur Battery

The Li-S battery has garnered considerable attentions as the successor to the Li-ion battery due to its high theoretical capacity (1672 mAh g^{-1}), natural abundance, and environmental compatibility of sulfur.^{31,38-39} These batteries operate by the reduction of a sulfur compound (S_8) to form various Li_2S_x during the discharge process (**Figure 1.8**).⁴⁰ Despite various attractive features, a few critical challenges remain for practical applications, such as (i) the insulating nature of solid discharge products (Li_2S and Li_2S_2), (ii) the structural instability of sulfur cathodes, and (iii) the shuttle phenomena of lithium polysulfides (Li_2S_x).³⁴⁻³⁷ Among these problems, the shuttle phenomenon arises because soluble polysulfides migrate to the Li metal anode, and deposit as insoluble Li_2S or Li_2S_2 . These deposits result in a significant reduction of Coulombic efficiency and capacity.⁴¹ Therefore, the shuttle phenomenon is the most critical challenge to sustainable electrochemical performance of Li-S batteries. Resolving the adsorption of lithium polysulfides is an important hurdle to develop the advanced Li-S batteries for practical use.

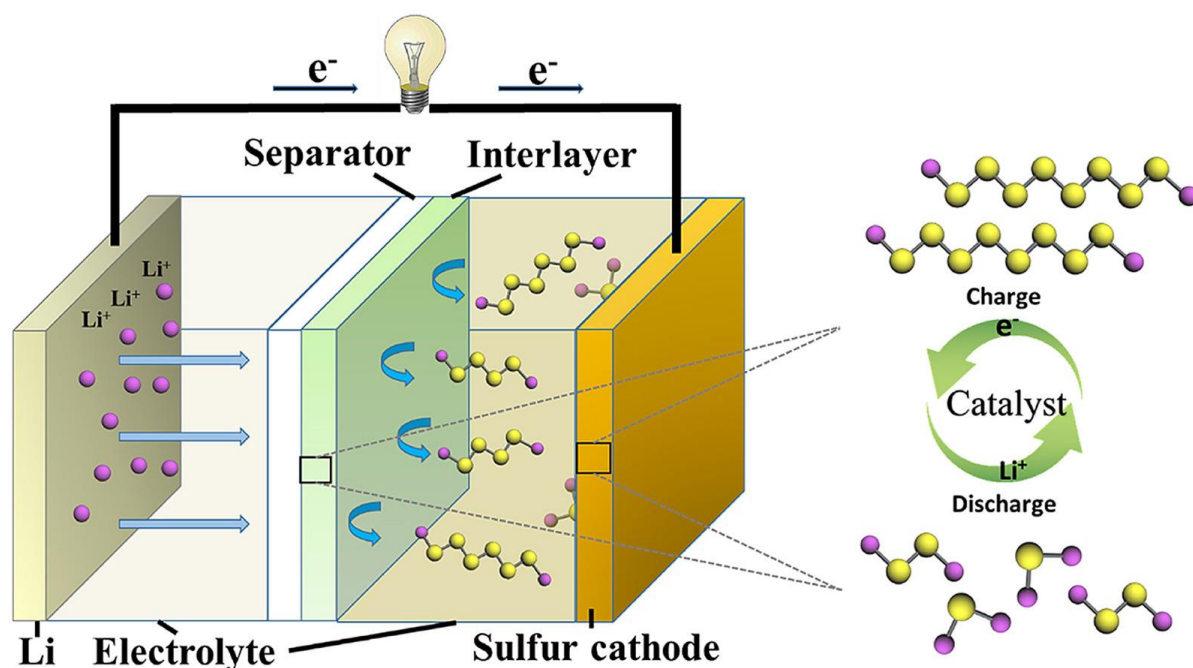


Figure 1.8 Schematic illustration of the electrochemical cycle of lithium polysulfides in Li-S battery. Reprinted from ref. 40. Copyright © 2019, Elsevier B.V.

1.4.2 Lithium-Oxygen Battery

The Li-O₂ battery, which uses O₂ as fuel, has the highest theoretical specific energy (3,500 Wh kg⁻¹) among any battery.^{42,43} Despite this energy storage advantage over many other technologies, the underlying electrochemistry is still lack of understanding. During the discharge process, O₂ is initially reduced to reactive superoxide species (O₂⁻ or LiO₂), and subsequently transformed into less reactive lithium peroxide (Li₂O₂) (**Figure 1.9**).⁴⁴ The performance of Li-O₂ battery is hampered by side reactions triggered by the nucleophile attack of reactive O₂⁻ species to the solvent molecules and carbon cathodes, leading to the formation of Li₂CO₃ and LiOH products.⁴⁵⁻⁴⁷ While forming the desired Li₂O₂ product from reactive O₂⁻ species, two different pathways exist that depend on whether the reaction occurs – on the electrode surface (“surface mechanism”) or in the electrolyte (“solution mechanism”).^{45,47,48,49} In the surface mechanism, O₂⁻ species combines with Li⁺ to become insoluble LiO₂ on the surface and are then, electrochemically converted to Li₂O₂. In the solution mechanism, O₂⁻ species, dissolved in the electrolyte, subsequently form toroidal Li₂O₂ nanoparticles without the transient formation of insoluble LiO₂. The solution mechanism is preferred for higher capacity and longer cycle life because the Li₂O₂ film formed *via* surface mechanism hinders electron transfer to the reactant due to the insulating nature of this film.⁵⁰ The key factor that determines to follow the solution pathway of Li₂O₂ formation is closely related to the adsorption strength of a reaction intermediate, LiO₂, and its relative stability in solution.⁴⁹ Therefore, investigations of catalysts that enable proper adsorption control of the reaction intermediate (O₂⁻ or LiO₂) are promising for the advanced design of Li-O₂ battery.

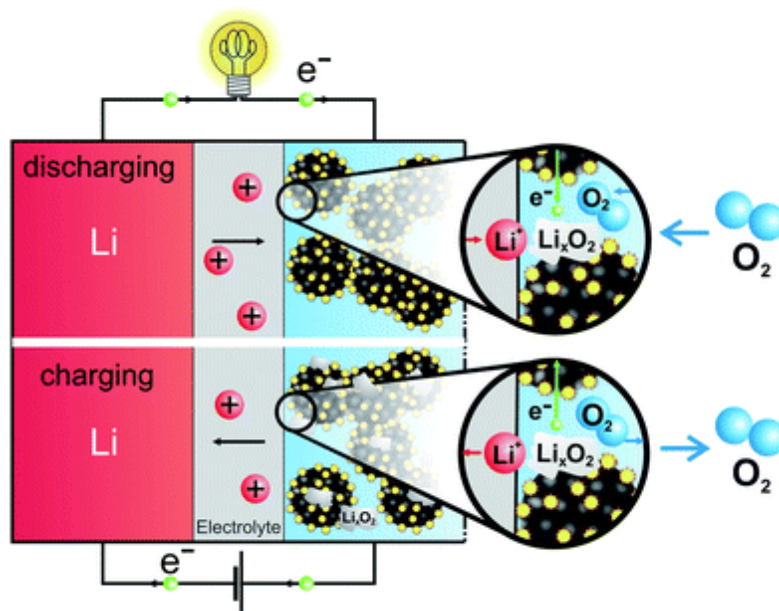


Figure 1.9 Schematic illustration of a rechargeable Li-O₂ battery. Reprinted from ref. 44. Copyright © 2011, Royal Society of Chemistry.

1.5 Multi-Scale Molecular Simulation

One goal in the development of energy conversion and storage technologies is to gain sufficient knowledge about key factors that determine the catalytic activity or battery performance. To achieve this goal, the reaction mechanisms for a variety of classes of materials in different operating conditions should be fully understood. This knowledge ultimately enables the fine-tuning of the physicochemical properties of catalysts and battery materials at the atomistic and molecular levels. In this context, multi-scale molecular simulations play a central role in understanding various physicochemical phenomena across different temporal and spatial scales (**Figure 1.10**). Notably, recent advances in computation power, particularly using parallel computing, have a great potential for interpreting the complex phenomena in catalysis and energy applications. The choice of proper simulation method to interpret the target phenomena at the respective time and length scales is crucially important (**Table 1.1**). Examples of simulation methods include density functional theory, molecular dynamics, and grand canonical Monte Carlo simulations, which will be described in further detail below.

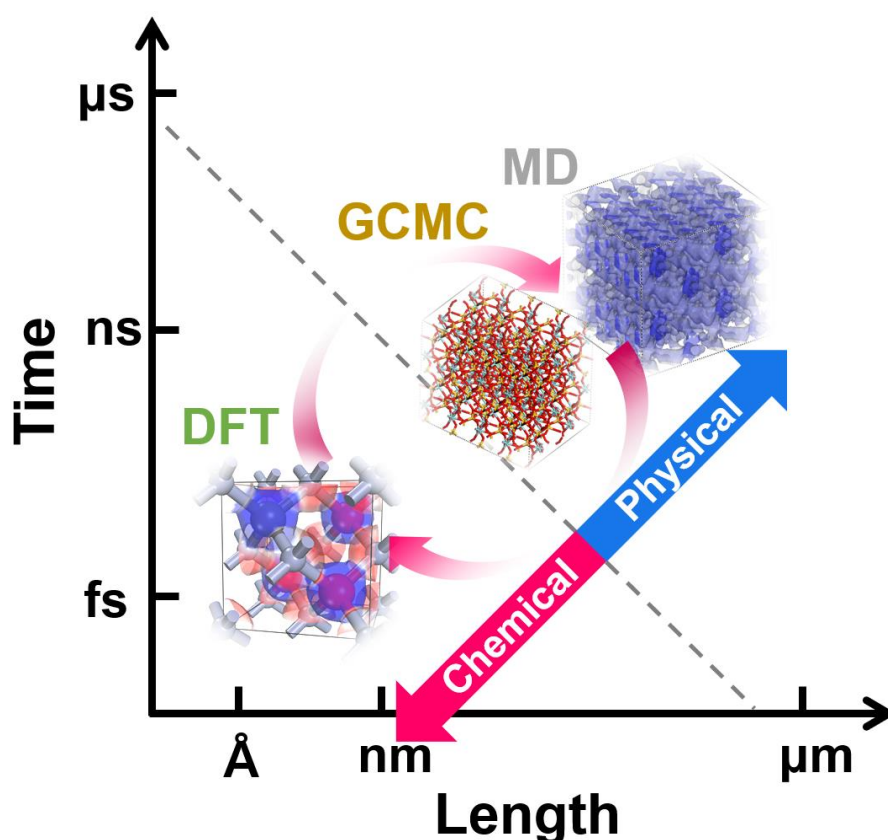


Figure 1.10 Time *versus* length of simulation methods. DFT, GCMC, and MD stand for density functional theory, grand canonical Monte Carlo, and molecular dynamics, respectively.

Table 1.1 Multi-scale simulation methods, applications and simulation packages.

Type	Methods	Applications	Simulation packages
Density functional theory (DFT)	Exchange-correlation functional (PBE, PW91, B3LYP, etc)	- Electronic structure analysis - Investigation of reaction pathways	DMol ³ , CASTEP, VASP, Gaussian, Quantum Espresso
All-atom molecular dynamics (MD)	Classical forcefield (COMPASS, OPLS-AA, CHARMM, etc)	- Dynamics and structural analysis - Physical movements of large molecules (conformational change)	FORCITE, LAMMPS, GROMACS
Grand canonical Monte Carlo (GCMC)	Classical forcefield (COMPASS, OPLS-AA, CHARMM, etc)	- Adsorption and diffusion of small molecules	Sorption, RASPA

1.5.1 Density Functional Theory

Density functional theory (DFT) is a quantum mechanics-based method to investigate the electronic structure of many-body systems, including atoms, molecules, and the condensed phases. In this theory, the total electronic energy of system can be defined from the spatially dependent electron density, which significantly reduce the computational costs compared to the conventional methods based on many-body wave functions (**Figure 1.11**).⁵¹ In energy conversion and storage technology applications, the rapid development of nano-scale catalysts and battery materials have urged a fundamental understanding of the underlying reaction mechanism. For this investigation, DFT calculations provide specific information about the energetics of reactants, intermediates, and products in a reaction pathway. From a thermodynamic perspective, electrocatalytic active sites can be identified and their theoretical activity (or performance) can be predicted by calculating the adsorption energy of plausible adsorbates and reaction intermediates. Moreover, the redistribution of electrons (*i.e.*, charge transfer) at the interface between catalyst (or electrode surface) and electrolyte can be examined during the electrochemical process.

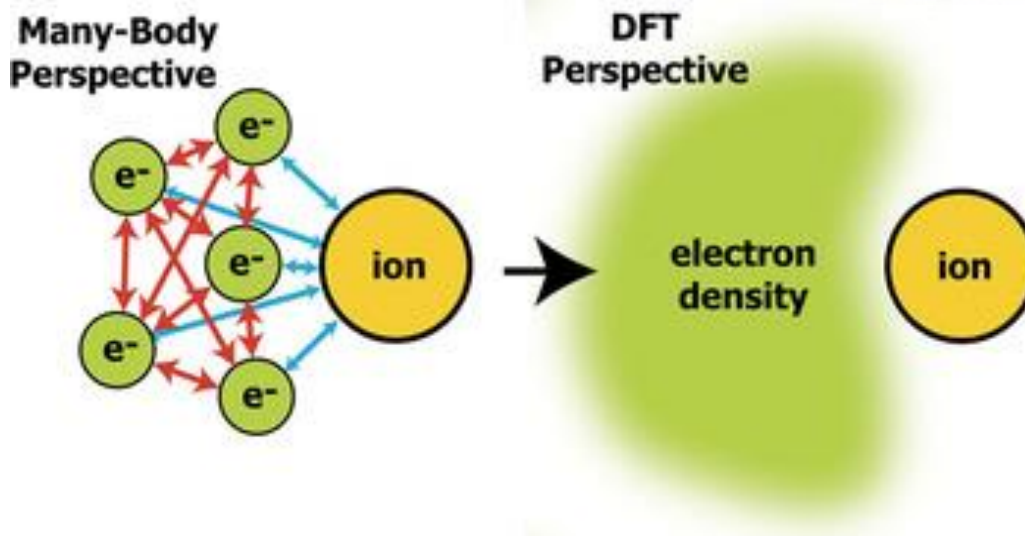


Figure 1.11 Schematic illustration for density functional theory calculation. Reprinted from ref. 51. Copyright © 2011, Materials Research Society.

1.5.2 Molecular Dynamics

Molecular dynamics (MD) simulation is a useful tool to describe the physical movements of atoms and molecules in terms of their structure and microscopic interactions. It involves the stepwise integration of Newton's equations from a certain starting point. All relevant interactions in the potential energy surface is mathematically described by the interatomic potentials, referred as 'forcefield'. The potential energy of a system can be expressed by a sum of valence, cross-term, and non-bond interactions,⁵²⁻⁵⁴

$$E_{\text{total}} = E_{\text{valence}} + E_{\text{cross-term}} + E_{\text{non-bond}} \quad (1.1)$$

where E_{valence} is the potential energy for valence terms, $E_{\text{cross-term}}$ is the potential energy for cross-terms, which accounts for bond or angle distortions caused by nearby atoms. $E_{\text{non-bond}}$ is the potential energy for long-range non-bond interactions, respectively. The E_{valence} can be expressed as,

$$E_{\text{valence}} = E_{\text{bond}} + E_{\text{angle}} + E_{\text{torsion}} + E_{\text{inv}} \quad (1.2)$$

where E_{bond} is the potential energy for bond stretching, E_{angle} is the potential energy for angle bending, E_{torsion} is the potential energy for dihedral angle torsion, and E_{inv} is the potential energy for inversion, also called out-of-plane (oop) interactions, respectively.

$$E_{\text{non-bond}} = E_{\text{vdW}} + E_{\text{Coulomb}} \quad (1.3)$$

where E_{vdW} is the potential energy for van der Waals (vdW) interactions, and E_{Coulomb} is the potential energy for electrostatic (Coulombic) interactions, respectively. The specific functional forms for each energy term depend on the forcefield. With rapid improvement of computational resources, MD simulations can reach up to microsecond level, and almost become compatible with biological processes (*i.e.*, biomineralization) in the experiment.

1.5.3 Grand Canonical Monte Carlo

Grand canonical Monte Carlo (GCMC) simulation is a statistical-mechanical method that uses a molecular-level model of adsorption from by density fluctuations as a result of the trial insertion and deletion of molecules. The thermodynamic variables of the grand canonical ensemble are chemical potential (μ), volume (V), and temperature (T). This method is widely used in the simulations of adsorption equilibrium, since it provides the number of molecules in the pore directly.⁵⁵ The adsorption amounts and configurations of guest molecules, which are usually reaction intermediates in the electrochemical process, can be examined using GCMC simulations.

1.6 Outline of Dissertation

With regard to the energy conversion and storage processes, the energetics of the adsorbed reaction intermediates is the most important properties that can determine the catalytic activity or battery performance. This dissertation includes the theoretical studies for adsorption behaviors in catalysis and energy applications *via* multi-scale molecular simulation approach. In **Chapter 2**, we theoretically demonstrated that the atomically dispersed Pt catalyst on carbon nanotube (Pt₁/CNT) could catalyze the chlorine evolution reaction with excellent activity and selectivity. In **Chapter 3**, we investigated the thermodynamics of ion adsorptions on the amorphous intermediate phases of calcium carbonate, which corresponded to vital precursor phases for catalytic biomineralization. **Chapters 4 and 5** commonly investigate the adsorption of reaction intermediates in next-generation rechargeable batteries such as Li-S and Li-O₂ battery. In **Chapter 4**, we investigated the polysulfide adsorption on the molecular designed chemical trap in Li-S battery. In **Chapter 5**, we studied the superoxide adsorption and subsequent disproportionation reaction with a biomimetic catalyst in Li-O₂ battery.

1.7 References

1. BP Statistical Review of World Energy; London, **2019**
2. Peter, S. C., Reduction of CO₂ to Chemicals and Fuels: A Solution to Global Warming and Energy Crisis. *ACS Energy Lett.* **2018**, 3, (7), 1557-1561.
3. Le Quere, C.; Andres, R. J.; Boden, T.; Conway, T.; Houghton, R. A.; House, J. I.; Marland, G.; Peters, G. P.; van der Werf, G. R.; Ahlstrom, A.; Andrew, R. M.; Bopp, L.; Canadell, J. G.; Ciais, P.; Doney, S. C.; Enright, C.; Friedlingstein, P.; Huntingford, C.; Jain, A. K.; Jourdain, C.; Kato, E.; Keeling, R. F.; Goldewijk, K. K.; Levis, S.; Levy, P.; Lomas, M.; Poulter, B.; Raupach, M. R.; Schwinger, J.; Sitch, S.; Stocker, B. D.; Viovy, N.; Zaehle, S.; Zeng, N., The global carbon budget 1959-2011. *Earth Syst Sci Data* **2013**, 5, (1), 165-185.
4. van de Wal, R. S. W.; de Boer, B.; Lourens, L. J.; Kohler, P.; Bintanja, R., Reconstruction of a continuous high-resolution CO₂ record over the past 20 million years. *Clim Past* **2011**, 7, (4), 1459-1469.
5. Seh, Z. W.; Kibsgaard, J.; Dickens, C. F.; Chorkendorff, I. B.; Nørskov, J. K.; Jaramillo, T. F., Combining theory and experiment in electrocatalysis: Insights into materials design. *Science* **2017**, 355, (6321).
6. Sabatier, P. *La Catalyse en Chimie Organique*; Librairie Polytechnique: Paris, 1913.
7. van Santen, R. A.; Neurock, M.; Shetty, S. G., Reactivity Theory of Transition-Metal Surfaces: A Bronsted-Evans-Polanyi Linear Activation Energy-Free-Energy Analysis. *Chem Rev* **2010**, 110, (4), 2005-2048.
8. Nørskov, J. K.; Rossmeisl, J.; Logadottir, A.; Lindqvist, L.; Kitchin, J. R.; Bligaard, T.; Jonsson, H., Origin of the overpotential for oxygen reduction at a fuel-cell cathode. *J Phys Chem B* **2004**, 108, (46), 17886-17892.
9. Nørskov, J. K.; Bligaard, T.; Logadottir, A.; Kitchin, J. R.; Chen, J. G.; Pandelov, S.; Nørskov, J. K., Trends in the exchange current for hydrogen evolution. *J Electrochem Soc* **2005**, 152, (3), J23-J26.
10. Nørskov, J. K.; Abild-Pedersen, F.; Studt, F.; Bligaard, T., Density functional theory in surface chemistry and catalysis. *P Natl Acad Sci USA* **2011**, 108, (3), 937-943.
11. Mass, T.; Giuffre, A. J.; Sun, C. Y.; Stiffler, C. A.; Frazier, M. J.; Neder, M.; Tamura, N.; Stan, C. V.; Marcus, M. A.; Gilbert, P. Amorphous Calcium Carbonate Particles Form Coral Skeletons. *Proc. Natl. Acad. Sci. U.S.A* **2017**, 114, E7670-E7678.
12. Addadi, L.; Joester, D.; Nudelman, F.; Weiner, S. Mollusk Shell Formation: A Source of New Concepts for Understanding Biomineralization Processes. *Chem. Eur. J.* **2006**, 12, 980-987.
13. Politi, Y.; Levi-Kalisman, Y.; Raz, S.; Wilt, F.; Addadi, L.; Weiner, S.; Sagi, I. Structural Characterization of the Transient Amorphous Calcium Carbonate Precursor Phase in Sea Urchin

- Embryos. *Adv. Funct. Mater.* **2006**, *16*, 1289-1298.
14. Gong, Y. U.; Killian, C. E.; Olson, I. C.; Appathurai, N. P.; Amasino, A. L.; Martin, M. C.; Holt, L. J.; Wilt, F. H.; Gilbert, P. U. Phase Transitions in Biogenic Amorphous Calcium Carbonate. *Proc. Natl. Acad. Sci. U.S.A* **2012**, *109*, 6088-6093.
 15. Nielsen, M. H.; Aloni, S.; De Yoreo, J. J. In situ TEM Imaging of CaCO₃ Nucleation Reveals Coexistence of Direct and Indirect Pathways. *Science* **2014**, *345*, 1158-1162.
 16. Radha, A. V.; Forbes, T. Z.; Killian, C. E.; Gilbert, P. U.; Navrotsky, A. Transformation and Crystallization Energetics of Synthetic and Biogenic Amorphous Calcium Carbonate. *Proc. Natl. Acad. Sci. U.S.A* **2010**, *107*, 16438-16443.
 17. Gebauer, D.; Kellermeier, M.; Gale, J. D.; Bergstrom, L.; Colfen, H. Pre-Nucleation Clusters as Solute Precursors in Crystallisation. *Chem. Soc. Rev.* **2014**, *43*, 2348-2371.
 18. Lam, R. S. K.; Charnock, J. M.; Lennie, A.; Meldrum, F. C. Synthesis-Dependant Structural Variations in Amorphous Calcium Carbonate. *CrystEngComm* **2007**, *9*, 1226-1236.
 19. Gower, L. B. Biomimetic Model Systems for Investigating the Amorphous Precursor Pathway and Its Role in Biomineralization. *Chem. Rev.* **2008**, *108*, 4551-4627.
 20. Seto, J.; Ma, Y. R.; Davis, S. A.; Meldrum, F.; Gourrier, A.; Kim, Y. Y.; Schilde, U.; Sztucki, M.; Burghammer, M.; Maltsev, S.; Jager, C.; Colfen, H. Structure-Property Relationships of a Biological Mesocrystal in the Adult Sea Urchin Spine. *Proc. Natl. Acad. Sci. U.S.A* **2012**, *109*, 3699-3704.
 21. Yoshida, N.; Higashimura, E.; Saeki, Y., Catalytic Biomineralization of Fluorescent Calcite by the Thermophilic Bacterium *Geobacillus thermoglucosidasius*. *Appl. Environ. Microb.* **2010**, *76*, 7322-7327.
 22. Gebauer, D.; Colfen, H.; Verch, A.; Antonietti, M. The Multiple Roles of Additives in CaCO₃ Crystallization: A Quantitative Case Study. *Adv. Mater.* **2009**, *21*, 435-439.
 23. Loste, E.; Wilson, R. M.; Seshadri, R.; Meldrum, F. C. The Role of Magnesium in Stabilising Amorphous Calcium Carbonate and Controlling Calcite Morphologies. *J. Cryst. Growth.* **2003**, *254*, 206-218.
 24. Sawada, K. The Mechanisms of Crystallization and Transformation of Calcium Carbonates. *Pure Appl. Chem.* **1997**, *69*, 921-928.
 25. Clarkson, J. R.; Price, T. J.; Adams, C. J. Role of Metastable Phases in the Spontaneous Precipitation of Calcium-Carbonate. *J. Chem. Soc. Faraday T.* **1992**, *88*, 243-249.
 26. Nagaura, T.; Tozawa, K. Lithium ion rechargeable battery. *Prog. Batteries Solar Cells* **1990**, *9*, 209.
 27. Tarascon, J. M.; Armand, M., Issues and challenges facing rechargeable lithium batteries. *Nature* **2001**, *414*, 359-367.
 28. van Schalkwijk, W. A.; Scrosati, B. *Advances in Lithium-Ion Batteries*; Kluwer Academic

- Publishers: Dordrecht, The Netherlands, 2002.
29. Nazri, G. A.; Pistoia, G. *Lithium Batteries: Science and Technology*; Springer: New York, 2009.
 30. Bruce, P. G.; Hardwick, L. J.; Abraham, K. M., Lithium-air and lithium-sulfur batteries. *MRS Bull.* **2011**, 36, 506-512.
 31. Bruce, P. G.; Freunberger, S. A.; Hardwick, L. J.; Tarascon, J. M., Li-O₂ and Li-S batteries with high energy storage. *Nat. Mater.* **2012**, 11, 19-29.
 32. Aurbach, D.; McCloskey, B. D.; Nazar, L. F.; Bruce, P. G., Advances in understanding mechanisms underpinning lithium-air batteries. *Nat Energy* **2016**, 1.
 33. Debart, A.; Dupont, L.; Patrice, R.; Tarascon, J. M., Reactivity of transition metal (Co, Ni, Cu) sulphides versus lithium: The intriguing case of the copper sulphide. *Solid State Sci* **2006**, 8, 640-651.
 34. Yuan, S. Y.; Bao, J. L.; Wang, L. N.; Xia, Y. Y.; Truhlar, D. G.; Wang, Y. G., Graphene-Supported Nitrogen and Boron Rich Carbon Layer for Improved Performance of Lithium-Sulfur Batteries Due to Enhanced Chemisorption of Lithium Polysulfides. *Adv. Energy Mater.* **2016**, 6, 1501733.
 35. Chung, S. H.; Manthiram, A., Bifunctional Separator with a Light-Weight Carbon-Coating for Dynamically and Statically Stable Lithium-Sulfur Batteries. *Adv. Funct. Mater.* **2014**, 24, 5299–5306.
 36. Yin, Y. X.; Xin, S.; Guo, Y. G.; Wan, L. J., Lithium-Sulfur Batteries: Electrochemistry, Materials, and Prospects. *Angew. Chem. Int. Ed.* **2013**, 52, 13186–13200.
 37. Barghamadi, M.; Best, A. S.; Bhatt, A. I.; Hollenkamp, A. F.; Musameh, M.; Rees, R. J.; Ruther, T., Lithium-sulfur batteries-the solution is in the electrolyte, but is the electrolyte a solution? *Energ. Environ. Sci.* **2014**, 7, 3902–3920.
 38. Manthiram, A.; Fu, Y. Z.; Chung, S. H.; Zu, C. X.; Su, Y. S., Rechargeable Lithium-Sulfur Batteries. *Chem Rev* **2014**, 114, 11751–11787.
 39. Manthiram, A.; Fu, Y. Z.; Su, Y. S., Challenges and Prospects of Lithium-Sulfur Batteries. *Accounts Chem Res* **2013**, 46, 1125–1134.
 40. He, J.; Manthiram, A. A review on the status and challenges of electrocatalysts in lithium-sulfur batteries. *Energy Storage Mater.* **2019**, 20, 55–70
 41. Carbone, L.; Greenbaum, S. G.; Hassoun, J., Lithium sulfur and lithium oxygen batteries: new frontiers of sustainable energy storage. *Sustain Energy Fuels* **2017**, 1, 228–247.
 42. Abraham, K. M.; Jiang, Z., A polymer electrolyte-based rechargeable lithium/oxygen battery. *J. Electrochem. Soc.* **1996**, 143, 1–5.
 43. Ogasawara, T.; Debart, A.; Holzappel, M.; Novak, P.; Bruce, P. G., Rechargeable Li₂O₂ electrode for lithium batteries. *J. Am. Chem. Soc.* **2006**, 128, 1390–1393.
 44. Lu, Y.-C.; Kwabi, D. G.; Yao, K. P. C.; Harding, J. R.; Zhou, J.; Zuin, L.; Shao-Horn, Y., The

- discharge rate capability of rechargeable Li-O₂ batteries. *Energy Environ. Sci.* **2011**, *4*, 2999–3007.
45. Freunberger, S. A.; Chen, Y. H.; Drewett, N. E.; Hardwick, L. J.; Barde, F.; Bruce, P. G., The Lithium-Oxygen Battery with Ether-Based Electrolytes. *Angew. Chem. Int. Edit.* **2011**, *50*, 8609-8613.
 46. Thotiyl, M. M. O.; Freunberger, S. A.; Peng, Z. Q.; Chen, Y. H.; Liu, Z.; Bruce, P. G., A Stable Cathode for the Aprotic Li-O₂ Battery. *Nat. Mater.* **2013**, *12*, 1049-1055.
 47. Black, R.; Oh, S. H.; Lee, J. H.; Yim, T.; Adams, B.; Nazar, L. F., Screening for Superoxide Reactivity in Li-O₂ Batteries: Effect on Li₂O₂/LiOH Crystallization. *J. Am. Chem. Soc.* **2012**, *134*, 2902-2905.
 48. Bryantsev, V. S.; Giordani, V.; Walker, W.; Blanco, M.; Zecevic, S.; Sasaki, K.; Uddin, J.; Addison, D.; Chase, G. V., Predicting Solvent Stability in Aprotic Electrolyte Li-Air Batteries: Nucleophilic Substitution by the Superoxide Anion Radical (O₂^{•-}). *J. Phys. Chem. A* **2011**, *115*, 12399-12409.
 49. Johnson, L.; Li, C. M.; Liu, Z.; Chen, Y. H.; Freunberger, S. A.; Ashok, P. C.; Praveen, B. B.; Dholakia, K.; Tarascon, J. M.; Bruce, P. G., The Role of LiO₂ Solubility in O₂ Reduction in Aprotic Solvents and Its Consequences for Li-O₂ Batteries. *Nat. Chem.* **2014**, *6*, 1091-1099.
 50. Aetukuri, N. B.; McCloskey, B. D.; Garcia, J. M.; Krupp, L. E.; Viswanathan, V.; Luntz, A. C., Solvating Additives Drive Solution-Mediated Electrochemistry and Enhance Toroid Growth in Non-Aqueous Li-O₂ Batteries. *Nat. Chem.* **2015**, *7*, 50-56.
 51. Lust, M. T.; Mattsson, A. E., High-performance computing for materials design to advance energy science, *MRS Bull.* **2011**, *36*, 169-174.
 52. Rigby, D.; Sun, H.; Eichinger, B. E., Computer simulations of poly(ethylene oxide): Force field, PVT diagram and cyclization behaviour. *Polym. Int.* **1997**, *44*, 311-330.
 53. Sun, H.; Ren, P.; Fried, J. R., The COMPASS force field: parameterization and validation for phosphazenes. *Comput. Theor. Polym. Sci.* **1998**, *8*, 229-246.
 54. Sun, H., COMPASS: An ab initio force-field optimized for condensed-phase applications - Overview with details on alkane and benzene compounds. *J. Phys. Chem. B* **1998**, *102*, 7338-7364.
 55. Yun, J. H.; He, Y.; Otero, M.; Duren, T.; Seaton, N. A., Adsorption equilibrium of polar/non-polar mixtures on MCM-41: experiments and Monte Carlo simulation. *Stud. Surf. Sci. Catal.* **2002**, *144*, 685-692.

Chapter 2. Atomically Dispersed Pt Catalyst for Highly Efficient and Selective Chlorine Evolution Reaction

This chapter includes the following content:

Lim, T.[†]; Jung, G. Y.[†]; Kim, J. H.; Park, S. O.; Park, J. H.; Kim, Y.-T.; Kang, S. J.; Jeong, H. Y.; Kwak, S. K.; Joo, S. H. *Nat. Comm.* **2020**, accepted. († : **equally contributed**)

2.1 Introduction

Electrochemical chlorine evolution reaction (CER) plays a pivotal role as the anodic reaction in the chloro-alkali electrolysis for industrial Cl₂ production.¹⁻⁴ Mixed metal oxides (MMO) based on precious metals (Ru and Ir), such as a dimensionally stable anode (DSA), have been prevalently used as CER catalyst.^{5,6} However, the MMO catalysts are also highly active for oxygen evolution reaction (OER).^{2,7-9} That is, they suffer from concomitant generation of oxygen during the CER. To mitigate the production of O₂, the contents of precious metals were reduced but still required high amounts (around 30 at%) to maintain sufficient electronic conductivity for CER.² However, the water activation and concomitant surface oxidation of MMO are unavoidable, leading to the degradation of the active sites.¹⁰⁻¹² Particularly for the membrane-based chlor-alkali electrolysis cell, even a small amount of O₂ can combine with permeated H₂ forming explosive gas mixtures.^{13,14} Hence, the development of highly efficient and selective CER catalysts that comprise minimal amounts of precious metal is of great importance.

To maximize the utilization efficiency of the precious metals, atomically dispersed catalyst^{15,16} or single-atom catalyst¹⁷ have been actively pursued. In this class of catalysts, the metal atoms are stabilized with the elements of the supports, whose structures are reminiscent of homogeneous catalysts.^{15,17-21} The atomically dispersed catalysts can often induce a different reaction pathway to that of widely used nanoparticle-based catalysts showing distinct selectivity and activity for many electrocatalytic reactions,^{22,23} including oxygen reduction reaction,^{19,24-26} OER,^{27,28} hydrogen evolution reaction,^{29,30} and fuel oxidation reaction.^{31,32} However, to the best of our knowledge, the atomically dispersed catalysts have never been exploited as an electrocatalyst for the CER; only homogenous electrocatalysts for generating Cl₂^{33,34} or ClO₂^{35,36} have been sparsely reported.

Herein, we demonstrate an atomically dispersed Pt–N₄ sites on carbon nanotube (Pt₁/CNT) catalyst, which produces Cl₂ with near 100% selectivity in acidic media. Notably, the Pt₁/CNT exhibited superior catalytic activity to Pt nanoparticles on CNT catalyst (PtNP/CNT) in terms of both on-set

potential and turnover frequency (TOF). From density functional theory (DFT) calculation, the origin of excellent CER activity was theoretically elucidated. As a precursor step for the investigation, *ab-initio* Pourbaix diagram identified the active adsorbate structures for the CER. Next, the superior CER activity of Pt₁/CNT, compared to the PtNP/CNT, was theoretically demonstrated based on the thermodynamic overpotentials. Moreover, by combining the experimental and theoretical data, the full free energy diagram for the CER was constructed. This provided an in-depth understanding on the mechanistic pathways of Pt₁/CNT, which follows the Volmer-Heyrovsky mechanism. The atomically dispersed Pt catalyst consisting of Pt–N₄ sites may extend the scope of CER catalysts beyond the hitherto-dominated MMOs, with maximised precious metal atom utilization for the CER and minimized activity for the OER.

2.2 Methods

2.2.1 Calculation Details

Spin-polarised DFT calculations were performed using the DMol³ program^{37,38}. The exchange-correlation energy was described by the generalised gradient approximation with Perdew-Burke-Ernzerhof (GGA-PBE) functional³⁹. The semi-empirical Tkatchenko-Scheffler (TS) approach⁴⁰ was applied to correct the van der Waals interactions. DFT semi-core pseudopotentials⁴¹ were used for the core treatment. The double numerical polarization (DNP) 4.4 level was employed as basis set with the orbital cut-off of 4.5 Å. The implicit water environment was applied by the conductor-like screening model (COSMO)⁴² using the dielectric constant of 78.54. For the geometry optimization, the convergence criteria were set to 1.0×10^{-5} for energy, $0.002 \text{ Ha } \text{Å}^{-1}$ for maximum force, and 0.005 Å for maximum displacement, respectively. For PtO₂ (110) surface, the Brillouin zone was sampled by the Monkhorst-Pack scheme⁴³ using $2 \times 2 \times 1$ *k*-points where the dipole slab correction was applied. The self-consistent field tolerance for single-point energy calculation was set to 1.0×10^{-6} Ha with the thermal smearing parameter of 0.005 Ha.

2.2.2 Model Systems for Calculation

For the Pt₁/CNT, three molecular species (*i.e.*, PtN₄C₁₂, PtN₄C₁₀, and PtN₂₊₂C₄₊₄) were chosen as the possible structural configurations of the Pt–N₄ sites. For the PtNP/CNT, we chose the (110) surface of distorted rutile PtO₂ (which was found as the thermodynamically most stable phase) as a representing model system, following the report that Pt nanoparticles exist in an oxidised form near 1.36 V vs. SHE.⁴⁴ First, the unit cell of β-PtO₂ was fully relaxed by DFT calculations (*i.e.*, $a = 4.58 \text{ Å}$, $b = 4.61 \text{ Å}$, and $c = 3.20 \text{ Å}$), where the lattice parameters were well matched with experimental values.⁴⁵ Subsequently, a $2 \times 1 \times 1$ supercell of PtO₂ (110) surface slab was modelled with nine atomic layers (3 O–Pt–O repeat

units), where bottom two layers were fixed to represent the bulk region (*i.e.*, $6.41 \times 6.49 \times 27.1 \text{ \AA}^3$). On top of the surface, four possible adsorption sites exist involving two coordinatively unsaturated (cus) sites and two bridging O sites.

2.3 Results and Discussion

2.3.1 Experimental Measurements of CER Activity and Selectivity

We investigated the electrocatalytic performances of the catalysts using a rotating ring-disk electrode (RRDE) setup⁴⁶ in 0.1 M HClO₄ in the presence and absence of 1.0 M of Cl⁻. **Figure 2.1** displays the CER polarization curves of the catalysts in the presence of 1.0 M NaCl, which clearly indicate the superior CER activity of Pt₁/CNT compared to CNT, PtNP/CNT, and commercial Ru/Ir-based DSA catalysts. Pt₁/CNT started to catalyse the CER at a potential of 1.38 V, which is 30 mV higher than the E_{CER} (1.35 V vs. reversible hydrogen electrode, RHE, for 25 °C). Pt₁/CNT delivered a current density of 10 mA cm⁻² at an overpotential of 50 mV, which is much lower than those of DSA (105 mV) and PtNP/CNT (120 mV). Notably, in the absence of NaCl, Pt₁/CNT delivered virtually no faradaic currents for Cl₂ evolution, suggesting near 100% CER selectivity.

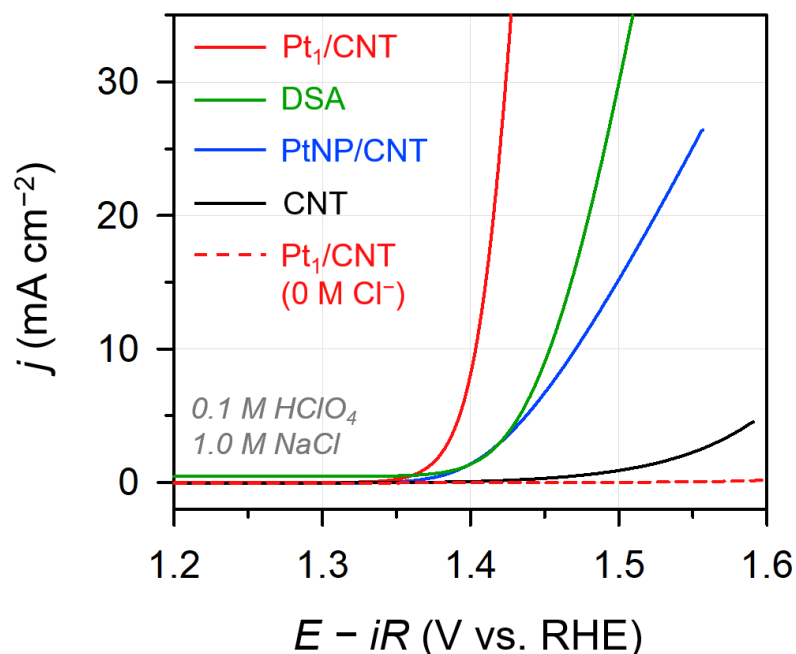


Figure 2.1 CER polarization curves of Pt₁/CNT, PtNP/CNT, DSA, and CNT catalysts obtained in 0.1 M HClO₄ + 1.0 M NaCl at an electrode rotation speed of 1600 rpm and a scan rate of 10 mV s⁻¹. The polarization curve of Pt₁/CNT catalyst measured in 0.1 M HClO₄ is also shown. The DSA catalyst (1 cm × 1 cm) was measured without electrode rotation.

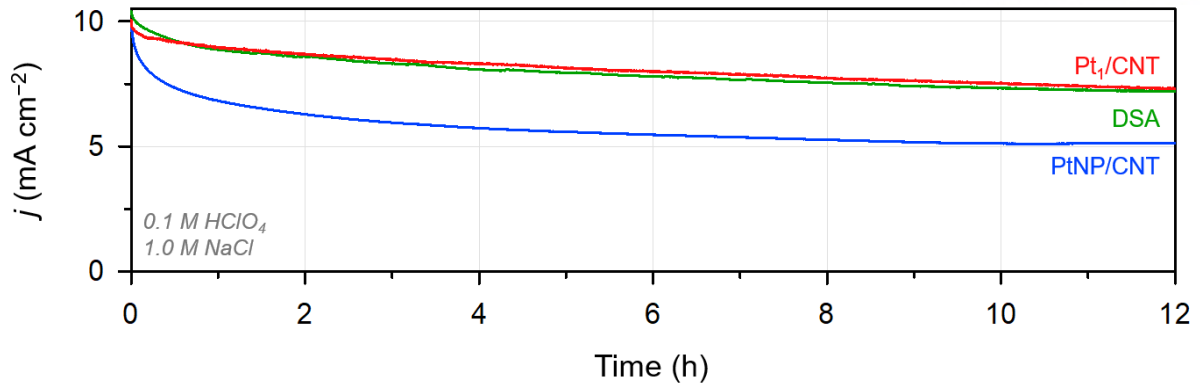


Figure 2.2 Chronoamperograms of Pt₁/CNT and PtNP/CNT catalysts deposited on a carbon paper (1 cm × 1 cm) and DSA catalyst (1 cm × 1 cm) measured in 0.1 M HClO₄ + 1.0 M NaCl for 12 h with a stirring speed of 300 rpm.

The stability of Pt₁/CNT was examined by chronoamperometry (CA) at an initial current density of 10 mA cm⁻² (**Figure 2.2**). Pt₁/CNT retained 72% of its initial current after 12 hours of CER operation, which was similar to that of DSA. In contrast, PtNP/CNT underwent more severe degradation preserving only 50%, which could originate from the dissolution of Pt, as even a trace amount of Cl⁻ accelerates the formation of metastable chloro-Pt complexes.⁴⁷ Meanwhile, the Pt-N₄ sites in the Pt₁/CNT could mitigate the formation of the chloro-Pt complexes by its strong ligation with N.

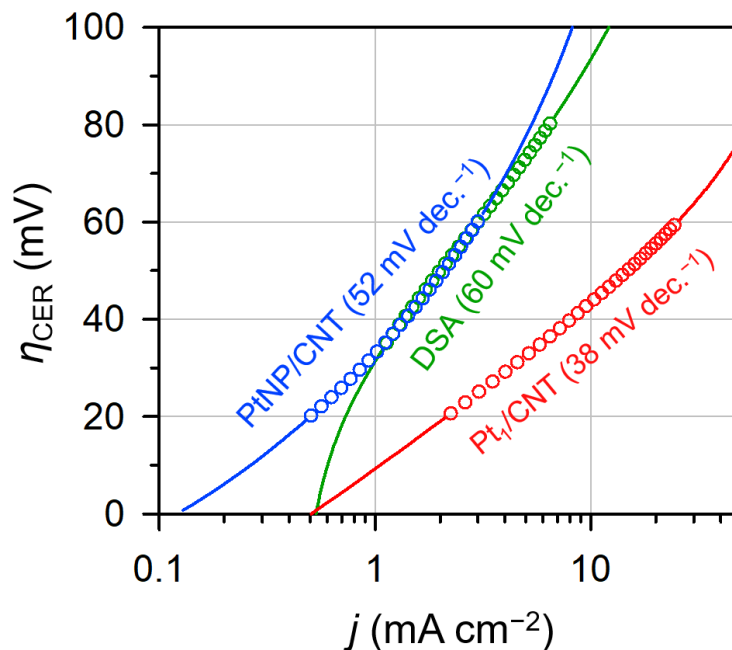
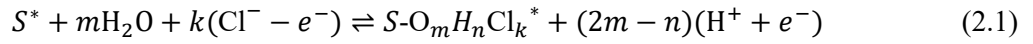


Figure 2.3 Tafel plots of Pt₁/CNT, PtNP/CNT, and DSA catalysts.

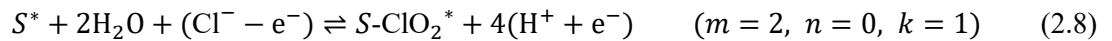
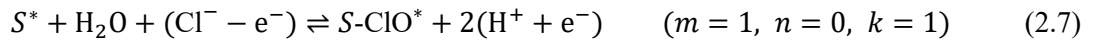
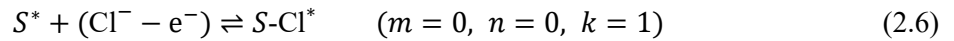
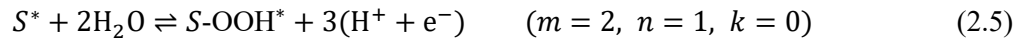
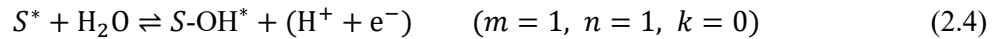
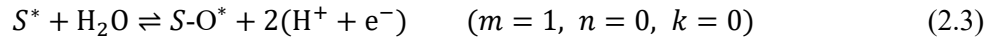
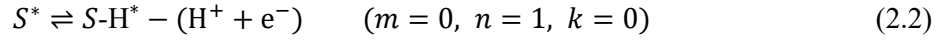
The kinetic information of the catalysts for CER was gleaned from Tafel analyses (**Figure 2.3**). Pt₁/CNT showed a Tafel slope of 38 mV dec.⁻¹ in the potential range of 30–70 mV, whereas those of PtNP/CNT and DSA were 52 mV dec.⁻¹ and 60 mV dec.⁻¹ in the range of 40–80 mV, respectively. The Tafel analyses suggest that the CER on Pt₁/CNT proceeded with faster kinetics than on PtNP/CNT and DSA. The Tafel slope of 38 mV dec.⁻¹ indicates that the CER on Pt₁/CNT may proceed *via* the Volmer-Heyrovsky mechanism.⁴⁸⁻⁵¹

2.3.2 *Ab Initio* Pourbaix Diagrams

The Pourbaix diagram represents the thermodynamically stable surface structures in electrochemical systems as a function of pH and electrode potential (U). Note that the detailed description about the Pourbaix diagram is reported elsewhere.^{49,52,53} In this study, we constructed the Pourbaix diagrams for Pt–N₄ sites and PtO₂ (110) surface by calculating the adsorption free energies for all plausible adsorbates (*i.e.*, H*, O*, OH*, OOH*, Cl*, ClO*, and ClO₂*, see **Figures 2.4 and 2.5**). Note that * denotes the adsorbed states on the surface. A generalised description for the adsorbates (denoted as O_{*m*}H_{*n*}Cl_{*k*}*) on the site (denoted as *S*) can be written as



By rewriting equation (2.1), each reaction can be represented as follows,



where S^* denotes the bare site without adsorbates.

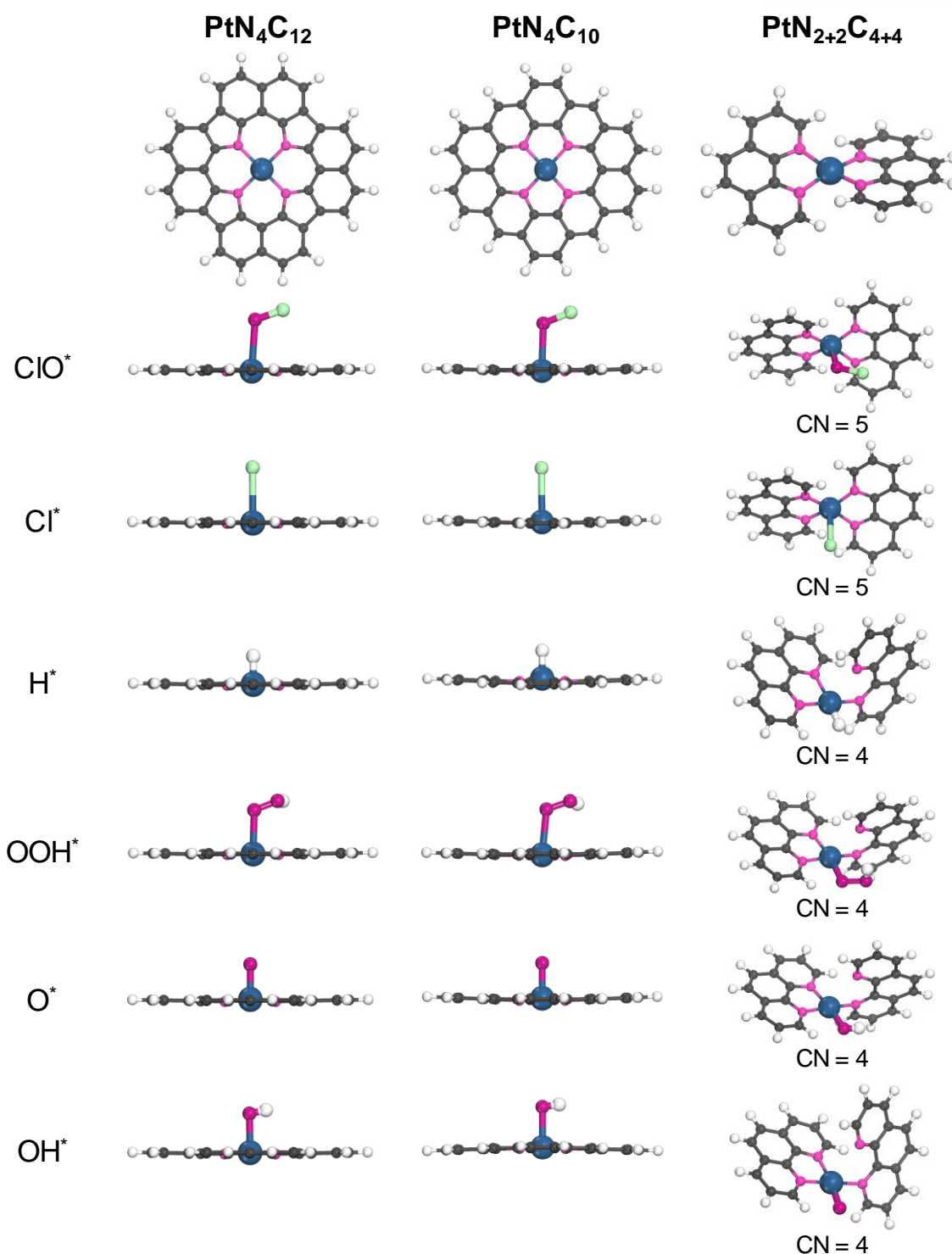


Figure 2.4 Model systems for plausible Pt–N₄ sites including PtN₄C₁₂, PtN₄C₁₀, and PtN₂₊₂C₄₊₄. Six plausible adsorbates (*i.e.*, ClO^{*}, Cl^{*}, H^{*}, OOH^{*}, O^{*}, and OH^{*}) were considered. Coordination numbers (CNs) of Pt atoms in the PtN₂₊₂C₄₊₄ are labelled below. The white, black, pink, dark-blue, purple, and yellow-green coloured spheres represent the hydrogen, carbon, nitrogen, platinum, oxygen, and chlorine atoms, respectively.

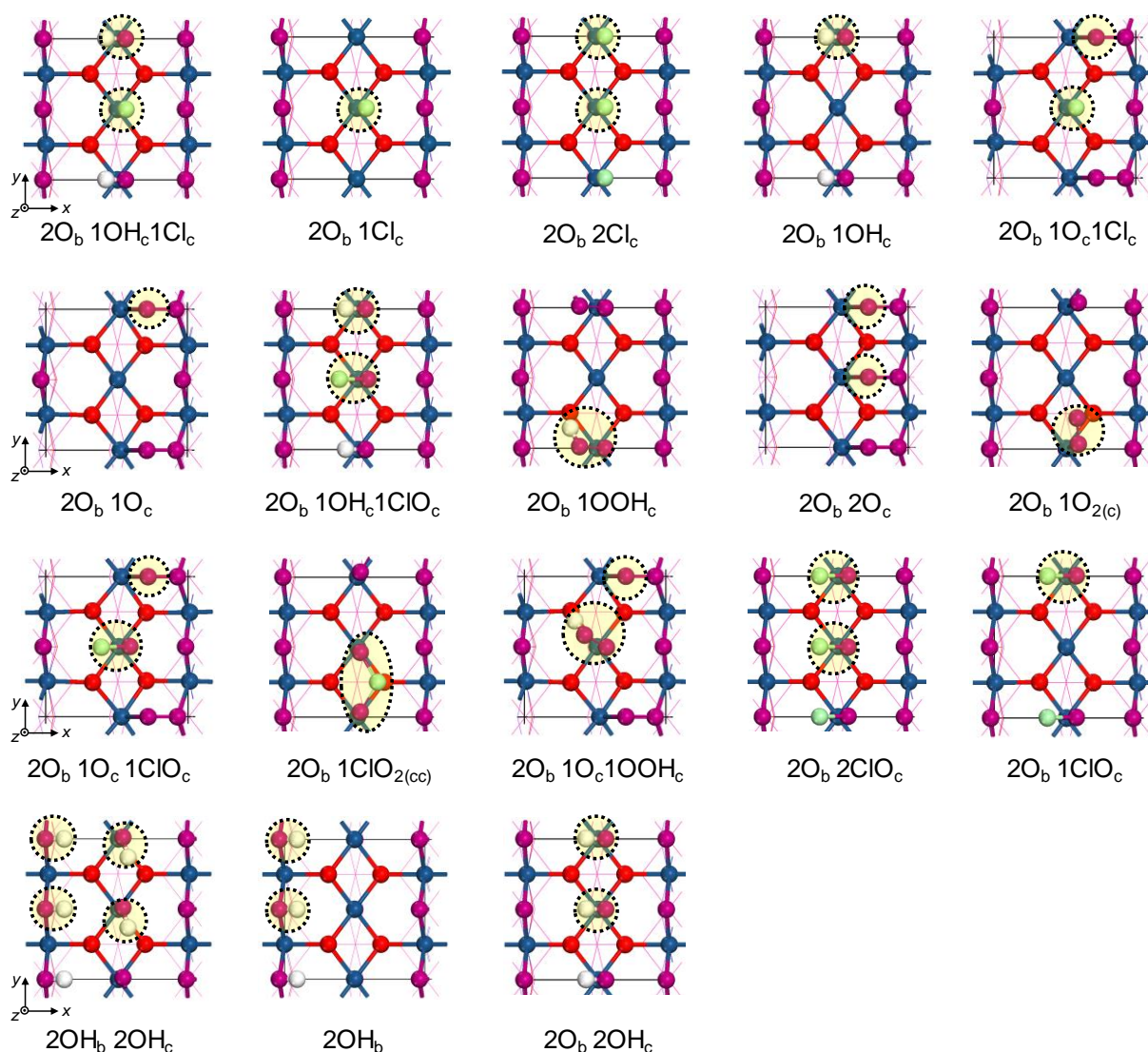


Figure 2.5 Model systems for PtO_2 (110) surface including four plausible adsorption sites in top view. Among four plausible adsorption sites, including two bridged oxygen and two coordinatively unsaturated (cus) sites, a total of 18 combinations of adsorbate species (*i.e.*, O_b , OH_b at bridge sites as well as OH_c , Cl_c , O_c , OOH_c , $\text{O}_{2(c)}$, ClO_c at cus sites, respectively) were considered. Black dotted circles represent the adsorbate structures. Topmost layers are magnified with ball-and-stick style for visualization. The dark-blue and red spheres represent the platinum and oxygen atoms at the surface. The white, yellow-green, and purple spheres represent the hydrogen, chlorine, and oxygen atoms for the adsorbates, respectively.

Then, the adsorption free energy (ΔG) for $O_mH_nCl_k$ species can be defined as follows,

$$\Delta G = G_{S-O_mH_nCl_k}^* + (2m - n)(G_{H^+} + G_{e^-}) - k(G_{Cl^-} - G_{e^-}) - G_{S^*} - mG_{H_2O} \quad (2.9)$$

where m , n , and k are the number of oxygen, hydrogen, and chlorine atoms, respectively. From DFT calculation, the ΔG for each adsorbate species can be calculated as follows,

$$\Delta G = \Delta E + \Delta ZPE - T\Delta S \quad (2.10)$$

where ΔE is the binding energy for each adsorbate, ΔZPE is the change in zero-point vibrational enthalpy, and $-T\Delta S$ is the entropic correction at room temperature.

By rewriting equation (2.9), the ΔG for each species can be represented as follows,

$$\Delta G_{H^*} = G_{S-H^*} - (G_{H^+} + G_{e^-}) - G_{S^*} \quad (m = 0, n = 1, k = 0) \quad (2.11)$$

$$\Delta G_{O^*} = G_{S-O^*} + 2(G_{H^+} + G_{e^-}) - G_{S^*} - G_{H_2O} \quad (m = 1, n = 0, k = 0) \quad (2.12)$$

$$\Delta G_{OH^*} = G_{S-OH^*} + (G_{H^+} + G_{e^-}) - G_{S^*} - G_{H_2O} \quad (m = 1, n = 1, k = 0) \quad (2.13)$$

$$\Delta G_{OOH^*} = G_{S-OOH^*} + 3(G_{H^+} + G_{e^-}) - G_{S^*} - 2G_{H_2O} \quad (m = 2, n = 1, k = 0) \quad (2.14)$$

$$\Delta G_{Cl^*} = G_{S-Cl^*} - (G_{Cl^-} - G_{e^-}) - G_{S^*} \quad (m = 0, n = 0, k = 1) \quad (2.15)$$

$$\Delta G_{ClO^*} = G_{S-ClO^*} + 2(G_{H^+} + G_{e^-}) - (G_{Cl^-} - G_{e^-}) - G_{S^*} - G_{H_2O} \quad (m = 1, n = 0, k = 1) \quad (2.16)$$

$$\Delta G_{ClO_2^*} = G_{S-ClO_2^*} + 4(G_{H^+} + G_{e^-}) - (G_{Cl^-} - G_{e^-}) - G_{S^*} - 2G_{H_2O} \quad (m = 2, n = 0, k = 1) \quad (2.17)$$

Herein, $G_{H^+} + G_{e^-}$ and $G_{Cl^-} - G_{e^-}$ is defined as a function of U_{SHE} , pH, and $\ln a_{Cl^-}$,

$$G_{H^+} + G_{e^-} = \frac{1}{2}G_{H_2} - U_{SHE} - \ln 10 \cdot k_B T \cdot \text{pH} \quad (2.18)$$

$$G_{Cl^-} - G_{e^-} = \frac{1}{2}G_{Cl_2} + U_{SHE} - 1.36 + \ln a_{Cl^-} \cdot k_B T \quad (2.19)$$

where U_{SHE} , k_B , and T is the electrode potential (vs. theoretical standard hydrogen electrode, SHE), Boltzmann constant, and temperature, respectively. Considering that Cl^- concentration is nearly constant under reaction condition by using NaClO_4 as a buffer solution, $\ln a_{\text{Cl}^-}$ was assumed to be negligible for our calculation.⁵⁰ At finite U_{SHE} and pH, the ΔG can be expressed as:

$$\begin{aligned} \Delta G(U, \text{pH}) &= G_{\text{S-O}_m\text{H}_n\text{Cl}_k^*} + (2m - n) \left(\frac{1}{2} G_{\text{H}_2} - U_{\text{SHE}} - \ln 10 \cdot k_B T \cdot \text{pH} \right) \\ &\quad - k \left(\frac{1}{2} G_{\text{Cl}_2} + U_{\text{SHE}} - 1.36 \right) - G_{\text{S}^*} - m G_{\text{H}_2\text{O}} \end{aligned} \quad (2.20)$$

By rewriting equation (2.20), the ΔG for each species as a function of U_{SHE} and pH can be defined as follows at standard conditions ($T = 298 \text{ K}$).

$$\begin{aligned} \Delta G_{\text{H}^*}(U, \text{pH}) &= G_{\text{S-H}^*} - \left(\frac{1}{2} G_{\text{H}_2} - U_{\text{SHE}} - \ln 10 \cdot k_B T \cdot \text{pH} \right) - G_{\text{S}^*} \\ &= \Delta G_{\text{H}^*} + U_{\text{SHE}} + 0.059 \cdot \text{pH} \end{aligned} \quad (2.21)$$

$$\begin{aligned} \Delta G_{\text{O}^*}(U, \text{pH}) &= G_{\text{S-O}^*} + 2 \left(\frac{1}{2} G_{\text{H}_2} - U_{\text{SHE}} - \ln 10 \cdot k_B T \cdot \text{pH} \right) - G_{\text{S}^*} - G_{\text{H}_2\text{O}} \\ &= \Delta G_{\text{O}^*} - 2U_{\text{SHE}} - 0.118 \cdot \text{pH} \end{aligned} \quad (2.22)$$

$$\begin{aligned} \Delta G_{\text{OH}^*}(U, \text{pH}) &= G_{\text{S-OH}^*} + \left(\frac{1}{2} G_{\text{H}_2} - U_{\text{SHE}} - \ln 10 \cdot k_B T \cdot \text{pH} \right) - G_{\text{S}^*} - G_{\text{H}_2\text{O}} \\ &= \Delta G_{\text{OH}^*} - U_{\text{SHE}} - 0.059 \cdot \text{pH} \end{aligned} \quad (2.23)$$

$$\begin{aligned} \Delta G_{\text{OOH}^*}(U, \text{pH}) &= G_{\text{S-OOH}^*} + 3 \left(\frac{1}{2} G_{\text{H}_2} - U_{\text{SHE}} - \ln 10 \cdot k_B T \cdot \text{pH} \right) - G_{\text{S}^*} - 2G_{\text{H}_2\text{O}} \\ &= \Delta G_{\text{OOH}^*} - 3U_{\text{SHE}} - 0.177 \cdot \text{pH} \end{aligned} \quad (2.24)$$

$$\begin{aligned} \Delta G_{\text{Cl}^*}(U, \text{pH}) &= G_{\text{S-Cl}^*} - \left(\frac{1}{2} G_{\text{Cl}_2} + U_{\text{SHE}} - 1.36 \right) - G_{\text{S}^*} \\ &= \Delta G_{\text{Cl}^*} - U_{\text{SHE}} + 1.36 \end{aligned} \quad (2.25)$$

$$\begin{aligned}
 \Delta G_{\text{ClO}^*}(U, \text{pH}) &= G_{\text{S-ClO}^*} + 2 \left(\frac{1}{2} G_{\text{H}_2} - U_{\text{SHE}} - \ln 10 \cdot k_{\text{B}} T \cdot \text{pH} \right) \\
 &\quad - \left(\frac{1}{2} G_{\text{Cl}_2} + U_{\text{SHE}} - 1.36 \right) - G_{\text{S}^*} - G_{\text{H}_2\text{O}} \\
 &= \Delta G_{\text{ClO}^*} - 3U_{\text{SHE}} + 1.36 - 0.118 \cdot \text{pH}
 \end{aligned} \tag{2.26}$$

$$\begin{aligned}
 \Delta G_{\text{ClO}_2^*}(U, \text{pH}) &= G_{\text{S-ClO}_2^*} + 4 \left(\frac{1}{2} G_{\text{H}_2} - U_{\text{SHE}} - \ln 10 \cdot k_{\text{B}} T \cdot \text{pH} \right) \\
 &\quad - \left(\frac{1}{2} G_{\text{Cl}_2} + U_{\text{SHE}} - 1.36 \right) - G_{\text{S}^*} - 2G_{\text{H}_2\text{O}} \\
 &= \Delta G_{\text{ClO}_2^*} - 5U_{\text{SHE}} + 1.36 - 0.236 \cdot \text{pH}
 \end{aligned} \tag{2.27}$$

Using above equations (2.21 ~ 2.27), ΔG 's for all species as a function of U_{SHE} were initially found for Pt-N₄ sites at pH = 0 (**Figure 2.6**). For the PtO₂ (110) surface, the ΔG 's for all plausible adsorbates and their relevant combinations (*i.e.*, O_b and OH_b at bridge sites and OH_c, Cl_c, O_c, OOH_c, O_{2(c)}, and ClO_c at coordinatively unsaturated (cus) sites, respectively) were calculated at pH = 0 (**Figure 2.7**).

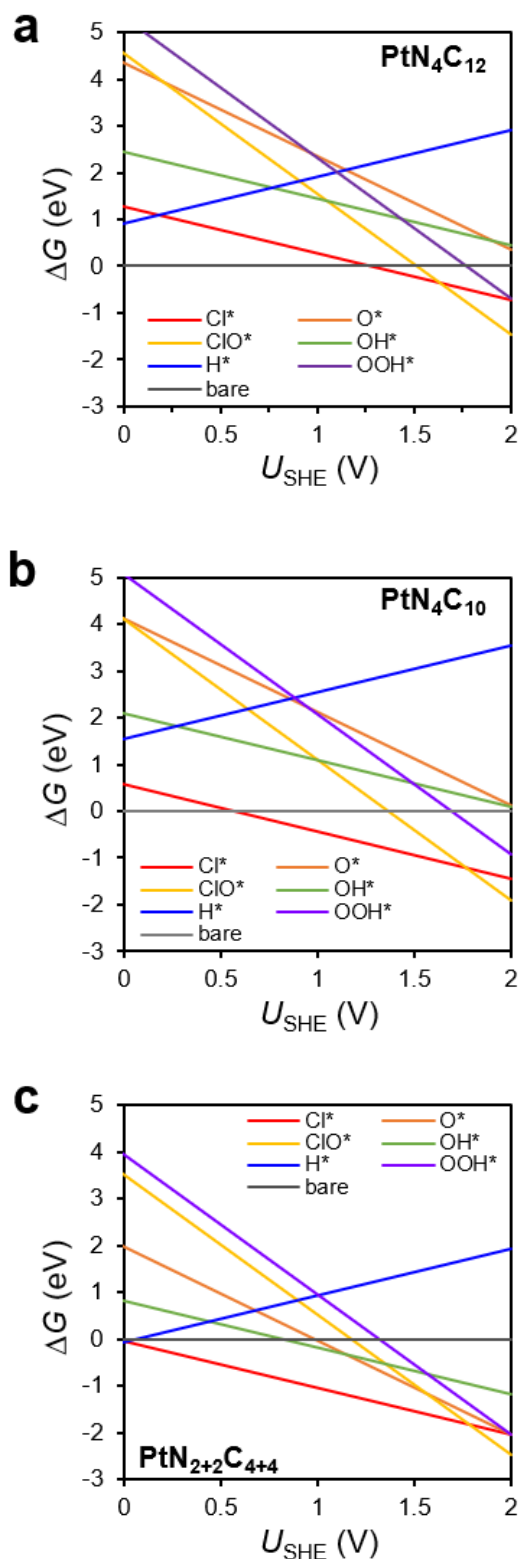


Figure 2.6 The adsorption free energy for plausible adsorbates on three Pt-N₄ sites. Seven plausible adsorbates (*i.e.*, bare (*), Cl*, O*, ClO*, OH*, H*, and OOH*) on Pt-N₄ sites were considered as a function of the theoretical standard hydrogen electrode potential (U_{SHE}) at pH = 0: **a**, PtN₄C₁₂, **b**, PtN₄C₁₀, and **c**, PtN₂₊₂C₄₊₄.

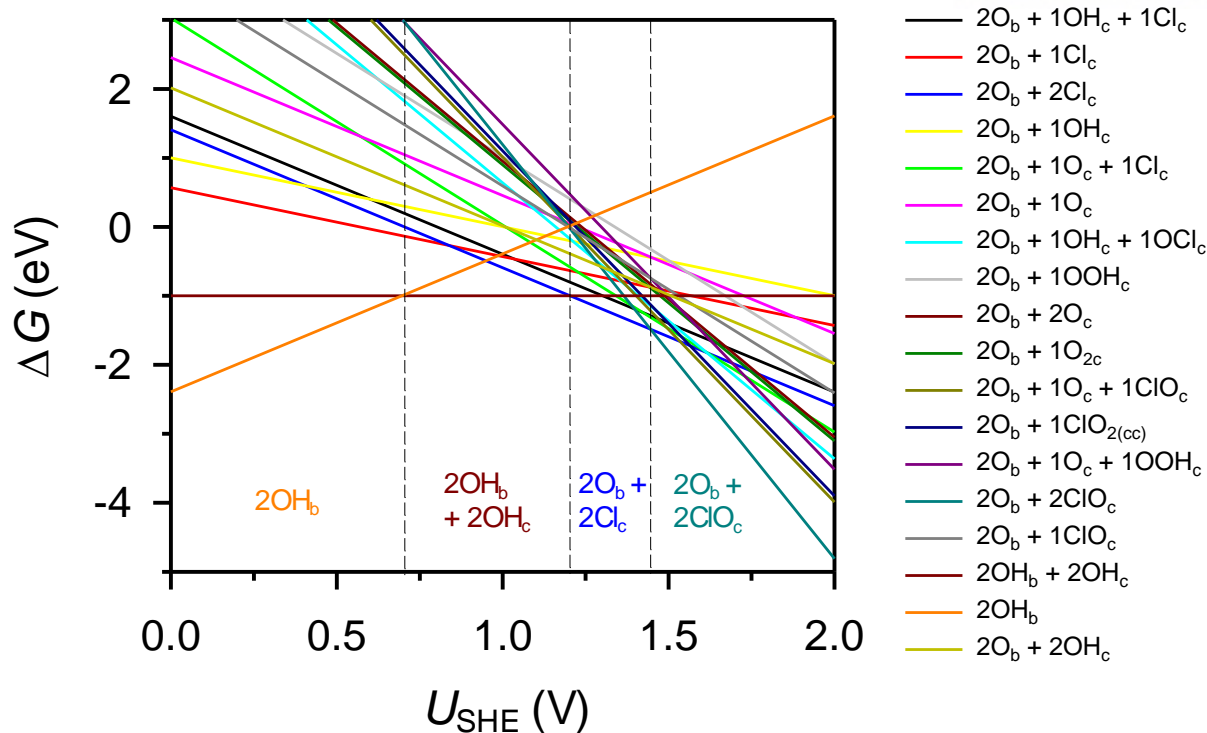


Figure 2.7 The adsorption free energy (ΔG) for plausible adsorbates on PtO_2 (110) surface. A total 18 plausible combinations of adsorbate species (*i.e.*, O_b , OH_b at bridge sites as well as OH_c , Cl_c , O_c , OOH_c , $\text{O}_{2(c)}$, ClO_c at cus sites, respectively) were considered as a function of the theoretical standard hydrogen electrode potential (U_{SHE}) at $\text{pH} = 0$. Black dotted lines represent the phase boundary where two adsorbate species exist in equilibrium. The most stable adsorbate species at each area (divided by black dotted line) are labelled below.

From the calculated adsorption free energies (ΔG 's) of possible adsorbates (*i.e.*, $*$, ClO^* , Cl^* , H^* , OOH^* , O^* , and OH^*) for Pt-N_4 sites (**Figure 2.6**), we constructed Pourbaix diagrams, which provide the thermodynamically most stable adsorbate structures under applied electrode potential (U) and pH (**Figure 2.8**). The Pourbaix diagram is constructed from an *ab-initio* constrained thermodynamics approach, *i.e.*, the reactants are adsorbed on surface while the subsequent formation of product does not proceed.⁵⁴ The active adsorbate structure, which is identified as the thermodynamically most stable, can promisingly serve as a starting point for the investigation of mechanistic pathways. The CER is pH -independent on the standard hydrogen electrode (SHE) scale and thus appears as a horizontal line at the equilibrium potential of 1.36 V *vs.* SHE. In contrast, the equilibrium potential for OER exhibits a decreasing trend with a slope of -59 mV pH^{-1} , starting from U_{SHE} (theoretical SHE potential) = 1.23 V and $\text{pH} = 0$.⁵³ Considering that the present CER operating condition was acidic for Pt_1/CNT ($\text{pH} = 1$), Cl^* species were predicted as the most probable adsorbate structures for CER on the Pt-N_4 sites.

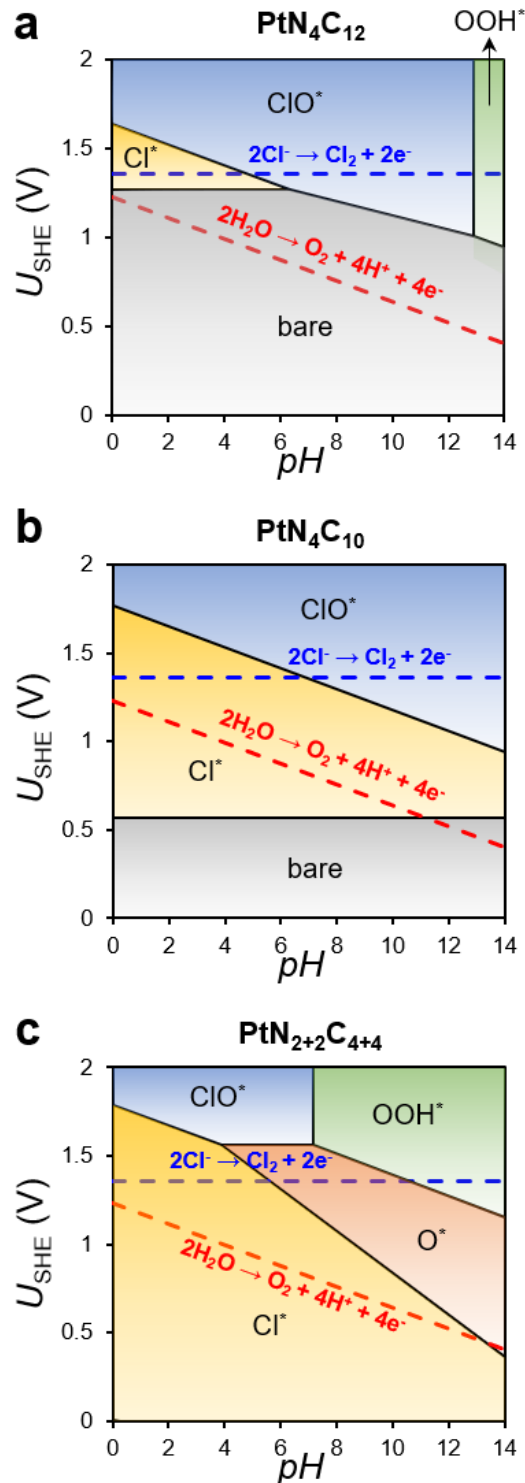


Figure 2.8 Pourbaix diagram of theoretical standard hydrogen electrode potential (U_{SHE}) vs. pH for three Pt–N₄ sites in equilibrium with H⁺, Cl[−] and H₂O at room temperature. **a**, PtN₄C₁₂, **b**, PtN₄C₁₀, and **c**, PtN₂₊₂C₄₊₄. Blue dashed line and red dashed line represent the equilibrium potential for CER in the SHE scale ($U_{\text{eq}} = 1.36$ V) and for OER ($U_{\text{eq}} = 1.23$ V – 0.059 pH), respectively. Black solid lines represent the phase boundary where two adsorbate species exist in equilibrium.

The Pourbaix diagrams for PtO₂ (110) surface (representing the PtNP/CNT) revealed that both 2O_b2Cl_c and 2O_b2ClO_c can be possible active adsorbate structures, especially at the acidic CER operating condition (*i.e.*, $U_{\text{SHE}} \approx 1.36$ V, pH \cong 1), where they had similar thermodynamic stability by sharing a phase boundary line (**Figure 2.9**).

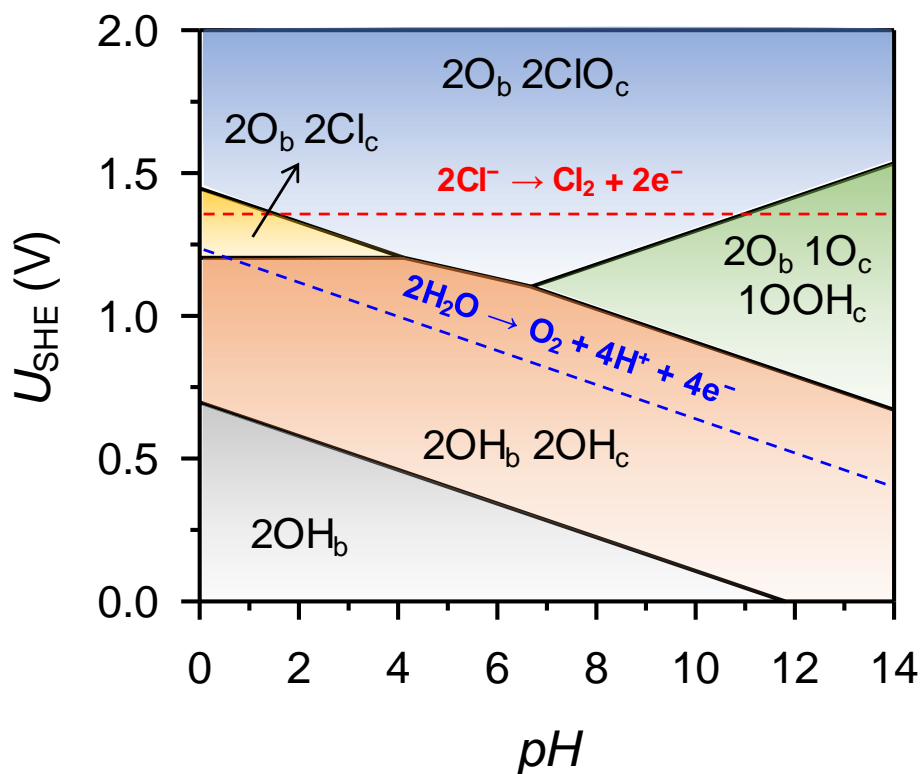
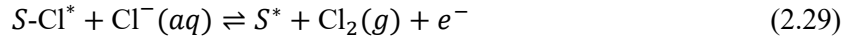


Figure 2.9 Pourbaix diagram of theoretical standard hydrogen electrode potential (U_{SHE}) vs. pH for PtO₂ (110) surface. Red dashed line and blue dashed line represent the equilibrium potential for CER ($U_{\text{SHE}} = 1.36$ V) and that for OER, respectively. Black solid lines represent the phase boundary where two adsorbate species exist in equilibrium.

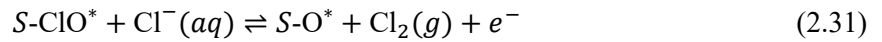
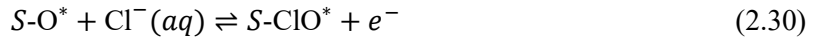
2.3.3 Theoretical Evaluations on the CER Activity

To theoretically investigate the CER activity, we calculated the free energy diagrams for CER in the Pt–N₄ sites and PtO₂ (110) surface. To do this, two possible reaction mechanisms including different intermediates (*i.e.*, Cl* or ClO*) were considered,

(I) Pathway mediated by the Cl* species:



(II) Pathway mediated by the ClO* species:



where (aq) and (g) represent aqueous and gaseous phases, respectively. The ΔE 's for each reaction intermediate were calculated relative to the Cl₂ gas molecule as follows,

$$\Delta E_{\text{Cl}^*} = E_{S\text{-Cl}^*} - E_{S^*} - 0.5E_{\text{Cl}_2} \quad (2.32)$$

$$\Delta E_{\text{ClO}^*} = E_{S\text{-ClO}^*} - E_{S^*} - 0.5E_{\text{Cl}_2} - (E_{\text{H}_2\text{O}} - E_{\text{H}_2}) \quad (2.33)$$

Using equation (2.10), (2.12), (2.15), and (2.16), ΔG_{Cl^*} , ΔG_{ClO^*} , and ΔG_{O^*} can be calculated. Then, the thermodynamic overpotential for CER at zero overpotential ($\eta_{\text{TD}(\text{CER})}$) can be defined as follows,

(I) For * and Cl* species:

$$\eta_{\text{TD}(\text{CER})} = \frac{|\Delta G_{\text{Cl}^*}|}{e} \quad (2.34)$$

(II) For O* and ClO* species:

$$\eta_{\text{TD}(\text{CER})} = \frac{|\Delta G_{\text{ClO}^*} - \Delta G_{\text{O}^*}|}{e} \quad (2.35)$$

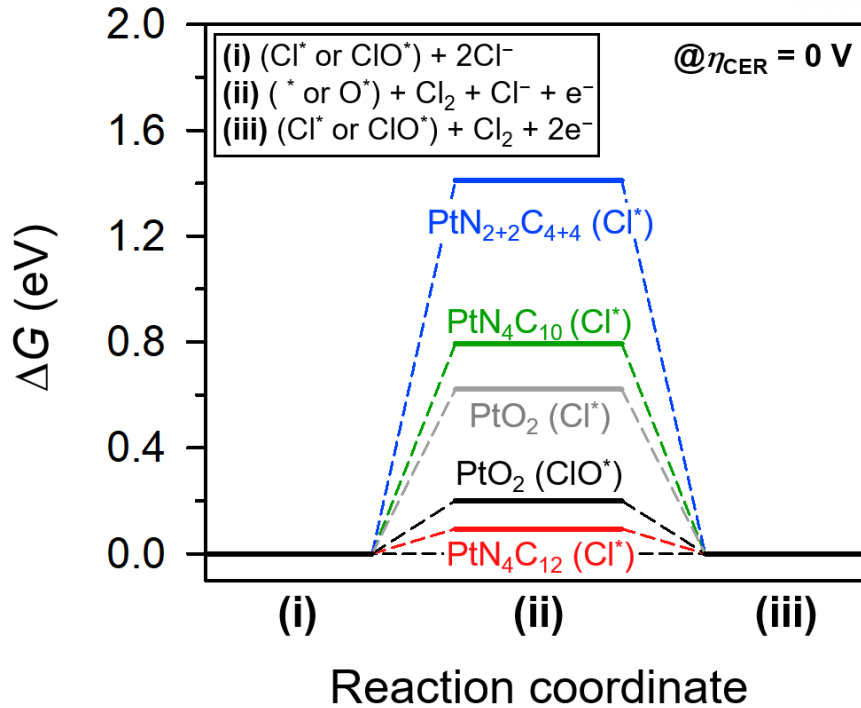


Figure 2.10 Free energy diagrams for CER over Pt–N₄ clusters and PtO₂ (110) surface at zero overpotential ($\eta_{\text{CER}} = 0$ V).

With the above-identified active adsorbate structures for Pt–N₄ sites and PtO₂ (110) surfaces, we calculated the free energy diagrams for CER to theoretically evaluate the catalytic activity (**Figure 2.10**). The thermodynamic overpotential for CER can be defined from the ΔG divided by the elementary charge at zero overpotential (*i.e.*, $\eta_{\text{TD(CER)}} = \Delta G/e$), which depends on the reaction intermediates as follows: ΔG_{Cl^*} for bare structure (*) and Cl* species, and $\Delta G_{\text{ClO}^*} - \Delta G_{\text{O}^*}$ for O* and ClO* species, respectively.⁵⁵ Among Pt–N₄ sites, PtN₄C₁₂ was identified as the most probable structure for CER due to its lowest $\eta_{\text{TD(CER)}}$ of 0.09 V at zero overpotential. In the case of PtO₂ (110) surface (**Figure 2.10** and **2.11**), ClO* species ($\eta_{\text{TD(CER)}} = 0.20$ V for 2O_b2ClO_c) were found to be closer to the thermoneutral state ($\Delta G = 0$) than Cl* species ($\eta_{\text{TD(CER)}} = 0.62$ V for 2O_b2Cl_c), implying that ClO* species were identified as the reaction intermediate for the CER on the PtO₂ surface of the PtNP/CNT, similar to other precious metal oxides, such as IrO₂ and RuO₂.^{49,51,56} Therefore, we theoretically demonstrated that the CER activity of Pt₁/CNT was superior to that of the PtNP/CNT.

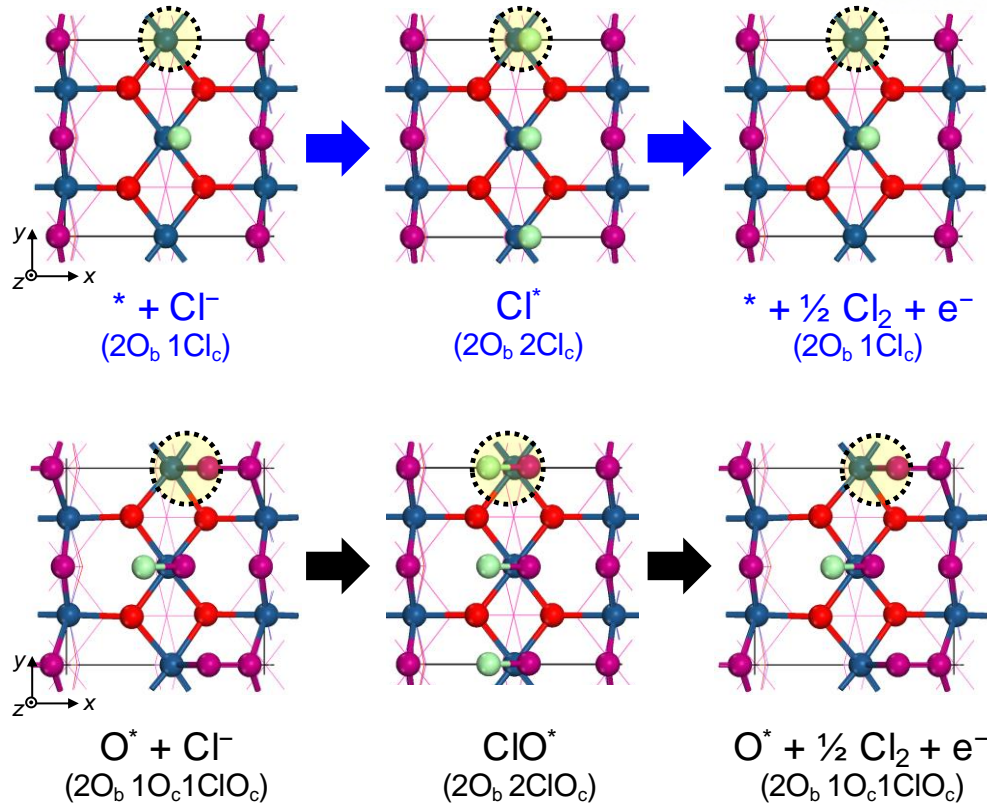


Figure 2.11 Model systems for PtO_2 (110) surface for CER (top view). Two plausible intermediate structures including $2\text{O}_b 2\text{Cl}_c$ and $2\text{O}_b 2\text{ClO}_c$ were considered. Black dotted circles represent reaction sites. Topmost layers are magnified with ball-and-stick style for visualization. Dark-blue and red spheres represent the platinum and oxygen atoms at the surface, while the yellow-green and purple spheres represent chlorine and oxygen atoms for the adsorbates, respectively.

2.3.4 Stability Against Pt Dissolution

The extent of dissolution of Pt from Pt-N_4 sites relative to that from $\text{Pt}(111)$ surface could be gauged with the electrode potential shift (ΔU) for reaction $\text{Pt} \rightarrow \text{Pt}^{2+} + 2\text{e}^-$, by following the previous reports (**Supplementary Fig. 32**).^{57,58} The ΔU is defined by,

$$\Delta U = -[\mu_{\text{Pt-N}_4} - \mu_{\text{Pt}(111)}]/2e \quad (2.36)$$

where $\mu_{\text{Pt-N}_4}$ and $\mu_{\text{Pt}(111)}$ are the chemical potentials of Pt atoms on the Pt-N_4 sites and $\text{Pt}(111)$ surface, respectively. Note that the dissolutions of Pt atoms are assumed to only occur on the outermost layer of the surface. Assuming the reference state as Pt bulk state, the $\mu_{\text{Pt-N}_4}$ and $\mu_{\text{Pt}(111)}$ were calculated as follows,

$$\mu_{\text{Pt-N}_4} = E_{\text{Pt-N}_4} - E_{\text{Pt-free}} - E_{\text{Pt-bulk}} \quad (2.37)$$

$$\mu_{\text{Pt(111)}} = E_{\text{Pt(111)}} - E_{\text{Pt-leached}} - E_{\text{Pt-bulk}} \quad (2.38)$$

where $E_{\text{Pt-N}_4}$, $E_{\text{Pt-free}}$, $E_{\text{Pt-bulk}}$, $E_{\text{Pt(111)}}$, and $E_{\text{Pt-leached}}$ represent the DFT-optimised energies of Pt–N₄ sites, Pt–N₄ sites where the Pt atom is not included, a Pt atom in the bulk unit cell, perfect Pt(111) surface, and Pt(111) surface where a single Pt atom on the outermost surface is leached, respectively.

The stability against Pt dissolution for the Pt–N₄ sites were evaluated based on the ΔU , which was gauged with reference to the dissolution on the Pt(111) surface (**Figure 2.12**).

Figure 2.12 shows the ΔU for reaction $\text{Pt} \rightarrow \text{Pt}^{2+} + 2\text{e}^-$ in the Pt–N₄ sites. The positive value of ΔU implies that the dissolution of Pt on the Pt–N₄ sites requires more energetic cost compared to that from Pt(111) surface.^{57,58} PtN₄C₁₂ species were found to be thermodynamically more stable than other ones. Thus, besides good CER activity (**Figure 2.10**), it further supports that PtN₄C₁₂ species are feasible to exist in the Pt1/CNT on a theoretical viewpoint.

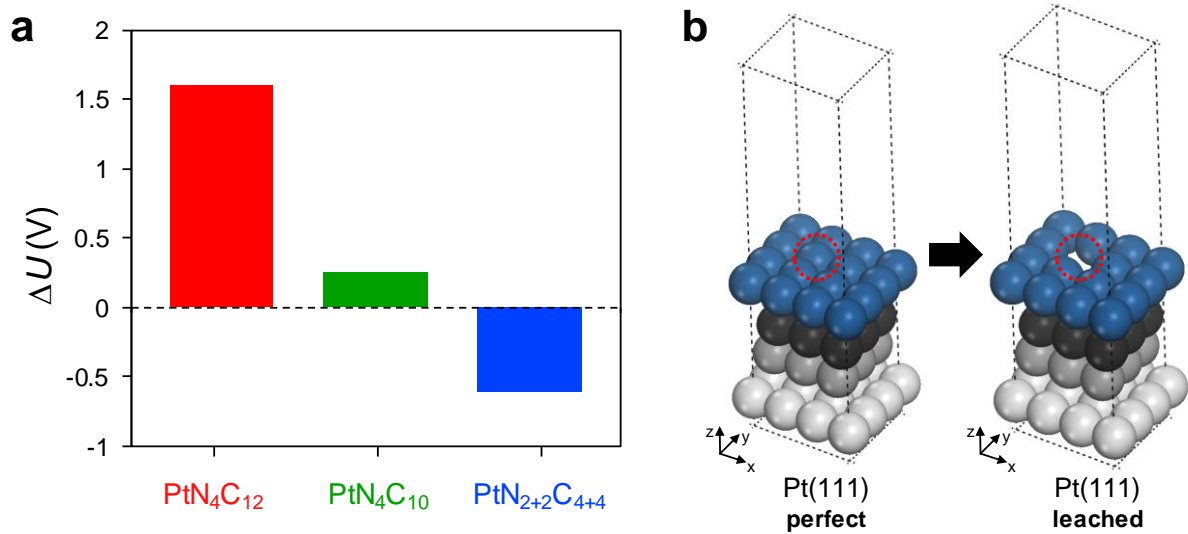


Figure 2.12 a, Electrode potential shift (ΔU), which was gauged with the difference in chemical potential of Pt atom in the Pt–N₄ sites and that on the Pt(111) surface [i.e., $\mu_{\text{Pt-N}_4} - \mu_{\text{Pt(111)}}$]. The black dotted line represents the dissolution potential of Pt(111) surface. **b**, Schematics for leaching a Pt atom on the Pt(111) surface, used for $\mu_{\text{Pt(111)}}$ calculation. Colour legends – Pt(top-most): dark-blue; Pt(second-most from top): black; Pt(third-most from top): gray; Pt(bottom-most): light-gray. The red dotted circle indicates the leaching site on the outermost layer.

2.3.5 Full Free Energy Diagram of CER over Pt₁/CNT

By combining the experimental data for kinetics and theoretical data for thermodynamics, we constructed a full free energy diagram along the reaction coordinate of CER over the Pt₁/CNT. In this approach, which was recently invented by Exner and co-workers,^{59,60} the free energies of the transition states (TS's) are obtained from the experimental Tafel plots, whereas the free energies of the reaction intermediates are determined from DFT calculations. Details regarding the definition and derivation of this approach are fully given in the earlier works by Exner and co-workers.^{59,60} Within the Butler-Volmer formalism, the Tafel slope, b , is defined by following equation,

$$b = \frac{k_B T \ln(10)}{e \cdot (\gamma + r_{\text{rds}} \alpha_k)} \quad (2.39)$$

where k_B is Boltzmann's constant, T is temperature, e is elementary charge, γ is integer number of transferred electrons before the rate-determining step (rds), r_{rds} is 0 for chemical (*i.e.*, no charge transfer) and 1 for electrochemical step, and α_k is transfer coefficient of the considered reaction step k , respectively. With increasing overpotential for the CER (η_{CER}), the experimental Tafel plot reveals two linear Tafel regions with b of 38 mV/dec ($0.030 \text{ V} \leq \eta_{\text{CER}} \leq 0.070 \text{ V}$), and 79 mV/dec ($0.075 \text{ V} \leq \eta_{\text{CER}} \leq 0.102 \text{ V}$), respectively (**Figure 2.13**).

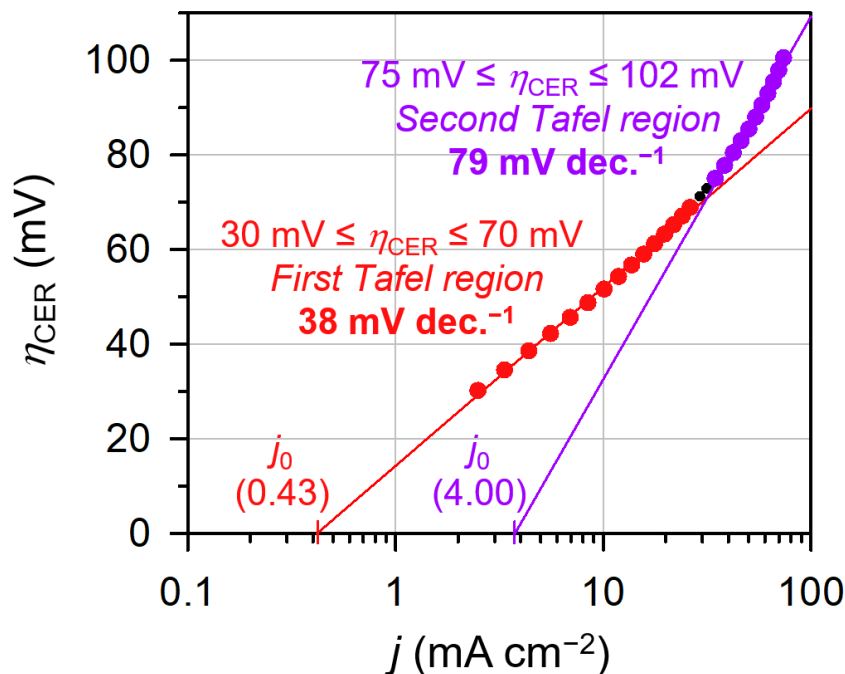


Figure 2.13 Experimental Tafel plot exhibiting two linear Tafel regions with Tafel slopes of 38 and 79 mV dec⁻¹. The fitting ranges of overpotential for CER (η_{CER}) are indicated. The exchange current density j_0 is given by the extrapolation.

At room temperature, the respective γ , r_{rds} , and α_k for each Tafel region were determined as $\gamma = 0$, $r_{\text{rds}} = 1$, $\alpha_1 = 0.83$ (for first region, $k = 1$) and $\gamma = 1$, $r_{\text{rds}} = 1$, $\alpha_2 = 0.58$ (for second region, $k = 2$), respectively. The overall current density (j) can be expressed as a function of η_{CER} ,

$$\log(j(\eta_{\text{CER}})) = \log\left(\frac{k_B T \cdot 2e\Gamma_{\text{act}}}{h}\right) - \frac{G_{\text{rds}}^{\#}}{k_B T \ln(10)} + \frac{\eta_{\text{CER}}}{b} = \log(j_0) + \frac{\eta_{\text{CER}}}{b} \quad (2.40)$$

where h is the Plank's constant, Γ_{act} is the number of active sites per area, $G_{\text{rds}}^{\#}$ is the TS free energy at the rds, and j_0 is the exchange current density, respectively.

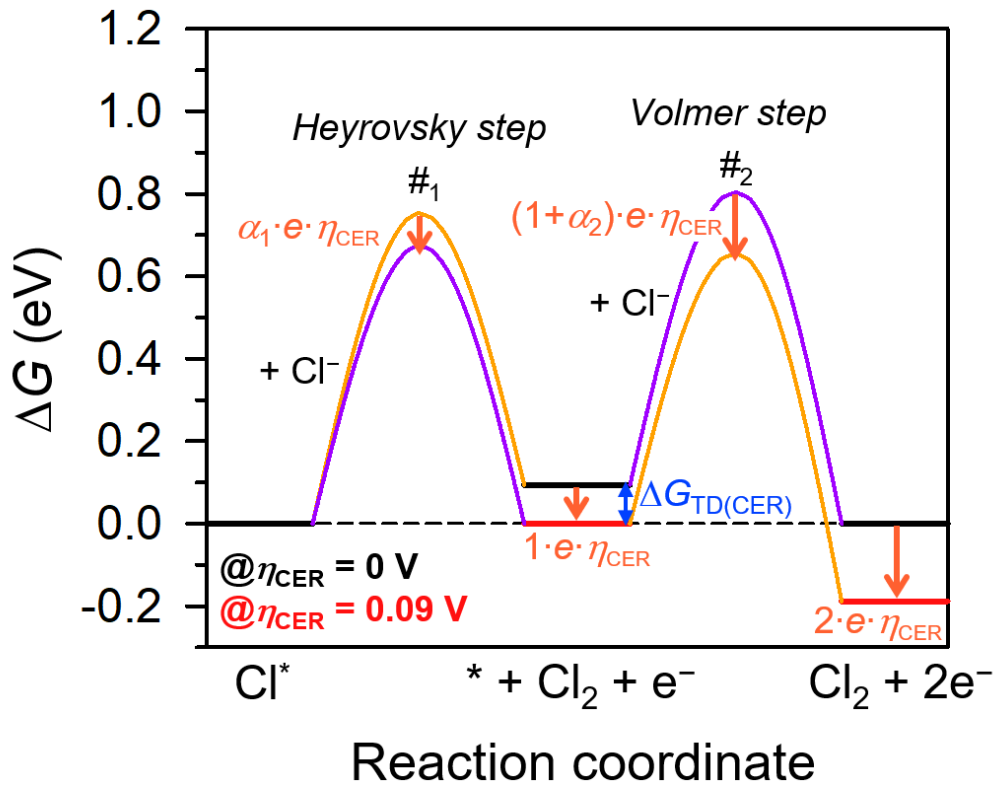


Figure 2.14 Full free energy diagram along the reaction coordinate of CER over the Pt₁/CNT at respective overpotential for CER (η_{CER}) of 0 V (black thick lines) and 0.09 V (red thick lines). #₁ and #₂ represent the transfer coefficients at each transition state (TS), which are determined as 0.83 and 0.58 from experimental Tafel plot, respectively. The TS with higher free energy at the respective η_{CER} is indicated by purple line. Orange arrows represent the decreased amounts of free energies by applied η_{CER} for each state (*i.e.*, first TS (denoted as ‘#₁’), intermediate state, second TS (denoted as ‘#₂’), and final state, respectively). The free energy change for reaction intermediate at zero overpotential ($\Delta G_{\text{TD}(\text{CER})}$) is indicated by blue arrow.

The Γ_{act} was obtained from the equation (2.41):

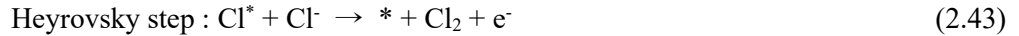
$$\Gamma_{\text{act}} = m \times N_A \quad (2.41)$$

where m is the molar number of Pt-catalyst loaded on the electrode (*i.e.*, 14.00 nmol/cm² for Pt₁/CNT), and N_A is Avogadro's number (6.022×10^{23}). From the $\log(j_0)$, we can determine the $G_{\text{rds}}^{\#}$ as follows,

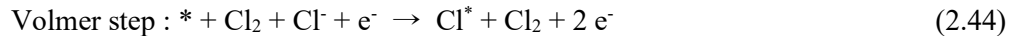
$$G_{\text{rds}}^{\#} = k_B T \ln(10) \left(\log \left(\frac{k_B T \cdot 2e \Gamma_{\text{act}}}{h} \right) - \log(j_0) \right) \quad (2.42)$$

The $G_{\text{rds}}^{\#}$'s were determined as 0.75 (for first TS) and 0.80 eV (for second TS) in the Pt₁/CNT. When the η_{CER} is applied ($\eta_{\text{CER}} > 0$), the free energies of each state are affected by the number of transferred electrons, z [*i.e.*, $z = 0, 1$, and 2 for initial state (IS), intermediate state (IM), and final state (FS)] and α_k [*i.e.*, $\alpha_1 = 0.83$ for first TS, and $(1 + \alpha_2) = 1.58$ for second TS, respectively]. Resultingly, with increasing η_{CER} , the free energies for the first TS, IM, second TS, and FS along the reaction coordinate of CER over Pt₁/CNT were lowered by $0.83 \cdot e \cdot \eta_{\text{CER}}$, $1 \cdot e \cdot \eta_{\text{CER}}$, $1.58 \cdot e \cdot \eta_{\text{CER}}$, and $2 \cdot e \cdot \eta_{\text{CER}}$, respectively (**Figure 2.14**).

The resulting full free energy diagram of CER over the Pt₁/CNT revealed that the Heyrovsky step is the first step in the reaction pathway since the PtN₄C₁₂ species, *i.e.*, active site in the Pt₁/CNT, already involved the Cl* species at acidic CER condition (**Figure 2.15**).



Subsequently, the Volmer step followed as the second step to close the electrocatalytic cycle, which was identified as the rds with higher TS free energy at zero overpotential (*i.e.*, $G_{\#1} = 0.75$ eV for Heyrovsky step, and $G_{\#2} = 0.80$ eV for Volmer step, respectively).



However, for $\eta_{\text{CER}} = 0.09$ V, which corresponded to the thermodynamic optimum of PtN₄C₁₂ species for the CER (*i.e.*, $\eta_{\text{CER}} = \eta_{\text{TD}(\text{CER})}$), the Heyrovsky step became the rds with a slightly higher TS free energy (*i.e.*, $G_{\#1} = 0.67$ eV for Heyrovsky step, and $G_{\#2} = 0.66$ eV for Volmer step, respectively, **Figure 2.14**). The TS free energies of step $\#_i$ ($G_{\#_i}(\eta_{\text{CER}})$) showed that with increasing η_{CER} , the rds was switched from the first TS (Heyrovsky step, $i = 1$) to the second TS (Volmer step, $i = 2$) due to the larger decrease of free energies by η_{CER} in the Volmer step (indicated by the slope, $dG_{\#_i}(\eta_{\text{CER}})/d\eta_{\text{CER}}$).

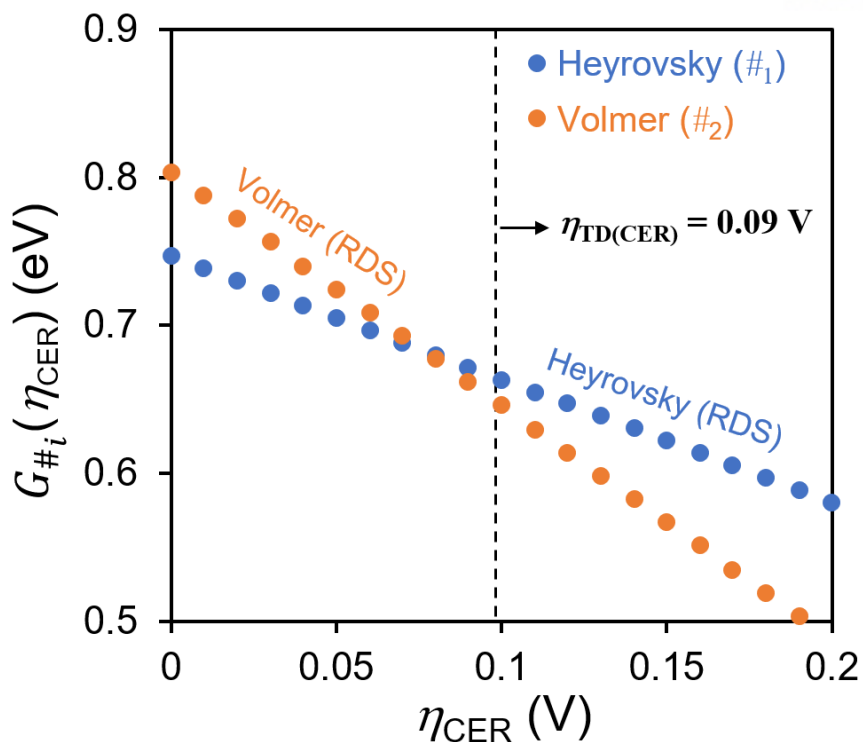


Figure 2.15 Transition state (TS) free energy corresponding to the step $\#_i$ ($G_{\#_i}(\eta_{\text{CER}})$) as a function of applied overpotential η_{CER} in the Pt₁/CNT. The first step ($\#_1$) corresponds to the Heyrovsky step, while the second step ($\#_2$) corresponds to the Volmer step, respectively. The black dotted line indicates the thermodynamic optimum of PtN₄C₁₂ species, where the η_{CER} equals to the thermodynamic overpotential for CER [*i.e.*, $\eta_{\text{CER}} = \eta_{\text{TD}(\text{CER})}$ (= 0.09 V)].

A recent study highlighted that the thermodynamic measure for the activity would be more helpful if it is evaluated at target overpotential ($\eta > 0$), not at zero overpotential ($\eta = 0$).⁶¹ Specifically, the use of η_{TD} would be only valid around zero overpotential because the connection between the BEP relation and Sabatier's principle was defined at zero overpotential. However, if the overpotential increases by ~ 0.10 V or higher, which is far from equilibrium, the linkage between two concepts cannot be convinced. From our results, the absolute value of free energy for the IM ($|\Delta G(\eta_{\text{CER}})|$) showed that it reached the thermoneutral state at the point where the η_{CER} equals to the thermodynamic overpotential for CER (*i.e.*, $\eta_{\text{TD}(\text{CER})} = 0.09$ V for PtN₄C₁₂ species, **Figure 2.16**). Considering that typical CER overpotentials for chlor-alkali process are about ~ 0.1 V,^{2,62} PtN₄C₁₂ species in the Pt₁/CNT would be more beneficial for industrial chlorine electrocatalysis since they can reach nearly thermoneutral state at target overpotential.

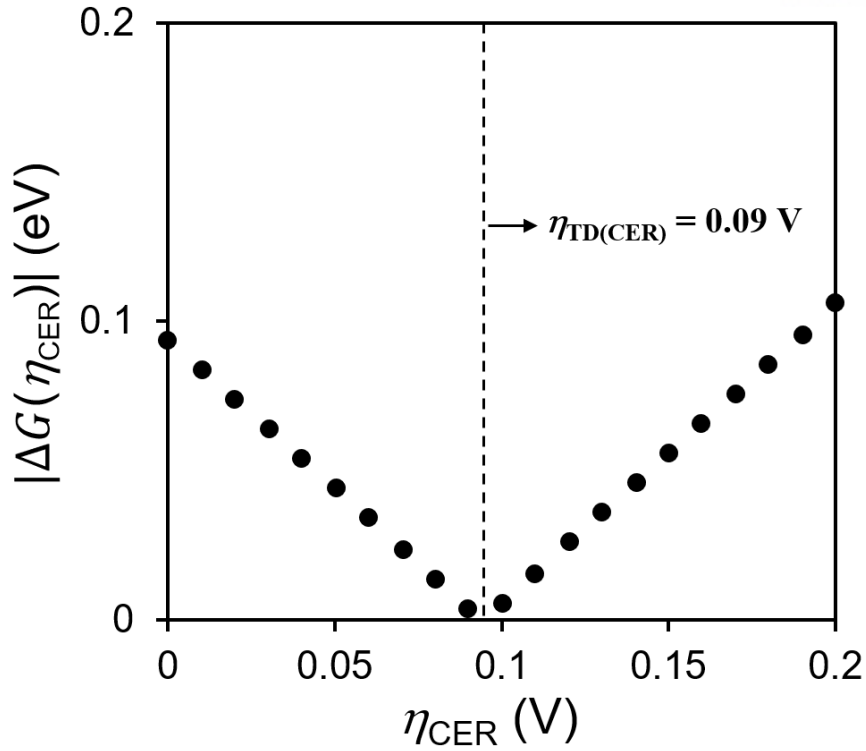
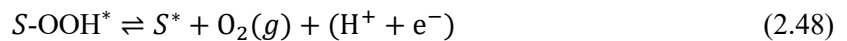
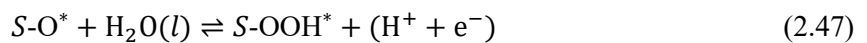
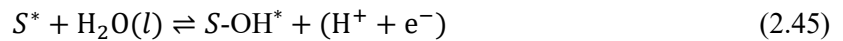


Figure 2.16 Transition state (TS) free energy corresponding to the step $\#_i$ ($G_{\#_i}(\eta_{\text{CER}})$) as a function of applied overpotential η_{CER} in the Pt₁/CNT. The first step ($\#_1$) corresponds to the Heyrovsky step, while the second step ($\#_2$) corresponds to the Volmer step, respectively. The black dotted line indicates the thermodynamic optimum of PtN₄C₁₂ species, where the η_{CER} equals to the thermodynamic overpotential for CER [*i.e.*, $\eta_{\text{CER}} = \eta_{\text{TD}(\text{CER})} (= 0.09 \text{ V})$].

2.3.6 CER Selectivity Compared to the OER

To investigate the thermodynamic overpotential for OER at zero overpotential ($\eta_{\text{TD}(\text{OER})}$) of Pt–N₄ sites, we assumed the conventional four-electron pathway for the OER as follows,



where (*l*) indicates the liquid phase. The ΔE 's for each reaction intermediate were calculated relative to H_2O and H_2 molecules as follows,

$$\Delta E_{OH^*} = E_{S-OH^*} - E_{S^*} - (E_{H_2O} - 0.5E_{H_2}) \quad (2.49)$$

$$\Delta E_{O^*} = E_{S-O^*} - E_{S^*} - (E_{H_2O} - E_{H_2}) \quad (2.50)$$

$$\Delta E_{OOH^*} = E_{S-OOH^*} - E_{S^*} - (2E_{H_2O} - 1.5E_{H_2}) \quad (2.51)$$

where E_{S-OH^*} , E_{S-O^*} , and E_{S-OOH^*} are the total energies of adsorbed state of the Pt- N_4 sites (*i.e.*, OH^* , O^* , and OOH^*); E_{S^*} is the total energy of bare state of the Pt- N_4 sites; E_{H_2O} and E_{H_2} are the total energies of an isolated water molecule and hydrogen gas, respectively. The reaction free energy of equations (2.45–2.48) (ΔG_1 , ΔG_2 , ΔG_3 , ΔG_4) for OER can be calculated as follows,

$$\Delta G_1 = \Delta G_{OH^*} \quad (2.52)$$

$$\Delta G_2 = \Delta G_{O^*} - \Delta G_{OH^*} \quad (2.53)$$

$$\Delta G_3 = \Delta G_{OOH^*} - \Delta G_{O^*} \quad (2.54)$$

$$\Delta G_4 = 4.92 - \Delta G_{OOH^*} \quad (2.55)$$

Finally, $\eta_{TD(OER)}$ can be defined as

$$\eta_{TD(OER)} = \frac{\max[\Delta G_1, \Delta G_2, \Delta G_3, \Delta G_4]}{e} - U_{eq} [V] \quad (2.56)$$

where U_{eq} indicates the equilibrium potential for OER (*i.e.*, 1.23 V vs. SHE).

Table 2.1 Adsorption free energies (ΔG 's) of OH^* , O^* , and OOH^* on Pt- N_4 sites (*i.e.*, Pt N_4C_{12} , Pt N_4C_{10} , and Pt $N_{2+2}C_{4+4}$) and thermodynamic overpotentials for OER ($\eta_{TD(OER)}$) at the overpotential (η_{OER}) of 0 and 0.13 V.

Sites	ΔG_{OH^*} (eV)	ΔG_{O^*} (eV)	ΔG_{OOH^*} (eV)	$\eta_{TD(OER)}$ (V) (@ $\eta_{OER} = 0$ V)	$\eta_{TD(OER)}$ (V) (@ $\eta_{OER} = 0.13$ V)
Pt N_4C_{12}	2.45	4.35	5.31	1.22	1.09
Pt N_4C_{10}	2.10	4.12	5.07	0.87	0.74
Pt $N_{2+2}C_{4+4}$	0.82	1.97	3.95	0.75	0.62

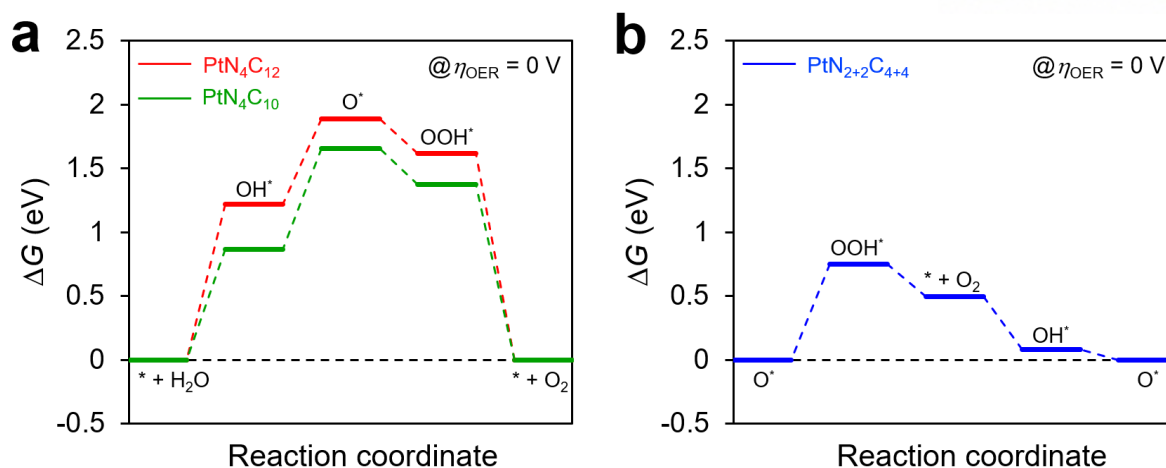


Figure 2.17 Free energy diagrams for the OER on Pt–N₄ sites at zero overpotential ($\eta_{\text{OER}} = 0$ V); **a**, PtN₄C₁₂, PtN₄C₁₀ and **b**, PtN₂₊₂C₄₊₄. The active adsorbate structures for each model were employed as initial steps (*i.e.*, bare structure (*)) for PtN₄C₁₂ and PtN₄C₁₀, and O* for PtN₂₊₂C₄₊₄, respectively). The black dotted line represents the thermoneutral state (*i.e.*, $\Delta G = 0$).

To further verify the high CER selectivity compared to the OER, we obtained the free energy diagrams for OER on the Pt–N₄ sites (**Figure 2.17**). Note that the thermodynamic overpotentials for OER ($\eta_{\text{TD(OER)}}$) of all Pt–N₄ sites were evaluated at the overpotential of 0.13 V (*i.e.*, $\eta_{\text{OER}} = 1.36$ V – 1.23 V = 0.13 V), to be referenced to the same potential for the CER (*i.e.*, $\eta_{\text{CER}} = 0$ V). For PtN₄C₁₂ and PtN₄C₁₀ species, OH* adsorption from H₂O(*l*) was found to be the most endothermic among reaction steps, corresponding to the potential determining step (PDS) with a large theoretical overpotentials for OER [*i.e.*, $\eta_{\text{TD(OER)}}$ above 0.74 V (**Table 2.1**)]. Although the PtN₂₊₂C₄₊₄ site exhibited relatively stable reaction pathways due to the CN = 4 for oxygen-involving intermediates compared to other Pt–N₄ sites (**Figure 2.4**), it was still considered inactive for OER with very high overpotential $\eta_{\text{TD(OER)}}$ of 0.62 V. This result was in good agreement with experimental observation, where OER did not occur even in the absence of Cl[–] for Pt₁/CNT. Particularly focusing on the PtN₄C₁₂ species, which most plausibly catalyzes the CER in the Pt₁/CNT, a huge difference between $\eta_{\text{TD(OER)}}$ and $\eta_{\text{TD(CER)}}$ at the PDS (*i.e.*, $\eta_{\text{TD(OER)}} - \eta_{\text{TD(CER)}} = 0.99$ V) further corroborates the excellent CER selectivity of Pt₁/CNT compared to the OER.

2.4 Conclusion

In this study, we demonstrated the atomically dispersed Pt–N₄ site on the CNT could catalyse the CER with high activity and selectivity. From the experimental results, Pt₁/CNT exhibited excellent CER activity with a lower overpotential and Tafel slope, compared to PtNP/CNT and commercial DSA catalysts. Notably, Pt–N₄ sites in the Pt₁/CNT could preserve more stable structure than PtNP/CNT, by mitigating the formation of the chloro-Pt complexes due to its strong ligation with N. From the *ab-initio* Pourbaix diagram, we initially identified the active adsorbate structures for the Pt–N₄ sites as the Cl* species, which corresponded to the most plausible reaction intermediate for the CER. Meanwhile, the active adsorbate structures for PtO₂ (110) surface representing the PtNP/CNT involved the ClO* species, similar to other MMO catalysts. Among Pt–N₄ sites, PtN₄C₁₂ was identified as the most plausible active sites for CER with the lowest $\eta_{TD(CER)}$ of 0.09 V at zero overpotential. Besides good CER activity, PtN₄C₁₂ species were also stable against Pt dissolution, which were feasible to exist in the Pt₁/CNT. Finally, the full free energy diagram of CER over the Pt₁/CNT, which combines the experimental data for kinetics and theoretical data for thermodynamics, revealed that the CER on Pt₁/CNT may follow Volmer-Heyrovsky mechanism, with the changes in RDS depending on the applied overpotential. The excellent CER selectivity of PtN₄C₁₂ species compared to the OER was further verified by a huge difference in η_{TD} at the PDS. In conclusion, this work presents the first use of atomically dispersed catalysts for CER. We envision that this type of catalysts may be exploited as a potential alternative to MMO-based catalysts, whose activity and selectivity are intrinsically by the scaling relationship between CER and OER.

2.5 References

1. Trasatti, S. Electrocatalysis: Understanding the Success of DSA[®]. *Electrochim. Acta* **2000**, *45*, 2377–2385.
2. Karlsson, R. K. B.; Cornell, A. Selectivity between Oxygen and Chlorine Evolution in the Chlor-Alkali and Chlorate Processes. *Chem. Rev.* **2016**, *116*, 2982–3028.
3. Amikam, G.; Nativ, P.; Gendel, Y. Chlorine-Free Alkaline Seawater Electrolysis for Hydrogen Production. *Int. J. Hydrogen Energy* **2018**, *43*, 6504–6514.
4. Kumar, A.; Phillips, K. R.; Thiel, G. P.; Schröder, U.; Lienhard, J. H. Direct Electrosynthesis of Sodium Hydroxide and Hydrochloric Acid from Brine Streams. *Nat. Catal.* **2019**, *2*, 106–113.
5. Hayfield, P. C. S. Development of the Noble Metal/Oxide Coated Titanium Electrode. Part II: The Move from Platinum/Iridium to Ruthenium Oxide Electrocatalysis. *Platinum Metals Rev.* **1998**, *42*, 46–55.
6. Hayfield, P. C. S. Development of the Noble Metal/Oxide Coated Titanium Electrode. Part III: Coated Titanium Anodes in Widely Ranging Oxygen Evolving Situations. *Platinum Metals Rev.* **1998**, *42*, 116–122.
7. Bune, N.; Losev, V. V.; Reznik, M. F.; Zaripova, E. Selectivity and Electrochemical Behavior of Titanium-Ruthenium Oxide Anodes Containing Different Levels of Ruthenium Dioxide. *Elektrokhimiya* **1986**, *22*, 396–398.
8. Petrykin, V.; Macounova, K.; Shlyakhtin, O. A.; Krtil, P. Tailoring the Selectivity for Electrocatalytic Oxygen Evolution on Ruthenium Oxides by Zinc Substitution. *Angew. Chem. Int. Ed.* **2010**, *49*, 4813–4815.
9. Sohrabnejad-Eskan, I.; Goryachev, A.; Exner, K. S.; Kibler, L. A.; Hensen, E. J. M.; Hofmann, J. P.; Over, H. Temperature-Dependent Kinetic Studies of the Chlorine Evolution Reaction over RuO₂(110) Model Electrodes. *ACS Catal.* **2017**, *7*, 2403–2411.
10. Zeradhanin, A. R.; Menzel, N.; Schuhmann, W.; Strasser, P. On the faradaic selectivity and the role of surface inhomogeneity during the chlorine evolution reaction on ternary Ti–Ru–Ir mixed metal oxide electrocatalysts. *Phys. Chem. Chem. Phys.* **2014**, *16*, 13741–13747.
11. Binninger, T.; Mohamed, R.; Waltar, K.; Fabbri, E.; Levecque, P.; Kotz, R.; Schmidt, T. J., Thermodynamic explanation of the universal correlation between oxygen evolution activity and corrosion of oxide catalysts. *Sci. Rep.* **2015**, *5*, 12167.
12. Geiger, S.; Kasian, O.; Ledendecker, M.; Pizzutilo, E.; Mingers, A. M.; Fu, W. T.; Diaz-Morales, O.; Li, Z. Z.; Oellers, T.; Fruchter, L.; Ludwig, A.; Mayrhofer, K. J. J.; Koper, M. T. M.; Cherevko, S., The stability number as a metric for electrocatalyst stability benchmarking. *Nat. Catal* **2018**, *1*, 508-515.
13. Barbir, F. PEM Electrolysis for Production of Hydrogen from Renewable Energy Sources. *Sol.*

- Energy* **2005**, *78*, 661–669.
14. Trinke, P.; Benschmann, B.; Hanke-Rauschenbach, R. Current Density Effect on Hydrogen Permeation in PEM Water Electrolyzers. *Int. J. Hydrogen Energy* **2017**, *42*, 14355–14366.
 15. Fu, Q.; Saltsburg, H.; Flytzani-Stephanopoulos, M. Active nonmetallic Au and Pt species on ceria-based water-gas shift catalysts. *Science* **2003**, *301*, 935–938.
 16. Kwak, J. H.; Hu, J. Z.; Mei, D.; Yi, C. W.; Kim, D. H.; Peden, C. H. F.; Allard, L. F.; Szanyi, J., Coordinatively Unsaturated Al³⁺ Centers as Binding Sites for Active Catalyst Phases of Platinum on gamma-Al₂O₃. *Science* **2009**, *325*, 1670–1673.
 17. Qiao, B. T.; Wang, A. Q.; Yang, X. F.; Allard, L. F.; Jiang, Z.; Cui, Y. T.; Liu, J. Y.; Li, J.; Zhang, T., Single-atom catalysis of CO oxidation using Pt₁/FeO_x. *Nat. Chem* **2011**, *3*, 634–641.
 18. Liu, J.; Lucci, F. R.; Yang, M.; Lee, S.; Marcinkowski, M. D.; Therrien, A. J.; Williams, C. T.; Sykes, E. C. H.; Flytzani-Stephanopoulos, M. Tackling CO Poisoning with Single-Atom Alloy Catalysts. *J. Am. Chem. Soc.* **2016**, *138*, 6396–6399.
 19. Yang, S.; Kim, J.; Tak, Y. J.; Soon, A.; Lee, H. Single-Atom Catalyst of Platinum Supported on Titanium Nitride for Selective Electrochemical Reactions. *Angew. Chem. Int. Ed.* **2016**, *55*, 2058–2062.
 20. Soorholtz, M.; Jones, L. C.; Samuelis, D.; Weidenthaler, C.; White, R. J.; Titirici, M.-M.; Cullen, D. A.; Zimmermann, T.; Antonietti, M.; Maier, J.; Palkovits, R.; Chmelka, B. F.; Schüth, F. Local Platinum Environments in a Solid Analogue of the Molecular Periana Catalyst. *ACS Catal.* **2016**, *6*, 2332–2340.
 21. Liu, L.; Corma, A. Metal Catalysts for Heterogeneous Catalysis: from Single Atoms to Nanoclusters and Nanoparticles. *Chem. Rev.* **2018**, *118*, 4981–5079.
 22. Zhu, C.; Fu, S.; Shi, Q.; Du, D.; Lin, Y. Single-Atoms Electrocatalysts. *Angew. Chem. Int. Ed.* **2017**, *56*, 13944–13960.
 23. Kim, J.; Kim, H.-E.; Lee, H.; Single-Atom Catalysis of Precious Metals for Electrochemical Reactions. *ChemSusChem* **2018**, *11*, 104–113.
 24. Cheon, J. Y.; Kim, T.; Choi, Y.; Jeong, H. Y.; Kim, M. G.; Sa, Y. J.; Kim, J.; Lee, Z.; Yang, T.-H.; Kwon, K.; Terasaki, O.; Park, G.-G.; Adzic, R. R.; Joo, S. H. Ordered Mesoporous Porphyrinic Carbons with Very High Electrocatalytic Activity for the Oxygen Reduction Reaction. *Sci. Rep.* **2013**, *3*, 2715.
 25. Sa, Y. J.; Seo, D.-J.; Woo, J.; Lim, J. T.; Cheon, J. Y.; Yang, S. Y.; Lee, J. M.; Kang, D.; Shin, T. J.; Shin, H. S.; Jeong, H. Y.; Kim, C. S.; Kim, M. G.; Kim, T.-Y.; Joo, S. H. A General Approach to Preferential Formation of Active Fe–N_x Sites in Fe–N/C Electrocatalysts for Efficient Oxygen Reduction Reaction. *J. Am. Chem. Soc.* **2016**, *138*, 15046–15056.
 26. Choi, C. H.; Kim, M.; Kwon, H. C.; Cho, S. J.; Yun, S.; Kim, H.-T.; Mayrhofer, K. J. J.; Kim, H.; Choi, M. Tuning Selectivity of Electrochemical Reactions by Atomically Dispersed Platinum

- Catalyst. *Nat. Commun.* **2016**, *7*, 10922.
27. Liang, H.-W.; Brüller, S.; Dong, R.; Zhang, J.; Feng, X.; Müllen, K. Molecular Metal–N_x Centres in Porous Carbon for Electrocatalytic Hydrogen Evolution. *Nat. Commun.* **2015**, *6*, 7992.
 28. Cheon, J. Y.; Kim, K.; Sa, Y. J.; Sahngong, S. H.; Hong, Y.; Woo, J.; Yim, S.-D.; Jeong, H. Y.; Kim, Y.; Joo, S. H. Graphitic Nanoshell/Mesoporous Carbon Nanohybrids as Highly Efficient and Stable Bifunctional Oxygen Electrocatalysts for Rechargeable Aqueous Na–Air Batteries. *Adv. Energy Mater.* **2016**, *6*, 1501794.
 29. Sa, Y. J.; Park, S. O.; Jung, G. Y.; Shin, T. J.; Jeong, H. Y.; Kwak, S. K.; Joo, S. H. Heterogeneous Co–N/C Electrocatalysts with Controlled Cobalt Site Densities for the Hydrogen Evolution Reaction: Structure–Activity Correlations and Kinetic Insights. *ACS Catal* **2019**, *9*, 83–97.
 30. Kwon, H. C.; Kim, M.; Grote, J.-P.; Cho, S. J.; Chung, M. W.; Kim, H.; Won, D. H.; Zeradjanin, A. R.; Mayrhofer, K. J. J.; Choi, M.; Kim, H.; Choi, C. H. Carbon Monoxide as a Promoter of Atomically Dispersed Platinum Catalyst in Electrochemical Hydrogen Evolution Reaction. *J. Am. Chem. Soc.* **2018**, *140*, 16198–16205.
 31. Neurock, M.; Janik, M.; Wieckowski, A. A First Principles Comparison of the Mechanism and Site Requirements for the Electrocatalytic Oxidation of Methanol and Formic Acid over Pt. *Faraday Discuss.* **2008**, *140*, 363–378.
 32. Kim, J.; Roh, C.-W.; Sahoo, S. K.; Yang, S.; Bae, J.; Han, J. W.; Lee, H. Highly Durable Platinum Single-Atom Alloy Catalyst for Electrochemical Reactions. *Adv. Energy Mater.* **2018**, *8*, 1701476.
 33. Ellis, C. D.; Gilbert, J. A.; Murphy, W. R.; Meyer, T. J. Electrocatalytic oxidation of chloride to chlorine based on polypyridine complexes of ruthenium. *J. Am. Chem. Soc.* **1983**, *105*, 4842–4843.
 34. Du, J.; Chen, Z.; Chen, C.; Meyer, T. J. A half-reaction alternative to water oxidation: chloride oxidation to chlorine catalyzed by silver ion. *J. Am. Chem. Soc.* **2015**, *137*, 3193–3196.
 35. Umile, T. P.; Groves, J. T. Catalytic generation of chlorine dioxide from chlorite using a water-soluble manganese porphyrin. *Angew. Chem., Int. Ed.* **2011**, *50*, 695–698.
 36. Hicks, S. D.; Petersen, J. L.; Bougher, C. J.; Abu-Omar, M. M. Chlorite dismutation to chlorine dioxide catalyzed by a water-soluble manganese porphyrin. *Angew. Chem., Int. Ed.* **2011**, *50*, 699–702.
 37. Delley, B. An all-electron numerical method for solving the local density functional for polyatomic molecules. *J. Chem. Phys.* **1990**, *92*, 508–517.
 38. Delley, B. From molecules to solids with the DMol³ approach. *J. Chem. Phys.* **2000**, *113*, 7756–7764.
 39. Perdew, J. P.; Burke, K.; Ernzerhof, M. Generalized gradient approximation made simple. *Phys. Rev. Lett.* **1996**, *77*, 3865–3868.

40. Tkatchenko, A.; Scheffler, M. Accurate molecular Van Der Waals interactions from ground-state electron density and free-atom reference data. *Phys. Rev. Lett.* **2009**, *102*, 073005.
41. Delley, B. Hardness conserving semilocal pseudopotentials. *Phys. Rev. B* **2002**, *66*, 155125.
42. Klamt, A.; Schüürmann, G. COSMO: a new approach to dielectric screening in solvents with explicit expressions for the screening energy and its gradient. *J. Chem. Soc. Perkin Trans 2.* **1993**, 799–805.
43. Monkhorst, H. J.; Pack, J. D. Special points for Brillouin-zone integrations. *Phys. Rev. B* **1976**, *13*, 5188–5192.
44. Cherevko, S.; Kulyk, N.; Mayrhofer, K. J. J. Durability of platinum-based fuel cell electrocatalysts: dissolution of bulk and nanoscale platinum. *Nano Energy* **2016**, *29*, 275–298.
45. Range, K.-J.; Rau, F.; Klement, U.; Heyns, A. M. β -PtO₂: high pressure synthesis of single crystals and structure refinement. *Mater. Res. Bull.* **1987**, *22*, 1541–1547.
46. Vos, J. G.; Koper, M. T. M. Measurement of competition between oxygen evolution and chlorine evolution using rotating ring-disk electrode voltammetry. *J. Electroanal. Chem.* **2018**, *819*, 260–268.
47. Geiger, S.; Cherevko, S.; Mayrhofer, K. J. J. Dissolution of platinum in presence of chloride traces. *Electrochim. Acta* **2015**, *179*, 24–31.
48. Trasatti, S. Progress in the understanding of the mechanism of chlorine evolution at oxide electrodes. *Electrochim. Acta* **1987**, *32*, 369–382.
49. Hansen, H. A.; Man, I. C.; Studt, F.; Abild-Pedersen, F.; Bligaard, T.; Rossmeisl, J., Electrochemical chlorine evolution at rutile oxide (110) surfaces. *Phys. Chem. Chem. Phys.* **2010**, *12*, 283-290.
50. Exner, K. S.; Anton, J.; Jacob, T.; Over, H. Chlorine evolution reaction on RuO₂(110): *Ab initio* atomistic thermodynamics study - Pourbaix diagrams. *Electrochim. Acta* **2014**, *120*, 460–466.
51. Kuo, D. Y.; Paik, H.; Nelson, J. N.; Shen, K. M.; Schlom, D. G.; Suntivich, J., Chlorine evolution reaction electrocatalysis on RuO₂(110) and IrO₂(110) grown using molecular-beam epitaxy. *J. Chem. Phys.* **2019**, *150*, 041726.
52. Pourbaix, M. *Atlas of Electrochemical Equilibria in Aqueous Solutions*, National Association of Corrosion Engineers, Houston, **1974**.
53. Hansen, H. A.; Rossmeisl, J.; Nørskov, J. K. Surface Pourbaix diagrams and oxygen reduction activity of Pt, Ag and Ni(111) surfaces studied by DFT. *Phys. Chem. Chem. Phys.* **2008**, *10*, 3722–3730.
54. Exner, K. A. Recent Advancements Towards Closing the Gap between Electrocatalysis and Battery Science Communities: The Computational Lithium Electrode and Activity-Stability Volcano Plots. *ChemSusChem* **2019**, *12*, 2330-2344.
55. Nørskov, J. K.; Rossmeisl, J.; Logadottir, A.; Lindqvist, L.; Kitchin, J. R.; Bligaard, T.; Jonsson,

- H., Origin of the overpotential for oxygen reduction at a fuel-cell cathode. *J. Phys. Chem. B* **2004**, *108*, 17886-17892.
56. Vos, J. G.; Liu, Z. C.; Speck, F. D.; Perini, N.; Fu, W. T.; Cherevko, S.; Koper, M. T. M., Selectivity Trends Between Oxygen Evolution and Chlorine Evolution on Iridium-Based Double Perovskites in Acidic Media. *ACS Catal.* **2019**, *9*, 8561-8574.
 57. Kattel, S.; Duan, Z.; Wang, Z., Density Functional Theory Study of an Oxygen Reduction Reaction on a Pt₃Ti Alloy Electrocatalyst. *J. Phys. Chem. C* **2013**, *117*, 7107-7113.
 58. Xiao, B. B.; Jiang, X. B.; Jiang, Q., Density functional theory study of oxygen reduction reaction on Pt/Pd₃Al(111) alloy electrocatalyst. *Phys. Chem. Chem. Phys.* **2016**, *18*, 14234-14243.
 59. Exner, K. S.; Sohrabnejad-Eskan, I.; Anton, J.; Jacob, T.; Over, H. Full free energy diagram of an electrocatalytic reaction over a single-crystalline model electrode. *ChemElectroChem* **2017**, *4*, 2902-2908.
 60. Exner, K. S.; Sohrabnejad-Eskan, I.; Over, H. A Universal approach to determine the free energy diagram of an electrocatalytic reaction. *ACS Catal.* **2018**, *8*, 1864-1879.
 61. Exner, K. S. Is thermodynamics a good descriptor for the activity? Re-investigation of Sabatier's principle by the free energy diagram in electrocatalysis. *ACS Catal.* **2019**, *9*, 5320-5329.
 62. Over, H. Atomic scale insights into electrochemical versus gas phase oxidation of HCl over RuO₂-based catalysts: a comparative review *Electrochim. Acta* **2013**, *93*, 314-333.

Chapter 3. Thermodynamic Control of Amorphous Calcium Carbonate Phases *via* Ion Adsorption in Catalytic Biomineralization

This chapter includes the published contents:

Jung, G. Y.; Shin, E.; Park, J. H.; Choi, B.-Y.; Lee, S.-W.; Kwak, S. K. *Chem. Mater.* **2019**, *31*, 7547-7557. Reproduced with permission. Copyright © 2019 American Chemical Society.

3.1 Introduction

Biomineralization refers to a process that living organisms produce minerals, which can be ubiquitously found in natural environments such as corals,¹ sea urchins,^{2,3} shells of mollusks,⁴ teeth⁵ and bones.⁶ Among them, calcium carbonate is the most abundant substance, which has been widely used in the fields of agriculture,⁷ medicine^{8,9} and industry.^{10,11} The specific interest regarding this material is mostly related to its disordered intermediate phase called amorphous calcium carbonate (ACC),^{2,3,12-15} which retains a prominent local order in the short range (within 5 Å).¹⁶ In general, ACC exists in a hydrated form and then transformed into final crystalline phases (*i.e.*, calcite, vaterite, and aragonite) *via* stepwise process, including dehydration into anhydrous ACC and its subsequent crystallization.^{17,18} In this regard, tuning the local structure of ACC has been increasingly recognized as a crucial factor for controlling the phase transition pathways¹⁹⁻²¹; however, its structure-property relationship is still lack of understanding.

From this viewpoint, the introduction of additive ions can catalyze the biomineralization process (referred as ‘catalytic biomineralization’)²² because it enables the tuning of local order in ACC by altering the hydrophilicity and coordination geometries with adjacent water molecules. In general, inorganic ions are soluble in aqueous environments and can control the phase transition pathways by affecting the lifetime of ACC phases, or by inducing different morphologies.²³⁻²⁶ For example, the Mg²⁺ and PO₄³⁻ ions are reported to retard the phase transition process.²⁷ Conversely, in the case of Fe²⁺ ions, most studies concluded that they have an inhibiting effect.²⁸ Meanwhile, in the presence of Ba²⁺, ACC phases became more ordered at short and medium ranges.²⁹

To date, the structural and energetic characteristics of ACC in the presence of additives have been widely studied using a variety of experimental techniques such as X-ray absorption spectroscopy combined with total distribution function (TDF) analysis,³⁰ thermogravimetric analysis (TGA),^{31,32} Raman spectra,³³ nuclear magnetic resonance (NMR),^{34,35} etc. However, these experimental techniques have some limitations in precisely describing the structural complexity and obtaining the accurate

thermodynamic properties for ACC. To resolve these issues, MD simulation can serve as a complement to experiments since it provides reliable structural information in atomistic level and energetic changes depending on the additive ions.³⁶⁻⁴²

In this study, we extensively performed MD studies to theoretically determine the effect of additive ions on the structure and stability of ACC phases of calcium carbonate. For this purpose, we investigated the stepwise phase transition process, including dehydration into anhydrous ACC from its hydrated nucleation clusters, and the subsequent transition into crystalline phases, for a wide range of water content (n) and molar ratio of additive ions (x) (*i.e.*, $\text{Ca}_{1-x}\text{M}_x\text{CO}_3 \cdot n\text{H}_2\text{O}$, where $0 \leq x \leq 1$ and $0 \leq n \leq 9$). Four kinds of additive ions, Mg^{2+} , Fe^{2+} , Sr^{2+} , and Ba^{2+} ions, were selected as models for catalytic biomineralization. Note that Mg^{2+} is one of the most abundant ions in marine environments where biomineralization occurs,⁴³ and the remaining three ions are also observed in sea water with carbonate forms in some bacteria.⁴⁴⁻⁴⁶ Our results showed that the local coordination structures of amorphous intermediate phases distinctively changed according to the intrinsic characteristics of additive ions, which are the hydrophilicity and ionic radius. Notably, each additive ion exhibited a promoting or inhibiting effect on the phase transition, which was determined by the thermodynamic balance between two opposing factors – endothermic dehydration and exothermic crystallization. In addition, we identified several structural characteristics for promoting or inhibiting additives by TDF analyses, which open a possibility for experimental observations. Our findings provide an in-depth understanding for the precise role of additive ions in controlling the phase transition pathways of calcium carbonate, which can shed light on the catalytic biomineralization processes.

3.2 Methods

3.2.1 Simulation Details

We investigated the dehydration and crystallization processes for amorphous intermediate phases of $\text{Ca}_{1-x}\text{M}_x\text{CO}_3 \cdot n\text{H}_2\text{O}$ systems using MD simulations. We started our investigations from the condition that the ratio of water to Ca^{2+} was 9.0 (*i.e.*, 200 Ca^{2+} , 200 CO_3^{2-} , and 1800 water molecules), assuming a locally high concentration just before aggregation. Subsequently, 50 to 200 additive ions were substituted by Ca^{2+} ions for the initial systems (*e.g.*, $x = 0.25, 0.5, 0.75$, and 1.0). Note that these high amounts of additive ions (*i.e.*, $x \geq 0.25$) have been reported to be actually feasible in the previous studies.^{30,47,48} Next, following the previously reported dehydration scheme by Wallace *et al.*,⁴⁹ we deleted water molecules until the water-to-cation ratio (n) became zero. It was achieved through a total of 18 sequential MD simulations under *NPT* ensemble; each simulation involved 200 (*i.e.*, $\text{H}_2\text{O}/\text{Ca}^{2+}$

ratio = ~2–9) or 40 (*i.e.*, H₂O/Ca²⁺ ratio = ~0–2) fewer water molecules than its previous one. Note that the water molecules to be deleted were selected as those farthest from the Ca²⁺ and CO₃²⁻ ions, to avoid unphysical distortion. In addition, the crystalline structures of calcium- or other metal- carbonates (*e.g.*, magnesite, calcite, strontianite, siderite, and witherite) were independently constructed by creating the 5×5×3 supercell structures. *NPT* MD simulations were performed for ~1–4 ns until reaching the equilibration, and the last 1 ns was used for the production stage. For all MD simulations, temperature and pressure were controlled by Nose-Hoover-Langevin thermostat and Berendsen barostat, respectively.^{50,51} The Ewald scheme⁵² and atom-based cutoff method (*i.e.*, a radius of 12.5 Å) were employed for treating the long-range Coulombic and van der Waals interactions, respectively.

3.2.2 Forcefield Parameterization

Previously reported interaction parameters for alkaline-earth metal carbonate (*i.e.*, Mg²⁺, Ba²⁺, and Sr²⁺) were incorporated to include the Fe²⁺ ions (**Table 3.1**). The interaction parameters for Mg²⁺, Ba²⁺ and Sr²⁺ ions were taken from Raiteri *et al.*'s work.⁵³ The interaction parameters for Ca²⁺, CO₃²⁻ ions and water molecules were taken from Demichelis *et al.*'s work.³⁸ For Fe²⁺ ion-relevant interactions, the Fe²⁺–water and the Fe²⁺–CO₃²⁻ interaction were respectively parameterized, following the procedures in the previous study.⁵³ The Fe²⁺–water interaction was parameterized by comparing the experimental values for coordination numbers (CNs), hydration free energy (ΔG_{hyd}), and distance between Fe²⁺ and water ($r_{\text{Ow-Fe}}$). The Lennard-Jones (LJ) 12-6 potential was employed for non-bond interaction between Fe²⁺ ions and water molecules,

$$E = D_0 \left[\left(\frac{R_0}{R} \right)^{12} - 2 \left(\frac{R_0}{R} \right)^6 \right] \quad (3.1)$$

where D_0 and R_0 indicate the energy well depth and equilibrium distance. Thermodynamic integration method was used to calculate the ΔG_{hyd} .⁵⁴ For this calculation, a single Fe²⁺ ion was packed in the cubic box (*i.e.*, 38.8 × 38.8 × 38.8 Å³) with 2000 water molecules. Next, each van der Waals and electrostatic interaction between Fe²⁺ ion and water molecules was progressively turned on through 20 steps, where each step was comprised of 200 ps and 500 ps for equilibration and production, respectively. Herein, to consider the size effect, finite size correction⁵⁵ was complemented into ΔG_{hyd} values (*i.e.*, $0.5q^2 \left((\epsilon - 1) / \epsilon \right) \cdot \left(\xi_{Ew} + 2\pi R^2 / 3L^3 \right) \approx 52.1$ kcal/mol). The CN and $r_{\text{Ow-Fe}}$ was obtained by last production run of simulation. Moreover, ΔG_{hyd} of respective ions were calculated to examine the

hydrophilicity, which were well agreed with experimentally values (**Table 3.1**).^{56,57} The Buckingham potential was employed for $\text{Fe}^{2+}\text{-CO}_3^{2-}$ interaction,

$$E = A \exp(-\beta R) - \frac{C}{R^6} \quad (3.2)$$

where A and β are the Buckingham parameters, which are related to repulsive force. C parameter is the parameter for attractive force, which was neglected in this work. These parameters were adjusted to experimental properties, such as bulk moduli⁵⁸ and lattice parameter⁵⁹ of FeCO_3 (siderite), by using the GULP relaxed fit method.⁶⁰ Note that volume thermal expansion coefficient (V) and lattice parameters of siderite were analyzed by Forcite program in Materials Studio 2019,⁶¹ and linear thermal expansion coefficients (α_a , α_c) were analyzed by LAMMPS program,⁶² which were estimated from *NPT* MD simulation at respective temperature (200, 300, 400, and 500 K) and 1 atm for 1 ns, while fixing the cell shape. The V (in K^{-1}) was calculated from *NPT* MD simulation at respective temperature (*i.e.*, 300 and 400 K) and atmospheric pressure conditions. The results were well agreed with experimental values although α_a , α_c , and V were not included in the training sets. This further supports the validity of our parameterization scheme.

Table 3.1 Interaction parameters of Fe^{2+} -water (O_w in H_2O) and $\text{Fe}^{2+}\text{-CO}_3^{2-}$ (O_c in CO_3^{2-}) and comparison of physical properties [*i.e.*, lattice parameters, bulk modulus (K), linear and volume thermal expansion coefficients (α_a , α_c , and V)], obtained from experiment and calculation.

Fe- O_w			Fe- O_c		
D_0 (kcal/mol)	0.0117		A (kcal/mol)	22091.19	
R_0 (Å)	3.255		β (Å ⁻¹)	3.44	
			C (kcal/mol/Å ⁶)	0.0	
Fe^{2+}	Expt. ^{57,63}	Calc.	Siderite	Expt. ^{58,59,64}	Calc.
ΔG_{hyd} (kcal/mol)	-439.8	-437.38	a (Å)	4.689	4.62
$r_{\text{Ow-Fe}}$ (Å)	2.1	2.012	c (Å)	15.37	15.07
CN	6	5.95	K (GPa)	117	116.93
			α_a (10^{-6}K^{-1})	5.4	5.7
			α_c (10^{-6}K^{-1})	16.1	27.1
			V (10^{-5}K^{-1})	2.69	3.4

3.2.3 Mean Square Displacement Analysis

To obtain the self-diffusion coefficient (D) of water and respective ions (*i.e.*, Ca^{2+} and CO_3^{2-}) in the $\text{CaCO}_3 \cdot n\text{H}_2\text{O}$ systems, mean square displacements (MSD) were analysed over time using the Stokes-Einstein relation as follows,

$$D = \frac{1}{6} \frac{\langle (\delta r)^2 \rangle}{\Delta t} \quad (3.3)$$

where δr is the change of displacement within the time interval, Δt . The factor 6 indicates three dimensions in the Cartesian coordinates (*i.e.*, x , y , and z) and two directions to move (*i.e.*, forward and backward). To secure the statistical accuracy, the MSD values were analysed over last 1 ns trajectory from the *NPT* MD simulation for 5 ~ 10 ns. Using equation (3.3), D was estimated by the slope of MSD. Note that the first 10% of the MSD curve (*i.e.*, about 100 ps MD run) was excluded for the fitting since it has not yet entered the linear diffusive regime (**Figure 3.1**).

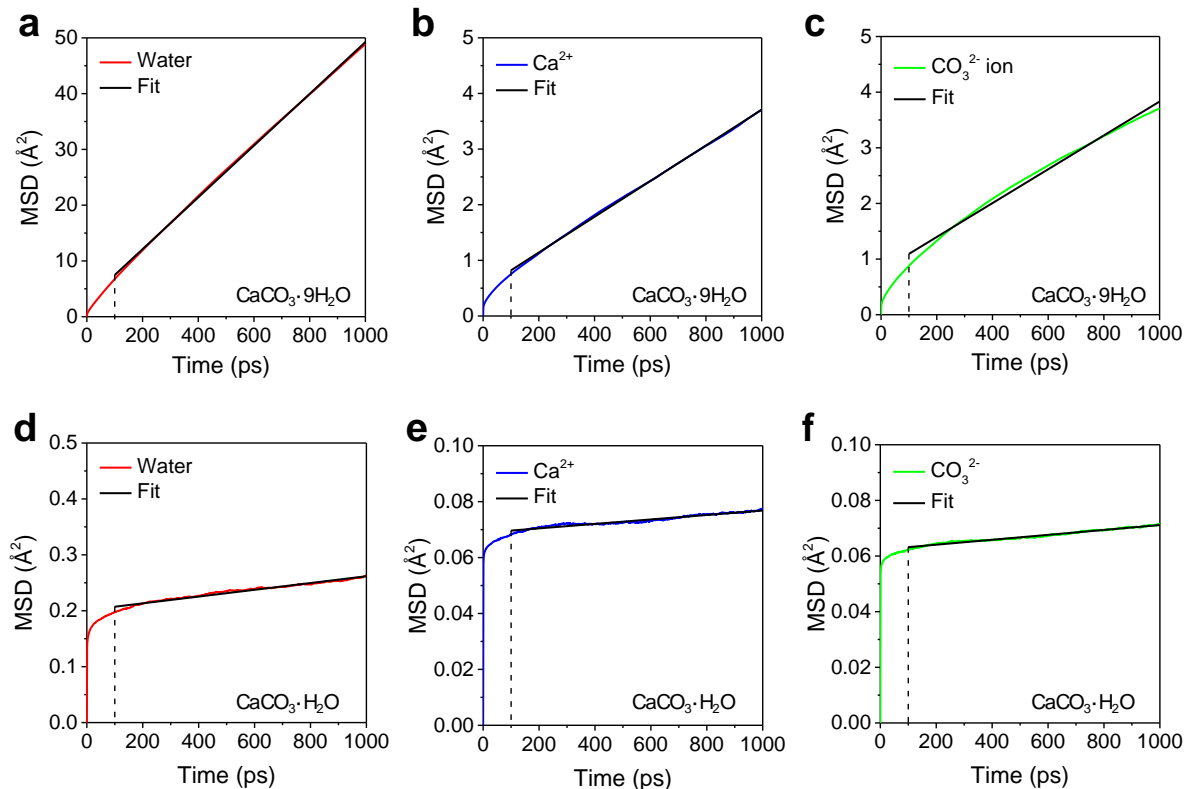


Figure 3.1 Mean square displacement analysis for water and ions (*i.e.*, Ca^{2+} and CO_3^{2-}) in the $\text{CaCO}_3 \cdot n\text{H}_2\text{O}$ system with different hydration levels **a-c**, at $n = 9$, and **d-f**, at $n = 1$. The black lines represent the fitting lines used for estimation of the self-diffusion coefficients.

3.3 Results and Discussion

3.3.1 Overview of Dehydration Process

In general, the phase transition of calcium carbonate is reported to take place in a stepwise manner from hydrated form, to its anhydrous ACC (*via* dehydration), and to the final crystalline structure (*via* crystallization).^{17,18} For the investigation, we constructed model systems for the dehydration process from hydrated nucleation clusters to anhydrous ACC for a wide range of molar compositions of additive ions (x) and water content (n) (*i.e.*, $\text{Ca}_{1-x}\text{M}_x\text{CO}_3 \cdot n\text{H}_2\text{O}$, where $0 \leq x \leq 1$ and $0 \leq n \leq 9$) (see **Figure 3.2** and **Table 3.1**). The initial structure was created by randomly packing 200 pairs of cations (*i.e.*, Ca^{2+} , Mg^{2+} , Fe^{2+} , Sr^{2+} , and Ba^{2+} ions) and CO_3^{2-} ions with the n of 9.0. The previously reported force field of the alkaline-earth carbonate-based system was incorporated to include the Fe^{2+} –water and Fe^{2+} – CO_3^{2-} interactions for our models.⁵³

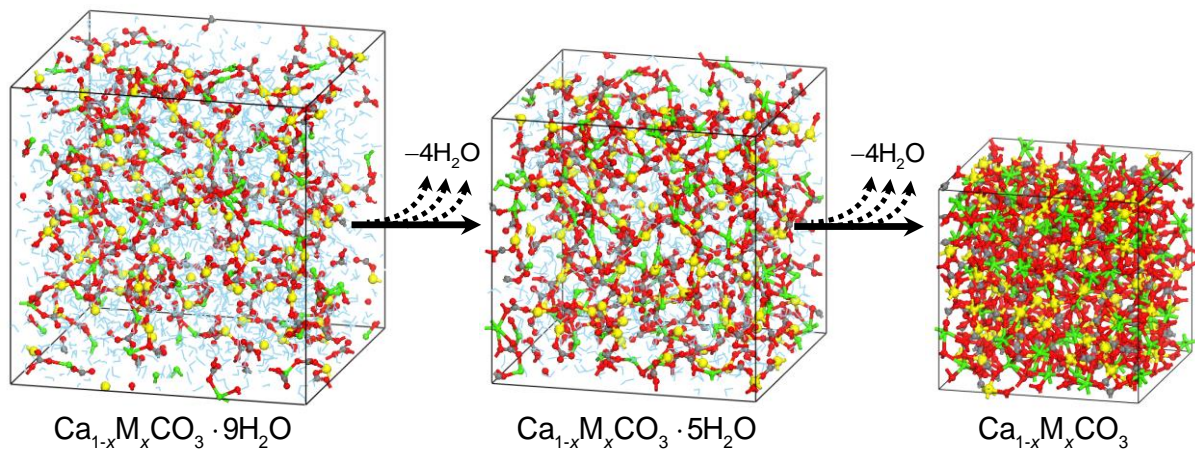


Figure 3.2 Dehydration scheme of the $\text{Ca}_{1-x}\text{M}_x\text{CO}_3 \cdot n\text{H}_2\text{O}$ system (*i.e.*, $x = 0 \sim 1$, $n = 0 \sim 9$), where $\text{M} = \text{Mg}^{2+}$, Fe^{2+} , Sr^{2+} , and Ba^{2+} . Color legends – C: gray; O: red; Ca: green; M: yellow; water: cyan.

Table 3.2 Summary of model systems for $\text{Ca}_{1-x}\text{M}_x\text{CO}_3 \cdot n\text{H}_2\text{O}$ used in MD simulations

System	$n(\text{Ca}^{2+})$	$n(\text{CO}_3^{2-})$	$n(\text{M}^{2+})$	$n(\text{H}_2\text{O})$
$\text{CaCO}_3 \cdot n\text{H}_2\text{O}$	200	200	-	1800 → ... → 400 → 200 → 180 → ... → 0
$\text{Ca}_{0.75}\text{Mg}_{0.25}\text{CO}_3 \cdot n\text{H}_2\text{O}$	150	200	50	1800 → ... → 400 → 200 → 180 → ... → 0
$\text{Ca}_{0.5}\text{Mg}_{0.5}\text{CO}_3 \cdot n\text{H}_2\text{O}$	100	200	100	1800 → ... → 400 → 200 → 180 → ... → 0
$\text{Ca}_{0.25}\text{Mg}_{0.75}\text{CO}_3 \cdot n\text{H}_2\text{O}$	50	200	150	1800 → ... → 400 → 200 → 180 → ... → 0
$\text{MgCO}_3 \cdot n\text{H}_2\text{O}$	-	200	200	1800 → ... → 400 → 200 → 180 → ... → 0
$\text{Ca}_{0.75}\text{Fe}_{0.25}\text{CO}_3 \cdot n\text{H}_2\text{O}$	150	200	50	1800 → ... → 400 → 200 → 180 → ... → 0
$\text{Ca}_{0.5}\text{Fe}_{0.5}\text{CO}_3 \cdot n\text{H}_2\text{O}$	100	200	100	1800 → ... → 400 → 200 → 180 → ... → 0
$\text{Ca}_{0.25}\text{Fe}_{0.75}\text{CO}_3 \cdot n\text{H}_2\text{O}$	50	200	150	1800 → ... → 400 → 200 → 180 → ... → 0
$\text{FeCO}_3 \cdot n\text{H}_2\text{O}$	-	200	200	1800 → ... → 400 → 200 → 180 → ... → 0
$\text{Ca}_{0.75}\text{Sr}_{0.25}\text{CO}_3 \cdot n\text{H}_2\text{O}$	150	200	50	1800 → ... → 400 → 200 → 180 → ... → 0
$\text{Ca}_{0.5}\text{Sr}_{0.5}\text{CO}_3 \cdot n\text{H}_2\text{O}$	100	200	100	1800 → ... → 400 → 200 → 180 → ... → 0
$\text{Ca}_{0.25}\text{Sr}_{0.75}\text{CO}_3 \cdot n\text{H}_2\text{O}$	50	200	150	1800 → ... → 400 → 200 → 180 → ... → 0
$\text{SrCO}_3 \cdot n\text{H}_2\text{O}$	-	200	200	1800 → ... → 400 → 200 → 180 → ... → 0
$\text{Ca}_{0.75}\text{Ba}_{0.25}\text{CO}_3 \cdot n\text{H}_2\text{O}$	150	200	50	1800 → ... → 400 → 200 → 180 → ... → 0
$\text{Ca}_{0.5}\text{Ba}_{0.5}\text{CO}_3 \cdot n\text{H}_2\text{O}$	100	200	100	1800 → ... → 400 → 200 → 180 → ... → 0
$\text{Ca}_{0.25}\text{Ba}_{0.75}\text{CO}_3 \cdot n\text{H}_2\text{O}$	50	200	150	1800 → ... → 400 → 200 → 180 → ... → 0
$\text{BaCO}_3 \cdot n\text{H}_2\text{O}$	-	200	200	1800 → ... → 400 → 200 → 180 → ... → 0

To overview the dehydration process in the absence of additive ions, including the phase transition from hydrated nucleation clusters to anhydrous ACC, we conducted MD simulations for the $\text{CaCO}_3 \cdot n\text{H}_2\text{O}$ systems (**Figure 3.3a**), which has been previously reported in several theoretical studies.³⁹⁻⁴¹ At the initial stage of dehydration (*i.e.*, $n = 9$), most of Ca^{2+} and CO_3^{2-} ions bound to each other in the form of nucleation clusters. As the dehydration progressed, the clusters initiated to aggregate, and at the last stage of dehydration (*i.e.*, $n = 0$), all calcium and carbonate ions comprised the ionic network, corresponding to the anhydrous ACC. To obtain the detailed structural information, we investigated the CN environments of $\text{Ca}-\text{O}_c$ (O in CO_3^{2-}) pairs as a function of n (**Figure 3.3b**).

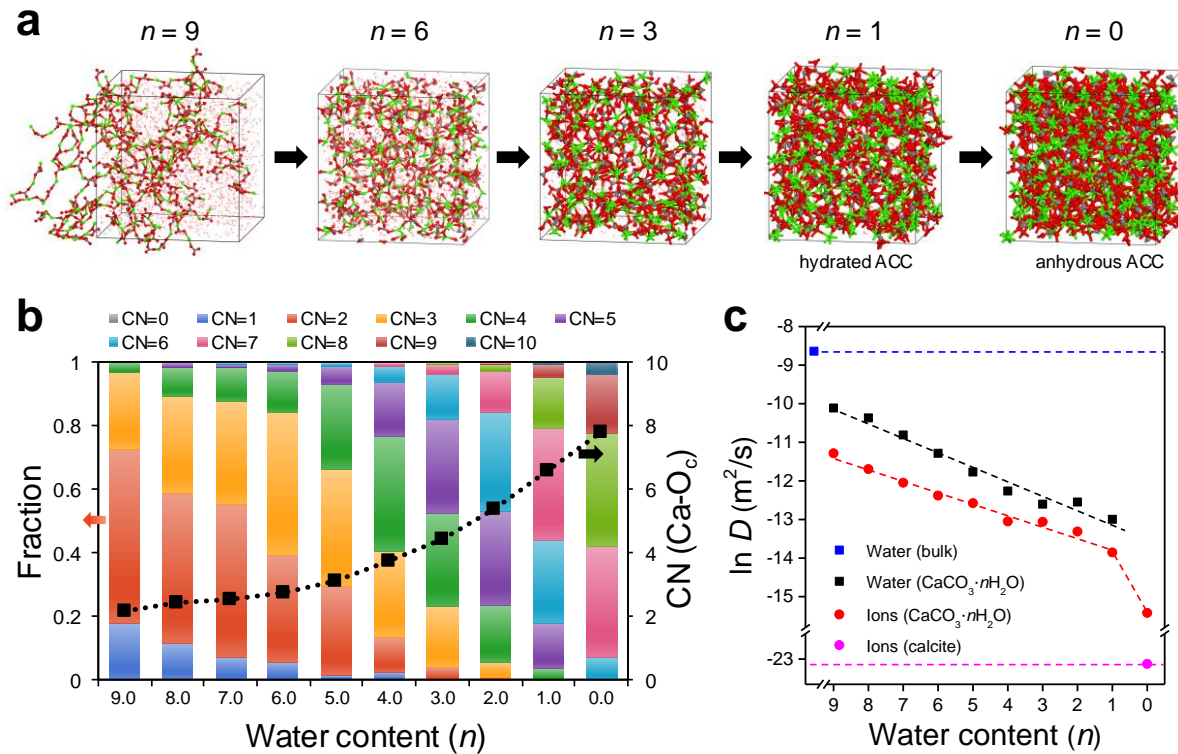


Figure 3.3 a, MD simulation snapshots for dehydration process of $\text{CaCO}_3 \cdot n\text{H}_2\text{O}$ system (*i.e.*, $n = 9, 6, 3, 1, \text{ and } 0$). Color legends – C: gray; O: red; Ca: green; H: white. **b**, CN of $\text{Ca}-\text{O}_c$ pairs in the $\text{CaCO}_3 \cdot n\text{H}_2\text{O}$ system (*i.e.*, $n = 0-9$). Left: fraction of the local structures corresponding to each CN; right: average CN of $\text{Ca}-\text{O}_c$ pairs as a function of n . **c**, Self-diffusion coefficients (D) for ions and water in $\text{CaCO}_3 \cdot n\text{H}_2\text{O}$ system and reported values for bulk water and ion pairs in calcite.^{65,66} The black and red dotted lines are guidance for the eye.

At the initial stage ($n = 9.0$), the most abundant configurations were chain-like form ($\text{CN} = 2$), followed by the terminal- ($\text{CN} = 1$) and branch-like ($\text{CN} = 3$) forms, implying that the hydrated clusters consisted of a polymeric chain. These chains were bound together by ionic interactions, and exhibited a dynamic characteristic by repetitively breaking and reforming with each other. Note that this chain configuration was previously referred as a dynamically ordered liquid-like oxyanion polymer (DOLLOP) by Gale and coworkers.³⁸ As dehydration proceeded, the average CNs eventually increased at high n (*i.e.*, $6.0 \leq n \leq 9.0$), and suddenly increased at low n (*i.e.*, $0.0 \leq n \leq 3.0$). This indicates that the aggregation occurred more dramatically when the systems were in close to the anhydrous state ($n = 0$). Notably, the average CNs of $\text{Ca}-\text{O}_c$ pairs for hydrated ACC ($n = 1$) and anhydrous ACC ($n = 0$) were 6.6 and 7.8, respectively. These values were similar to the previously reported values (*i.e.*, $\text{CN} = 6.0$ for hydrated ACC and $\text{CN} = 7.1$ or 7.7 for anhydrous ACC).^{29,41}

Moreover, the D of water and the ion pairs (*i.e.*, Ca^{2+} and CO_3^{2-}) were estimated using MSD analysis (**Figure 3.3c**). The detailed procedure and examples of fitting are given in the Methods section. The diffusivities of the Ca^{2+} and CO_3^{2-} ions are averaged for two ion species because they were very similar in the systems of our consideration. On the whole, the diffusivities of the ion pairs were much lower than those of water molecules in the $\text{CaCO}_3 \cdot n\text{H}_2\text{O}$ system. The D for ion pairs and water in the amorphous intermediate phases (*i.e.*, $n = 0\text{--}9$) were located between those of liquid water (*i.e.*, $2.3 \times 10^{-9} \text{ m}^2/\text{s}$) and calcite (*i.e.*, $0.8 \times 10^{-23} \text{ m}^2/\text{s}$),^{65,66} which was similarly reported by Bushuev *et al.*'s work.³⁹ Accordingly, the structural water, which has a lower mobility than that of liquid water, was predicted to be formed in the precursor phases.⁶⁷ Also, the ionic species of the amorphous phase exhibited a higher mobility than those of the crystalline phase. Additionally, the D for water and ion pairs in the amorphous intermediate phases steadily decreased, except for the anhydrous state ($n = 0$). From the sudden changes of D for ion pairs at the range of $n = 0\text{--}1$, the solution phase was predicted to be transformed to the solid phase, specifically identified at $n \approx 0.8\text{--}0.9$ in the previous literature.³⁹

3.3.2 Structural Analysis Based on CN Environment

The dehydration-induced structural transformations of calcium carbonate, from hydrated clusters to anhydrous ACC, were systematically analyzed by examining the CN environment of comprising atom pairs. First, we chose two representative atom pairs of $\text{M}\text{--}\text{O}_c$ and $\text{M}\text{--}\text{O}_w$, consisting of divalent cations (*i.e.*, M_{total} , including Ca^{2+} and additive ions (M^{2+})) and oxygen atoms in CO_3^{2-} (O_c) or in water molecules (O_w) (**Figure 3.4**). Note that the average CNs were obtained based on the first minimum of the radial distribution function for each pair within the first coordination shell (**Table 3.3**). Regardless of the type of additive ions, the CNs of $\text{M}_{\text{total}}\text{--}\text{O}_c$ pairs commonly increased as the dehydration progressed, whereas those of $\text{M}_{\text{total}}\text{--}\text{O}_w$ pairs reduced throughout (**Figures 3.4a** and **3.4b**). Especially, the average CNs for either $\text{M}_{\text{total}}\text{--}\text{O}_c$ or $\text{M}_{\text{total}}\text{--}\text{O}_w$ pairs exponentially changed (in positive or negative direction) with decreasing n , implying that aggregation intensely occurred at the end of dehydration.

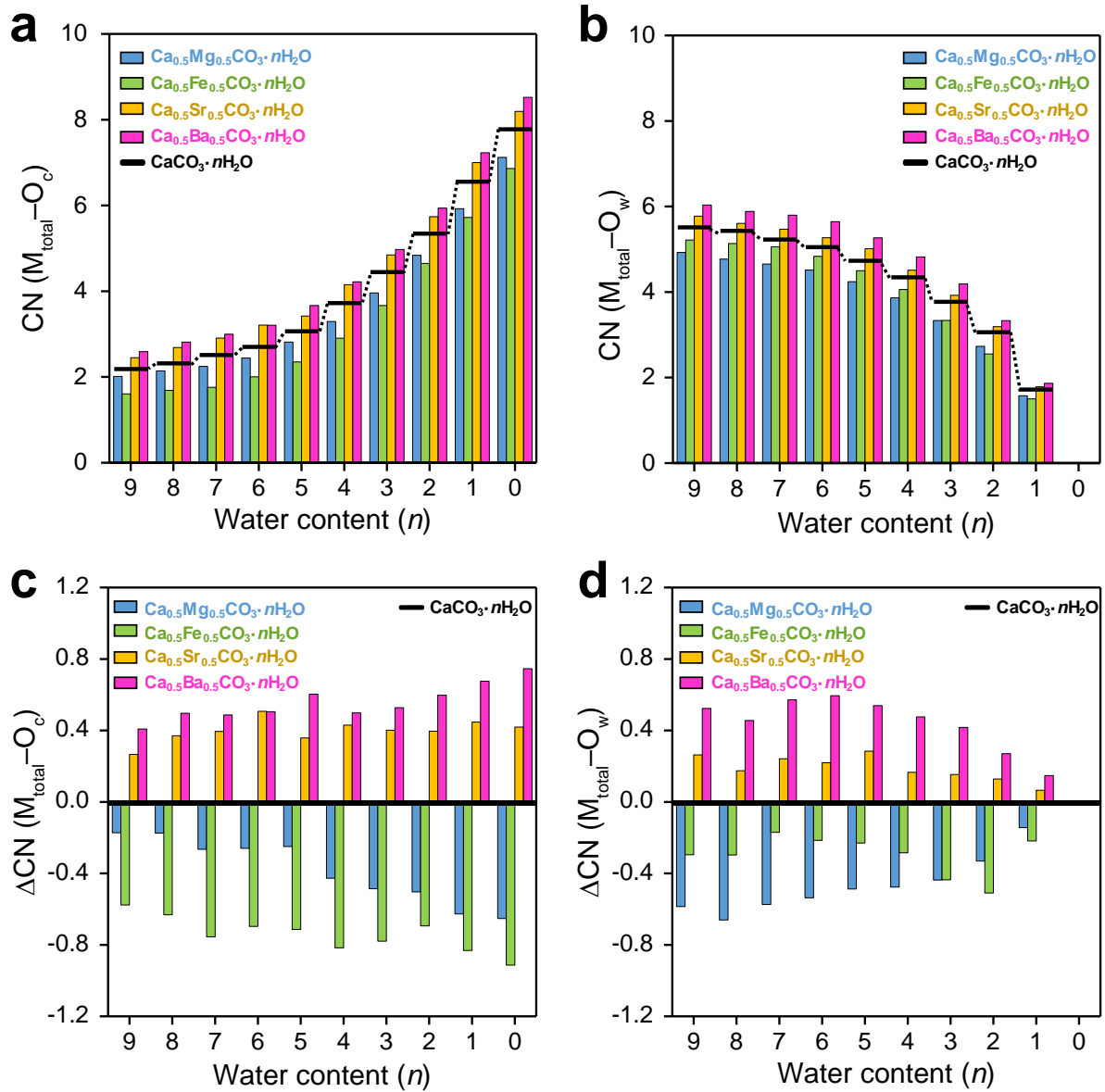


Figure 3.4 CN environment for divalent cations (M_{total} , including Ca^{2+} and M^{2+}) with oxygen atoms in the $\text{Ca}_{1-x}\text{M}_x\text{CO}_3 \cdot n\text{H}_2\text{O}$ systems. Molar composition (x) for M^{2+} were set to 0.5. **a** and **b**, Average CN for **a**, $M_{\text{total}}-O_c$ (O in CO_3^{2-}), **b**, $M_{\text{total}}-O_w$ (O in water) pairs. **c** and **d**, Relative CN (ΔCN) from the system without M^{2+} for **c**, $M_{\text{total}}-O_c$ and **d**, $M_{\text{total}}-O_w$ pairs.

Table 3.3 First minimum of radial distribution function for M–O_c and M–O_w pairs (*i.e.*, M = Ca, Mg, Fe, Sr, and Ba).

	M–O _c (Å)	M–O _w (Å)
Ca ²⁺	3.15	3.05
Mg ²⁺	2.75	2.63
Fe ²⁺	2.69	2.57
Sr ²⁺	3.35	3.23
Ba ²⁺	3.53	3.45

To independently evaluate the effect of each M²⁺ ion, we compared the relative change of CNs from those without M²⁺ ion (*i.e.*, $\Delta\text{CN} = \text{CN}(\text{Ca}_{1-x}\text{M}_x\text{CO}_3 \cdot n\text{H}_2\text{O}) - \text{CN}(\text{CaCO}_3 \cdot n\text{H}_2\text{O})$), **Figures 3.4c** and **3.4d**). Evidently, the variation trends depending on the additive ions were different for both M_{total}–O_c and M_{total}–O_w pairs. Mg²⁺ and Fe²⁺ ions had a declining effect on the ΔCN of both atom pairs, while Sr²⁺ and Ba²⁺ ions had an increasing effect. These results were agreed with the order of ionic radii for comprising ions (*i.e.*, Mg²⁺ < Fe²⁺ < Ca²⁺ < Sr²⁺ < Ba²⁺ ions, **Table 3.3**), implying that the coordination capacity is proportional to the ionic size. Note that as the M²⁺ ions were more involved, the variation trends of ΔCN s for atom pairs appeared more evidently either in the increasing (*i.e.*, Sr²⁺ and Ba²⁺) or decreasing direction (*i.e.*, Mg²⁺ and Fe²⁺) (**Figures 3.5** and **3.6**).

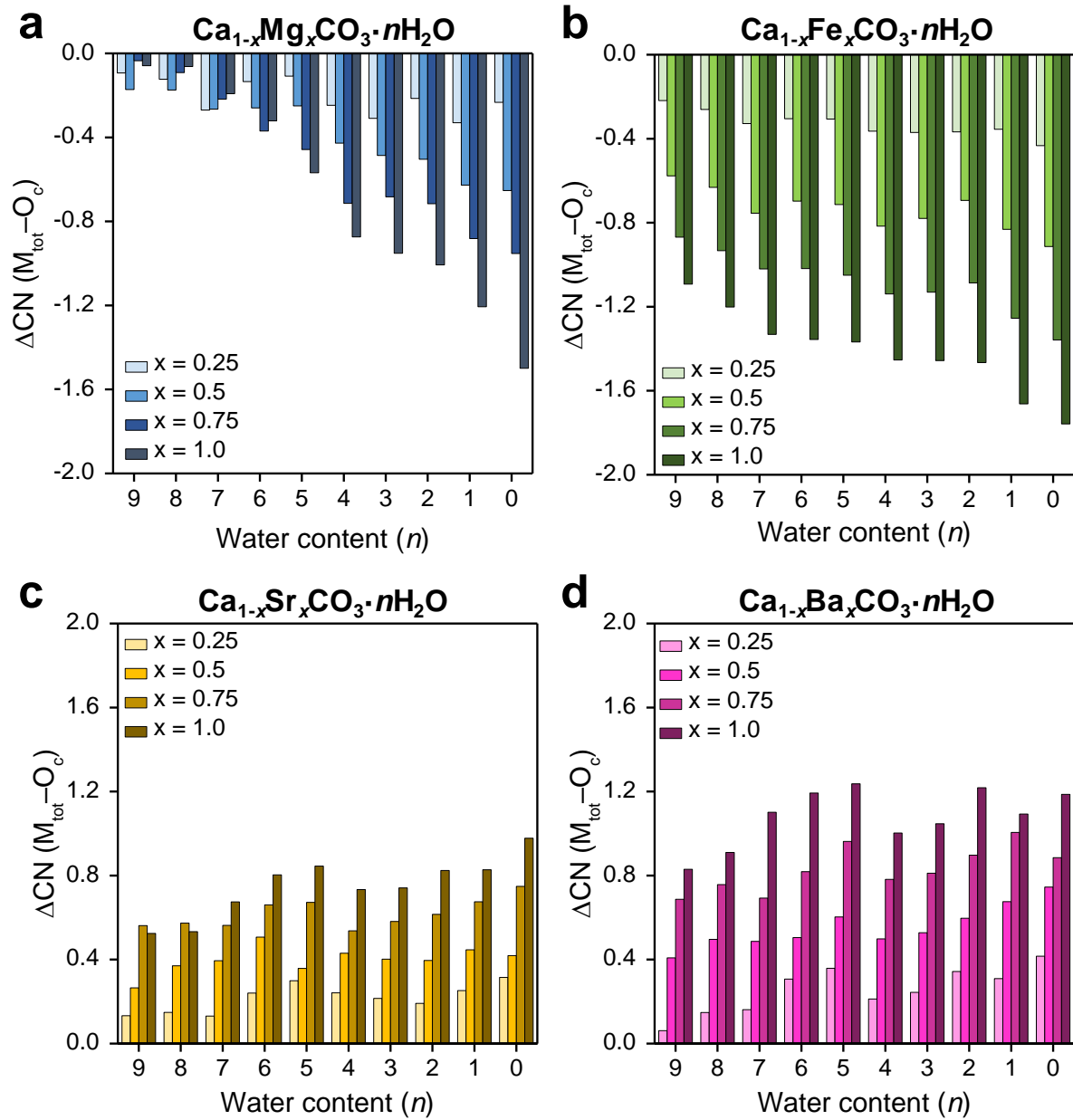


Figure 3.5 Relative CN (ΔCN) environment of O_c (O in CO_3^{2-}) around divalent cations [M_{total} , including Ca^{2+} and additive ions (*i.e.*, Mg^{2+} , Fe^{2+} , Sr^{2+} , and Ba^{2+})] in the $\text{Ca}_{1-x}\text{M}_x\text{CO}_3 \cdot n\text{H}_2\text{O}$ systems, where $M =$ **a**, Mg, **b**, Fe, **c**, Sr, and **d**, Ba [*i.e.*, $\Delta\text{CN} = \text{CN}(\text{Ca}_{1-x}\text{M}_x\text{CO}_3 \cdot n\text{H}_2\text{O}) - \text{CN}(\text{CaCO}_3 \cdot n\text{H}_2\text{O})$].

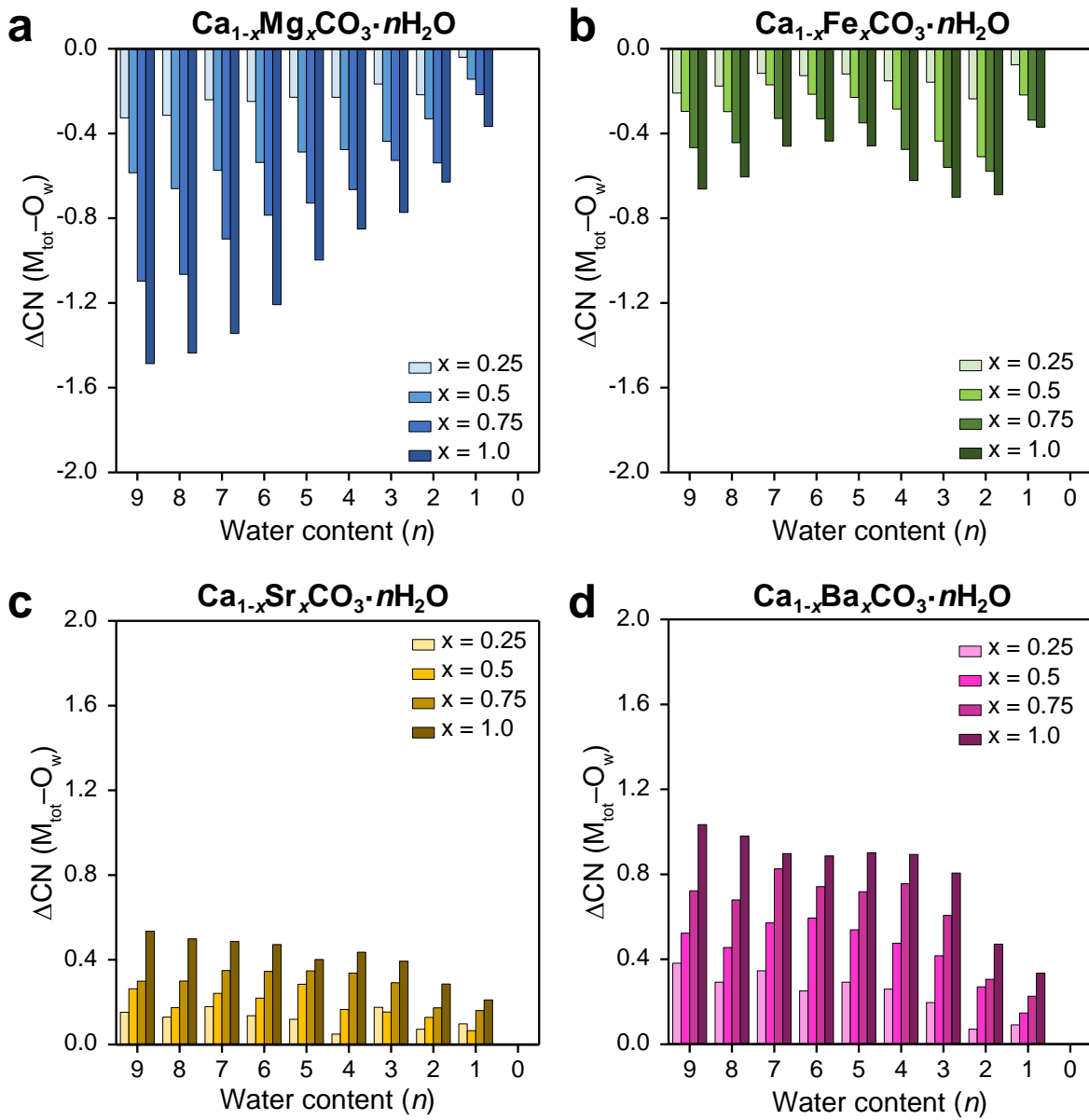


Figure 3.6 Relative CN (ΔCN) environment of O_w (O in water) around divalent cations [M_{total} , including Ca^{2+} and additive ions (*i.e.*, Mg^{2+} , Fe^{2+} , Sr^{2+} , and Ba^{2+})] in the $\text{Ca}_{1-x}\text{M}_x\text{CO}_3 \cdot n\text{H}_2\text{O}$ systems, where $M =$ **a**, Mg, **b**, Fe, **c**, Sr, and **d**, Ba [*i.e.*, $\Delta\text{CN} = \text{CN}(\text{Ca}_{1-x}\text{M}_x\text{CO}_3 \cdot n\text{H}_2\text{O}) - \text{CN}(\text{CaCO}_3 \cdot n\text{H}_2\text{O})$].

Table 3.4 Ionic radius and hydration free energy (ΔG_{hyd}) of divalent cations in the comparison of experiments and calculations.

	Ionic radius (\AA) ⁶⁸	ΔG_{hyd} (kcal/mol)	
		Expt. ^{56,57}	Calc.
Ca ²⁺	1.14	-345.12	-339.47
Mg ²⁺	0.86	-422.56	-423.68
Fe ²⁺	0.92	-439.8	-437.38
Sr ²⁺	1.32	-314.77	-319.16
Ba ²⁺	1.49	-284.42	-291.43

Furthermore, it is interesting to note that $M_{\text{total}}\text{-O}_c$ and $M_{\text{total}}\text{-O}_w$ pair exhibited the reverse tendency for Mg²⁺- and Fe²⁺-involving atom pairs at relatively high n (*i.e.*, $n = \sim 3\text{--}9$, **Figures 3.4c** and **3.4d**). Concretely, Fe²⁺ ions favored the coordination with adjacent water ($\Delta\text{CN} = \text{Fe-O}_w > \text{Mg-O}_w$), while Mg²⁺ ions preferred the coordination with CO₃²⁻ ions ($\Delta\text{CN} = \text{Mg-O}_c > \text{Fe-O}_c$). These results could be related to the superior hydrophilicity of Fe²⁺ ions (*i.e.*, $\Delta G_{\text{hyd}} = -437.4$ kcal/mol for Fe²⁺ ions, and -423.7 kcal/mol for Mg²⁺ ions, **Table 3.4**). Therefore, the hydrophilicity as well as the ionic size of comprising ions are predicted to play a pivotal role in determining the local geometries of ACC phases.

We also examined the overall molar volume changes (ΔV_m) of the systems depending on the M²⁺ and n (**Figure 3.7**). The ΔV_m indicates the difference in molar volume between the amorphous intermediate phases ($\text{Ca}_{1-x}\text{M}_x\text{CO}_3 \cdot n\text{H}_2\text{O}$) and phase-separated crystalline mixture with liquid water. During the dehydration process, the ΔV_m gradually declined in a quasi-linear manner, which was similar with the variation tendency for CNs (**Figure 3.4b**). Overall, additive ions had a negligible effect on the ΔV_m with an exception for the Mg²⁺ ions, exhibiting a decreasing effect at high n (*i.e.*, $n = \sim 3\text{--}9$). This result agreed with reported experimental work,⁶⁹ which verified the little effect on the ACC particle size in the presence of inorganic ions (*i.e.*, Mg²⁺, Sr²⁺, and Ba²⁺).

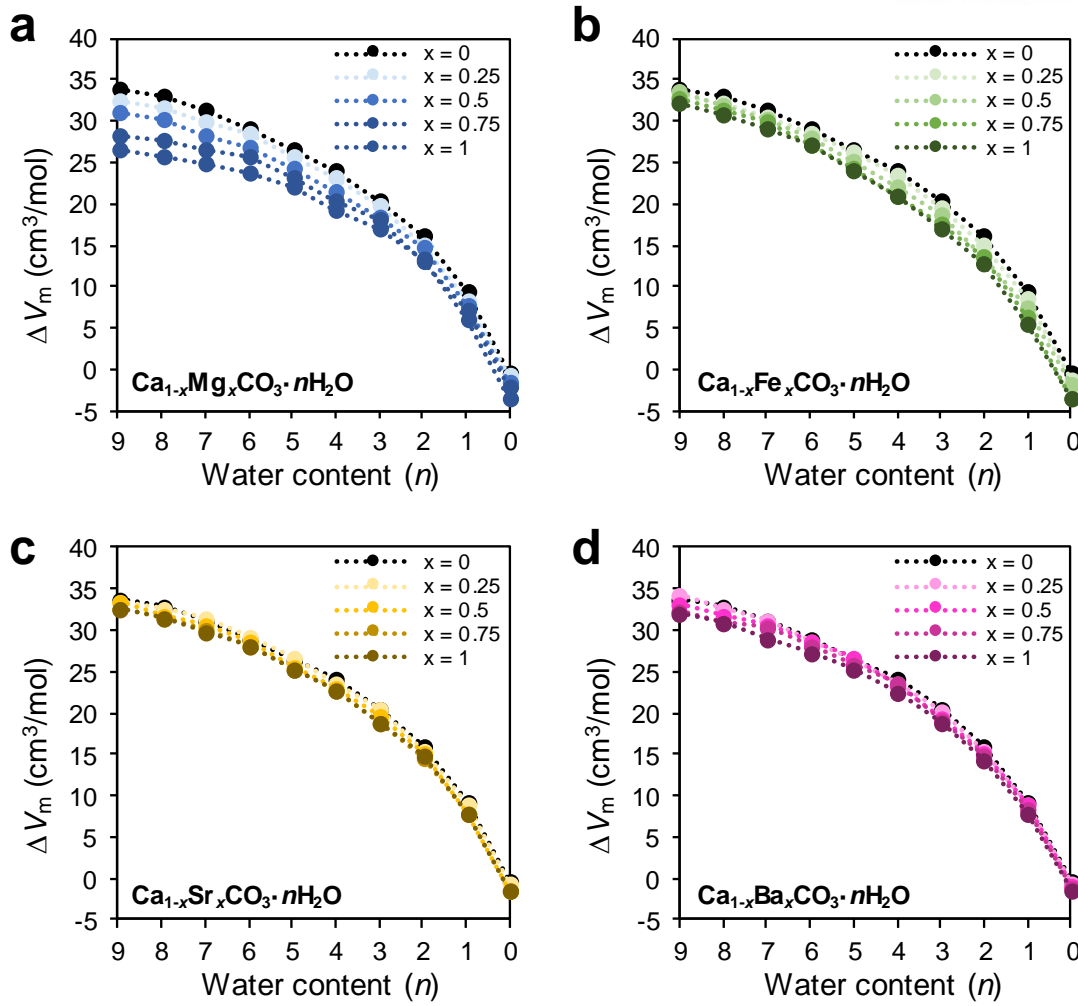


Figure 3.7 Molar volume change (ΔV_m) for $\text{Ca}_{1-x}\text{M}_x\text{CO}_3 \cdot n\text{H}_2\text{O}$ systems in the range of $n = 0-9$, where $\text{M} = \text{a, Mg, b, Fe, c, Sr, and d, Ba}$.

3.3.3 Thermodynamic Analysis for Dehydration and Crystallization Processes

To examine the thermodynamics of phase transition for CaCO_3 , the enthalpy of formation (ΔH_f), from the amorphous intermediate phases to the phase-separated crystalline mixture and liquid water, was calculated. The ΔH_f was defined as follows,

$$\Delta H_f = (1-x)E_{\text{calcite}} + xE_{\text{MCO}_3(\text{cryst.})} + nE_{\text{water}} - E_{\text{Ca}_{1-x}\text{M}_x\text{CO}_3 \cdot n\text{H}_2\text{O}} \quad (3.4)$$

where E_{calcite} is the enthalpy of calcite; $E_{\text{MCO}_3(\text{cryst.})}$ is the enthalpy of crystalline structures of metal carbonates (*i.e.*, magnesite, siderite, strontianite, witherite); and $E_{\text{Ca}_{1-x}\text{M}_x\text{CO}_3 \cdot n\text{H}_2\text{O}}$ is the enthalpy of each amorphous precursor phases of $\text{Ca}_{1-x}\text{M}_x\text{CO}_3 \cdot n\text{H}_2\text{O}$ systems.

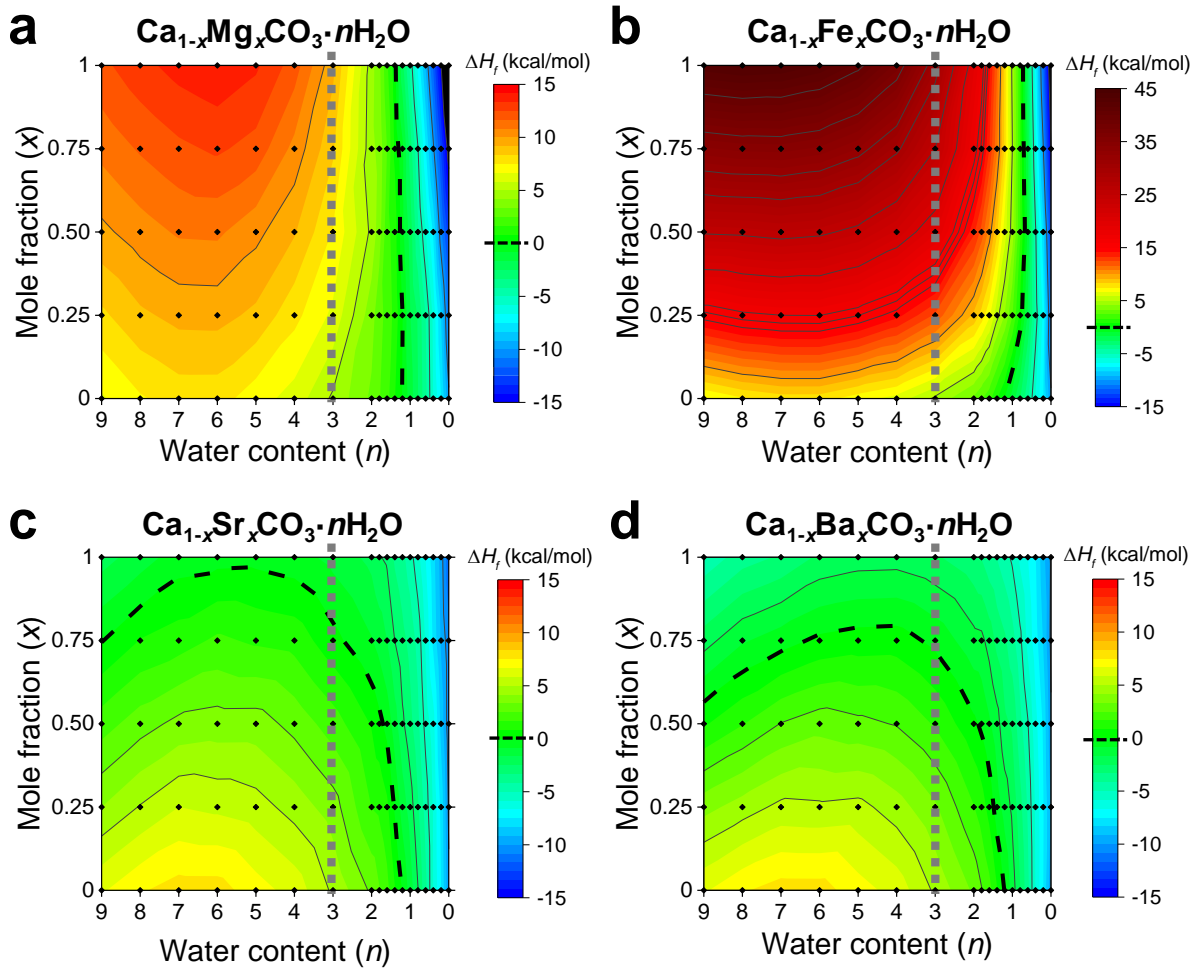


Figure 3.8 Enthalpy of formation (ΔH_f) for $\text{Ca}_{1-x}\text{M}_x\text{CO}_3 \cdot n\text{H}_2\text{O}$ systems in the range of $n = 0-9$, where $M = \mathbf{a}$, Mg, \mathbf{b} , Fe, \mathbf{c} , Sr, and \mathbf{d} , Ba. The black circles represent the actual simulation points used for constructing the contour plot. The black dotted lines represent the base line for the thermo-neutral state (*i.e.*, $\Delta H_f = 0$). The gray dotted lines represent the line for guidance of the location at $n = 3$.

Figure 3.8 shows the ΔH_f of the $\text{Ca}_{1-x}\text{M}_x\text{CO}_3 \cdot n\text{H}_2\text{O}$ systems in the range of x and n . Noteworthy, the ΔH_f from the anhydrous ACC (without M^{2+} ions) to the calcite was similar to an experimentally reported value (*i.e.*, -9.81 kcal/mol for $x = 0$, $n = 0$),¹³ supporting the validity for our results. Overall, the variation trends for ΔH_f were markedly changed depending on the n , specifically at $n = \sim 3$ as a branch line. At high n (*i.e.*, $n = \sim 3-9$), the ΔH_f changed distinctively along the y -axis direction of the plot. This result indicated that the dependence of ΔH_f on the x was much stronger than that on the n . In contrast, the ΔH_f at low n (*i.e.*, $n = \sim 0-3$) was more dependent on the n (along x -axis direction in the plot).

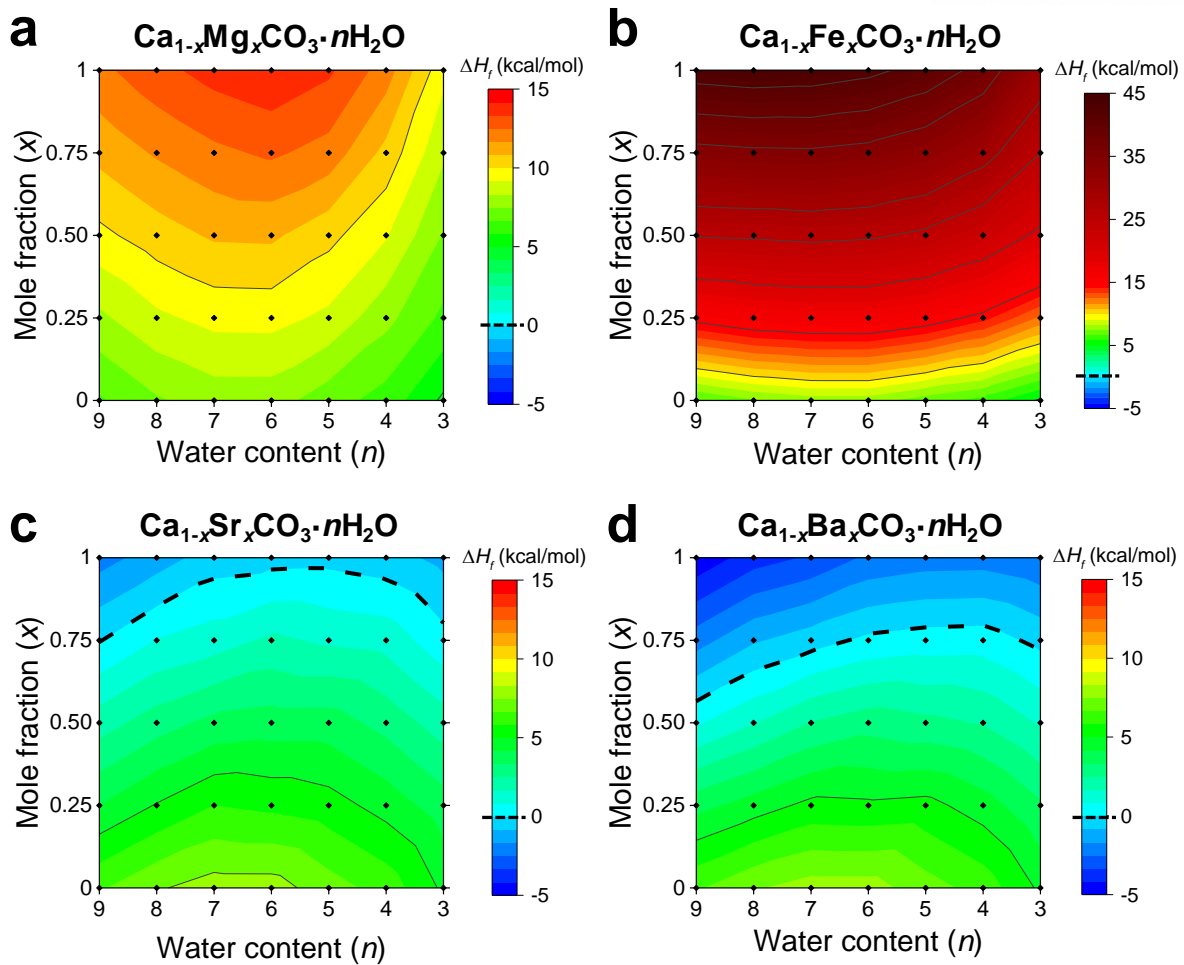


Figure 3.9 Enthalpy of formation (ΔH_f) for $\text{Ca}_{1-x}\text{M}_x\text{CO}_3 \cdot n\text{H}_2\text{O}$ systems in the range of $n = \sim 3-9$, where $\text{M} = \text{a, Mg, b, Fe, c, Sr, and d, Ba}$. The black circles represent the actual simulation points used for constructing the contour plot. The black dotted lines represent the base line for the thermo-neutral state (*i.e.*, $\Delta H_f = 0$).

To further demarcate the different trends regarding with n , we examined the ΔH_f with two divided regions; at $n = \sim 3-9$ and $n = \sim 0-3$ (**Figures 3.9 and 3.10**). At $n = \sim 3-9$, the ΔH_f showed clearly different trends for the more hydrophilic ions (*i.e.*, Mg^{2+} , Fe^{2+}) and the less hydrophilic ones (*i.e.*, Sr^{2+} , Ba^{2+}) compared to the Ca^{2+} ions (**Figure 3.9**). Specifically, with an increase in the x of Mg^{2+} or Fe^{2+} ions, the endothermicity of the ΔH_f increased further, implying that the dehydration process for amorphous intermediate phases became more difficult to occur due to the stronger hydration stability (**Figures 3.9a and 3.9b**). Especially, the endothermicity of the ΔH_f for Fe^{2+} ions significantly increased, induced by their stronger hydration. Meanwhile, with an increase in the x of Sr^{2+} or Ba^{2+} ions, the endothermicity of the ΔH_f clearly decreased, mainly due to the more facile dehydration (**Figures 3.9c and 3.9d**).

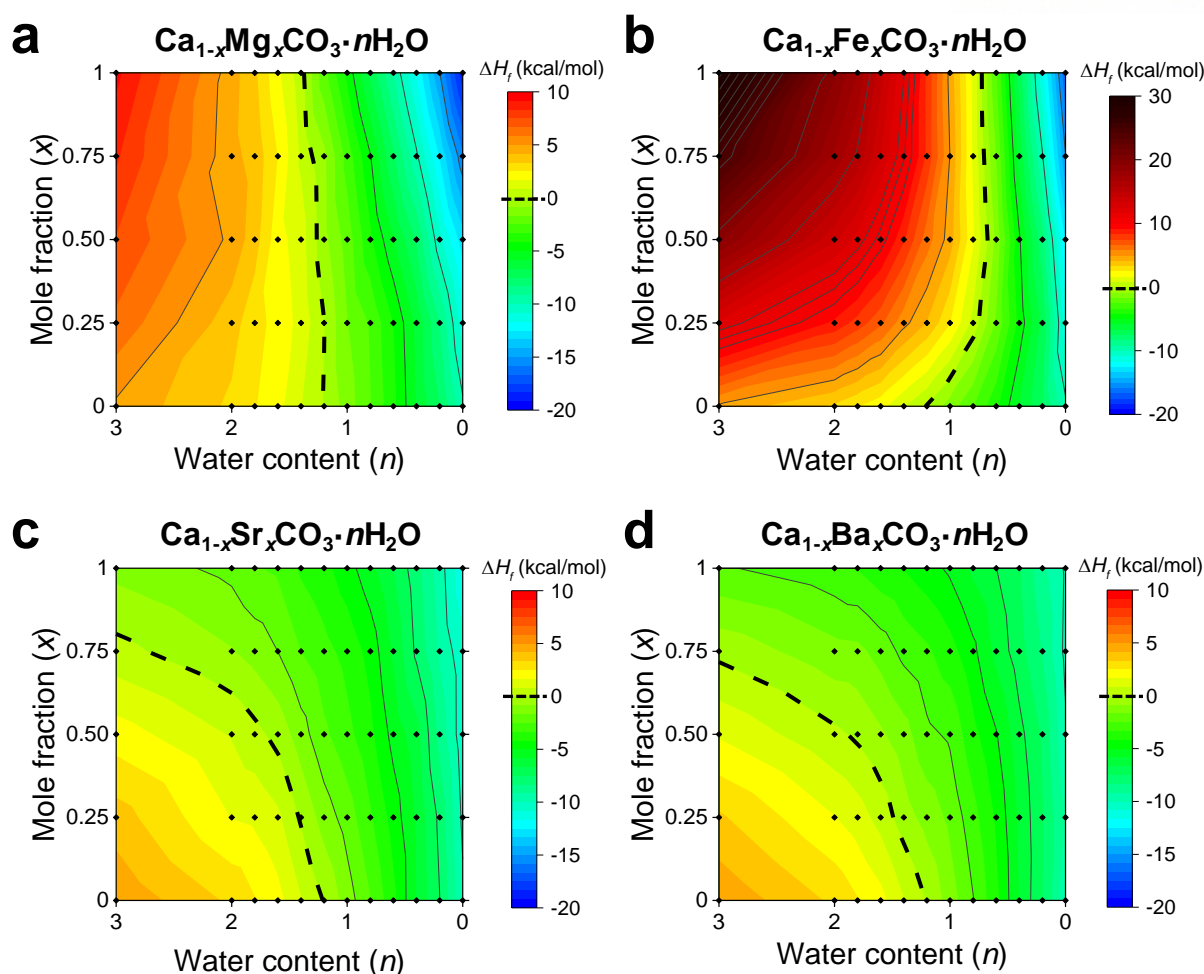


Figure 3.10 Enthalpy of formation (ΔH_f) for $\text{Ca}_{1-x}\text{M}_x\text{CO}_3 \cdot n\text{H}_2\text{O}$ systems in the range of $n = \sim 0-3$, where $\text{M} = \text{a, Mg, b, Fe, c, Sr, and d, Ba}$. The black circles represent the actual simulation points used for constructing the contour plot. The black dotted lines represent the base line for the thermo-neutral state (*i.e.*, $\Delta H_f = 0$).

With an extremely high x (*i.e.*, $x_{\text{Sr}} > \sim 0.75-0.9$, and $x_{\text{Ba}} > \sim 0.55-0.75$), some exothermic regions were observed by crossing over the thermo-neutral line (represented by black dotted lines), where the phase transition can occur without any energetic cost during the dehydration process.

Figure 3.10 shows the ΔH_f of the $\text{Ca}_{1-x}\text{M}_x\text{CO}_3 \cdot n\text{H}_2\text{O}$ system at low n (*i.e.*, $n = \sim 0-3$), including the phase transition from solution to solid phase, as above-identified by sudden change of D at $n \approx 1$ (**Figure 3.3c**). The notable change of the ΔH_f at $n = \sim 0-3$ is the increasing trend of exothermicity with decreasing n (along the x -axis direction). Assuming that the dehydration process of hydrated clusters in the amorphous intermediate phases is probably related to the endothermic behavior, the subsequent crystallization can be speculated as the origin of exothermicity.

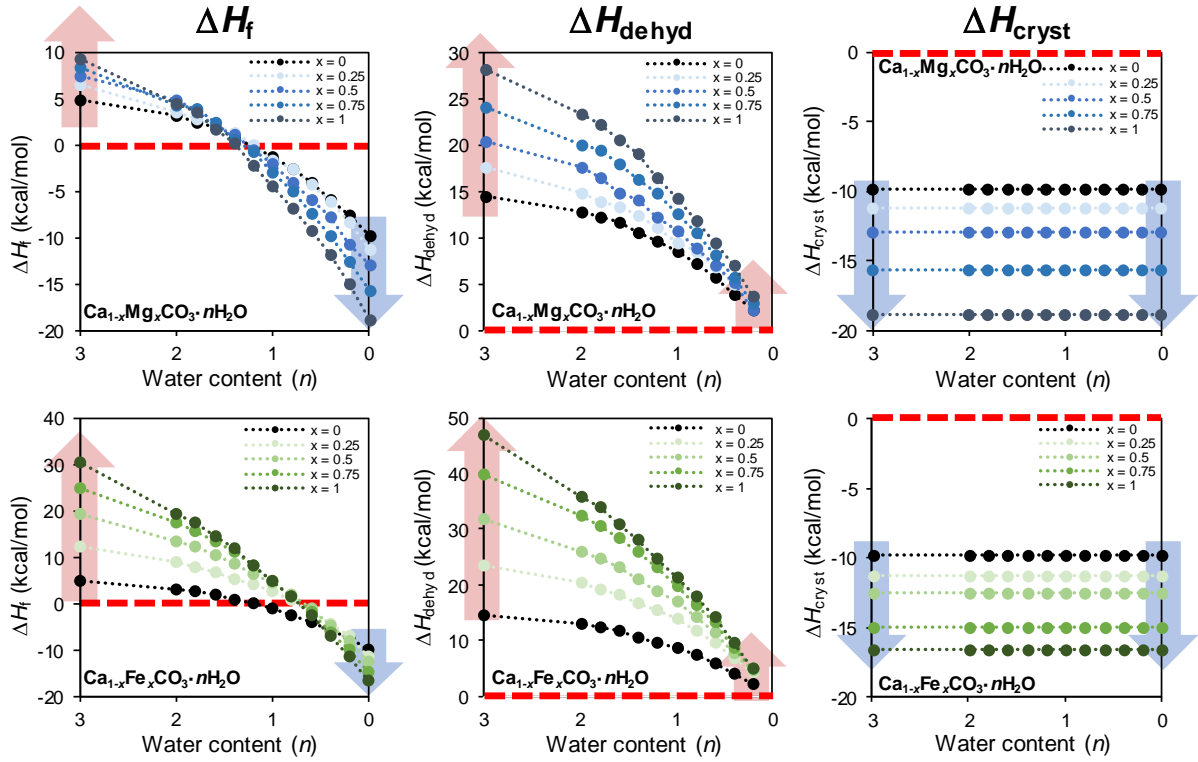


Figure 3.11 Enthalpy of formation (ΔH_f) and its decomposed energy contributions including dehydration (ΔH_{dehyd}) and crystallization (ΔH_{cryst}) for $\text{Ca}_{1-x}\text{M}_x\text{CO}_3 \cdot n\text{H}_2\text{O}$ systems (*i.e.*, $M = \text{Mg, Fe}$ and $x = 0, 0.25, 0.5, 0.75$ and 1) in the range of $n = 0-3$. The red (or blue) shaded arrows represent the direction of increasing the endothermicity (or exothermicity). The red dotted lines represent the base line for the thermo-neutral state (*i.e.*, $\Delta H_f = 0$).

To further delineate these processes from the thermodynamic perspective, we decomposed the ΔH_f into each enthalpic contribution for dehydration (ΔH_{dehyd}) and crystallization (ΔH_{cryst}) of the $\text{Ca}_{1-x}\text{M}_x\text{CO}_3 \cdot n\text{H}_2\text{O}$ systems as follows,

$$\Delta H_f = \Delta H_{\text{dehyd}} + \Delta H_{\text{cryst}} \quad (3.5)$$

where ΔH_{dehyd} is the enthalpy change of dehydration (from hydrated form of amorphous intermediate phase into anhydrous ACC and liquid water), and ΔH_{cryst} is the enthalpy change of crystallization (from anhydrous ACC into phase-separated crystalline structures of metal carbonates).

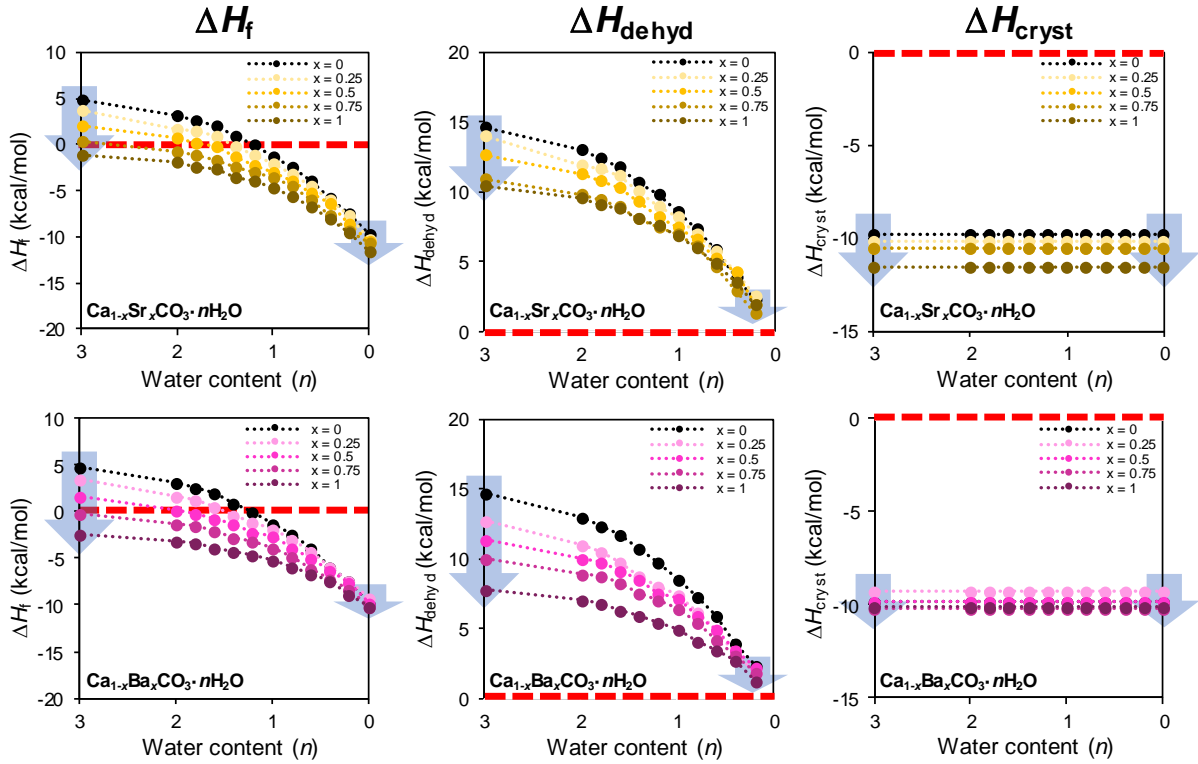


Figure 3.12 Enthalpy of formation (ΔH_f) and its decomposed energy contributions including dehydration (ΔH_{dehyd}) and crystallization (ΔH_{cryst}) for $\text{Ca}_{1-x}\text{M}_x\text{CO}_3 \cdot n\text{H}_2\text{O}$ systems (*i.e.*, $\text{M} = \text{Sr}, \text{Ba}$ and $x = 0, 0.25, 0.5, 0.75$ and 1) in the range of $n = 0-3$. The blue shaded arrows represent the direction of increasing the endothermicity (or exothermicity). The red dotted lines represent the base line for the thermo-neutral state (*i.e.*, $\Delta H_f = 0$).

Each enthalpic contribution was defined as follows,

$$\Delta H_{\text{dehyd}} = E_{\text{anhyd}} + nE_{\text{water}} - E_{\text{hyd}} \quad (3.6)$$

$$\Delta H_{\text{cryst}} = (1-x)E_{\text{calcite}} + xE_{\text{MCO}_3(\text{cryst.})} - E_{\text{Ca}_{1-x}\text{M}_x\text{CO}_3} \quad (3.7)$$

where E_{hyd} is the enthalpy of hydrated forms of amorphous precursor phases of $\text{Ca}_{1-x}\text{M}_x\text{CO}_3 \cdot n\text{H}_2\text{O}$ systems; and E_{anhyd} is the enthalpy of anhydrous ACC (*i.e.*, $n = 0$), respectively.

The results for decomposed enthalpic contributions including ΔH_{dehyd} and ΔH_{cryst} of the $\text{Ca}_{1-x}\text{M}_x\text{CO}_3 \cdot n\text{H}_2\text{O}$ systems are shown in the **Figures 3.11** and **3.12**. Basically, the ΔH_{dehyd} is responsible for the endothermic part, whereas ΔH_{cryst} is in charge of the exothermic part of the ΔH_f . Consequently, the thermodynamic spontaneity of the ΔH_f was determined by the balance between the two opposing factors

of dehydration and crystallization; it was endothermic in the solution phase (*i.e.*, $n = \sim 3$), and exothermic in the solid phase (*i.e.*, $n = 0$). Each enthalpic contribution changed according to the type and x of M^{2+} , and n . Among these determining factors, we initially focused on the variation trends of ΔH_f according to the n . As the dehydration progressed (from $n = \sim 3$ to 0), the ΔH_{dehyd} was steadily decreased, while the ΔH_{cryst} remained constant since it is basically independent on the n at the solid-state ($n = 0$). As a consequence, the ΔH_f varied from endothermic to exothermic by crossing over the thermo-neutral line (*i.e.*, $\Delta H_f = 0$), which implies that dehydration effect was more dominant in the solution phase (*i.e.*, $n = \sim 3$), whereas the crystallization effect accordingly won over the opposite as it got closer to the solid phase. Note that these trends (from endothermic to exothermic) during dehydration process were also observed in the **Figure 3.10** (from left to the right along the x -axis direction in the plots).

Next, we extended our investigations to the variation trends of ΔH_f according to the x . With an increase in the x of Mg^{2+} or Fe^{2+} (from bottom to top in the **Figures 3.10a** and **3.10b**), the endothermicity slightly (for Mg^{2+}) or largely (for Fe^{2+}) increased at the hydration level of $n = \sim 3$, but the tendency reversed in the anhydrous phase (*i.e.*, $n = 0$) by propagating in the exothermic direction. These different trends for ΔH_f with increasing amount of Mg^{2+} and Fe^{2+} uptake were further examined from each enthalpic contribution (**Figure 3.11**). The increased ΔH_{dehyd} at $n = \sim 3$ was predicted to be originated from the stronger hydrophilic effect of Mg^{2+} and Fe^{2+} additives, as similarly stated above at high hydration levels ($n = \sim 3-9$). These results are in line with previous experimental observations regarding with the extended lifetime of ACC phases in the presence of Mg^{2+} or Fe^{2+} additives,^{27,28} which can be interpreted as the increased endothermicity of dehydration (ΔH_{dehyd}). Meanwhile, the increased ΔH_{cryst} in the exothermic direction was mainly due to the decreased stability of the anhydrous $Ca_{1-x}M_xCO_3$ system. It is noteworthy that similar effect of the structural instability due to Mg^{2+} substitution was previously reported for Mg-calcite systems, which was verified using surface energy calculations.⁵² Conversely, with an increase in the Sr^{2+} or Ba^{2+} uptake (**Figures 3.10c**, **3.10d** and **Figure 3.12**), the endothermicity tended to decrease due to the more facile dehydration at all hydration levels, but the degree of variation decreased as the dehydration progressed. Finally, in the anhydrous phase (*i.e.*, $n = 0$), the thermodynamic stability was nearly preserved regardless of the additive content, without an increase in the exothermicity.

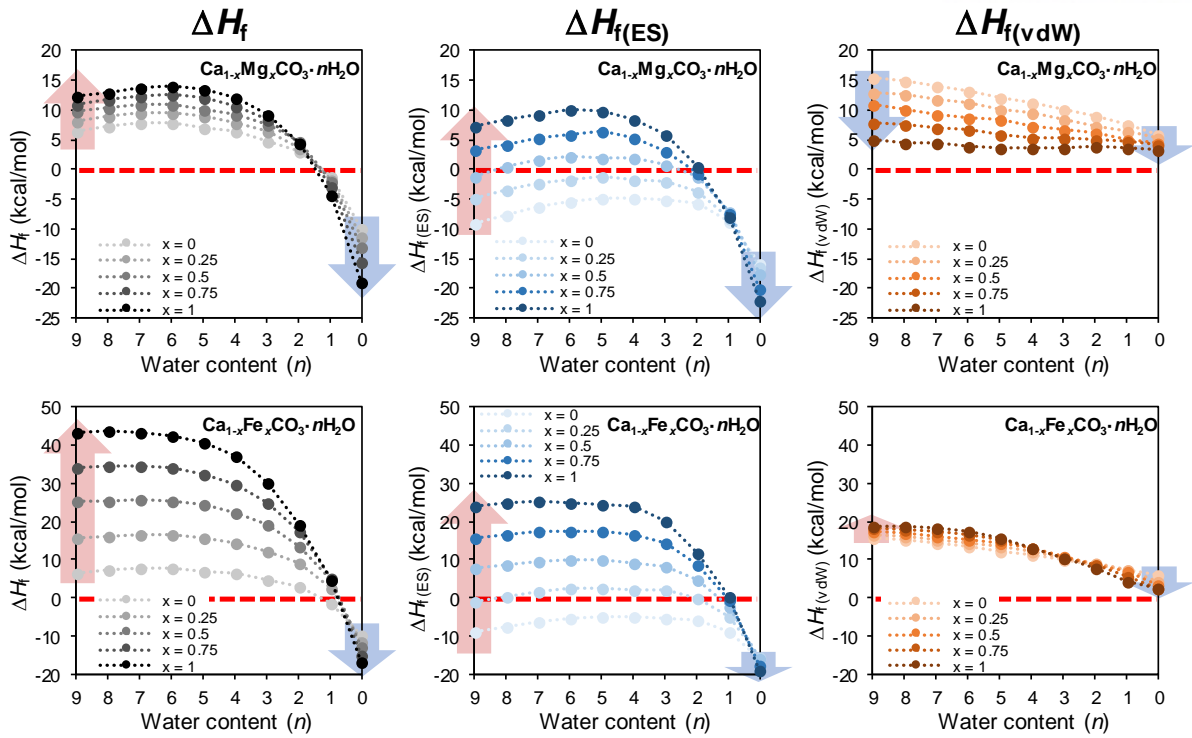


Figure 3.13 Enthalpy of formation (ΔH_f) and its decomposed enthalpic contributions including electrostatic ($\Delta H_{f(\text{ES})}$) and van der Waals interactions ($\Delta H_{f(\text{vdW})}$) for $\text{Ca}_{1-x}\text{M}_x\text{CO}_3 \cdot n\text{H}_2\text{O}$ systems (*i.e.*, $M = \text{Mg, Fe}$ and $x = 0, 0.25, 0.5, 0.75$ and 1) in the range of $n = 0-9$. The red (or blue) shaded arrows represent the direction of increasing the endothermicity (or exothermicity). The red dotted lines represent the base line for the thermo-neutral state (*i.e.*, $\Delta H_f = 0$).

These different trends depending on the additive ions were also observed from each contribution for electrostatic and van der Waals interactions (**Figures 3.13** and **3.14**). Note that the ΔH_f can be decomposed into two enthalpic contributions including electrostatic ($\Delta H_{f(\text{ES})}$) and van der Waals ($\Delta H_{f(\text{vdW})}$) interactions as follows.

$$\Delta H_f = \Delta H_{f(\text{ES})} + \Delta H_{f(\text{vdW})} \quad (3.8)$$

In the presence of Mg^{2+} or Fe^{2+} ions, the variation tendency of ΔH_f was mainly responsible for the electrostatic interactions, which increased the endothermicity in the solution phase (*i.e.*, $n = \sim 3-9$) while increased exothermicity in the solid phase (*i.e.*, $n = \sim 0$) (**Figure 3.13**). Meanwhile, in the cases of Sr^{2+} or Ba^{2+} ions, the van der Waals interactions were mostly attributed to the variation tendency of ΔH_f , where the exothermicity increased for both solution and solid phases (**Figure 3.14**). These results implied that the hydrophilicity is closely related to the electrostatic interactions, but the van der Waals effect can play a major role for larger size ions.

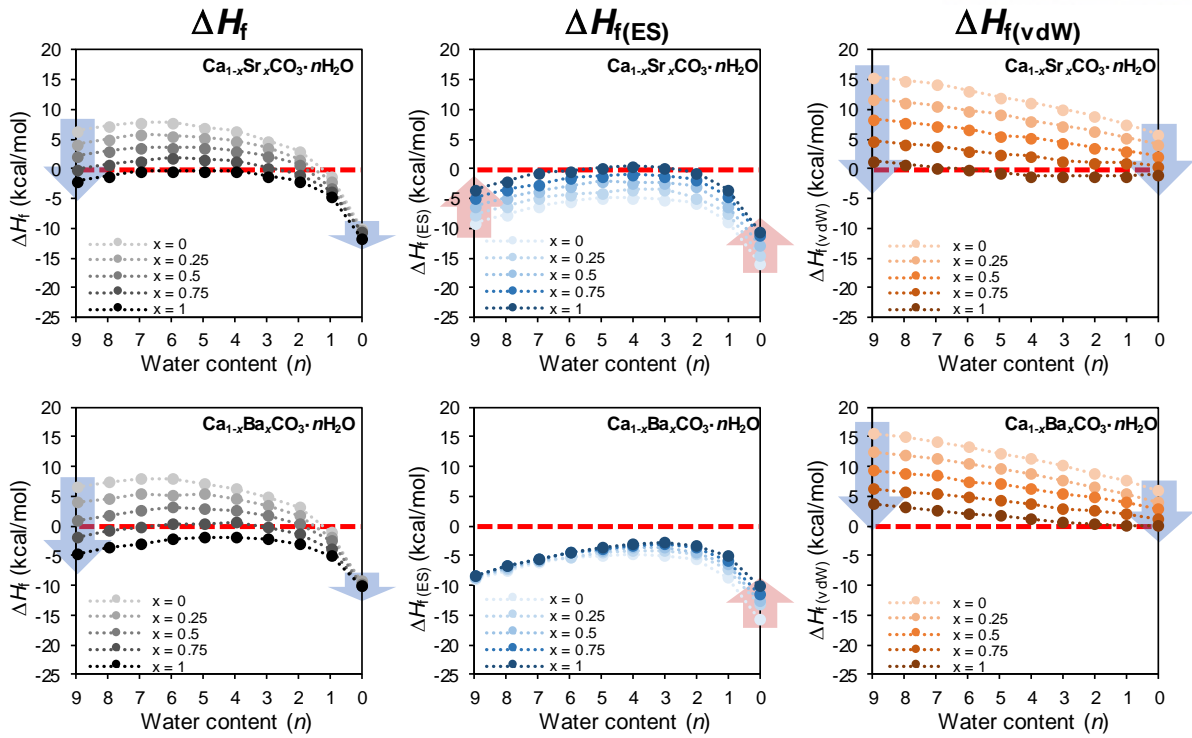


Figure 3.14 Enthalpy of formation (ΔH_f) and its decomposed enthalpic contributions including electrostatic ($\Delta H_{f(\text{ES})}$) and van der Waals interactions ($\Delta H_{f(\text{vdW})}$) for $\text{Ca}_{1-x}\text{M}_x\text{CO}_3 \cdot n\text{H}_2\text{O}$ systems (*i.e.*, $\text{M} = \text{Sr}, \text{Ba}$ and $x = 0, 0.25, 0.5, 0.75$ and 1) in the range of $n = 0-9$. The red (or blue) shaded arrows represent the direction of increasing the endothermicity (or exothermicity). The red dotted lines represent the base line for the thermo-neutral state (*i.e.*, $\Delta H_f = 0$).

To sum up with the results, we schematically redesigned the results in the **Figure 3.10**, which represents the ΔH_f as a function of water content (n) and mole fraction of additive ions (x) at low hydration levels, by signifying the relationship between two opposing factors – dehydration and crystallization (**Figure 3.15**). Two contrasting factors were exerted on the ΔH_f either in the same or opposite directions; the former refers to a synergistic relationship (*i.e.*, for Sr^{2+} and Ba^{2+} cases) and the latter to a rivalry relationship (*i.e.*, for Mg^{2+} and Fe^{2+} cases). Based on these concepts, we constructed a schematic diagram to describe the phase transition from hydrated forms of amorphous precursor phases (*i.e.*, $\text{Ca}_{1-x}\text{M}_x\text{CO}_3 \cdot n\text{H}_2\text{O}$) into phase-separated crystalline structures and liquid water (*i.e.*, $(1-x)\text{CaCO}_3 + x\text{MCO}_3 + n\text{H}_2\text{O}$), including dehydration and crystallization processes (**Figure 3.16**).

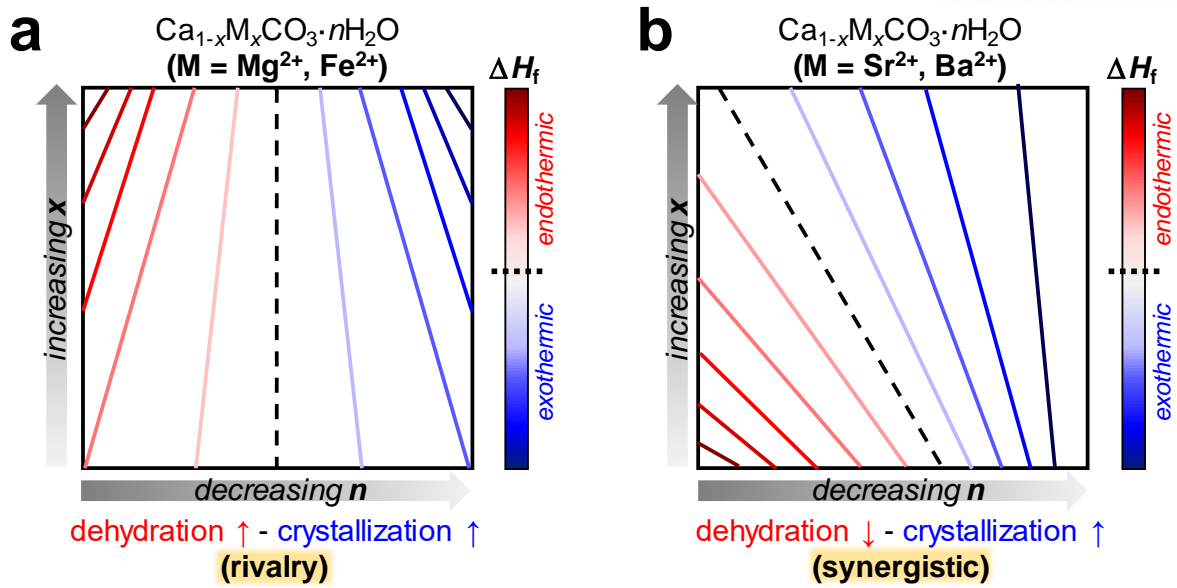


Figure 3.15 a and b, Schematics for the relationships of two opposing factors (*i.e.*, dehydration and crystallization) acting on the ΔH_f as a function of water content (n) and mole fraction of additive ions (x) in the $\text{Ca}_{1-x}\text{M}_x\text{CO}_3 \cdot n\text{H}_2\text{O}$ systems, where **a**, $\text{M} = \text{Mg}$ or Fe and **b**, $\text{M} = \text{Sr}$ or Ba , respectively.

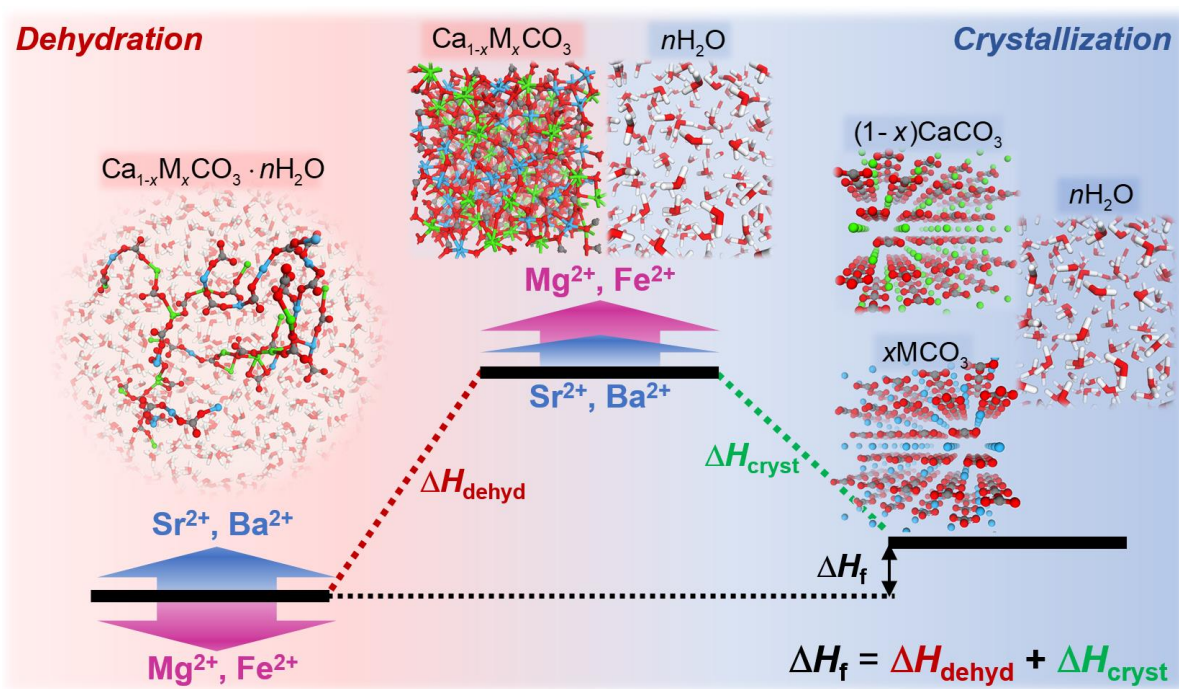


Figure 3.16 Schematics for dehydration and crystallization process from amorphous precursor phases (*i.e.*, $\text{Ca}_{1-x}\text{M}_x\text{CO}_3 \cdot n\text{H}_2\text{O}$) to phase-separated crystalline structures (*i.e.*, $(1-x)\text{CaCO}_3$ and $x\text{MCO}_3$) and liquid water (*i.e.*, $n\text{H}_2\text{O}$).

In the cases of Mg^{2+} and Fe^{2+} , which had stronger hydration strengths than Ca^{2+} , the endothermicity increased at the dehydration stage. However, at the crystallization stage, the exothermicity increased due to an increase in the structural instability, owing to additive substitution. Accordingly, the inhibiting effect in the solution phase and the promoting effect in the solid phase can simultaneously coexist in the Mg- (or Fe-) substituted carbonate systems. Notably, Fe^{2+} had a higher effect in the dehydration stage than Mg^{2+} , but a lower effect in the crystallization stage, thus exhibiting the strongest inhibitory effect among the additives of our interest (**Figure 3.10b**). On the contrary, in the cases of Sr^{2+} and Ba^{2+} , the promoting effects were enhanced due to the propagation in the exothermic direction, both in the dehydration (solution) and crystallization (solid) stages. Finally, Ba^{2+} had the strongest promoting effect among the additives of our consideration (**Figure 3.10d**).

3.3.4 TDF Analysis for ACC Structure Involving Additive Ions

The TDF, $D(r)$, is a commonly used method for the examination of the atomic structure of ACC, which can be determined from X-ray scattering spectroscopy,⁷⁰ and is thus directly comparable with computational models. The TDF is defined as the weighted sum of the partial distribution functions (PDFs) for all the atom pairs, as shown by the following equation:

$$D(r) = 4\pi\rho_0 r \sum_{i,j=1}^n c_i c_j \frac{z_i z_j}{\left(\sum_{k=1}^n c_k z_k\right)^2} [g_{ij}(r) - 1] \quad (3.9)$$

where ρ_0 is the total number density in system; c_i and c_j are the concentrations of atoms i and j , respectively; z_i and z_j are the atomic numbers of atoms i and j , respectively; and $g_{ij}(r)$ is the PDF between atoms i and j . First, the TDF of the $\text{CaCO}_3 \cdot n\text{H}_2\text{O}$ system with $n = 1$, which corresponds to the hydrated ACC, was compared with available experimental data⁷⁰ (**Figure 3.17**). The simulation results showed a good agreement with the experimental models for the whole range (up to ~ 13 Å), implying that our ACC model structures would be actually accessible in a real situation.

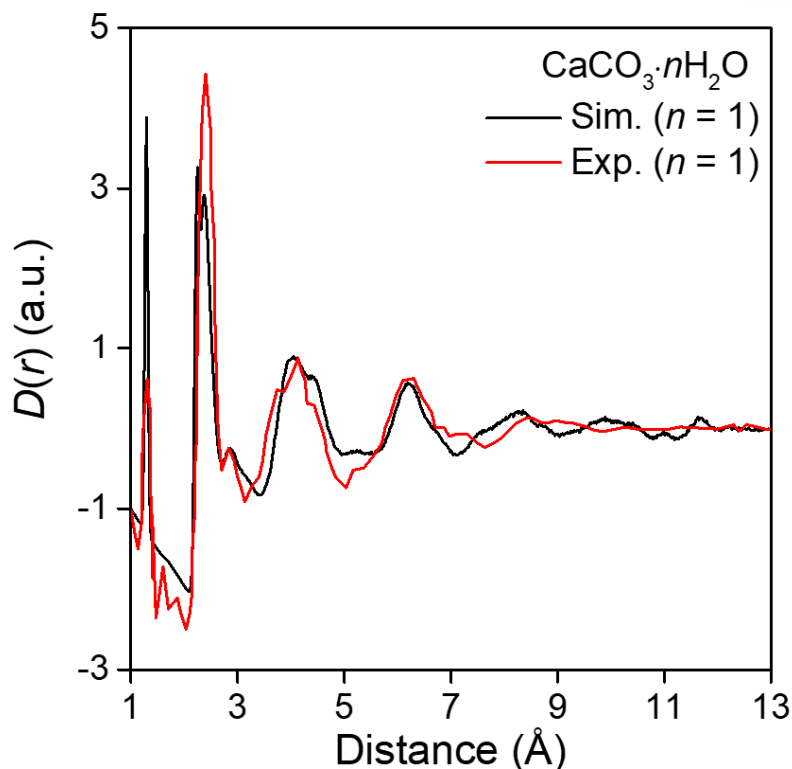


Figure 3.17 Comparison of total distribution function (TDF, $D(r)$) between experiment⁷⁰ and calculated model system for hydrated ACC (*i.e.*, $\text{CaCO}_3 \cdot n\text{H}_2\text{O}$, $n = 1$), obtained from our simulation.

Next, we investigated the TDFs for hydrated ACCs (*i.e.*, $\text{Ca}_{1-x}\text{M}_x\text{CO}_3 \cdot n\text{H}_2\text{O}$, where $n = 1$) in a wide range of molar compositions for additive ions (*i.e.*, $x = 0.25, 0.5, 0.75,$ and 1) (**Figures 3.18** and **3.19**). In common, all the systems with additive ions exhibited very sharp peaks at 1.3 and 2.2 Å, which corresponded to the C–O_c and O_c–O_c pair for the internal atom pairs of the carbonate ion. We particularly note that the shoulder peaks associated with M–O_w pairs slightly appeared in the short-range only for both the Mg- and Fe-ACC systems, at 2.0 Å (*i.e.*, Mg–O_w pair) and 1.9 Å (*i.e.*, Fe–O_w pair) (**Figure 3.18**). For detailed examination of these structural differences, we separated the PDF for M–O_w pairs from each TDF. It was found that M–O_w contribution decreased in the order of Fe²⁺, Mg²⁺, Sr²⁺, and Ba²⁺ (**Figure 3.20**), and this tendency was originated from the relative hydrophilicity of the additive ions. On the other hand, the Sr- and Ba-ACC systems exhibited the pronounced peaks for the M–O_c pair at 2.6 and 2.8 Å, corresponding to Sr–O_c and Ba–O_c, respectively (**Figure 3.19**).

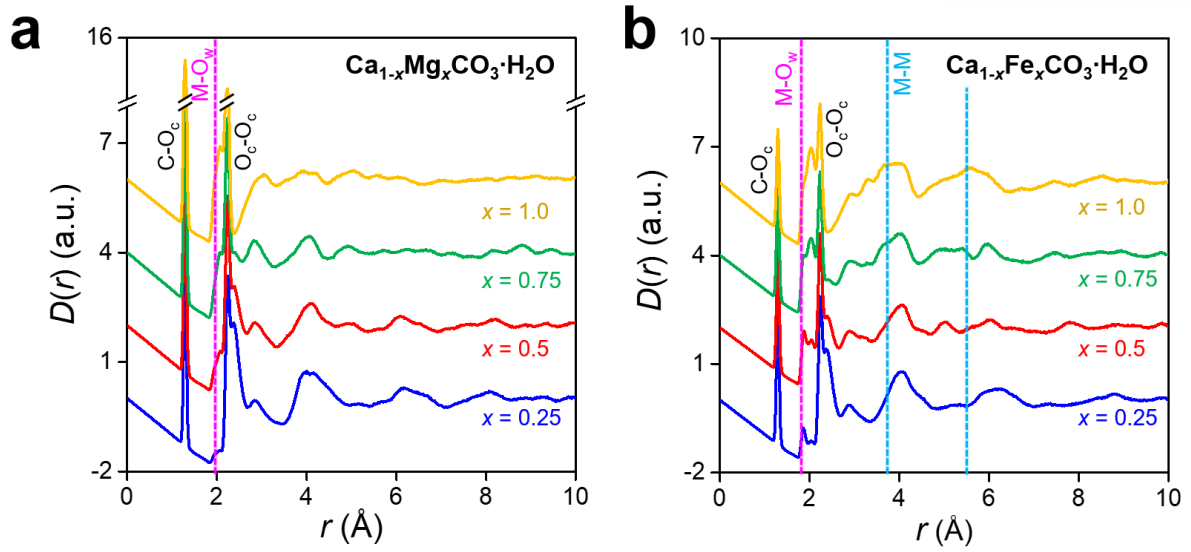


Figure 3.18 a and b, Total distribution functions (TDFs, $D(r)$) for $\text{Ca}_{1-x}\text{M}_x\text{CO}_3 \cdot n\text{H}_2\text{O}$ systems with $n = 1$, where $M = \mathbf{a}$, Mg and \mathbf{b} , Fe. The pink, brown, and sky-blue dashed lines represent the M–O_w, M–O_c, and M–M pairs of each ACC system, respectively.

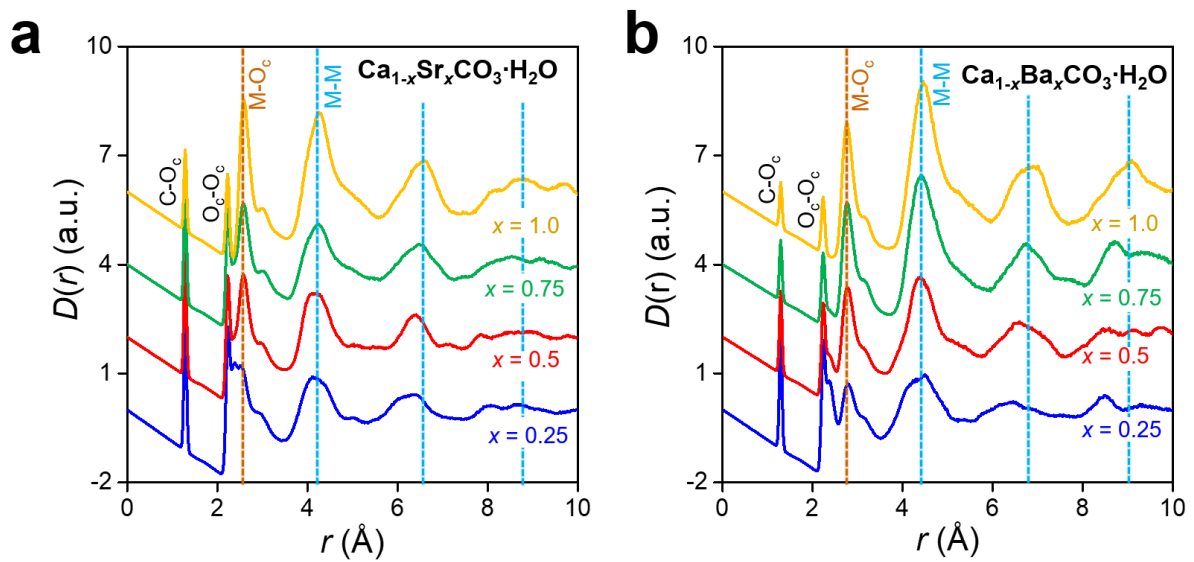


Figure 3.19 a and b, Total distribution functions (TDFs, $D(r)$) for $\text{Ca}_{1-x}\text{M}_x\text{CO}_3 \cdot n\text{H}_2\text{O}$ systems with $n = 1$, where $M = \mathbf{a}$, Sr and \mathbf{b} , Ba. The pink, brown, and sky-blue dashed lines represent the M–O_w, M–O_c, and M–M pairs of each ACC system, respectively.

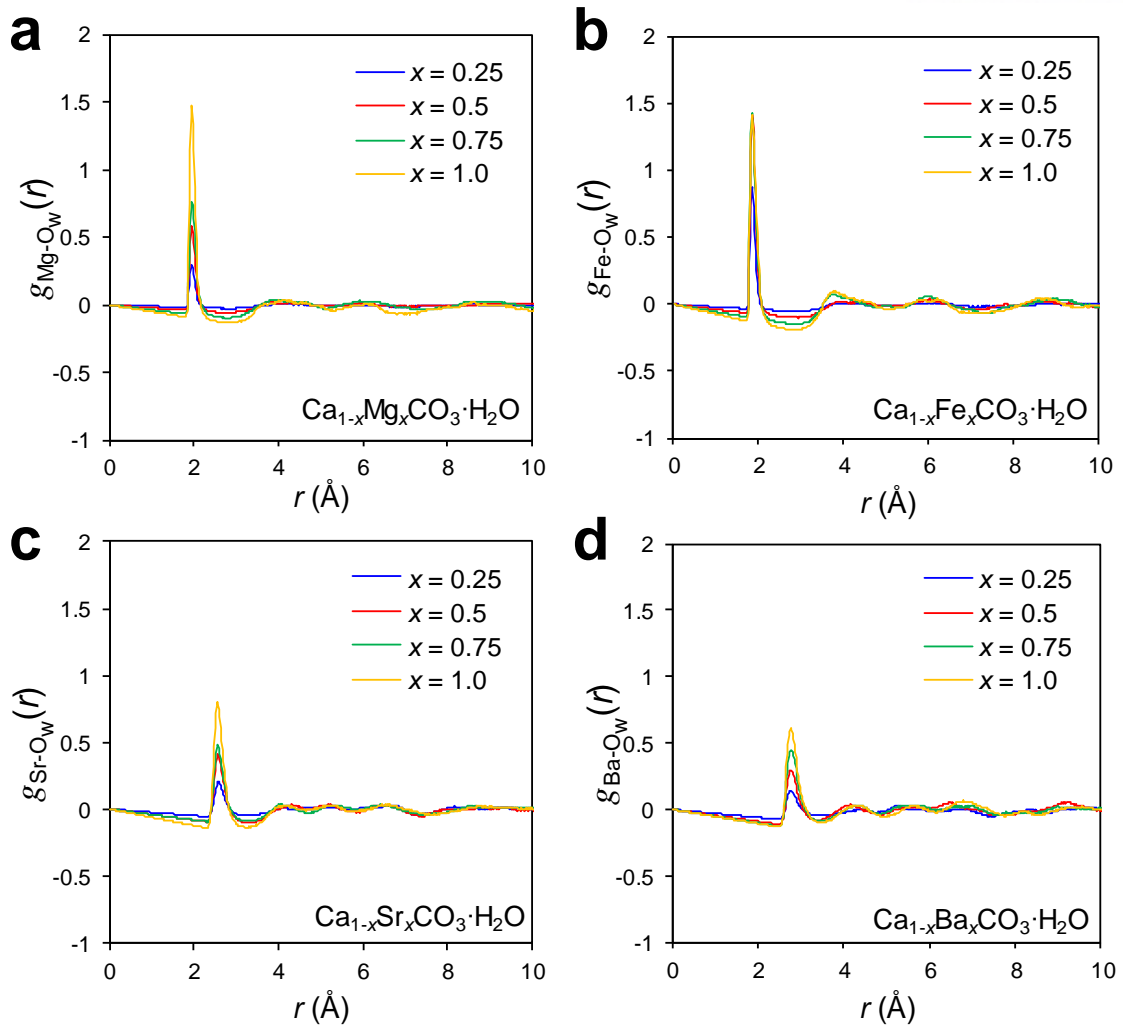


Figure 3.20 Pair-distribution function (PDF, $g(r)$) of $\text{Ca}_{1-x}\text{M}_x\text{CO}_3 \cdot n\text{H}_2\text{O}$ systems for $\text{M}-\text{O}_w$ (O in water) pairs with $n = 1$, where M = **a**, Mg, **b**, Fe, **c**, Sr, and **d**, Ba. Note that PDF were scaled by a factor $(4\pi\rho_0 r \left[c_i c_j \cdot z_i z_j / \left(\sum_{k=1}^n c_k z_k \right)^2 \right])$ for each pair in the $D(r)$.

These developed peaks indicated the higher coordination capacities for Sr^{2+} and Ba^{2+} ions due to their larger ionic size, as previously observed in the amorphous precursor phases for Sr^{2+} - or Ba^{2+} -containing systems at all hydration levels (**Figures 3.4a** and **3.4c**). In addition, the Sr- and Ba-ACC systems showed an increase in the peak intensity for the $\text{M}-\text{M}$ pairs at three regions including the new peaks in the mid-range, which corresponded to 4.3~4.4, 6.4~6.8, and 8.6~9.1 Å, respectively.

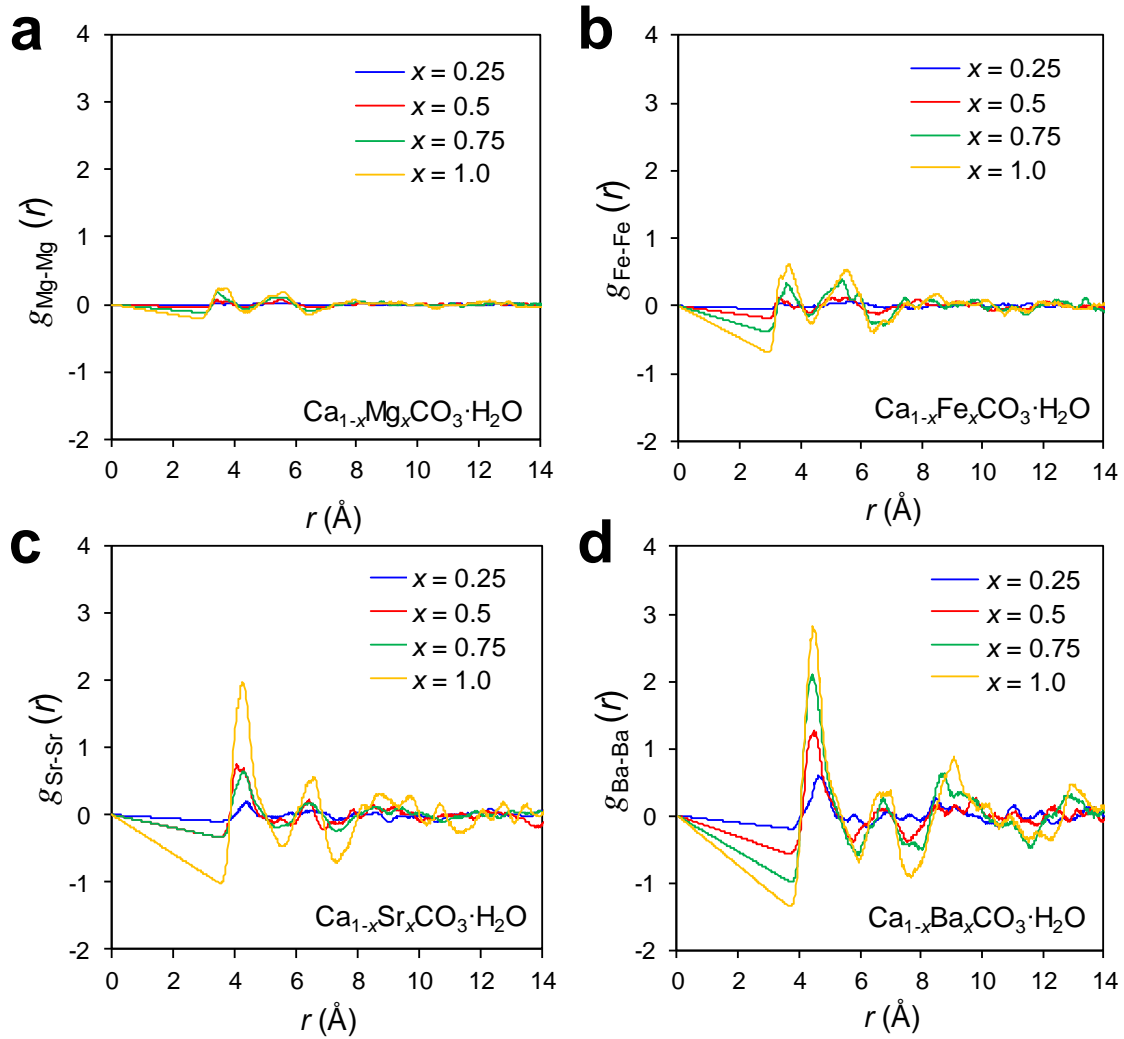


Figure 3.21 Pair-distribution function (PDF, $g(r)$) of $\text{Ca}_{1-x}\text{M}_x\text{CO}_3 \cdot n\text{H}_2\text{O}$ systems for M–M pairs with $n = 1$, where M = **a**, Mg, **b**, Fe, **c**, Sr, and **d**, Ba. Note that PDF were scaled by a factor $(4\pi\rho_0 r \left[c_i c_j \cdot z_i z_j / \left(\sum_{k=1}^n c_k z_k \right)^2 \right])$ for each pair in the $D(r)$.

The PDF for M–M pairs further clearly showed that the contributions for M–M pairs dominantly pronounced in the Ba- and Sr-ACC systems, compared to the Mg- and Fe-ACC systems (**Figure 3.21**). Note that similar observations for Ba-ACC systems were recently reported by Whittaker *et al.*,²⁹ which stated that next-nearest-neighbor cation ordering at the mid-range increased with increasing barium content. Consequently, there were evidently different correlation patterns depending on the additive species; Ba- and Sr-ACC showed a more ordered structure than that of Mg- and Fe-ACC, and these structural features were mainly attributable to the developed M–M pairs in the mid-range. These developed mid-range order may contribute to the rapid formation of crystalline structures by lowering the barrier for subsequent transformation.

3.4 Conclusion

In this study, the effects of additive ions on the local structure and stability of amorphous precursor phases for calcium carbonate were theoretically elucidated using MD simulations. Starting from the nucleation clusters to the anhydrous ACC, a variety of forms in the amorphous precursor phases were systematically characterized for a wide range of water content and additive ions (*i.e.*, $\text{Ca}_{1-x}\text{M}_x\text{CO}_3 \cdot n\text{H}_2\text{O}$, where $x = 0-1$, $n = 0-9$). Overall, the structural and thermodynamic characteristics of amorphous intermediate states were strongly related to the intrinsic properties of additive ions such as hydrophilicity and ionic size. Specifically, each additive ion was identified as inhibitors (*e.g.* Mg^{2+} and Fe^{2+} ions) or promoters (*e.g.* Sr^{2+} and Ba^{2+} ions) on the phase transition of amorphous precursor phases. Furthermore, we found that two opposing factors, which are the endothermic dehydration and exothermic crystallization processes, can work for the ΔH_f either in a rivalry (*e.g.*, for Mg^{2+} , Fe^{2+} additives) or synergistic relationship (*e.g.*, for Sr^{2+} , Ba^{2+} additives) depending on the additive ions. TDF analysis captured the structural features for different trends of Mg^{2+} or Fe^{2+} additives by enhanced M– O_w contributions in the short-range, and Sr^{2+} or Ba^{2+} ions by enhanced M–M pairs up to the mid-range (~ 10 Å), which might be observable by experimental technique such as EXAFS in the future works. These findings will contribute to a fundamental understanding for controlling the phase transition pathways of aqueous calcium carbonate-based systems by additives. We note that a deeper understanding of how the local structures and thermodynamics of amorphous precursor phases vary as a function of temperature, pressure, pH, and other organic and inorganic additives is needed for practical applications into the biomineralization process, which are worthy of future investigations.

3.5 References

1. Mass, T.; Giuffre, A. J.; Sun, C. Y.; Stiffler, C. A.; Frazier, M. J.; Neder, M.; Tamura, N.; Stan, C. V.; Marcus, M. A.; Gilbert, P. Amorphous Calcium Carbonate Particles Form Coral Skeletons. *Proc. Natl. Acad. Sci. U.S.A* **2017**, *114*, E7670-E7678.
2. Politi, Y.; Levi-Kalisman, Y.; Raz, S.; Wilt, F.; Addadi, L.; Weiner, S.; Sagi, I. Structural Characterization of the Transient Amorphous Calcium Carbonate Precursor Phase in Sea Urchin Embryos. *Adv. Funct. Mater.* **2006**, *16*, 1289-1298.
3. Gong, Y. U.; Killian, C. E.; Olson, I. C.; Appathurai, N. P.; Amasino, A. L.; Martin, M. C.; Holt, L. J.; Wilt, F. H.; Gilbert, P. U. Phase Transitions in Biogenic Amorphous Calcium Carbonate. *Proc. Natl. Acad. Sci. U.S.A* **2012**, *109*, 6088-6093.
4. Addadi, L.; Joester, D.; Nudelman, F.; Weiner, S. Mollusk Shell Formation: A Source of New Concepts for Understanding Biomineralization Processes. *Chem. Eur. J.* **2006**, *12*, 980-987.
5. Gordon, L. M.; Cohen, M. J.; MacRenaris, K. W.; Pasteris, J. D.; Seda, T.; Joester, D. Amorphous Intergranular Phases Control the Properties of Rodent Tooth Enamel. *Science* **2015**, *347*, 746-750.
6. Tolba, E.; Müller, W. E. G.; Abd EI-Hady, B. M.; Neufurth, M.; Wurm, F.; Wang, S.; Schröder, H. C.; Wang, X. High Biocompatibility and Improved Osteogenic Potential of Amorphous Calcium Carbonate/Vaterite. *J. Mater. Chem. B* **2016**, *4*, 376-386.
7. Anbu, P.; Kang, C. H.; Shin, Y. J.; So, J. S. Formations of Calcium Carbonate Minerals by Bacteria and Its Multiple Applications. *Springerplus* **2016**, *5*, 250.
8. Zhao, Y.; Luo, Z.; Li, M. H.; Qu, Q. Y.; Ma, X.; Yu, S. H.; Zhao, Y. L. A Preloaded Amorphous Calcium Carbonate/Doxorubicin@Silica Nanoreactor for pH-Responsive Delivery of an Anticancer Drug. *Angew. Chem. Int. Edit* **2015**, *54*, 919-922.
9. Svenskaya, Y.; Parakhonskiy, B.; Haase, A.; Atkin, V.; Lukyanets, E.; Gordin, D.; Antolini, R. Anticancer Drug Delivery System Based on Calcium Carbonate Particles Loaded with a Photosensitizer. *Biophys. Chem.* **2013**, *182*, 11-15.
10. Xu, N.; Li, Y. A.; Zheng, L.; Gao, Y. X.; Yin, H. W.; Zhao, J. T.; Chen, Z. G.; Chen, J. P.; Chen, M. Synthesis and Application of Magnesium Amorphous Calcium Carbonate for Removal of High Concentration of Phosphate. *Chem. Eng. J.* **2014**, *251*, 102-110.
11. Cai, H. H.; Li, S. D.; Tian, G. R.; Wang, H. B.; Wang, J. H. Reinforcement of Natural Rubber Latex Film by Ultrafine Calcium Carbonate. *J. Appl. Polym. Sci.* **2003**, *87*, 982-985.
12. Nielsen, M. H.; Aloni, S.; De Yoreo, J. J. In situ TEM Imaging of CaCO₃ Nucleation Reveals Coexistence of Direct and Indirect Pathways. *Science* **2014**, *345*, 1158-1162.
13. Radha, A. V.; Forbes, T. Z.; Killian, C. E.; Gilbert, P. U.; Navrotsky, A. Transformation and Crystallization Energetics of Synthetic and Biogenic Amorphous Calcium Carbonate. *Proc. Natl.*

- Acad. Sci. U.S.A* **2010**, *107*, 16438-16443.
14. Gebauer, D.; Kellermeier, M.; Gale, J. D.; Bergstrom, L.; Colfen, H. Pre-Nucleation Clusters as Solute Precursors in Crystallisation. *Chem. Soc. Rev.* **2014**, *43*, 2348-2371.
 15. Lam, R. S. K.; Charnock, J. M.; Lennie, A.; Meldrum, F. C. Synthesis-Dependant Structural Variations in Amorphous Calcium Carbonate. *CrystEngComm* **2007**, *9*, 1226-1236.
 16. Cartwright, J. H. E.; Checa, A. G.; Gale, J. D.; Gebauer, D.; Sainz-Diaz, C. I. Calcium Carbonate Polyamorphism and Its Role in Biomineralization: How Many Amorphous Calcium Carbonates Are There? *Angew. Chem. Int. Edit* **2012**, *51*, 11960-11970.
 17. Gower, L. B. Biomimetic Model Systems for Investigating the Amorphous Precursor Pathway and Its Role in Biomineralization. *Chem. Rev.* **2008**, *108*, 4551-4627.
 18. Seto, J.; Ma, Y. R.; Davis, S. A.; Meldrum, F.; Gourrier, A.; Kim, Y. Y.; Schilde, U.; Sztucki, M.; Burghammer, M.; Maltsev, S.; Jager, C.; Colfen, H. Structure-Property Relationships of a Biological Mesocrystal in the Adult Sea Urchin Spine. *Proc. Natl. Acad. Sci. U.S.A* **2012**, *109*, 3699-3704.
 19. Gebauer, D.; Colfen, H. Prenucleation Clusters and Non-Classical nucleation. *Nano Today* **2011**, *6*, 564-584.
 20. Carino, A.; Testino, A.; Andalibi, M. R.; Pilger, F.; Bowen, P.; Ludwig, C. Thermodynamic-Kinetic Precipitation Modeling. A Case Study: The Amorphous Calcium Carbonate (ACC) Precipitation Pathway Unravelling. *Cryst. Growth. Des.* **2017**, *17*, 2006-2015.
 21. Henzler, K.; Fetisov, E. O.; Galib, M.; Baer, M. D.; Legg, B. A.; Borca, C.; Xto, J. M.; Pin, S.; Fulton, J. L.; Schenter, G. K.; Govind, N.; Siepmann, J. I.; Mundy, C. J.; Huthwelker, T.; De Yoreo, J. J. Supersaturated Calcium Carbonate Solutions Are Classical. *Sci. Adv.* **2018**, *4*, eaa06283.
 22. Yoshida, N.; Higashimura, E.; Saeki, Y., Catalytic Biomineralization of Fluorescent Calcite by the Thermophilic Bacterium *Geobacillus thermoglucosidasius*. *Appl. Environ. Microb.* **2010**, *76*, 7322-7327.
 23. Gebauer, D.; Colfen, H.; Verch, A.; Antonietti, M. The Multiple Roles of Additives in CaCO₃ Crystallization: A Quantitative Case Study. *Adv. Mater.* **2009**, *21*, 435-439.
 24. Lose, E.; Wilson, R. M.; Seshadri, R.; Meldrum, F. C. The Role of Magnesium in Stabilising Amorphous Calcium Carbonate and Controlling Calcite Morphologies. *J. Cryst. Growth.* **2003**, *254*, 206-218.
 25. Sawada, K. The Mechanisms of Crystallization and Transformation of Calcium Carbonates. *Pure Appl. Chem.* **1997**, *69*, 921-928.
 26. Clarkson, J. R.; Price, T. J.; Adams, C. J. Role of Metastable Phases in the Spontaneous Precipitation of Calcium-Carbonate. *J. Chem. Soc. Faraday T.* **1992**, *88*, 243-249.
 27. Alberic, M.; Bertinetti, L.; Zou, Z. Y.; Fratzl, P.; Habraken, W.; Politi, Y. The Crystallization of

- Amorphous Calcium Carbonate is Kinetically Governed by Ion Impurities and Water. *Adv. Sci.* **2018**, *5*, 1701000.
28. Mejri, W.; Ben Salah, I.; Tlili, M. M., Speciation of Fe(II) and Fe(III) Effect on CaCO₃ Crystallization. *Cryst. Res. Technol.* **2015**, *50*, 236-243.
 29. Whittaker, M. L.; Sun, W. H.; DeRocher, K. A.; Jayaraman, S.; Ceder, G.; Joester, D., Structural Basis for Metastability in Amorphous Calcium Barium Carbonate (ACBC). *Adv. Funct. Mater.* **2018**, *28*, 1704202.
 30. Whittaker, M. L.; Joester, D., ACBC to Balcrite: Bioinspired Synthesis of a Highly Substituted High-Temperature Phase from an Amorphous Precursor. *Adv. Mater.* **2017**, *29*, 1606730.
 31. Radha, A. V.; Navrotsky, A., Direct Experimental Measurement of Water Interaction Energetics in Amorphous Carbonates MCO₃ (M = Ca, Mn, and Mg) and Implications for Carbonate Crystal Growth. *Cryst. Growth. Des.* **2015**, *15*, 70-78.
 32. Wolf, S. L. P.; Jähme, K.; Gebauer, D., Synergy of Mg²⁺ and Poly(Aspartic Acid) in Additive-Controlled Calcium Carbonate Precipitation. *CrystEngComm* **2015**, *17*, 6857-6862.
 33. Cantaert, B.; Kim, Y.-Y.; Ludwig, H.; Nudelman, F.; Sommerdijk, N. A. J. M.; Meldrum, F. C., Think Positive: Phase Separation Enables a Positively Charged Additive to Induce Dramatic Changes in Calcium Carbonate Morphology. *Adv. Funct. Mater.* **2012**, *22*, 907-915.
 34. Singer, J. W.; Yazaydin, A. O.; Kirkpatrick, R. J.; Bowers, G. M., Structure and Transformation of Amorphous Calcium Carbonate: A Solid-State ⁴³Ca NMR and Computational Molecular Dynamics Investigation. *Chem. Mater.* **2012**, *24*, 1828-1836.
 35. Reeder, R. J.; Tang, Y. Z.; Schmidt, M. P.; Kubista, L. M.; Cowan, D. F.; Phillips, B. L., Characterization of Structure in Biogenic Amorphous Calcium Carbonate: Pair Distribution Function and Nuclear Magnetic Resonance Studies of Lobster Gastrolith. *Cryst. Growth. Des.* **2013**, *13*, 1905-1914.
 36. Raiteri, P.; Gale, J. D., Water Is the Key to Nonclassical Nucleation of Amorphous Calcium Carbonate. *J. Am. Chem. Soc.* **2010**, *132*, 17623-17634.
 37. Smeets, P. J. M.; Finney, A. R.; Habraken, W. J. E. M.; Nudelman, F.; Friedrich, H.; Laven, J.; De Yoreo, J. J.; Rodger, P. M.; Sommerdijk, N. A. J. M., A Classical View on Nonclassical Nucleation. *Proc. Natl. Acad. Sci. U.S.A* **2017**, *114*, E7882-E7890.
 38. Demichelis, R.; Raiteri, P.; Gale, J. D.; Quigley, D.; Gebauer, D., Stable Prenucleation Mineral Clusters Are Liquid-Like Ionic Polymers. *Nat. Comm.* **2011**, *2*, 590.
 39. Bushuev, Y. G.; Finney, A. R.; Rodger, P. M., Stability and Structure of Hydrated Amorphous Calcium Carbonate. *Cryst. Growth. Des.* **2015**, *15*, 5269-5279.
 40. Tribello, G. A.; Bruneval, F.; Liew, C.; Parrinello, M., A Molecular Dynamics Study of the Early Stages of Calcium Carbonate Growth. *J. Phys. Chem. B* **2009**, *113*, 11680-11687.
 41. Saharay, M.; Yazaydin, A. O.; Kirkpatrick, R. J., Dehydration-Induced Amorphous Phases of

- Calcium Carbonate. *J. Phys. Chem. B* **2013**, *117*, 3328-3336.
42. Malini, R. I.; Bushuev, Y. G.; Hall, S. A.; Freeman, C. L.; Rodger, P. M.; Harding, J. H., Using Simulation to Understand the Structure and Properties of Hydrated Amorphous Calcium Carbonate. *CrystEngComm* **2016**, *18*, 92-101.
 43. Sancho-Tomas, M.; Fermani, S.; Reggi, M.; Garcia-Ruiz, J. M.; Gomez-Morales, J.; Falini, G., Polypeptide Effect on Mg²⁺ Hydration Inferred from CaCO₃ Formation: A Biomineralization Study by Counter-Diffusion. *CrystEngComm* **2016**, *18*, 3265-3272.
 44. Martignier, A.; Pacton, M.; Filella, M.; Jaquet, J. M.; Barja, F.; Pollok, K.; Langenhorst, F.; Lavigne, S.; Guagliardo, P.; Kilburn, M. R.; Thomas, C.; Martini, R.; Ariztegui, D., Intracellular Amorphous Carbonates Uncover a New Biomineralization Process in Eukaryotes. *Geobiology* **2017**, *15*, 240-253.
 45. Roh, Y.; Zhang, C. L.; Vali, H.; Lauf, R. J.; Zhou, J.; Phelps, T. J., Biogeochemical and Environmental Factors in Fe Biomineralization: Magnetite and Siderite Formation. *Clays Clay Miner.* **2003**, *51*, 83-95.
 46. Roden, E. E.; Leonardo, M. R.; Ferris, F. G., Immobilization of Strontium During Iron Biomineralization Coupled to Dissimilatory Hydrous Ferric Oxide Reduction. *Geochim. Cosmochim. Acta* **2002**, *66*, 2823-2839.
 47. Radha, A.V.; Fernandez-Martinez, A.; Hu, Y.; Jun, Y.-S.; Waychunas, G. A.; Navrotsky, A., Energetic and Structural Studies of Amorphous Ca_{1-x}Mg_xCO₃·nH₂O (0≤x≤1). *Geochim. Cosmochim. Acta* **2012**, *90*, 83-95.
 48. Schmidt, I.; Zolotoyabko, E.; Lee, K.; Gjardy, A.; Berner, A.; Lakin, E.; Fratzl, P.; Wagermaier, W. Effect of Strontium Ions on Crystallization of Amorphous Calcium Carbonate. *Cryst. Res. Technol.* **2019**, *54*, 1900002.
 49. Wallace, A. F.; Hedges, L. O.; Fernandez-Martinez, A.; Raiteri, P.; Gale, J. D.; Waychunas, G. A.; Whitlam, S.; Banfield, J. F.; De Yoreo, J. J., Microscopic Evidence for Liquid-Liquid Separation in Supersaturated CaCO₃ Solutions. *Science* **2013**, *341*, 885-889.
 50. Samoletov, A. A.; Dettmann, C. P.; Chaplain, M. A. J., Thermostats for "Slow" Configurational Modes. *J. Stat. Phys.* **2007**, *128*, 1321-1336.
 51. Berendsen, H. J. C.; Postma, J. P. M.; Vangunsteren, W. F.; Dinola, A.; Haak, J. R., Molecular-Dynamics with Coupling to an External Bath. *J. Chem. Phys.* **1984**, *81*, 3684-3690.
 52. Ewald, P. P. Die Berechnung Optischer und Elektrostatischer Gitterpotentiale. *Ann. Phys.* **1921**, *64*, 253
 53. Raiteri, P.; Demichelis, R.; Gale, J. D., Thermodynamically Consistent Force Field for Molecular Dynamics Simulations of Alkaline-Earth Carbonates and Their Aqueous Speciation. *J. Phys. Chem. C* **2015**, *119*, 24447-24458.
 54. Mezei, M. The Finite-Difference Thermodynamic Integration, Tested on Calculating the

- Hydration Free-Energy Difference between Acetone and Dimethylamine in Water. *J. Chem. Phys.* **1987**, *86*, 7084-7088.
55. Hummer, G.; Pratt, L. R.; Garcia, A. E. Ion Sizes and Finite-Size Corrections for Ionic-Solvation Free Energies. *J. Chem. Phys.* **1997**, *107*, 9275-9277.
 56. David, F.; Vokhmin, V.; Ionova, G. Water Characteristics Depend on the Ionic Environment. Thermodynamics and Modelisation of the Aquo Ions. *J. Mol. Liq.* **2001**, *90*, 45-62.
 57. Marcus, Y. Thermodynamics of Solvation of Ions. 5. Gibbs Free-Energy of Hydration at 298.15-K. *J. Chem. Soc. Faraday T.* **1991**, *87*, 2995-2999.
 58. Shi, H.; Luo, W.; Johansson, B.; Ahuja, R. First-Principles Calculations of the Electronic Structure and Pressure-Induced Magnetic Transition in Siderite FeCO₃. *Phys. Rev. B* **2008**, *78*, 155119.
 59. Graf, D. L. Crystallographic Tables for the Rhombohedral Carbonates. *Am. Mineral* **1961**, *46*, 1283-1316.
 60. Gale, J. D. Empirical Potential Derivation for Ionic Materials. *Philos. Mag. B* **1996**, *73*, 3-19.
 61. Dassault Systèmes BIOVIA, *Materials Studio 2019*, San Diego: Dassault Systèmes **2019**.
 62. Plimpton, S. Fast Parallel Algorithms for Short-Range Molecular-Dynamics. *J. Comput. Phys.* **1995**, *117*, 1-19.
 63. Marcus, Y. Ionic-Radii in Aqueous-Solutions. *Chem. Rev.* **1988**, *88*, 1475-1498.
 64. Marini, L. *Geological sequestration of carbon dioxide : thermodynamics, kinetics, and reaction path modeling.*; 1st ed.; Elsevier: Amsterdam ; Boston, **2007**; Vol. 11; pp 79-167.
 65. Holz, M.; Heil, S. R.; Sacco, A., Temperature-Dependent Self-Diffusion Coefficients of Water and Six Selected Molecular Liquids for Calibration in Accurate ¹H NMR PFG Measurements. *Phys. Chem. Chem. Phys.* **2000**, *2*, 4740-4742.
 66. Lahav, N.; Bolt, G. H., Self-Diffusion of Ca⁴⁵ into Certain Carbonates. *Soil Sci.* **1964**, *97*, 293-299.
 67. Agarwal, M.; Singh, M.; Sharma, R.; Alam, M. P.; Chakravarty, C., Relationship between Structure, Entropy, and Diffusivity in Water and Water-Like Liquids. *J. Phys. Chem. B* **2010**, *114*, 6995-7001.
 68. Shannon, R. D. Revised Effective Ionic-Radii and Systematic Studies of Interatomic Distances in Halides and Chalcogenides. *Acta Crystallogr. A* **1976**, *32*, 751-767.
 69. Zou, Z.; Polishchuk, I.; Bertinetti, L.; Pokroy, B.; Politi, Y.; Fratzl, P.; Habraken, W. J. E. M., Additives Influence the Phase Behavior of Calcium Carbonate Solution by a Cooperative Ion-Association Process. *J. Mater. Chem. B* **2018**, *6*, 449-457
 70. Michel, F. M.; MacDonald, J.; Feng, J.; Phillips, B. L.; Ehm, L.; Tarabrella, C.; Parise, J. B.; Reeder, R. J., Structural Characteristics of Synthetic Amorphous Calcium Carbonate. *Chem. Mater.* **2008**, *20*, 4720-4728.

Chapter 4. Molecularly Designed Chemical Trap for Polysulfide Adsorption in Lithium-Sulfur Battery

This chapter includes the published contents:

Yoo, J. T.;[†] Cho, S.-J.;[†] Jung, G. Y.;[†] Kim, S. H.; Choi, K.-H.; Kim, J.-H.; Lee, C. K.; Kwak, S. K.; Lee, S.-Y. *Nano Lett.* **2016**, *16*, 3292-3300 († : **equally contributed**). Reproduced with permission. Copyright © 2016 American Chemical Society.

4.1 Introduction

Lithium-sulfur (Li-S) batteries have garnered a great deal of attention as a promising alternative to the lithium-ion batteries (LIBs) due to high theoretical capacity ($= 1672 \text{ mAh g}^{-1}$), low cost, natural abundance, and environmental benignity of sulfur active materials.¹⁻³ However, their progress towards commercialization has been delayed due to some serious drawbacks such as electrical insulating nature of sulfur and solid-state reduction products (Li_2S_2 and Li_2S), structural instability of sulfur cathodes, shuttle effect of lithium polysulfides (Li_2S_x) and unstable Li metal/electrolyte interface.¹⁻⁶ Especially, rapid capacity fading with cycling, mainly due to the shuttle effect and subsequent accumulation of electrically-inert reduction products on electrodes, poses the most critical challenge for securing sustainable electrochemical performance in Li-S batteries.

Enormous efforts have been undertaken to address the aforementioned issues. In this context, a chemical trap (as polysulfide reservoirs) based on electrically-conductive porous structure has been widely studied, including the application in nanostructured sulfur composite cathodes,⁷⁻¹¹ self-standing interlayers positioning between cathodes and separator membranes,¹²⁻¹⁴ and interlayer-integrated separator membranes.¹⁵⁻¹⁷ Fundamental demands for an ideal chemical trap can be outlined as follows^{5, 21}: (1) high electronic conduction; (2) mesoporous structure for fast ion transport; (3) microporous structure (pore diameter $< 2 \text{ nm}$) for polysulfide adsorption, and (4) facile solid-liquid conversion (*i.e.*, electrochemical reversibility) of electrically-inert Li_2S_2 and Li_2S . Importantly, the insoluble $\text{Li}_2\text{S}_2/\text{Li}_2\text{S}$ molecules are reported to be aggregated favorably in micropores of chemical traps during charging/discharging reaction,^{12,19-21} hampering the cycling performance of Li-S batteries.¹⁹ Accordingly, significant attention should be dedicated to pore size and chemical affinity of microporous structure. However, in most previous studies, microporous phases tend to be randomly mingled with mesoporous ones,^{7,8,12,16,17} which makes it difficult to understand the adsorption/dissolution phenomena of Li_2S_x in micropores and mesopores. In addition, there have been no reports on molecular design-

based synthesis of electrochemical responsive micropores (for selective adsorption of insoluble polysulfides) and their influence on solid-liquid conversion kinetics of the polysulfides.

In this study, to resolve the above-mentioned challenging issues of the chemical traps, we demonstrate “microporous covalent organic framework (COF) net on mesoporous CNT net” hybrid architecture as a new class of molecularly-designed, hierarchical porous chemical trap for Li_2S_x in Li-S batteries. The concept of hierarchical porous structure has garnered a lot of attentions as a multiscale engineering to bring unprecedented synergistic effects in a variety of functional materials.^{22,23} As a proof-of-concept for the hybrid architecture proposed herein, self-standing COF-net on CNT-net interlayers (referred to as “NN interlayers”) are fabricated and their potential applicability as an alternative polysulfide trap is explored.

To theoretically determine the effects of pore size and chemical affinity of microporous COF nets (possessing boronate ester groups), the Li_2S_x adsorption behaviors on COFs were thoroughly investigated by multi-scale simulations including DFT and GCMC methods. Two different COFs [COF-1 (micropore size = 0.7 nm) and COF-5 (2.7 nm)] are chosen as model systems. GCMC simulations showed that all Li_2S_x species are randomly dispersed in the COF-5 bulk, whereas the Li_2S exclusively penetrates to the COF-1 bulk due to its smaller-sized micropore, demonstrating the pore-size-enabled selective adsorption of Li_2S . DFT calculations revealed that Li_2S -adsorbed COF-1 exhibited the electrostatic stabilization-driven formation of chemical bonds between sulfur (in Li_2S_x) and boron (in COF-1). These theoretical results demonstrate that COF-1 possesses a well-designed micropore size and (boron-mediate) chemical affinity suitable for selective binding with Li_2S , which can improve the electrochemical performance of Li-S cells.

Benefiting from the chemical/structural uniqueness (in specific, COF net-based micropores as polysulfide traps, CNT net-based mesopores as ion-conducting channels, and CNT nets as electronic networks), the NN interlayer is predicted to effectively capture polysulfides without damaging ion/electron transport in its through-thickness direction. Consequently, the NN interlayer significantly improved the electrochemical reversibility of polysulfides, ultimately leading to the outstanding cycling performance far beyond those achievable with conventional Li-S technologies.

4.2 Methods

4.2.1 Model Systems for Calculation

The most stable geometries of Li_2S_x ($x = 1, 4, 6,$ and 8) molecules were identified by DFT calculations²⁴ (**Figure 4.1a**). A zig-zag (10,0) CNT model with a diameter of 15.0 Å was used to represent the outermost surface with an inter-wall distance of 3.6 Å. The model was cut in half to set the model condition suitable for DFT calculation. The partial optimization was performed under fixed coordinates of terminated-hydrogen atoms (*i.e.*, 232 atoms). The single crystals of the COF-1 and COF-5,²⁵ which were chosen as the unit cells for calculation, where the full relaxation including both atomic positions and lattice parameters was carried out. The $1 \times 1 \times 2$ and $1 \times 1 \times 3$ supercells for the COF-1 and COF-5 were respectively modeled to represent bulk state. For thin film models, the vacuum was sufficiently applied in the z -direction (*i.e.*, ~ 20 Å) for each $1 \times 1 \times 3$ supercell structure of the COF-1 with fixed two bottom layers (**Figure 4.1b**) and the COF-5 systems (**Figure 4.1c**). The adsorption energies of Li_2S_x molecules and corresponding conformational search, in these bulk and thin film models of the CNT, COF-1, and COF-5, were systematically analyzed using the DFT calculations and GCMC simulations.

4.2.2 Simulation Details

The initial binding configurations for Li_2S_x molecules in the COFs were investigated *via* the GCMC simulation²⁶ using a Sorption program (Materials Studio 8.0)²⁷, in which the equilibration for 1×10^6 MC steps and following analysis for 1×10^6 steps were applied to the simulation. The non-bond interactions between Li_2S_x molecules and COFs, including electrostatic and van der Waals forces, were calculated with the Universal forcefield,²⁸ wherein Ewald summation and atom-based cutoff (a cutoff of 15.5 Å) method were applied to the electrostatic force and van der Waals interaction, respectively.

DFT calculations were carried out using a DMol³ program^{29,30} under the generalized gradient approximation (GGA) with the Perdew-Burke-Ernzerhof (PBE) functional,³¹ in which the semi-empirical Tkatchenko-Scheffler (TS) scheme³² for the dispersion correction was included. The spin-polarized calculations were performed with the basis set of the DNP 4.4, therein the relativistic effect of all electrons on core electrons was also included. The Monkhorst-Pack³³ was applied for the sampling of the Brillouin-zone as follows: Γ -point for the CNT; $2 \times 2 \times 4$ k -point for the COF-1 unit cell; $1 \times 1 \times 4$ k -point for the COF-5 unit cell; and Γ -point for all the adsorbed systems. The convergence criteria for the geometry optimization were set to 1.0×10^{-5} Ha, 0.002 Ha/Å, and 0.005 Å for the energy, force, and displacement, respectively. The self-consistent field convergence for was set less than 1.0×10^{-6} Ha.

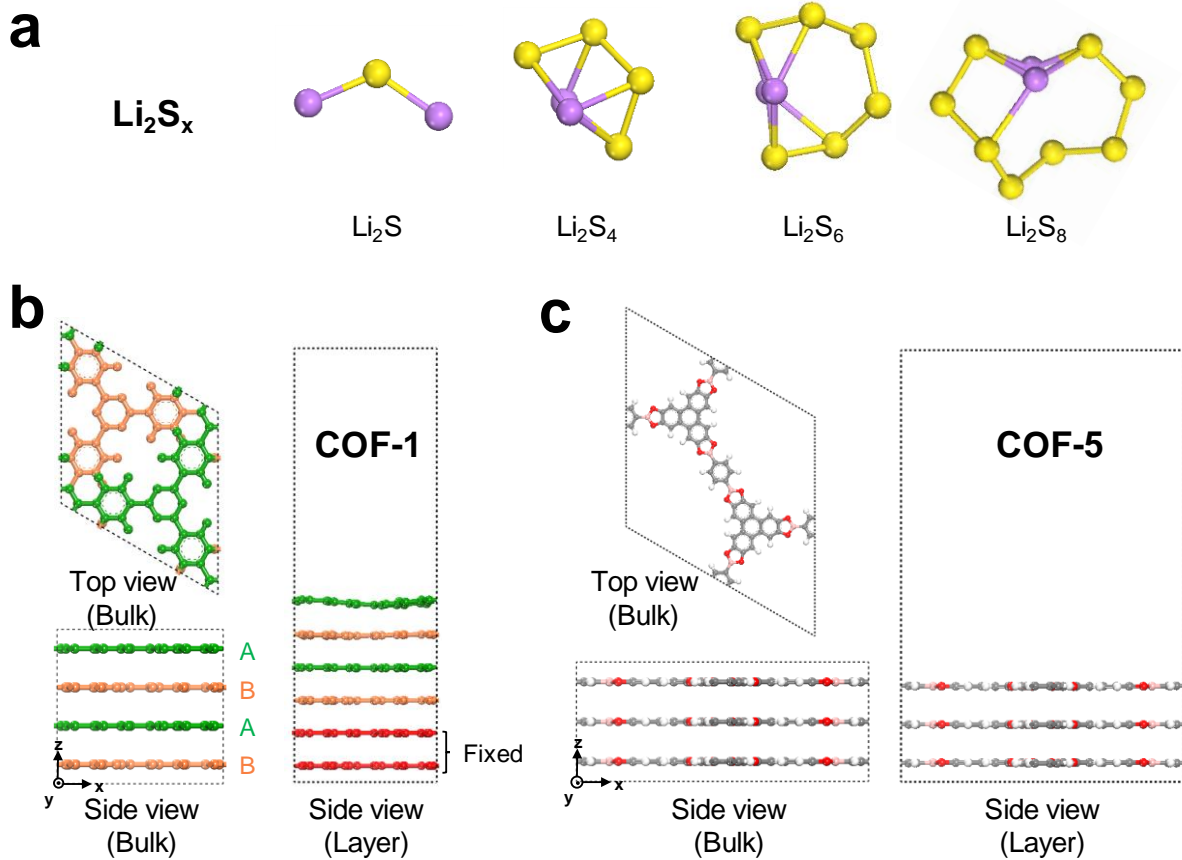


Figure 4.1 Model systems of Li_2S_x and COFs. **a**, Optimized geometries of Li_2S_x ($x = 1, 4, 6,$ and 8) molecules identified by DFT calculations. Purple and yellow colored atoms represent the lithium and sulfur, respectively. **b**, Optimized unit cell model of COF-1 by full relaxation including both atomic positions and lattice parameters. The $1 \times 1 \times 2$ supercell was built for representing the bulk state. For layer models, the vacuum was sufficiently applied in the z -direction (*i.e.*, $\sim 20 \text{ \AA}$) for the $1 \times 1 \times 3$ supercell with fixed two bottom layers. **c**, Optimized unit cell model of the COF-5. The $1 \times 1 \times 2$ and $1 \times 1 \times 3$ supercells were built for the bulk state and layer model, respectively.

4.2.3 Energy Calculations

The total adsorption energy (ΔE_{ads}) was calculated as follows,

$$\Delta E_{ads} = E_{Li_2S_x+X} - E_{Li_2S_x} - E_X \quad (X = \text{CNT, COF-1, and COF-5}) \quad (4.1)$$

where $E_{Li_2S_x}$ and E_X represent the total energy of the isolated Li_2S_x molecule and pristine CNT, COF-1, and COF-5, respectively, $E_{Li_2S_x+X}$ is obtained from the Li_2S_x -adsorbed CNT, COF-1, and COF-5. The total adsorption energy (ΔE_{ads}) can be decomposed into few types of energy contributions as follows:

$$\Delta E_{ads} = \Delta E_{bond} + \Delta E_{recon} + \Delta E_{Li_2S_x} \quad (4.2)$$

in which ΔE_{bond} indicates the energy contribution for the bond formation, ΔE_{recon} and $\Delta E_{Li_2S_x}$ represent the energy contribution due to the reconstruction and structural change of the hosts (CNT, COF-1, and COF-5) and Li_2S_x guests, respectively.

Each energy component was calculated as follows:

$$\Delta E_{recon} = E_{X(recon)} - E_{X(bare)} \quad (X = \text{CNT, COF-1, and COF-5}) \quad (4.3)$$

The ΔE_{recon} is calculated by subtracting the single point energy of bare structures from that of reconstructed structures for hosts (CNT, COF-1, and COF-5).

$$\Delta E_{Li_2S_x} = E_{Li_2S_x(ads)} - E_{Li_2S_x(gas)} \quad (4.4)$$

The $\Delta E_{Li_2S_x}$ is calculated by subtracting the single point energy of Li_2S_x molecule in gas phase from that of adsorbed ones.

$$\Delta E_{bond} = E_{Li_2S_x+X} - E_{Li_2S_x(ads)} - E_{X(recon)} \quad (X = \text{CNT, COF-1, and COF-5}) \quad (4.5)$$

The ΔE_{bond} contains the remaining contribution for bond formation in its adsorbed geometry.

4.3 Results and Discussion

4.3.1 Pore-Size Dependent Adsorption of Polysulfides

Two COFs (*i.e.*, COF-1 (0.7 nm) and COF-5 (2.7 nm)) with different micropore sizes but boronate ester functional groups in common were chosen as model systems (**Figure 4.2**). COF-1 and COF-5 are composed of benzene-1,4-diboronic acid (BDDBA)³⁴ alone (for COF-1) and BDDBA/2,3,6,7,10,11-hexahydroxytriphenylene (HHTP)³⁴ (for COF-5), respectively. Both COFs, driven by their excellent compatibility (specifically, *via* π - π intermolecular interaction) with CNTs,^{35,36} can be conformally deposited on the curvilinear CNT surface.

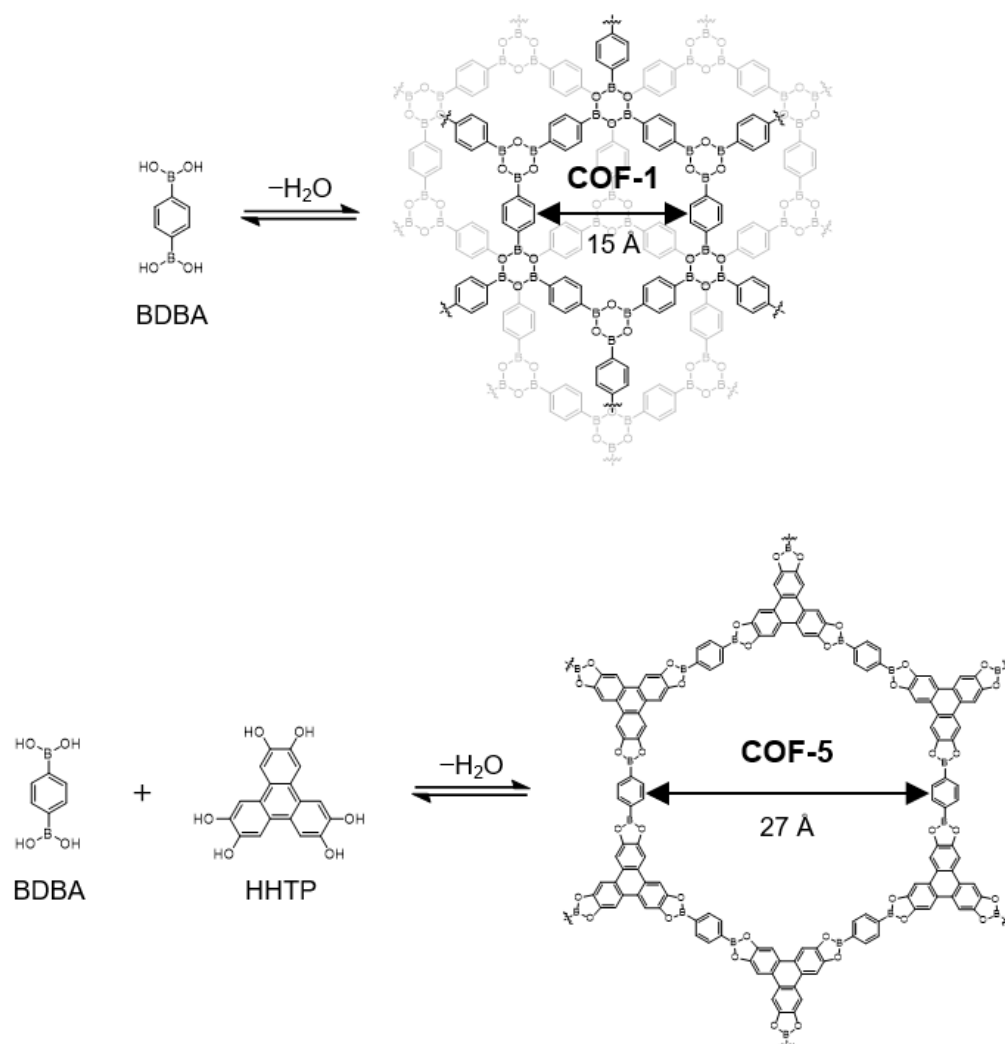


Figure 4.2 Synthetic scheme and chemical structures of COF-1 and COF-5.

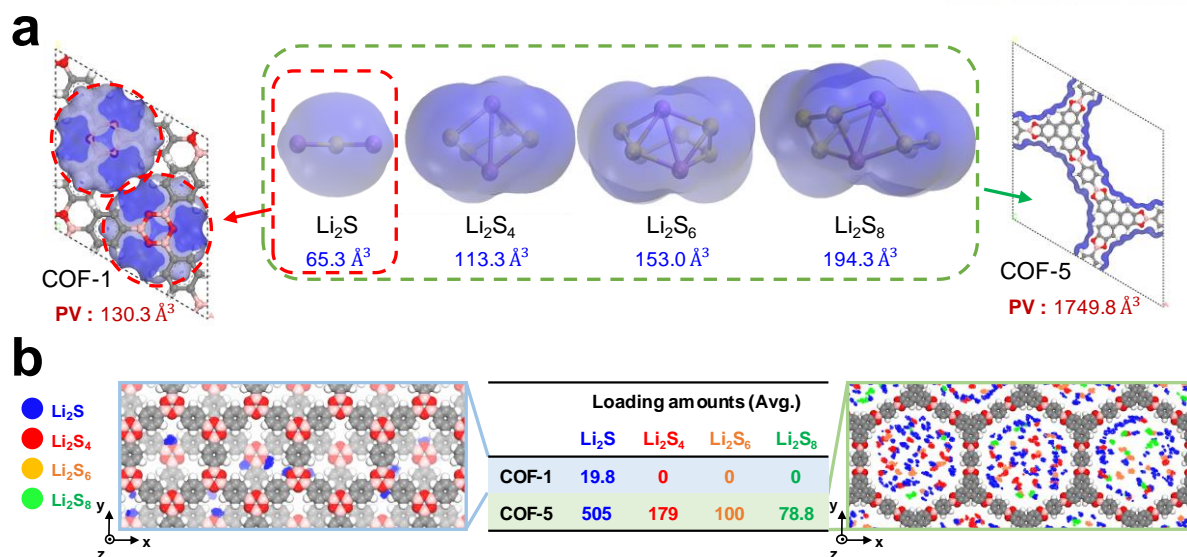


Figure 4.3 a, Pore size and of COFs (COF-1 and COF-5) and molecular size of Li₂S_x species (x = 1, 4, 6, and 8). Pore volume (PV) and molecular volume (estimated by Connolly surface method³⁷) are labelled below. Color legends – C: gray; O: red; H: white; B: pink; Li: purple; S: yellow. **b**, Snapshots depicting the binding configurations of polysulfides in COF-1 (blue box, left) and COF-5 (green box, right), and averaged loading amounts of Li₂S_x species (x = 1, 4, 6, and 8), calculated through GCMC simulation. Blue, red, orange, and green circles represent Li₂S, Li₂S₄, Li₂S₆, and Li₂S₈, respectively.

The initial binding configurations of Li₂S_x molecules in the COFs were examined by the GCMC simulation. The model systems of the Li₂S_x and COFs used for this theoretical calculation were shown in **Figure 4.1**. A diversity of initial binding configurations of Li₂S_x species (x = 1, 4, 6, and 8) in the COF-1 and COF-5 were depicted in **Figure 4.1c**. In MWCNT, as all carbon atoms are equivalent, the specific binding sites of Li₂S_x molecules are nonexistent and thus predicted to be located in outside surface of the wall. In COF-1, on the other hand, because of its small pore size (~0.7 nm) and reported AB stacking arrangement, it has a small pore volume (PV) per layer (*i.e.*, 130.3 Å³, estimated by Connolly surface method,³⁷ **Figure 4.3a (left)**). In COF-5, because of its AA stacking, it has a large 1D pore channels (~2.7 nm) with a large PV per layer (*i.e.*, 1749.8 Å³, **Figure 4.3a (right)**). Thus, the adsorption sites in the COF-5 are equivalent for all Li₂S_x species without preferential intermolecular interaction, wherein Li₂S_x molecules are randomly dispersed in the COF-5 bulk (**Figure 4.3b**). The COF-1 bulk allows for exclusive penetration of Li₂S due to its smaller-sized micropore (0.7 nm), demonstrating the pore size-enabled selective adsorption of Li₂S in the COF-1.

4.3.2 Chemical Affinity of Polysulfide Adsorption

Based on the initial binding configurations described above, adsorption energies of Li_2S_x on the COFs and CNT were theoretically investigated using the DFT calculation, with an aim to further elucidate the binding behavior of Li_2S_x species. The total adsorption energies were decomposed into three energy contributions including bond formation (ΔE_{bond}), reconstruction of host structures of CNT, COF-1 and COF-5 (ΔE_{recon}) and structural change of Li_2S_x guests ($\Delta E_{\text{Li}_2\text{S}_x}$), respectively (for the calculation details, see ‘Energy Calculations’ in the Methods section). First, we focused on the adsorption of Li_2S_x on CNT surface (**Figure 4.4**). The results showed that Li_2S_x ($x = 4, 6, \text{ and } 8$) molecules build Li-C bonds without undergoing structural change (*i.e.*, reconstruction energy (ΔE_{recon}) ≤ 0.06 eV) (**Table 4.1**). Meanwhile, for Li_2S , driven by its electron donation to conjugated π -bonds of CNTs, a specific bidentate binding of two Li atoms on the CNT surface was observed (**Figure 4.4a**).

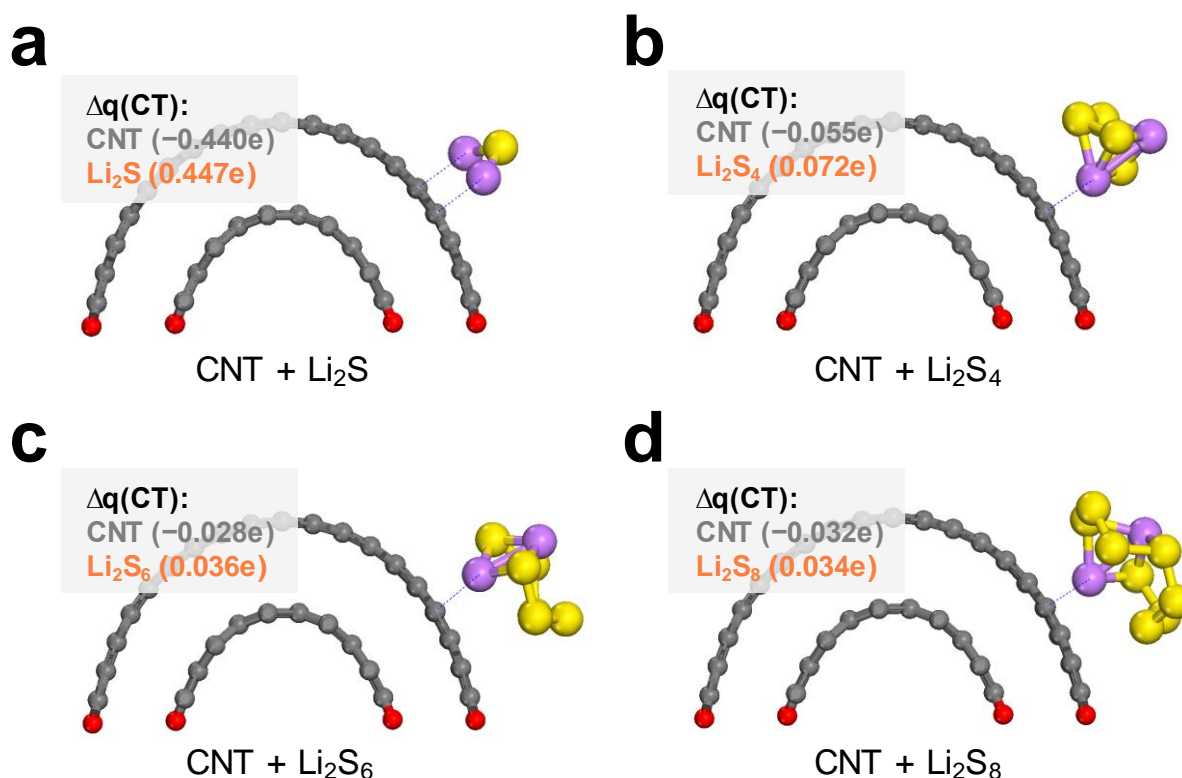


Figure 4.4 Binding configurations of Li_2S_x molecules on partially cleaved CNT surface; **a**, Li_2S , **b**, Li_2S_4 , **c**, Li_2S_6 , and **d**, Li_2S_8 . $\Delta q(\text{CT})$ values indicate the transferred charges of molecules. Gray, purple, and yellow balls represent C, Li, and S atoms, respectively. Red balls signify the fixed hydrogen-terminated sites.

Table 4.1 Total adsorption energies (ΔE_{ads}), chemical bond formation energies (ΔE_{bond}), and reconstruction energies (ΔE_{recon}) of various lithium polysulfide (Li_2S_x) species on the CNT surface and in the bulk and layer of COF-1 and COF-5.

	CNT	Bulk		Layer	
		COF-1	COF-5	COF-1	COF-5
ΔE_{ads} (eV)	-2.99	-3.05	-3.35	-3.05	-3.34
Li_2S ΔE_{bond} (eV)	-3.06	-5.28	-1.55	-4.94	-1.87
ΔE_{recon} (eV)	0.06	1.93	-1.89	1.67	-1.54
ΔE_{ads} (eV)	-2.46	-	-3.36	-1.48	-2.78
Li_2S_4 ΔE_{bond} (eV)	-2.53	-	-1.67	-1.59	-1.26
ΔE_{recon} (eV)	0.06	-	-2.00	0.07	-1.54
ΔE_{ads} (eV)	-2.59	-	-3.21	-1.61	-3.08
Li_2S_6 ΔE_{bond} (eV)	-2.68	-	-1.32	-1.90	-1.61
ΔE_{recon} (eV)	0.05	-	-2.04	0.20	-1.63
ΔE_{ads} (eV)	-2.71	-	-3.33	-1.86	-3.11
Li_2S_8 ΔE_{bond} (eV)	-2.82	-	-1.42	-1.99	-1.62
ΔE_{recon} (eV)	0.06	-	-2.04	0.06	-1.62

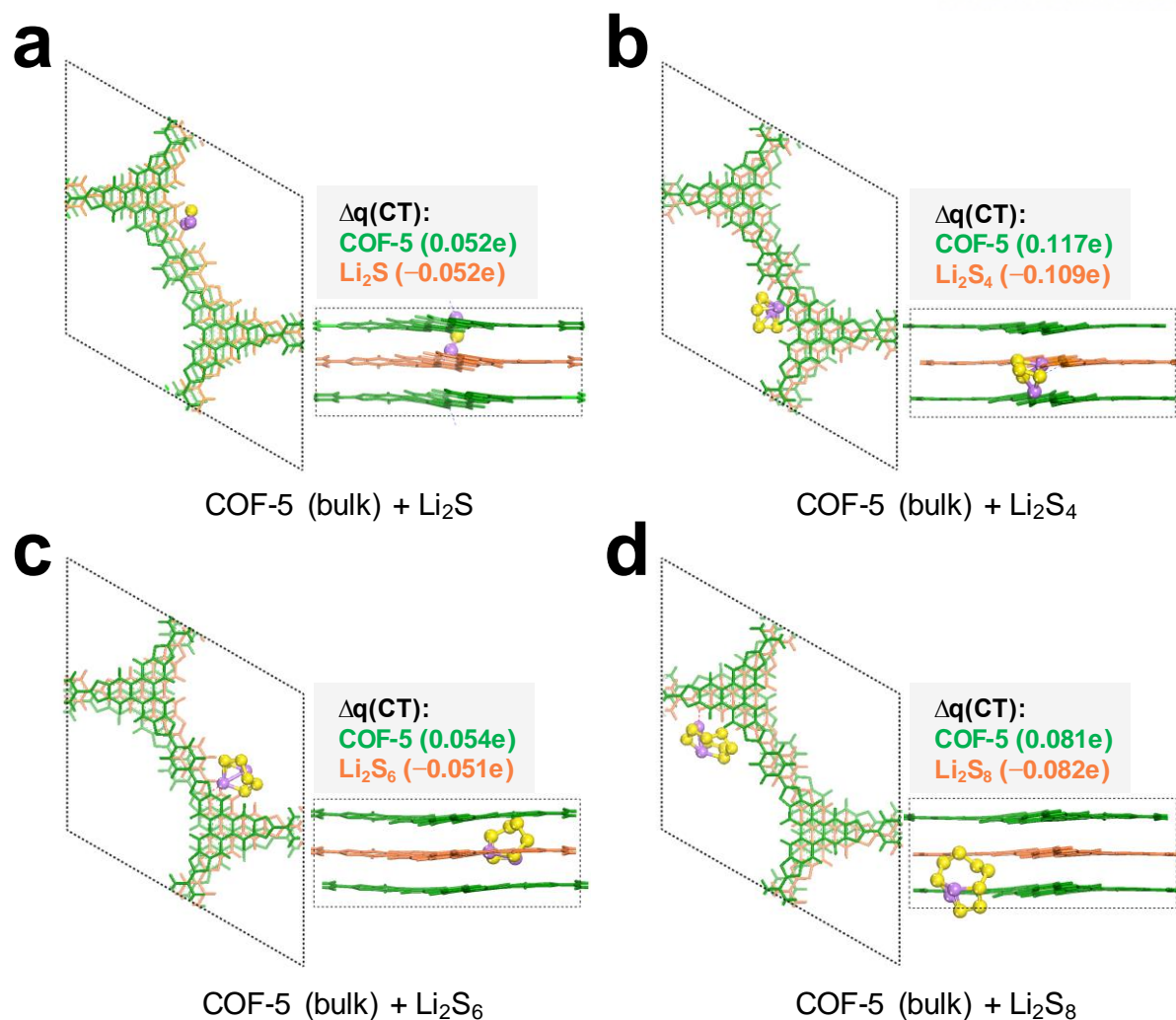


Figure 4.5 Binding configurations of Li_2S_x ($x = 1, 4, 6,$ and 8) molecules in the bulk state of COF-5; **a**, Li_2S , **b**, Li_2S_4 , **c**, Li_2S_6 , and **d**, Li_2S_8 . $\Delta q(\text{CT})$ values indicate the transferred charges of molecules. Purple and yellow balls represent the Li and S atoms of the Li_2S_x , respectively. Alternate multi-plies between green and orange layers represent the AA-eclipsed stacking arrangement.

As a next step, the adsorption behavior of Li_2S_x molecules to the COF-5 was investigated both for bulk and layer models (**Figures 4.5** and **4.6**). The total adsorption energies of Li_2S_x molecules were relatively larger than those in CNT of COF-1 (ranging from -3.36 to -2.78 eV, **Table 4.1**), revealing their superior capability for Li_2S_x capture. Notably, besides its good adsorption strengths, the adsorption amounts were also much larger in COF-5 than in COF-1 (**Figure 4.3b**).

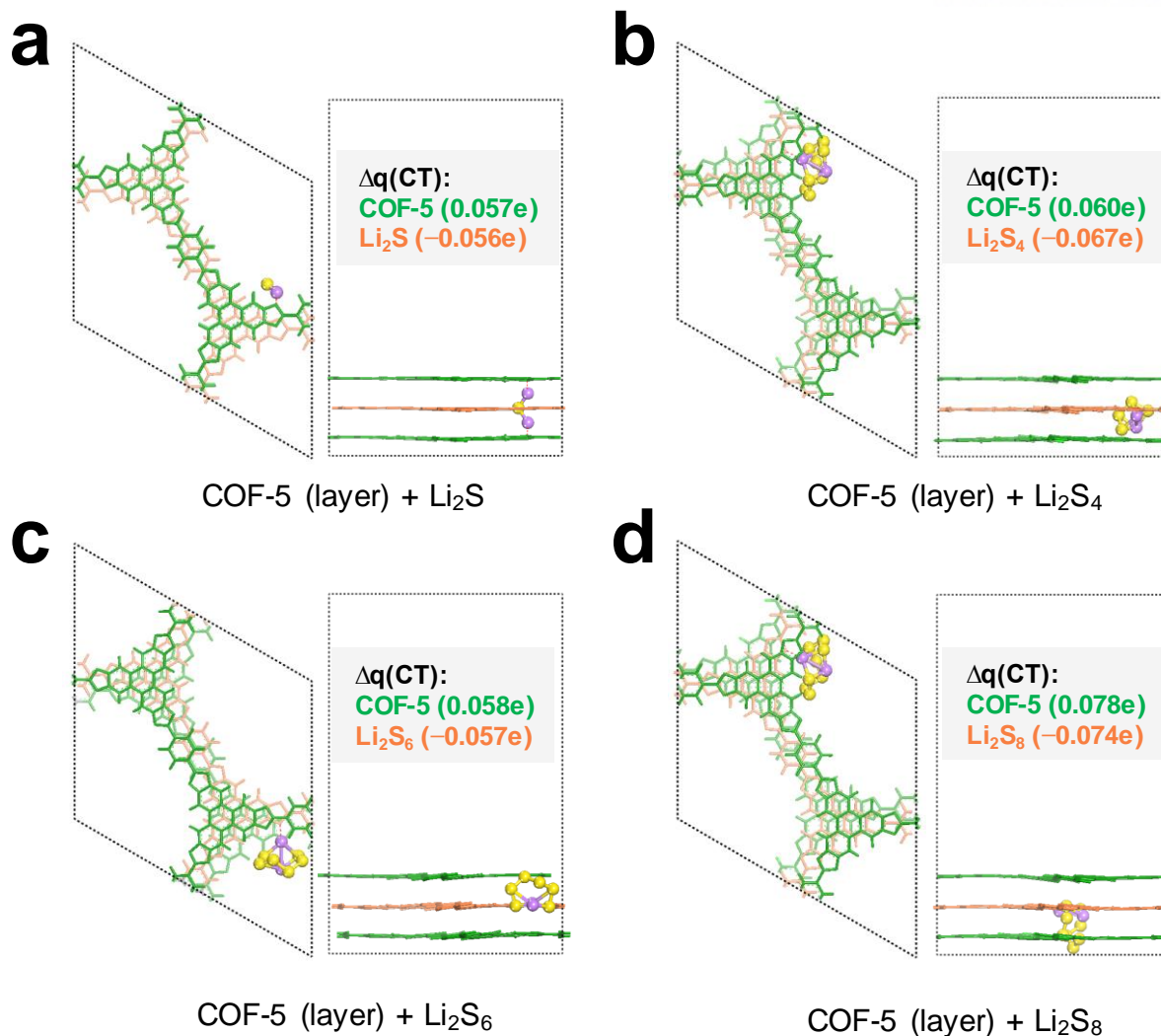


Figure 4.6 Binding configurations of Li₂S_x ($x = 1, 4, 6,$ and 8) molecules in the layer models of COF-5; **a**, Li₂S, **b**, Li₂S₄, **c**, Li₂S₆, and **d**, Li₂S₈. $\Delta q(\text{CT})$ values indicate the transferred charges of molecules. Purple and yellow balls represent the Li and S atoms of the Li₂S_x, respectively. Alternate multi-plies between green and orange layers represent the AA-eclipsed stacking arrangement.

The major contribution for adsorption was the structural stabilization of COF-5 after Li₂S_x adsorption (ΔE_{recon} , ranging from $-2.04 \sim -1.54$ eV in **Table 4.1**), from perfect AA- into slightly shifted AA-stacking in armchair direction. Due to its AA-stacking arrangement of COF-5, the Li₂S molecules can't adsorb on boron sites and only shows the weak Li \cdots O interactions, where the little amounts of electron-withdrawing occur (**Figures 4.5a** and **4.6a**).

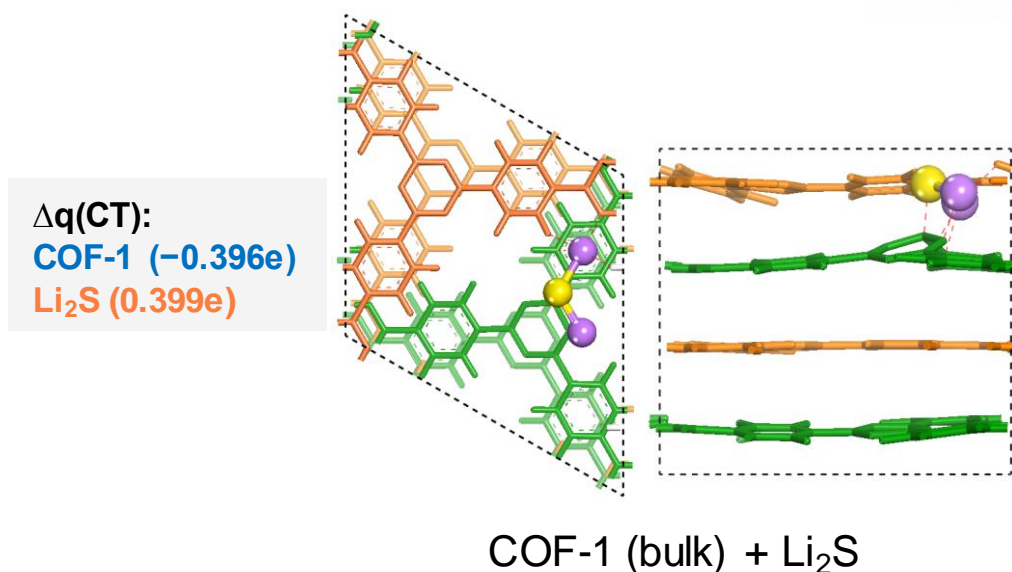


Figure 4.7 Binding configurations of Li₂S in the bulk state of COF-1, in which $\Delta q(\text{CT})$ values indicate the transferred charges of molecules. Purple and yellow balls represent the Li and S atoms of the Li₂S, respectively. Alternate multi-plies between green and orange layers represent the AB-staggered stacking arrangement.

On the other hand, as examined in the GCMC simulation, the large-sized Li₂S_x ($x = 4, 6,$ and 8) molecules are difficult to be embedded into the COF-1 but the small-sized Li₂S can exclusively penetrate into the COF-1 bulk (**Figure 4.7**). A notable finding is that during the adsorption of Li₂S, the AB-staggered stacking arrangement of COF-1 was slightly shifted along the zig-zag direction, which was apparently different in COF-5 (AA-stacking shift along the arm-chair direction). The Li₂S adsorbed inside the COF-1 bulk shows the higher ΔE_{ads} (-3.05 eV), whereas the large Li₂S_x ($x = 4, 6,$ and 8) molecules merely adsorb on the outermost surface of the COF-1 with relatively low ΔE_{ads} (ranging from -1.86 to -1.48 eV, **Table 4.1** and **Figure 4.8**). Such energetically favorable chemical bond formation between Li₂S and COF-1 was verified by the higher bond energy ($\Delta E_{bond} = -5.28$ eV) between sulfur (of Li₂S) and boron atoms (of COF-1), which is much higher than those of the CNTs ($\Delta E_{bond} = -3.06$ eV) and COF-5 ($\Delta E_{bond} = -1.55$ eV). In addition, the (sulfur-boron) bond energy is sufficiently high enough to compensate energetic cost ($\Delta E_{recon} = +1.93$ eV, **Table 4.1**), induced by structural change of the COF-1.

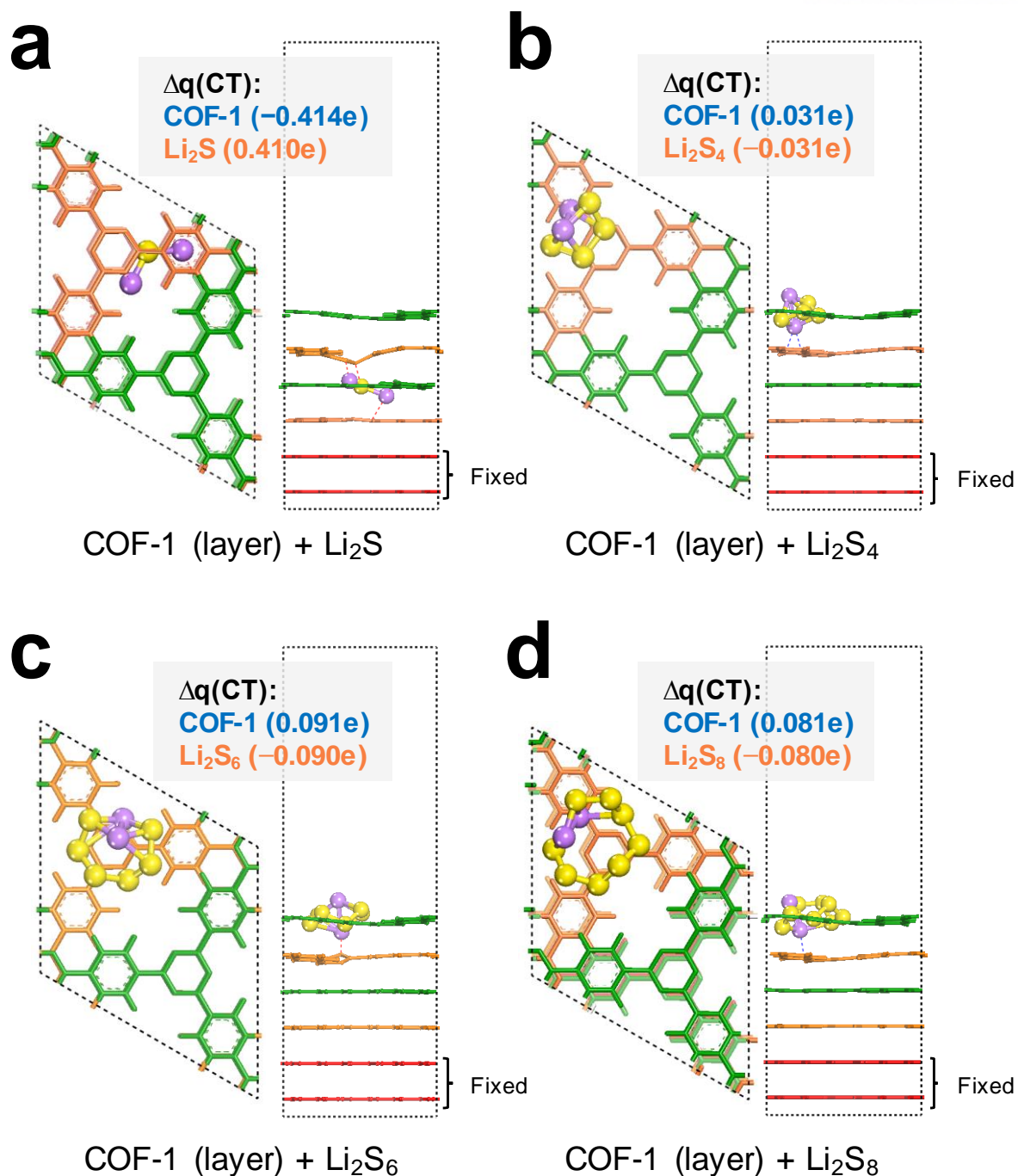


Figure 4.8 Binding configurations of Li_2S_x ($x = 1, 4, 6,$ and 8) molecules in the layer models of COF-1; **a**, Li_2S , **b**, Li_2S_4 , **c**, Li_2S_6 , and **d**, Li_2S_8 . $\Delta q(\text{CT})$ values indicate the transferred charges of molecules. Purple and yellow balls represent the Li and S atoms of the Li_2S_x , respectively. Alternate multi-plies between green and orange layers with fixed two bottom layers (red) represent the AB-staggered stacking arrangement.

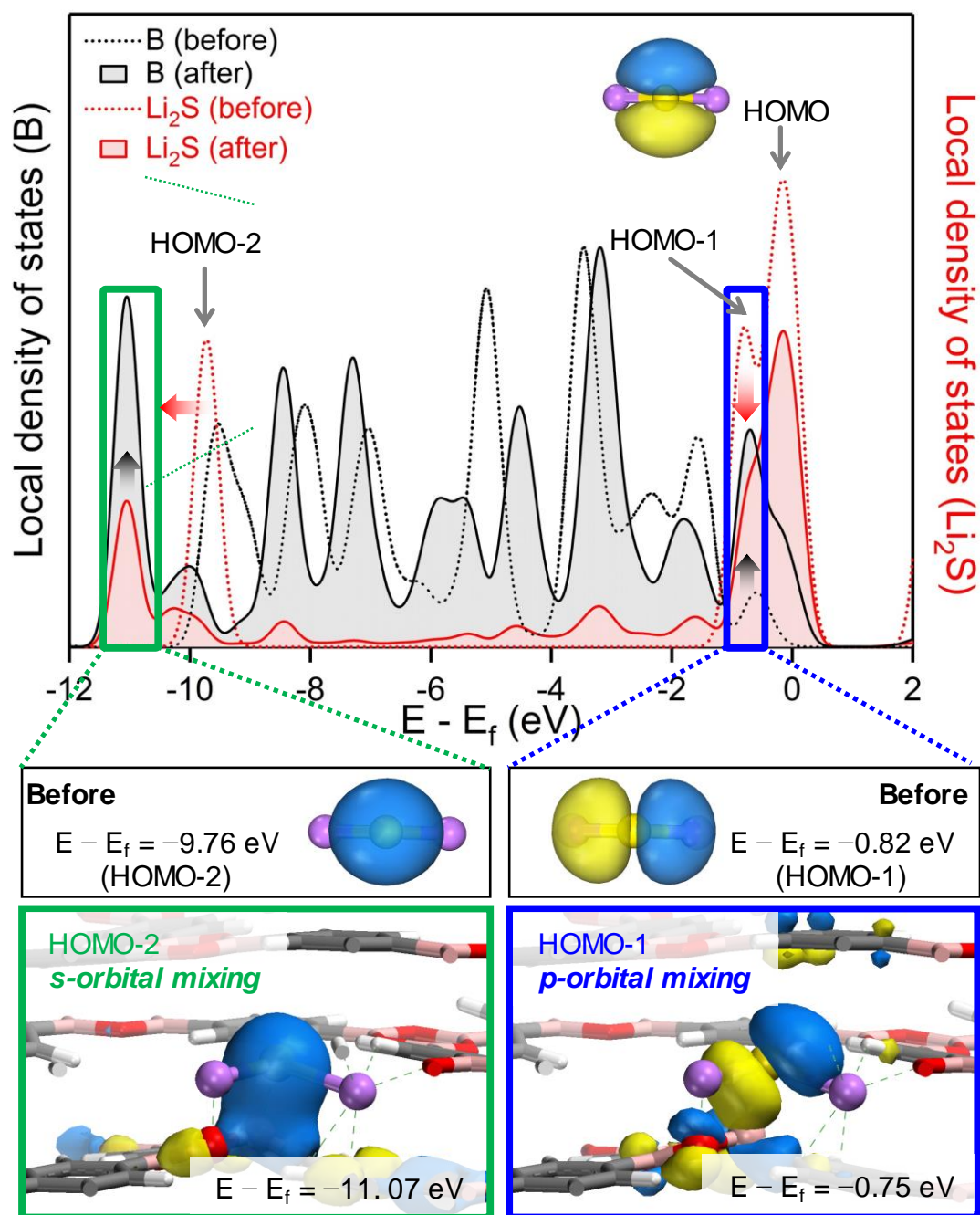


Figure 4.9 Change in the local density of states (LDOS) of Li₂S (red line) and boron of COF-1 (black line), before (dotted line) and after Li₂S adsorption (solid line). Electronic structures of Li₂S-adsorbed COF-1 [*i.e.*, HOMO-2 (green box, left) and HOMO-1 (blue box, right)] are shown, along with those of pristine Li₂S [*i.e.*, HOMO-2 (black box, left) and HOMO-1 (black box, right)]. The overlapped peaks in the LDOSs and obvious orbital mixing in both HOMO-2 and HOMO-1 verify the electrostatic stabilization-driven formation of chemical bonds between sulfur and boron.

The local density of state (LDOS) for the Li_2S -adsorbed COF-1 was investigated to elucidate the aforementioned chemical bond formation in more detail. **Figure 4.9** shows the overlapped peaks between Li_2S and boron of COF-1, wherein the mixing of p -orbital and s -orbital in HOMO-1 and HOMO-2 levels was respectively identified. Notably, the decrease in the LDOS of HOMO-1 level and also the shift of HOMO-2 level to lower energies were observed, verifying the electrostatic stabilization-driven formation of chemical bonds between sulfur and boron. These theoretical results demonstrate that the COF-1 possesses the well-designed micropore size and (boron-mediated) chemical affinity suitable for selective binding with Li_2S , which would be expected to exert beneficial influence on electrochemical performance of Li-S cells.

4.3.4 Electrochemical Performance of Li-S Battery

Assuming the theoretical results as a proof of concept, the NN interlayer was fabricated as a model system to explore the potential applicability of the “COF-net on CNT-net” hybrid architecture as an alternative polysulfide trap in Li-S batteries. The NN interlayer was inserted between a sulfur cathode and separator membrane and its influence on electrochemical performance of Li-S cells was evaluated. For this investigation, the charge/discharge cyclability of cells was examined at charge/discharge current density of 2 C ($= 2\text{ mA cm}^{-2}$)/ 2 C (**Figure 4.10**). Notably, the cell incorporating the COF-1 NN interlayer exhibited significant improvement in capacity retention with cycling ($= 84\%$ (632 mAh g^{-1}) after 300 cycles), in comparison with other cells showing the very poor capacity retention below 16%.

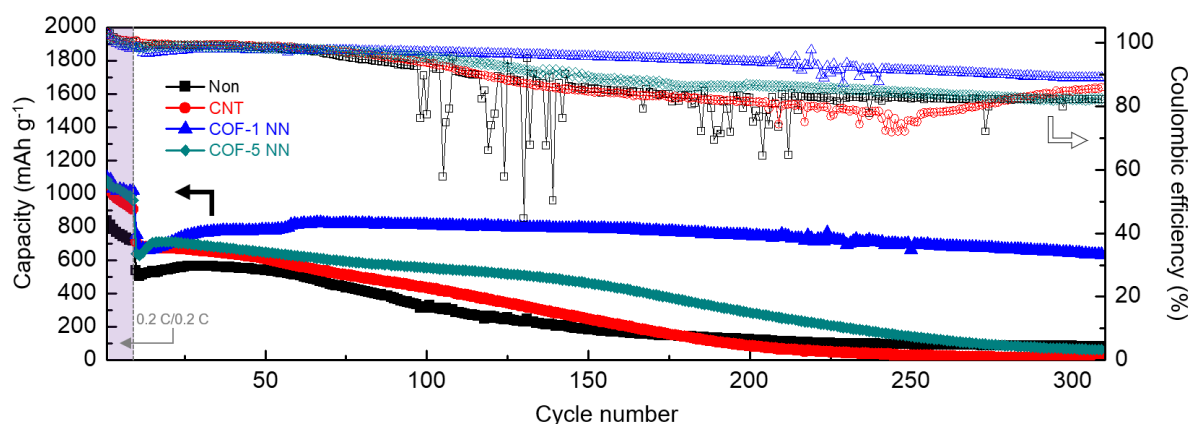


Figure 4.10 Effect of NN interlayers on the electrochemical performance of Li-S cells. Cycling performance (at charge/discharge current density = $2.0\text{ C}/2.0\text{ C}$).

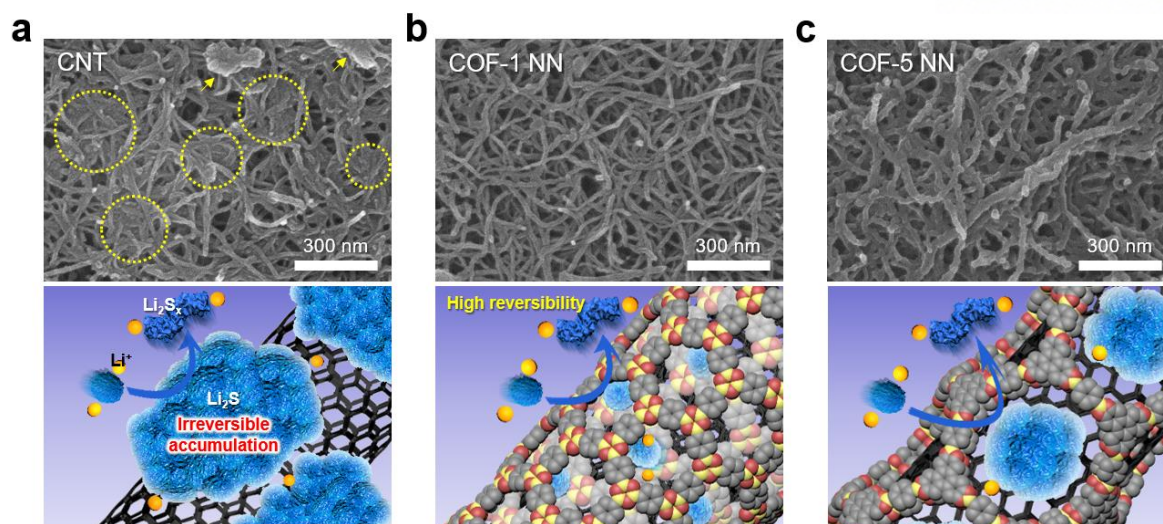


Figure 4.11 a-c, SEM images (top) of **a**, CNT, **b**, COF-1 NN interlayer, **c**, COF-5 NN interlayers after the 300th cycle (at charge/discharge current density = 2 C/2 C). The yellow arrows and circles indicate the Li_2S aggregates and clogged pores, respectively. Schematic illustrations (bottom) represent the deposition/dissolution behavior of Li_2S on CNT, the COF-1 NN interlayer, and the COF-5 NN interlayer.

This result demonstrates that COF-1 NN interlayer, due to its facile ion (*via* mesopores)/electron (along CNT networks) transport, contributes to facilitating charge/discharge reaction kinetics of the cell. This also indicates the suppression of polysulfide (such as electrically-inert Li_2S_2 and Li_2S) accumulation on electrodes. Therefore, it is speculated that the preferential adsorption of Li_2S in the COF-1 NN interlayer allows better utilization of active materials, thus contributing to the improvement of cycling performance.

The morphological change of the NN interlayers was discussed in detail, with a particular focus on solid-liquid conversion kinetics of Li_2S in terms of pore size and chemical affinity of microporous COF nets. Reduction in size of Li_2S is known to be favorable for its solid-liquid conversion kinetics, leading to the better utilization of sulfur active materials.³⁸⁻⁴⁰ The CNT paper accommodates all Li_2S_x species without any specific intermolecular interactions. Notably, the randomly-deposited/large-sized aggregates in the CNT paper give rise to the unwanted accumulation of “electrically-isolated” Li_2S molecules during cycling (**Figure 4.11a**). By contrast, the COF-1 NN interlayer, enabled by the well-designed micropores (~ 0.7 nm) suitable for deposition/dissolution (*i.e.*, solid-liquid conversion) of Li_2S , effectively suppressed the accumulation of “electrically-isolated” Li_2S molecules (**Figure 4.11b**), eventually facilitating the electrochemical reversibility of Li_2S in the charge/discharge reaction of cells. For the COF-5 NN interlayer, although it exhibited the “Net on Net” architecture, the relatively large-

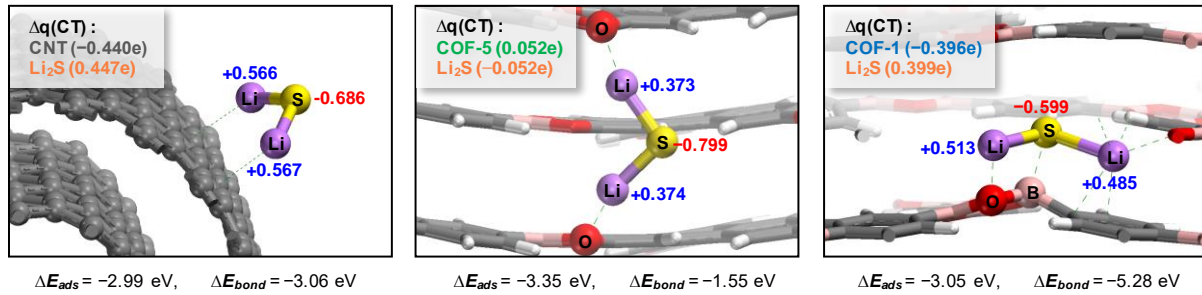


Figure 4.12 Binding configurations, total adsorption energies (ΔE_{ads}) and chemical bond formation energies (ΔE_{bond}) of Li_2S on CNT surface (left) and in the bulk of COF-5 (center) and COF-1 (right). Gray, purple, yellow, red, pink, and white balls represent the carbon, lithium, sulfur, oxygen, boron, and hydrogen atoms, respectively. The $\Delta q(\text{CT})$ values represent the transferred amount of Mulliken charges of respective systems. Atomic charges of Li_2S and Li_2S -adsorbed COF atoms are indicated on the balls.

sized micropores (~ 2.7 nm) of the COF-5 nets and their intimate interaction with polysulfides lead to easy and random deposition of all Li_2S_x species (**Figure 4.11c**), resulting in the unwanted accumulation of incompletely-oxidized polysulfide residuals along the COF-5-shelled CNTs.

In addition to the pore size effect described above, it is speculated that chemical affinity between boron-bound sulfur (*i.e.*, sulfur of polysulfides adsorbed on boron of COF nets) and S_6^{2-} (S_3^*)⁻ plays an important role in the solid-liquid conversion kinetics of Li_2S . At the end of discharge, the reduced solid Li_2S reacts with S_6^{2-} (S_3^*)⁻, thus yielding an equilibrium state^{41,42}: $2/5 \text{Li}_2\text{S} + 3/5 \text{S}_6^{2-}$ (S_3^*)⁻ = $\text{S}_4^{2-} + 4/5\text{Li}^+$. The electron-deficient state of the boron-bound sulfur in the COF-1, which was analyzed by the Mulliken population analysis,⁴³ exhibited the weakened negative charge (-0.599e) than those of the CNT (-0.686e) and COF-5 (-0.799e) (**Figure 4.12**). Such mitigated negative charge of the boron-bound sulfur leads to relatively weak electrostatic repulsion with S_6^{2-} (S_3^*)⁻, which is favorable for facilitating the equilibrium reaction. This electrostatic stabilization-driven formation of chemical bonds between sulfur and boron was theoretically discussed in **Figure 4.9**. As a consequence, solid-liquid conversion reaction of Li_2S can be promoted in the COF-1 NN interlayer.

4.4 Conclusion

In summary, we demonstrated the “microporous COF-net on mesoporous CNT-net” (NN) hybrid architecture as a new concept of molecularly-designed, hierarchical porous chemical trap for lithium polysulfides (Li_2S_x) in Li-S batteries. The effects of pore size and (boron-mediated) chemical affinity of the microporous COF nets on the adsorption of Li_2S_x (in particular, insoluble Li_2S) were theoretically analyzed using multi-scale simulation approach, including DFT and GCMC methods. The NN interlayers created the unprecedented synergistic effects: microporous COF nets as Li_2S_x trap; mesoporous CNT nets as ion-conducting channels and also electronic networks. More notably, the COF-1 NN interlayer, driven by the well-tailored microporous structure (in terms of pore size and chemical affinity) for the deposition/dissolution of Li_2S , facilitated the solid-liquid conversion (*i.e.*, electrochemical reversibility) of Li_2S . As a consequence, the COF-1 NN interlayers provided remarkable improvement in the cell performance far beyond those attainable with conventional Li-S technologies. We envisage that the “COF-net on CNT-net” strategy based on the molecularly-designed hierarchical porous architecture is highly effective and versatile, thus opening up a new opportunity for next-generation permselective materials in urgent need for a variety of energy storage systems (such as redox-flow and metal-air batteries as well as Li-S ones) and membrane-mediated separation/purification processes.

4.5 References

1. Bruce, P. G.; Freunberger, S. A.; Hardwick, L. J.; Tarascon, J.-M. Li-O₂ and Li-S batteries with high energy storage. *Nat. Mater.* **2012**, *11*, 19-29.
2. Chung, S.-H.; Manthiram, A. Bifunctional Separator with a Light-Weight Carbon-Coating for Dynamically and Statically Stable Lithium-Sulfur Batteries. *Adv. Funct. Mater.* **2014**, *24*, 5299-5306.
3. Wang, J.-G.; Xie, K.; Wei, B. Advanced engineering of nanostructured carbons for lithium-sulfur batteries. *Nano Energy* **2015**, *15*, 413-444.
4. Song, M.-K.; Cairns, E. J.; Zhang, Y. Lithium/sulfur batteries with high specific energy: old challenges and new opportunities. *Nanoscale* **2013**, *5*, 2186-2204.
5. Manthiram, A.; Chung, S.-H.; Zu, C. Lithium-Sulfur Batteries: Progress and Prospects. *Adv. Mater.* **2015**, *27*, 1980-2006.
6. Zhang, J.; Hu, H.; Li, Z.; Lou, X. W. Double-Shelled Nanocages with Cobalt Hydroxide Inner Shell and Layered Double Hydroxides Outer Shell as High-Efficiency Polysulfide Mediator for Lithium-Sulfur Batteries. *Angew. Chem., Int. Ed.* **2016**, *55*, 3982-3986.
7. Pang, Q.; Tang, J.; Huang, H.; Liang, X.; Hart, C.; Tam, K. C.; Nazar, L. F. A Nitrogen and Sulfur Dual-Doped Carbon Derived from Polyrhodanine@Cellulose for Advanced Lithium-Sulfur Batteries. *Adv. Mater.* **2015**, *27*, 6021-6028.
8. Zhou, G.; Paek, E.; Hwang, G. S.; Manthiram, A. Long-life Li/polysulphide batteries with high sulphur loading enabled by lightweight three-dimensional nitrogen/sulphur-codoped graphene sponge. *Nat. Commun.* **2015**, *6*, 7760.
9. Pope, M. A.; Aksay, I. A., Structural Design of Cathodes for Li-S Batteries. *Adv. Energy Mater.* **2015**, *5*, 1500124.
10. Li, Z.; Zhang, J.; Lou, X. W. Hollow Carbon Nanofibers Filled with MnO₂ Nanosheets as Efficient Sulfur Hosts for Lithium-Sulfur Batteries. *Angew. Chem., Int. Ed.* **2015**, *54*, 12886-12890.
11. Li, Z.; Zhang, J. T.; Chen, Y. M.; Li, J.; Lou, X. W. A sulfur host based on titanium monoxide@carbon hollow spheres for advanced lithium-sulfur batteries. *Nat. Commun.* **2015**, *6*, 8850.
12. Su, Y.-S.; Manthiram, A. Lithium-sulphur batteries with a microporous carbon paper as a bifunctional interlayer. *Nat. Commun.* **2012**, *3*, 1166.
13. Chai, L.; Wang, J.; Wang, H.; Zhang, L.; Yu, W.; Mai, L. Porous carbonized graphene-embedded fungus film as an interlayer for superior Li-S batteries. *Nano Energy* **2015**, *17*, 224-232
14. Su, Y.-S.; Manthiram, A. A new approach to improve cycle performance of rechargeable lithium-

- sulfur batteries by inserting a free-standing MWCNT interlayer. *Chem. Commun.* **2012**, 48, 8817-8819.
15. Peng, H.-J.; Wang, D.-W.; Huang, J.-Q.; Cheng, X.-B.; Yuan, Z.; Wei, F.; Zhang, Q., Janus Separator of Polypropylene-Supported Cellular Graphene Framework for Sulfur Cathodes with High Utilization in Lithium–Sulfur Batteries. *Adv. Sci.* **2015**, 3, 1500268.
 16. Balach, J.; Jaumann, T.; Klose, M.; Oswald, S.; Eckert, J.; Giebeler, L., Functional Mesoporous Carbon-Coated Separator for Long-Life, High-Energy Lithium–Sulfur Batteries. *Adv. Funct. Mater.* **2015**, 25, 5285-5291.
 17. Chang, C.-H.; Chung, S.-H.; Manthiram, A., Effective Stabilization of a High-Loading Sulfur Cathode and a Lithium-Metal Anode in Li-S Batteries Utilizing SWCNT-Modulated Separators. *Small* **2016**, 12, 174-179.
 18. Manthiram, A.; Fu, Y.; Chung, S.-H.; Zu, C.; Su, Y.-S., Rechargeable Lithium–Sulfur Batteries. *Chem. Rev.* **2014**, 114, 11751-11787.
 19. Zheng, J.; Gu, M.; Wang, C.; Zuo, P.; Koech, P. K.; Zhang, J.-G.; Liu, J.; Xiao, J. Controlled Nucleation and Growth Process of $\text{Li}_2\text{S}_2/\text{Li}_2\text{S}$ in Lithium-Sulfur Batteries. *J. Electrochem. Soc.* **2013**, 160, A1992-A1996.
 20. Ji, X.; Evers, S.; Black, R.; Nazar, L. F., Stabilizing lithium–sulphur cathodes using polysulphide reservoirs. *Nat. Commun.* **2011**, 2, 325.
 21. Xin, S.; Gu, L.; Zhao, N.-H.; Yin, Y.-X.; Zhou, L.-J.; Guo, Y.-G.; Wan, L.-J., Smaller Sulfur Molecules Promise Better Lithium–Sulfur Batteries. *J. Am. Chem. Soc.* **2012**, 134, 18510-18513.
 22. Yoo, S.; Kim, J.-H.; Shin, M.; Park, H.; Kim, J.-H.; Lee, S.-Y.; Park, S. Hierarchical multiscale hyperporous block copolymer membranes via tunable dual-phase separation. *Sci. Adv.* **2015**, 1, e1500101
 23. Xiao, Y.; Liu, S.; Li, F.; Zhang, A.; Zhao, J.; Fang, S.; Jia, D., 3D Hierarchical Co_3O_4 Twin-Spheres with an Urchin-Like Structure: Large-Scale Synthesis, Multistep-Splitting Growth, and Electrochemical Pseudocapacitors. *Adv. Funct. Mater.* **2012**, 22, 4052-4059.
 24. Wang, L.; Zhang, T.; Yang, S.; Cheng, F.; Liang, J.; Chen, J. A quantum-chemical study on the discharge reaction mechanism of lithium-sulfur batteries. *J. Energy Chem.* **2013**, 22, 72-77.
 25. Côté, A. P.; Benin, A. I.; Ockwig, N. W.; O'Keeffe, M.; Matzger, A. J.; Yaghi, O. M., Porous, Crystalline, Covalent Organic Frameworks. *Science* **2005**, 310, 1166-1170.
 26. Smit, B., Grand canonical Monte Carlo simulations of chain molecules: adsorption isotherms of alkanes in zeolites. *Mol. Phys.* **1995**, 85, 153-172.
 27. *Materials Studio 8.0*, BIOVIA Inc.: San Diego, CA, **2015**.
 28. Rappe, A. K.; Casewit, C. J.; Colwell, K. S.; Goddard, W. A.; Skiff, W. M. UFF, a full periodic table force field for molecular mechanics and molecular dynamics simulations. *J. Am. Chem. Soc.* **1992**, 114, 10024-10035.

29. Delley, B., An all-electron numerical method for solving the local density functional for polyatomic molecules. *J. Chem. Phys.* **1990**, *92*, 508-517.
30. Delley, B., From molecules to solids with the DMol3 approach. *J. Chem. Phys.* **2000**, *113*, 7756-7764.
31. Perdew, J. P.; Burke, K.; Ernzerhof, M., Generalized Gradient Approximation Made Simple. *Phys. Rev. Lett.* **1996**, *77*, 3865-3868.
32. Tkatchenko, A.; Scheffler, M., Accurate Molecular Van Der Waals Interactions from Ground-State Electron Density and Free-Atom Reference Data. *Phys. Rev. Lett.* **2009**, *102*, 073005.
33. Monkhorst, H. J.; Pack, J. D., Special points for Brillouin-zone integrations. *Phys. Rev. B* **1976**, *13*, 5188-5192.
34. Ding, S.-Y.; Wang, W., Covalent organic frameworks (COFs): from design to applications. *Chem. Soc. Rev.* **2013**, *42*, 548-568.
35. Yoo, J.; Ozawa, H.; Fujigaya, T.; Nakashima, N., Evaluation of affinity of molecules for carbon nanotubes. *Nanoscale* **2011**, *3*, 2517-2522.
36. Yoo, J.; Fujigaya, T.; Nakashima, N., Molecular recognition at the nanoscale interface within carbon nanotube bundles. *Nanoscale* **2013**, *5*, 7419-7424.
37. Connolly, M. Solvent-accessible surfaces of proteins and nucleic acids. *Science* **1983**, *221*, 709-713.
38. Zhang, K.; Wang, L.; Hu, Z.; Cheng, F.; Chen, J. Ultrasmall Li₂S Nanoparticles Anchored in Graphene Nanosheets for High-Energy Lithium-Ion Batteries. *Sci. Rep.* **2014**, *4*, 6467.
39. Cai, K.; Song, M.-K.; Cairns, E. J.; Zhang, Y. Nanostructured Li₂S-C Composites as Cathode Material for High-Energy Lithium/Sulfur Batteries. *Nano Lett.* **2012**, *12*, 6474-6479;
40. Yang, Y.; Zheng, G.; Misra, S.; Nelson, J.; Toney, M. F.; Cui, Y. High-Capacity Micrometer-Sized Li₂S Particles as Cathode Materials for Advanced Rechargeable Lithium-Ion Batteries. *J. Am. Chem. Soc.* **2012**, *134*, 15387-15394.
41. Wild, M.; O'Neill, L.; Zhang, T.; Purkayastha, R.; Minton, G.; Marinescu, M.; Offer, G. J., Lithium sulfur batteries, a mechanistic review. *Energ. Environ. Sci.* **2015**, *8*, 3477-3494
42. Wang, Q.; Zheng, J.; Walter, E.; Pan, H.; Lv, D.; Zuo, P.; Chen, H.; Deng, Z. D.; Liaw, B. Y.; Yu, X.; Yang, X.; Zhang, J.-G.; Liu, J.; Xiao, J., Direct Observation of Sulfur Radicals as Reaction Media in Lithium Sulfur Batteries. *J. Electrochem. Soc.* **2015**, *162*, A474-A478.
43. Mulliken, R. S., Electronic Population Analysis on LCAO-MO Molecular Wave Functions. I. *J. Chem. Phys.* **1955**, *23*, 1833-1840.

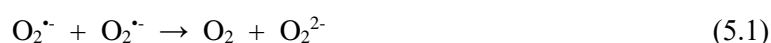
Chapter 5. Biomimetic Catalyst for Superoxide Adsorption and Disproportionation in Lithium-Oxygen Battery

This chapter includes the published contents:

Hwang, C.;[†] Yoo, J. T.;[†] Jung, G. Y.;[†] Joo, S. H.; Kim, J.; Cha, A.; Han, J.-G.; Choi, N.-S.; Kang, S.J.; Lee, S.-Y.; Kwak, S. K.; Song, H.-K. *ACS Nano* **2019**, *13*, 9190-9197 († : **equally contributed**).
Reproduced with permission. Copyright © 2019 American Chemical Society.

5.1 Introduction

In living organisms, energy is stored in a form of adenosine triphosphate (ATP) by mitochondria. The ATP is generated through an electron transport chain where the final electron acceptor is an oxygen molecule. The most of oxygen molecules are completely reduced to water during the process. However, reactive oxygen species including superoxide radical ($O_2^{\cdot-}$) are often generated as a result of incomplete reduction of oxygen. The superoxide radical makes damages to mitochondria and resultantly triggers an apoptosis process of cells.¹⁻³ Superoxide dismutase (SOD) is the most important actor in the defense mechanism of organisms against the superoxide-triggered apoptosis. The enzyme catalyzes dismutation or disproportionation of superoxide radicals into less reactive species, oxygen or hydrogen peroxide in biological systems:



In artificial energy storage devices using oxygen as electron acceptors, also, harmful effects of chemically reactive superoxide are found. Li-O₂ batteries (LOBs) have received considerable attentions due to their high theoretical energy densities (3505 Wh kg⁻¹ for LOBs *versus* 387 Wh kg⁻¹ for lithium ion batteries).⁴⁻¹⁰ During the discharge process of LOBs, O₂ is initially reduced to superoxide intermediate ($O_2^{\cdot-}$). Unstable and reactive superoxide species ($O_2^{\cdot-}$ or LiO₂) is converted to lithium peroxide (Li₂O₂) *via* two different routes (**Figure 5.1a**).¹¹⁻¹³ Superoxide radical is combined with Li⁺ to be insoluble LiO₂ on electrode surface immediately after its formation, followed by electrochemical conversion to Li₂O₂ (surface mechanism). A dense *layer* of Li₂O₂ on the surface of electrode *via* the surface mechanism. Alternatively, superoxide radicals dissolved in electrolyte forms toroidal Li₂O₂ particles on cathode without transient formation of insoluble LiO₂ (solution mechanism). Superoxide disproportionation reaction plays an important role of producing peroxide in the solution mechanism (equation 5.1).¹⁴ In addition to the superoxide-to-peroxide conversion for discharge, superoxide triggers side reactions like in organisms, which are serious hurdles limiting LOB performances. Superoxide as

a strong nucleophile attacks organic solvent molecules and carbon cathodes to form by-product deposits including Li_2CO_3 and LiOH (**Figure 5.1b**).^{11,13,15} The by-products are accumulated on cathode to hinder oxygen evolution reaction during the following charge process and to develop large polarization.

Superoxide disproportionation is a part of solution mechanism of Li_2O_2 formation during discharge. From the lesson of SOD in biological systems, the superoxide-triggered side reaction pathways could be detoured by adopting the SOD. The catalyzed disproportionation would bring additional merits in LOBs in addition to the side-reaction suppression resulting in more durable operation. By accelerating one of the constituent steps, disproportionation, the solution mechanism could be favored rather than the surface mechanism in the presence of SOD, guaranteeing higher capacity with smaller overpotential during discharge. However, it looks difficult to use SOD in LOB systems because natural enzymes work in an aqueous (not organic) environment and their stability is not guaranteed for a long-term operation. Fortunately, various organic and inorganic compounds, the function of which is that of SOD or superoxide dismutation (equivalent to disproportionation), have been reported in the field of anti-aging.^{16,17}

Herein, we used a SOD-mimetic compound (SODm) to scavenge superoxide and then convert superoxide to peroxide *chemically* during Li-O₂ battery operation. Malonic-acid-decorated fullerene (MA-C₆₀), one of the SODm showing the superior chemical stability, captured or stabilized superoxide radicals on their π -conjugated surface and the malonate functionality (**Figure 5.1b**).¹⁸ Disproportionation of two superoxide molecules adsorbed on MA-C₆₀ was catalyzed to form Li_2O_2 by the help of Li^+ electrostatically combined with carboxylates of malonic acid groups (equation 5.1). Therefore, the electrolyte decomposition and the side reactions with carbon, which are triggered by superoxide species, were detoured. Li_2O_2 formation *via* solution mechanism, rather than *via* surface mechanism, was encouraged in the presence of MA-C₆₀. It should be notified that the solution route is more beneficial than the surface route because electrode surface can be used in a more efficient way without the formation of insoluble Li_2O_2 films blocking the access of O_2 to electrically conductive surface.

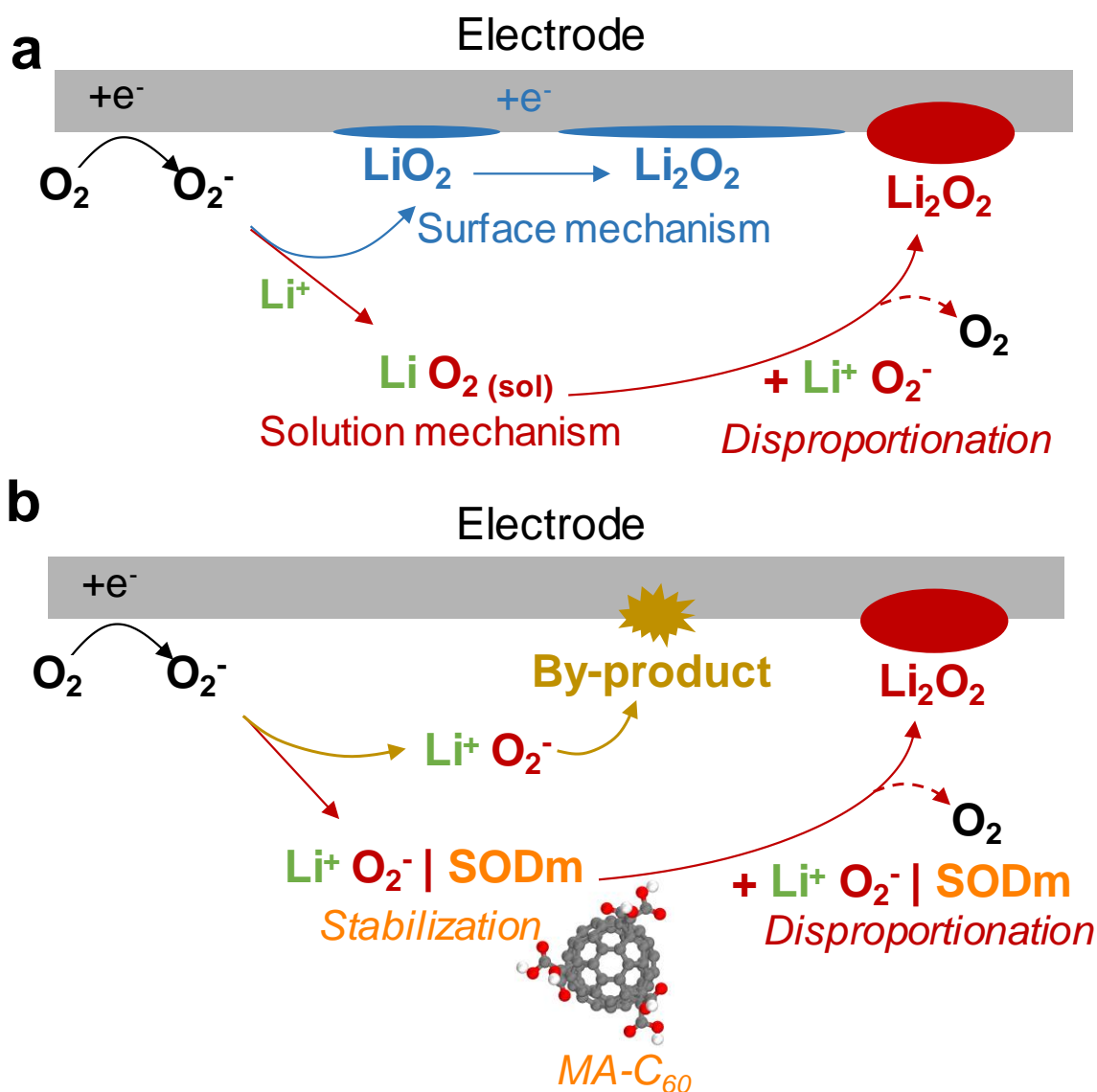


Figure 5.1 a and b, Discharge process of oxygen to Li_2O_2 on air cathode of LOBs. **a**, Two dominant mechanisms of the discharge process of oxygen to Li_2O_2 : surface mechanism *versus* solution mechanism. Superoxide radicals ($O_2^{\cdot-}$) generated from electrochemical reduction of oxygen are deposited on electrode surface and/or dissolved in electrolyte. Two molecules of the dissolved $O_2^{\cdot-}$ are *chemically* disproportionated to oxygen and peroxide in the solution mechanism while the lithium superoxide deposit on electrode surface is *electrochemically* reduced to lithium peroxide. **b**, Superoxide-triggered side reactions decomposing carbon constituents of electrodes and electrolytes. The solution mechanism encouraged by a SOD-mimetic superoxide disproportionation catalyst, MA-C₆₀. Two superoxide molecules adsorbed on MA-C₆₀ are *chemically* disproportionated by: $2 O_2^{\cdot-} \rightarrow O_2 + O_2^{2-}$. The peroxide (O_2^{2-}) is combined with Li^+ captured by MA-C₆₀ to form toroidal Li_2O_2 on electrode surface.

5.2 Methods

5.2.1 DFT Calculations

DFT calculations were carried out to compare the adsorption energies (ΔE_{ads} 's) of superoxide radicals or lithium superoxide on the MA-C₆₀ or Li₂O₂ surface, and to investigate the reaction pathway of Li₂O₂ formation *via* solution mechanism. First, the MA-C₆₀ with three malonic acid groups was modeled by following the experimentally reported structure (*i.e.*, C₆₀-tris-malonic acid derivative).¹⁹ Also, we representatively constructed the Li₂O₂ (100) stepped surface, which was found to be the most stable and thus expected to be the most abundant surface on the Li₂O₂ particles, previously reported by Hummelshøj *et al.*²⁰ The model surface consisted of 72 Li and 72 O atoms with sufficient vacuum regions in both *x*- and *z*-directions (*i.e.*, 50.0×7.7×40.0 Å³). Note that a single Li⁺ ion was introduced in vacuum to maintain the charge neutrality of the periodic cell. For solution mechanism calculation, we followed the elementary steps for reaction path recently proposed by Zhang *et al.*'s work.²¹ The implicit solvent environment was applied using conductor-like screening model (COSMO) scheme²² with a dielectric constant for experimental condition (*i.e.*, $\epsilon = 5.8$ for DEGDME). All DFT calculations were performed using the DMol³ program,^{23,24} with the generalized gradient approximation (GGA) with the Perdew-Burke-Ernzerhof (PBE) functional.²⁵ The semi-empirical Grimme scheme was applied for the dispersion correction.²⁶ Spin-polarized calculations were carried out with DNP 4.4 level. All electron relativistic effect was included for core treatment with a smearing value of 0.005 Ha. The Brillouin zone was sampled with 1×2×1 *k*-point by Monkhorst-Pack mesh for all surface systems.²⁷ The convergence criterion of self-consistent field was set to 1.0×10⁻⁶ Ha, and the geometry optimization was performed until satisfying the criteria (*i.e.*, 1.0×10⁻⁵ Ha for energy, 0.002 Ha/Å for force, and 0.005 Å for displacement, respectively).

5.2.2 MD Simulations

MD simulations were performed to investigate the capturing ability of Li⁺ ion of MA-C₆₀ in each solvent system (*i.e.*, DEGDME and TEGDME). Since the solvent molecules were known to form the complex structures in the presence of Li⁺ ions, the stable geometries of complex structures for [Li(DEGDME)]⁺ and [Li(TEGDME)]⁺ were initially identified by DFT calculations. The mole ratios between solvents and LiTFSI used in our simulations were taken from the experimental condition of 1 M LiTFSI in solvents. Five MA-C₆₀'s were initially placed in a periodic box with LiTFSI and solvents (*i.e.*, 200 LiTFSI with 1098 DEGDME or 712 TEGDME, respectively). Subsequently, MD simulations with *NPT* (*i.e.*, isobaric-isothermal) ensemble were conducted at room temperature and 1 atm for 2 ns

with the time step of 1 fs. Configurations of the last 1 ns were analyzed for the results. All MD simulations were performed using the COMPASSII forcefield.^{28,29} The temperature was controlled by Nosé-Hoover Langevin (NHL) thermostat,³⁰ and the pressure was controlled by Berendsen barostat.³¹ Ewald scheme and atom-based cutoff method (*i.e.*, a length of 15.5 Å) were used to treat the electrostatic and van der Waals forces, respectively.

5.3 Results and Discussion

5.3.1 Effect of MA-C₆₀ on LOB Performance

In the galvanostatic operation of LOB cells, the MA-C₆₀ significantly improved discharge capacities based on cathodic ORR and anodic lithium metal stripping (**Figure 5.2**). Capacities in the presence of MA-C₆₀ was more than doubled in three different ethers when compared with capacities of the MA-C₆₀-absent controls at 0.1 mA cm⁻². As current densities increased, the superiorities of MA-C₆₀-present cells to their controls became more evident. The control cells hardly worked at 0.5 mA cm⁻² while capacity of MA-C₆₀-present cells at the same current was comparable to the value obtained at 0.1 mA cm⁻². The capacities of MA-C₆₀-present cells at 0.5 mA cm⁻² were ~ 50 fold higher than those of MA-C₆₀-absent controls. Such high capacities obtained in the presence of MA-C₆₀ are considered due to the reduction of superoxide-triggered side reactions.

Solvent dependency of capacity was observed in the presence of MA-C₆₀: discharge capacity in diethylene glycol dimethyl ether (DEGDME) was larger than that in tetraethylene glycol dimethyl ether (TEGDME) and 1,2-Dimethoxyethane (DME). The interaction between superoxide and MA-C₆₀ was considered to be independent of solvent molecules because the DN_s of ethers tested in this work were too small to make differences in solvation/desolvation of superoxide.^{32,33} On the other hand, the solvent dependency of Li⁺ solvation should be considered. For this investigation, we compared the capturing ability of Li⁺ ion of MA-C₆₀ in each solvent system through multi-scale molecular simulations including DFT and MD methods.

The weaker binding strength between Li⁺ and solvent molecules (solvation energy, ΔE_{bind} by DFT calculation in **Figure 5.3a**) allowed MA-C₆₀ to capture a more number of Li⁺ in solvent environments (n_{Li} by molecular dynamics calculation in **Figure 5.3b to d**): $\Delta E_{bind} = -3.97$ eV for Li(DEGDME)⁺, weaker than -5.02 eV for Li(TEGDME)⁺, while $n_{Li} = 1$ for Li(DEGDME)⁺ higher than 0.6 for Li(TEGDME)⁺. Weak solvation indicated by less negative ΔE_{bind} encourages desolvation that is required for adsorption of Li⁺ on MA-C₆₀. Higher effective Li⁺ concentration or higher values of n_{Li} to

participate in Li_2O_2 formation on MA- C_{60} possibly facilitates disproportionation reaction on MA- C_{60} in a faster way. Therefore, disproportionation is more accelerated by MA- C_{60} in DEGDME rather than in TEGDME and DME.

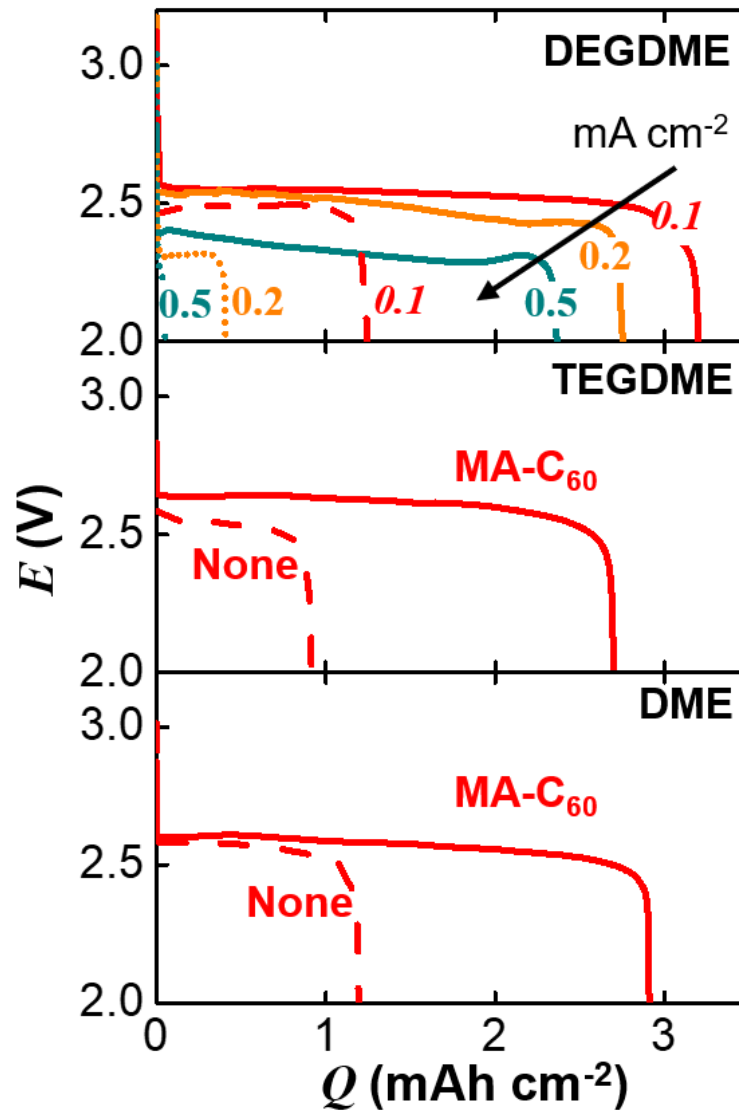


Figure 5.2 MA- C_{60} for LOB cells. Potential profiles of LOBs at galvanostatic discharge in three different ether solvents having low donor and acceptor numbers. MA- C_{60} -free (dashed) and MA- C_{60} -containing (solid) LOB cells were compared. TEGDME = tetraethylene glycol dimethyl ether; DME = dimethoxyethane. The current densities in mA cm^{-2} are indicated in the top; 0.1 mA cm^{-2} was used for the middle and bottom.

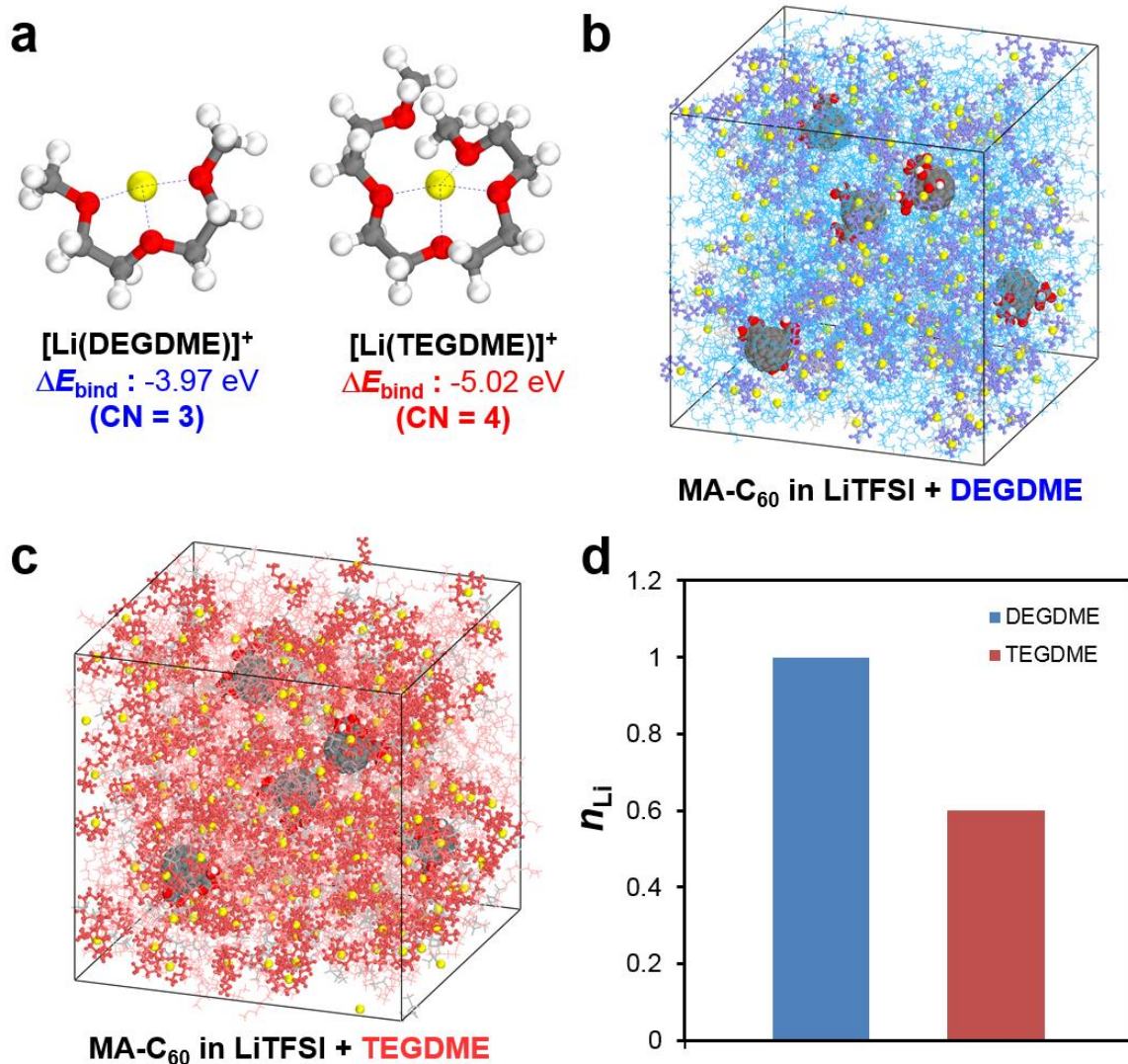
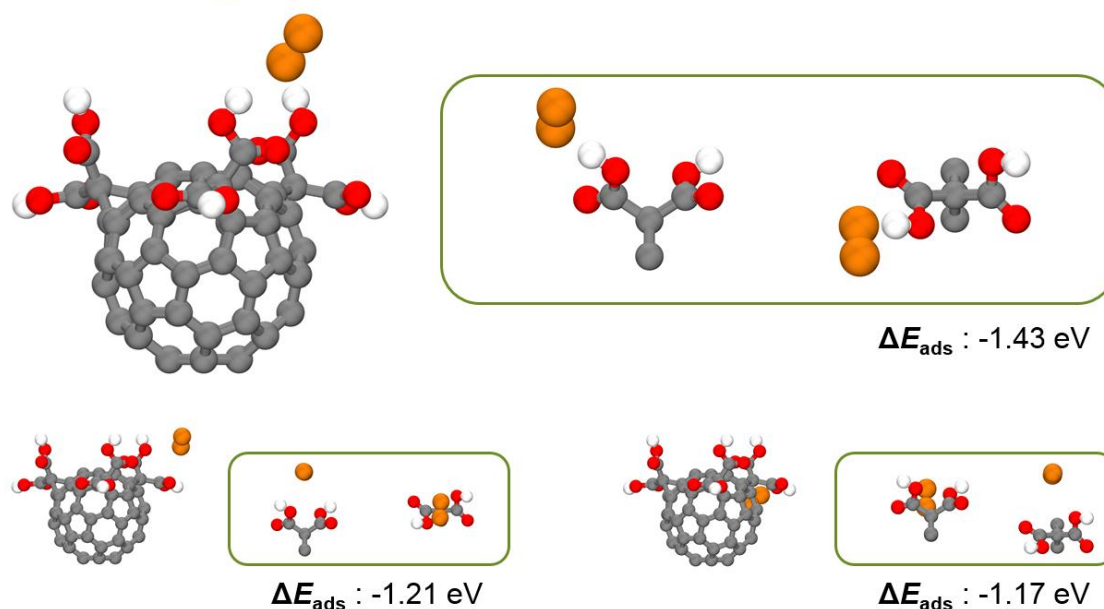


Figure 5.3 a, The optimized structures of $[\text{Li}(\text{DEGDME})]^+$ and $[\text{Li}(\text{TEGDME})]^+$ complexes: yellow = lithium, gray = carbon, red = oxygen, hydrogen = white. The binding energies (ΔE_{bind}) and the coordination number of the solvent molecule to a lithium ion (CN) were indicated. **b** and **c**, Molecular dynamics model systems of MA-C₆₀ dispersed in **b**, DEGDME and **c**, TEGDME in the presence of LiTFSI: sky blue = DEGDME, cyan = $[\text{Li}(\text{DEGDME})]^+$, red = TEGDME, light pink = $[\text{Li}(\text{TEGDME})]^+$, gray = TFSI. **d**, The average number of lithium ions captured by MA-C₆₀'s (n_{Li}) in DEGDME *versus* TEGDME.

5.3.2 Solution Mechanism of Li_2O_2 Formation Induced by MA- C_{60}

The preference to solution mechanism over surface mechanism in the presence of the SOD-mimic compound was theoretically demonstrated by DFT calculation. Initially, the adsorption configuration of superoxide on MA- C_{60} was determined by adsorption energies (ΔE_{ads}) of superoxide radical or soluble lithium superoxide on MA- C_{60} (Figures 5.4 and 5.5). The ΔE_{ads} was maximized when a superoxide radical as well as lithium superoxide was bound to $-\text{OH}$ of a carboxylic acid group of MA- C_{60} . The most stable adsorption configurations identified that hydrogen bonding is the origin of thermodynamically favoured interaction.

MA functional group



Carbon surface

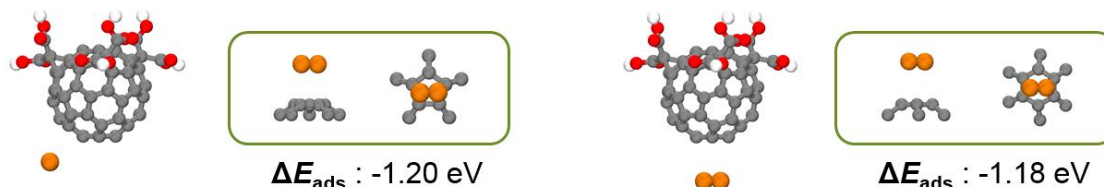
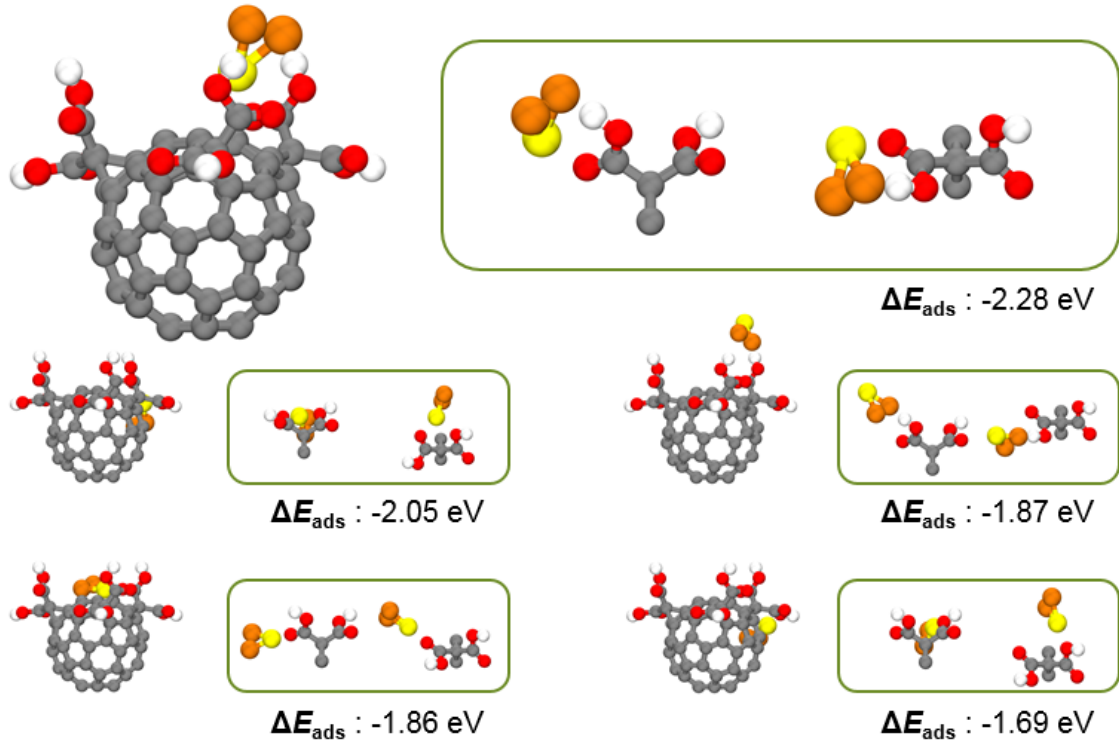


Figure 5.4 Model systems of MA- C_{60} 's for O_2^- adsorption energy (ΔE_{ads}) calculation. Carbon, hydrogen, and oxygen atoms of MA- C_{60} are colored in gray, white, and red, respectively. Oxygen atoms of superoxide are colored in orange.

MA functional group



Carbon surface

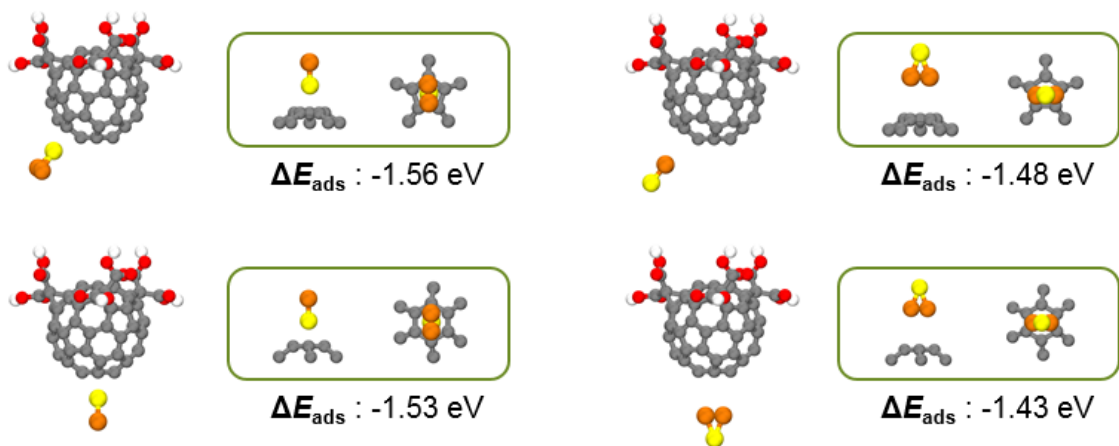


Figure 5.5 Model systems of MA-C₆₀'s for LiO₂ adsorption energy (ΔE_{ads}) calculation. Carbon, hydrogen, and oxygen atoms of MA-C₆₀ are colored in gray, white, and red, respectively. Lithium and oxygen atoms of LiO₂ are colored in yellow and orange, respectively.

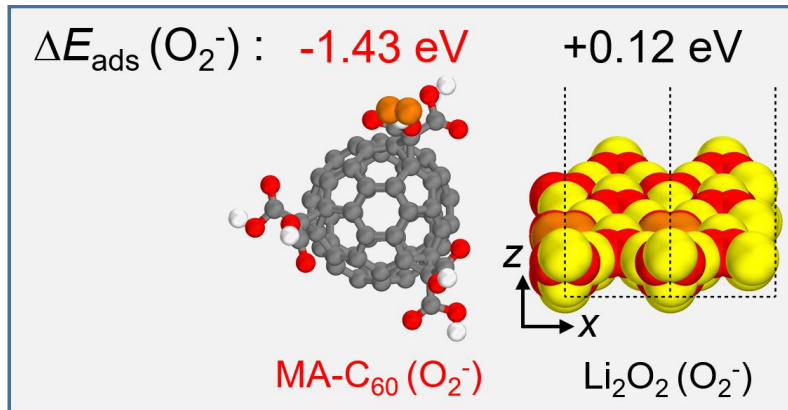


Figure 5.6 Superoxide ($\text{O}_2^{\bullet-}$) adsorption energy (ΔE_{ads}) on MA-C₆₀ versus on the (100) surface of Li₂O₂. C = gray; H = white; O = orange only for superoxide and yellow for the rest; Li = yellow.

Next, to theoretically determine which reaction path is more preferred between surface or solution routes, the adsorption energies (ΔE_{ads}) of superoxide radicals ($\text{O}_2^{\bullet-}$ or LiO_2) have been evaluated by DFT calculations. Since the superoxide species are key reaction intermediates in both surface and solution mechanisms, the ΔE_{ads} 's of these intermediates can be used as descriptors to predict the subsequent Li₂O₂ growth models.³⁴ Resultingly, $\text{O}_2^{\bullet-}$ adsorption was much preferred at MA-C₆₀ than at the Li₂O₂ surface (*i.e.*, $\Delta E_{\text{ads}}(\text{O}_2^{\bullet-}) = -1.43$ eV for MA-C₆₀ and +0.12 eV for Li₂O₂ (100) surface, **Figure 5.6**). This implies that $\text{O}_2^{\bullet-}$ radicals generated on electrode surface can be facily diffused into electrolyte and then captured by MA-C₆₀ rather than staying on the electrode surface. That is to say, the solution mechanism is expected to be preferred to the surface mechanism when MA-C₆₀ is present. This calculation result is consistent with the formation of Li₂O₂ toroids in the presence of MA-C₆₀.^{33,35}

Benefit of the use of superoxide disproportionation catalyst was more clearly understood from a mechanistic standpoint by sketching free energy diagram along reaction pathways of the solution mechanism (**Figures 5.7** and **5.8**). The dissolved superoxide radicals in the electrolytes interacts with Li⁺ to form soluble lithium superoxide (equation 5.2)



Subsequently, the Li₂O₂ solid can be formed in solution *via* disproportionation of the soluble LiO₂ (equation 5.3).



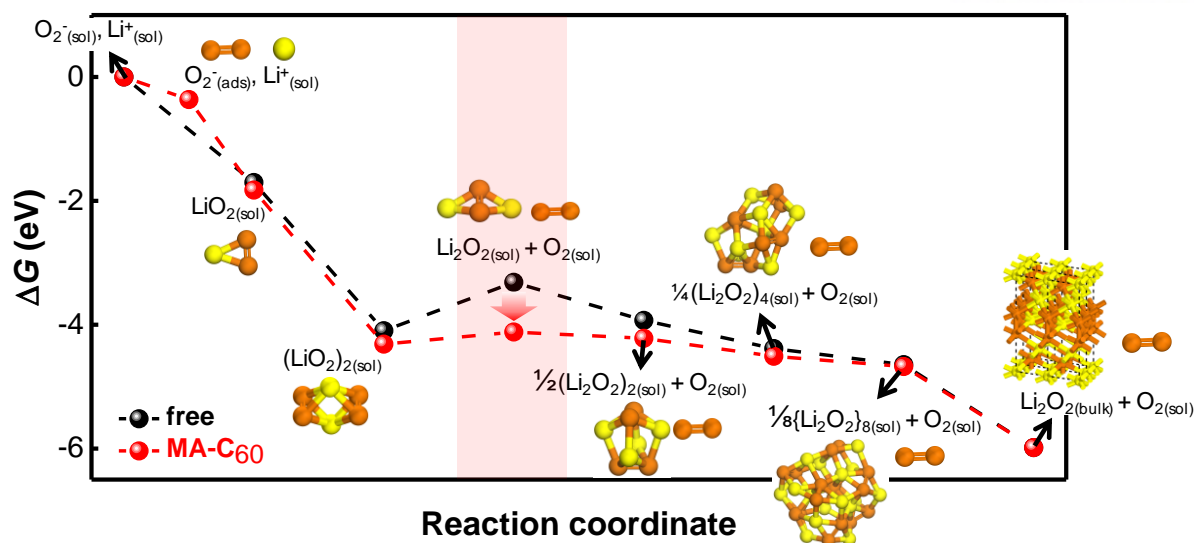


Figure 5.7 Free energy diagrams for Li_2O_2 formation through reaction pathways of the solution mechanism in the presence of MA-C₆₀ *versus* in the absence of MA-C₆₀. The pin-colored region indicates the disproportionation step from LiO_2 dimers into Li_2O_2 and solvated oxygen.

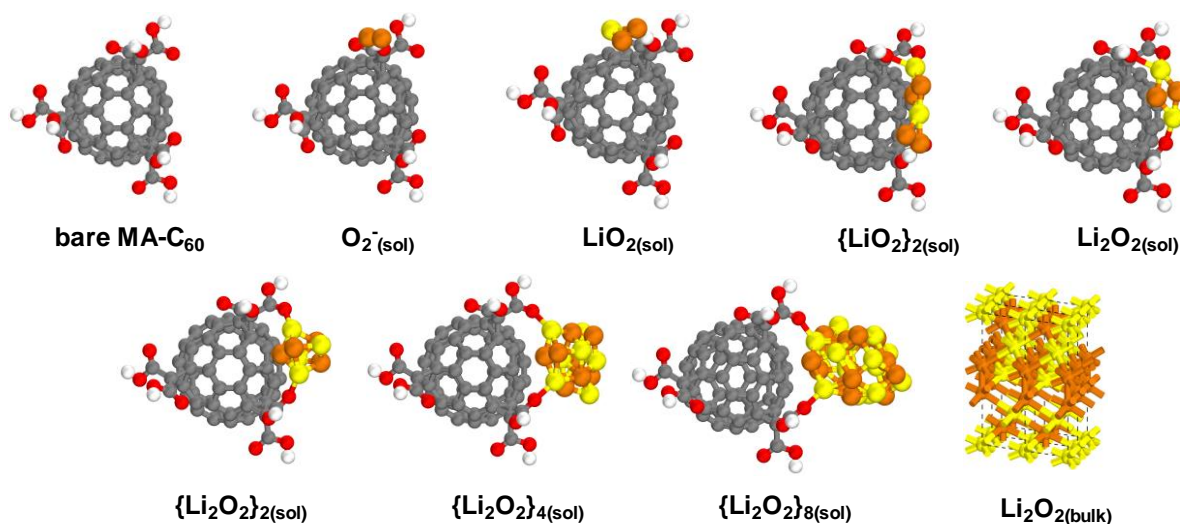


Figure 5.8 Model systems used for calculating the free energy diagram of Li_2O_2 formation *via* solution mechanism in the presence of MA-C₆₀ (denoted as ‘MA-C₆₀’ in **Figure 5.7**). Carbon, hydrogen, and oxygen atoms of MA-C₆₀ are colored in gray, white and red, respectively. Lithium and oxygen atoms of O_2^- , LiO_2 and Li_2O_2 species are colored in yellow and orange, respectively.

It should be notified that in the solution phase, the energetics cannot be expressed by a function of electrode potential since the reaction intermediates do not directly contact with the electrode surface, but the electrons are transferred by $O_2^{\cdot-}$ radicals.²¹ Resultingly, the thermodynamic barrier of the disproportionation step of $(LiO_2)_2 \rightarrow Li_2O_2 + O_2$ ($\Delta[\Delta G] = \Delta G(Li_2O_2 + O_2) - \Delta G((LiO_2)_2)$) was +0.69 eV for MA-C₆₀-free situation. The barrier decreased significantly to +0.07 eV when MA-C₆₀ was adopted. Consequently, the solution-phase reaction is considered more favored in the presence of MA-C₆₀ by lowering the endothermicity of the disproportionation barrier.

5.3.3 MA-C₆₀ versus Malonic Acid

We tested the possibility that the malonic acid (MA) without C₆₀ moiety plays the same role of MA-C₆₀ since the MA moiety of the MA-C₆₀ was revealed to be the thermodynamically most favoured adsorption sites for superoxide (**Figure 5.9**). Although we are not yet sure what the reaction promoted by MA is, the reaction is not supposed to be the superoxide disproportionation, given the inferior

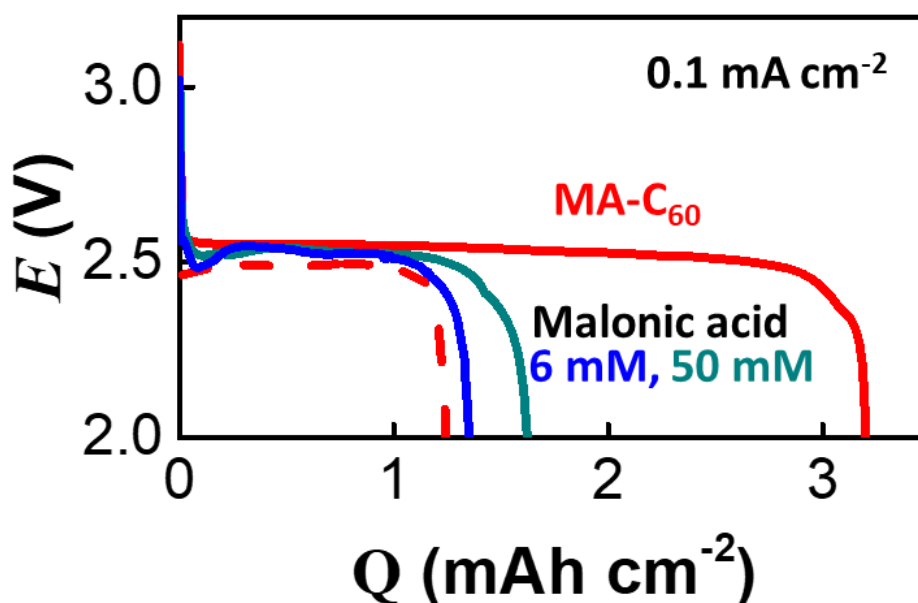


Figure 5.9 Voltage profiles of LOB cells containing MA-C₆₀ or malonic acid (MA) as an additive. 2 mM MA-C₆₀ was used while 6 mM or 50 mM malonic acid was used. The LOB cells were galvanostatically discharged at 0.1 mA cm⁻² as indicated. Lab-made Swagelok-type LOB cells were constructed with a binder-free carbon-fibre gas diffusion layer (GDL, P50, AvCarb) as a cathode and lithium metal disk of 12 mm in diameter as an anode. 1 M LiTFSI in DEGDME was used as electrolyte.

contribution of MA to the LOB capacity. When the MA was used as the additive instead of MA-C₆₀, equivalent to 2 mM MA-C₆₀ in terms of the number of MA (3 MA functionality in 1 MA-C₆₀), on LOB capacity was totally negligible. A small improvement was observed when 50 mM MA, ~10 times more MA than 2 mM MA-C₆₀, was introduced.

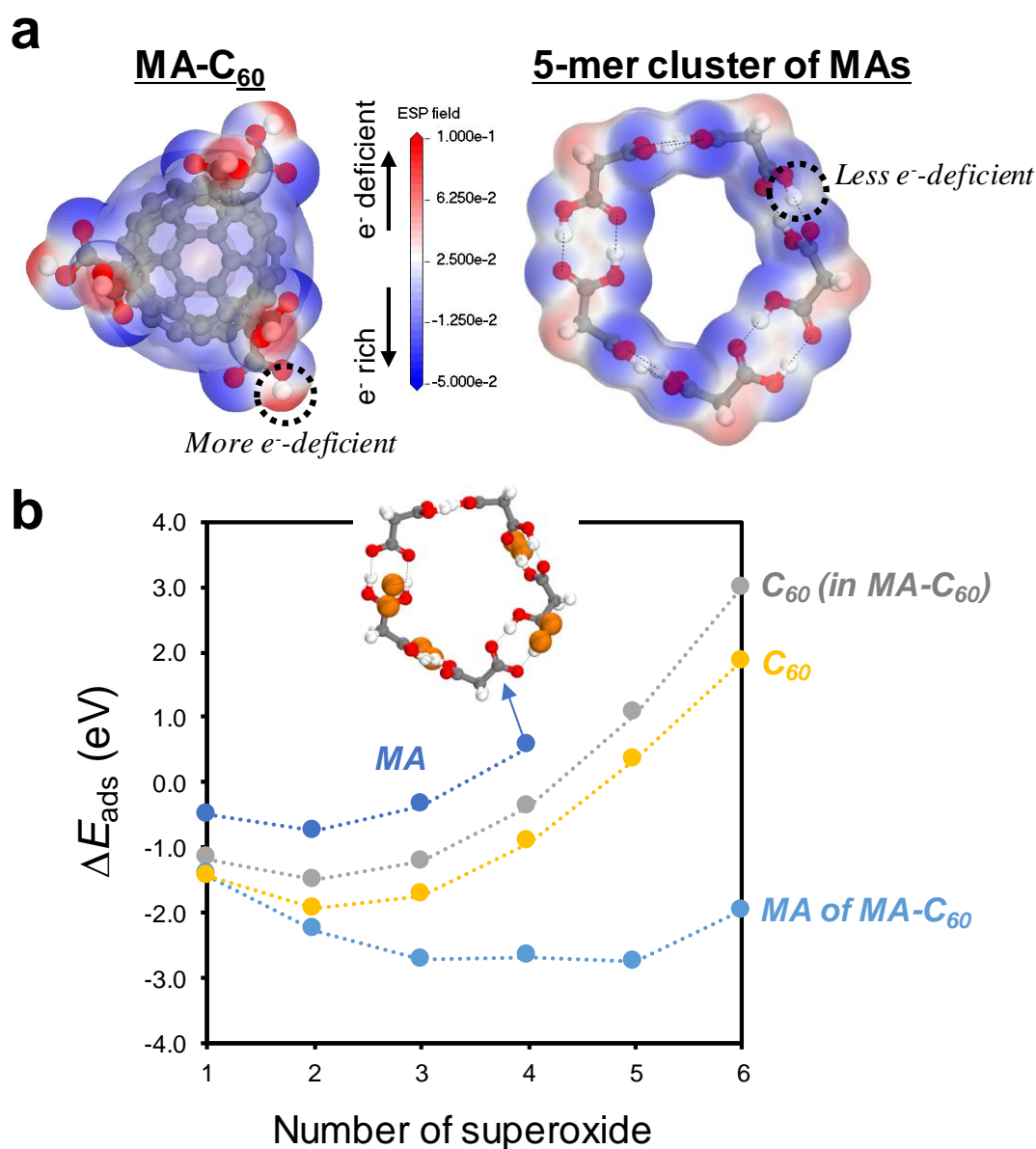


Figure 5.10 a, Electrostatic potential maps around the electron density isosurfaces of the optimized structure of MA-C₆₀ and MA. The 5-mer cluster configuration based on hydrogen bonding was used for representing the MAs in an aprotic solvent. **b**, The adsorption energy (ΔE_{ads}) of superoxide to MA and MA-C₆₀. ΔE_{ads} changed with the number of superoxide adsorbed on the indicated fraction of molecules.

Moreover, the adsorption of superoxide to the MA in solution was found to be much weaker than that to the MA-C₆₀ (**Figure 5.10**). The hydrogen-bond-based 5-mer cluster of MAs was thermodynamically favoured in an aprotic environment.³⁶ The inter-MA hydrogen bonds made the superoxide-MA interaction weaker than the superoxide-MA-C₆₀ interaction: the adsorption energy of four superoxide molecules: +0.55 eV to HO⁻ of MA > -0.38 eV to -C₆₀ of MA-C₆₀ > -0.92 eV to -C₆₀ > -2.68 eV to HO⁻ of MA-C₆₀. Therefore, both MA moiety and C₆₀ moiety are required for facilitating the superoxide disproportionation.

5.4 Conclusion

MA-C₆₀, a SOD mimic, catalyzed disproportionation reaction of reactive superoxide to molecular oxygen and peroxide. Superoxide-triggered side reactions were suppressed while lithium peroxide as a final product of ORR in LOBs was dominantly produced *via* solution mechanism in a toroidal form on electrode surface. As a result, discharge capacities of LOB cells containing MA-C₆₀ were tremendously improved especially at high rates. This MA-C₆₀ strategy should be distinguished from previously reported superoxide-controlling strategies. Both high donor number solvent molecules and discharge mediators help superoxide *electrochemically* converted to peroxide without side reactions or in a fast manner. However, MA-C₆₀ drives *chemical* disproportionation of superoxide. Peroxide is generated without electron gain from electrode while generated oxygen is recycled for electrochemical ORR. In particular, theoretical results further demonstrated that hydrogen bonding at the MA group plays a major role for superoxide adsorption and subsequent disproportionation reactions. It should be notified that a comprehensive library of SOD mimics is ready for improving performances of LOBs and sodium-oxygen batteries. Research societies would find more opportunities on extending the use of SOD mimics for superoxide management in energy storage and generation systems.

5.5 References

1. Turrens, J. F. Mitochondrial Formation of Reactive Oxygen Species. *J. Physiol-London* **2003**, 552, 335-344.
2. Han, D.; Williams, E.; Cadenas, E. Mitochondrial Respiratory Chain-Dependent Generation of Superoxide Anion and Its Release into the Intermembrane Space. *Biochem. J.* **2001**, 353, 411-416.
3. Li, X. Y.; Fang, P.; Mai, J. T.; Choi, E. T.; Wang, H.; Yang, X. F., Targeting Mitochondrial Reactive Oxygen Species as Novel Therapy for Inflammatory Diseases and Cancers. *J. Hematol. Oncol.* **2013**, 6, 19.
4. Bruce, P. G.; Freunberger, S. A.; Hardwick, L. J.; Tarascon, J. M. Li-O₂ and Li-S Batteries with High Energy Storage. *Nat. Mater.* **2012**, 11, 19-29.
5. Aurbach, D.; McCloskey, B. D.; Nazar, L. F.; Bruce, P. G. Advances in Understanding Mechanisms Underpinning Lithium-Air Batteries. *Nat. Energy* **2016**, 1, 16128.
6. Choi, J. W.; Aurbach, D. Promise and Reality of Post-Lithium-Ion Batteries with High Energy Densities. *Nat. Rev. Mater.* **2016**, 1, 16013.
7. Lim, H. D.; Lee, B.; Bae, Y.; Park, H.; Ko, Y.; Kim, H.; Kim, J.; Kang, K. Reaction Chemistry in Rechargeable Li-O₂ Batteries. *Chem. Soc. Rev.* **2017**, 46, 2873-2888.
8. Chen, Z.; Yu, A.; Higgins, D.; Li, H.; Wang, H.; Chen, Z. Highly Active and Durable Core-Corona Structured Bifunctional Catalyst for Rechargeable Metal-Air Battery Application. *Nano Lett.* **2012**, 12, 1946-1952.
9. Kim, J. G.; Noh, Y.; Kim, Y.; Lee, S.; Kim, W. B. Fabrication of Three-Dimensional Ordered Macroporous Spinel CoFe₂O₄ as Efficient Bifunctional Catalysts for the Positive Electrode of Lithium-Oxygen Batteries. *Nanoscale* **2017**, 9, 5119-5128.
10. Kim, J. G.; Kim, Y.; Noh, Y.; Lee, S.; Kim, W. B. Bifunctional Hybrid Catalysts with Perovskite LaCo_{0.8}Fe_{0.2}O₃ Nanowires and Reduced Graphene Oxide Sheets for an Efficient Li-O₂ Battery Cathode. *ACS Appl. Mater. Interfaces* **2018**, 10, 5429-5439.
11. Freunberger, S. A.; Chen, Y. H.; Drewett, N. E.; Hardwick, L. J.; Barde, F.; Bruce, P. G., The Lithium-Oxygen Battery with Ether-Based Electrolytes. *Angew. Chem. Int. Edit.* **2011**, 50, 8609-8613.
12. Bryantsev, V. S.; Giordani, V.; Walker, W.; Blanco, M.; Zecevic, S.; Sasaki, K.; Uddin, J.; Addison, D.; Chase, G. V., Predicting Solvent Stability in Aprotic Electrolyte Li-Air Batteries: Nucleophilic Substitution by the Superoxide Anion Radical (O₂^{•-}). *J. Phys. Chem. A* **2011**, 115, 12399-12409.
13. Thotiyl, M. M. O.; Freunberger, S. A.; Peng, Z. Q.; Chen, Y. H.; Liu, Z.; Bruce, P. G., A Stable Cathode for the Aprotic Li-O₂ Battery. *Nat. Mater.* **2013**, 12, 1049-1055.

14. Lu, Y. C.; Gallant, B. M.; Kwabi, D. G.; Harding, J. R.; Mitchell, R. R.; Whittingham, M. S.; Shao-Horn, Y. Lithium-Oxygen Batteries: Bridging Mechanistic Understanding and Battery Performance. *Energ. Environ. Sci.* **2013**, *6*, 750-768.
15. Black, R.; Oh, S. H.; Lee, J. H.; Yim, T.; Adams, B.; Nazar, L. F. Screening for Superoxide Reactivity in Li-O₂ Batteries: Effect on Li₂O₂/LiOH Crystallization. *J. Am. Chem. Soc.* **2012**, *134*, 2902-2905.
16. Melov, S.; Ravenscroft, J.; Malik, S.; Gill, M. S.; Walker, D. W.; Clayton, P. E.; Wallace, D. C.; Malfroy, B.; Doctrow, S. R.; Lithgow, G. J. Extension of Life-Span with Superoxide Dismutase/Catalase Mimetics. *Science* **2000**, *289*, 1567-1569.
17. Ogata, T.; Senoo, T.; Kawano, S.; Ikeda, S. Mitochondrial Superoxide Dismutase Deficiency Accelerates Chronological Aging in the Fission Yeast *Schizosaccharomyces Pombe*. *Cell. Biol. Int.* **2016**, *40*, 100-106.
18. Ali, S. S.; Hardt, J. I.; Quick, K. L.; Kim-Han, J. S.; Erlanger, B. F.; Huang, T. T.; Epstein, C. J.; Dugan, L. L., A Biologically Effective Fullerene (C₆₀) Derivative with Superoxide Dismutase Mimetic Properties. *Free Radical Bio. Med.* **2004**, *37*, 1191-1202.
19. Yan, W. B.; Seifermann, S. M.; Pierrat, P.; Brase, S., Synthesis of Highly Functionalized C₆₀ Fullerene Derivatives and Their Applications in Material and Life Sciences. *Org. Biomol. Chem.* **2015**, *13*, 25-54.
20. Hummelshøj, J. S.; Blomqvist, J.; Datta, S.; Vegge, T.; Rossmesl, J.; Thygesen, K. S.; Luntz, A. C.; Jacobsen, K. W.; Nørskov, J. K. Communications: Elementary Oxygen Electrode Reactions in the Aprotic Li-Air Battery. *J. Chem. Phys.* **2010**, *132*, 071101.
21. Zhang, Y. L.; Zhang, X. M.; Wang, J. W.; McKee, W. C.; Xu, Y.; Peng, Z. Q. Potential-Dependent Generation of O₂⁻ and LiO₂ and Their Critical Roles in O₂ Reduction to Li₂O₂ in Aprotic Li-O₂ Batteries. *J. Phys. Chem. C* **2016**, *120*, 3690-3698.
22. Klamt, A.; Schuurmann, G. COSMO - A New Approach to Dielectric Screening in Solvents with Explicit Expressions for the Screening Energy and Its Gradient. *J. Chem. Soc. Perk. T. 2* **1993**, 799-805.
23. Delley, B., An All-Electron Numerical-Method for Solving the Local Density Functional for Polyatomic-Molecules. *J. Chem. Phys.* **1990**, *92*, 508-517.
24. Delley, B., From Molecules to Solids with the DMol³ Approach. *J. Chem. Phys.* **2000**, *113*, 7756-7764.
25. Perdew, J. P.; Burke, K.; Ernzerhof, M., Generalized Gradient Approximation Made Simple. *Phys. Rev. Lett.* **1996**, *77*, 3865-3868.
26. Grimme, S., Semiempirical GGA-Type Density Functional Constructed with a Long-range Dispersion Correction. *J. Comput. Chem.* **2006**, *27*, 1787-1799.
27. Monkhorst, H. J.; Pack, J. D., Special Points for Brillouin-Zone Integrations. *Phys. Rev. B* **1976**,

- 13, 5188-5192.
28. Sun, H.; Ren, P.; Fried, J. R., The COMPASS Force Field: Parameterization and Validation for Phosphazenes. *Comput. Theor. Polym. S.* **1998**, *8*, 229-246.
 29. Sun, H., COMPASS: An *Ab Initio* Force-Field Optimized for Condensed-Phase Applications - Overview with Details on Alkane and Benzene Compounds. *J. Phys. Chem. B* **1998**, *102*, 7338-7364.
 30. Samoletov, A. A.; Dettmann, C. P.; Chaplain, M. A. J., Thermostats for "Slow" Configurational Modes. *J. Stat. Phys.* **2007**, *128*, 1321-1336.
 31. Berendsen, H. J. C.; Postma, J. P. M.; Vangunsteren, W. F.; Dinola, A.; Haak, J. R., Molecular-Dynamics with Coupling to an External Bath. *J. Chem. Phys.* **1984**, *81*, 3684-3690.
 32. Burke, C. M.; Pande, V.; Khetan, A.; Viswanathan, V.; McCloskey, B. D. Enhancing Electrochemical Intermediate Solvation through Electrolyte Anion Selection to Increase Nonaqueous Li-O₂ Battery Capacity. *Proc. Natl. Acad. Sci. U.S.A.* **2015**, *112*, 9293-9298.
 33. Aetukuri, N. B.; McCloskey, B. D.; Garcia, J. M.; Krupp, L. E.; Viswanathan, V.; Luntz, A. C. Solvating Additives Drive Solution-Mediated Electrochemistry and Enhance Toroid Growth in Non-Aqueous Li-O₂ Batteries. *Nat. Chem.* **2015**, *7*, 50-56.
 34. Yang, Y.; Liu, W.; Wu, N. A.; Wang, X. C.; Zhang, T.; Chen, L. F.; Zeng, R.; Wang, Y. M.; Lu, J. T.; Fu, L.; Xiao, L.; Zhuang, L. Tuning the Morphology of Li₂O₂ by Noble and 3d Metals: A Planar Model Electrode Study for Li-O₂ Battery. *ACS Appl. Mater. Inter.* **2017**, *9*, 19800-19806.
 35. Xu, J. J.; Wang, Z. L.; Xu, D.; Zhang, L. L.; Zhang, X. B. Tailoring Deposition and Morphology of Discharge Products Towards High-Rate and Long-Life Lithium-Oxygen Batteries. *Nat. Commun.* **2013**, *4*, 2438.
 36. Dick-Perez, M.; Windus, T. L. Computational Study of the Malonic Acid Tautomerization Products in Highly Concentrated Particles. *J. Phys. Chem. A* **2017**, *121*, 2259-2264.

Chapter 6. Summary and Future Perspectives

6.1 Summary

Adsorption is important in energy conversion and storage technologies because the energy states of adsorbed reaction intermediates can possibly determine the overall mechanistic pathway of electrochemical processes. This dissertation presents the theoretical studies on adsorption behaviors in catalysis and energy applications using multi-scale simulation methods.

First, we theoretically demonstrated the origin of excellent activity and selectivity of atomically dispersed Pt catalyst on CNT (Pt₁/CNT) for the CER. Notably, the active Pt–N₄ sites in the Pt₁/CNT could preserve a more stable structure than those of PtNP/CNT and commercial DSA catalysts. Based on the adsorption free energies for all the relevant adsorbate species by DFT calculations, we identified the PtN₄C₁₂ as the most plausible active site structure for the CER. By combining the theoretical and experimental results, the mechanistic pathways for CER over Pt₁/CNT was fully investigated.

Next, we theoretically elucidated the role of ion adsorption in the catalytic biomineralization of calcium carbonate. Each ion could promote or inhibit the phase transition, depending on hydration stability and ionic size. Thermodynamically, we could construct the fundamental relationship between two opposing factors in the phase transition process, endothermic dehydration and exothermic crystallization.

In addition, the adsorption of floating reaction intermediates, such as polysulfides (Li₂S_x) in the Li-S battery and superoxide species (O₂^{•-} or LiO₂) in the Li-O₂ battery, were thoroughly investigated. First, we demonstrated a molecularly designed chemical trap for polysulfide adsorption in the Li-S battery. The results revealed that the pore-size-enabled adsorption and boron-mediated chemical affinity of COF-1 enabled the exclusive adsorption of Li₂S in its molecular size, which can remarkably improve the Li-S cell performance. Next, we investigated the superoxide dismutase-mimetic (SODm) catalyst, MA-C₆₀, for adsorption and disproportionation of reactive superoxide species in the Li-O₂ battery. These results revealed that MA-C₆₀ could *chemically* catalyze the Li₂O₂ formation by significantly reducing the thermodynamic barrier at the disproportionation step in the solution mechanism.

Overall, we theoretically investigated the adsorption behaviors of (electro-)chemical conversion and storage processes, which can function as descriptors with reliable predictive ability for the (electro-)chemical performance. These fundamental knowledge regarding adsorption chemistry will pave a way to develop the design of advanced catalysts and battery materials for a sustainable energy future.

6.2 Future Perspectives

We propose future works related to present investigations on adsorption behaviors in catalysis and energy applications. Also, we discuss limitations of current research and propose future research directions to address them.

First, we note that structure-activity relationships in transition metal- and nitrogen codoped carbon (M–N/C) catalysts have not been fully established. Although we present one example regarding the atomically dispersed Pt catalysts on the CNT (Pt₁/CNT) with high activity and selectivity for the CER (**Chapter 2**), a fundamental understanding about the role of active metal centers (Pt atom) and their ligands (N atoms) remains unclear, particularly related to the electronic structures. A recent study highlighted that a design principle for M–N/C catalysts, relevant to the hydrogen and oxygen electrocatalysis, could be constructed based on the intrinsic characteristics of active centers, such as the electronegativity of metal atom and its ligand atoms, and coordination numbers.¹ We expect that this kind of design principle can be extended to include the CER based on the scaling relationships of adsorption free energies, which enable to find the active metal centers for each target reaction in the M–N/C catalyst.

Although the scaling relationships of adsorption free energies for reaction intermediates are useful to find the thermodynamic optimum for each target reaction, the application of these relationships may be detrimental to the design space for advanced catalysts due to the constraints by the energetic connection between key reaction intermediates. For example, ORR and OER typically have different thermodynamic optimums for adsorption free energies, implying that a single active site cannot simultaneously achieve the desired adsorption energies for both reactions.² Therefore, breaking the scaling relations can be advantageous for enhancing electrocatalytic performance. To resolve this issue in single-atom catalysts, we suggest fine-tuning the neighboring ligand atoms in addition to the active metal centers. Currently, many studies have related the *d*-band centers of active metal atoms with catalytic activity; however, the precise role of neighboring ligands such as nitrogen, carbon, oxygen and sulfur atoms, is not clearly understood. In this context, the *d*-*p* hybridization between the *d*-electrons of the metal center and the *p*-electrons of ligands (*i.e.*, N, C, O, S, etc) can ultimately determine the hydrophobicity of adsorption sites, enabling a promising exploration of the active site configurations that obey the constrained scaling relations. A recent study demonstrated that the OER could occur by alternating the adsorption sites from metal centers to N atoms in the MN₄C₄ catalyst (*i.e.*, M = Fe, Co, and Ni), referred as ‘dual-site mechanism’.³ Therefore, our future research efforts will be directed to build a guide principle for single-atom catalysts, which can be deduced from both construction and breakage of scaling relations by exploring the plausible combinations of metal centers and ligands.

Another interesting topic of future research is broadening the concept of SODm catalysts (**Chapter 5**) to understand the factors that determine the electrochemical performance of the LOB. One of the most challenging aspects of this topic is that the adsorption of reaction intermediates in the LOB (*i.e.*, $\text{O}_2^{\cdot-}$ or LiO_2) cannot be directly expressed as a function of electrode potential, unlike other electrochemical reactions (*i.e.*, OER, ORR, CER, etc), because the reaction occurs with the electron carrier of $\text{O}_2^{\cdot-}$ radicals rather than on the electrode surface.⁴ Therefore, thermodynamic descriptors based on scaling relationships, which have been widely used in hydrogen and oxygen electrocatalysis, are inappropriate for these (electro-)chemical processes. In this context, the development of a new descriptor that can interpret the solution chemistry of the adsorption energies of superoxide species (*i.e.*, $\text{O}_2^{\cdot-}$ or LiO_2) is highly demanded. We will start our investigations by defining the relationships between the adsorption energies of relevant species, including i) candidate SODm catalysts, ii) organic electrolytes (depending on the donor number), and iii) possible reactants, intermediates and product species (*i.e.*, O_2 , $\text{O}_2^{\cdot-}$, LiO_2 , O_2^{2-} , and Li_2O_2). By comparing these relationships with the actual LOB performance obtained from experiments, we expect that a valid descriptor of SODm catalysis that predicts the LOB performance could be developed.

6.3 References

1. Xu, H. X.; Cheng, D. J.; Cao, D. P.; Zeng, X. C. A universal principle for a rational design of single-atom electrocatalysts. *Nat Catal* **2018**, *1*, 339-348.
2. Calle-Vallejo, F.; Martinez, J. I.; Rossmeisl, J. Density functional studies of functionalized graphitic materials with late transition metals for oxygen reduction reactions. *Phys. Chem. Chem. Phys.* **2011**, *13*, 15639-15643.
3. Fei, H. L.; Dong, J. C.; Feng, Y. X.; Allen, C. S.; Wan, C. Z.; Voloskiy, B.; Li, M. F.; Zhao, Z. P.; Wang, Y. L.; Sun, H. T.; An, P. F.; Chen, W. X.; Guo, Z. Y.; Lee, C.; Chen, D. L.; Shakir, I.; Liu, M. J.; Hu, T. D.; Li, Y. D.; Kirkland, A. I.; Duan, X. F.; Huang, Y. General synthesis and definitive structural identification of MN₄C₄ single-atom catalysts with tunable electrocatalytic activities. *Nat. Catal.* **2018**, *1*, 63-72.
4. Zhang, Y. L.; Zhang, X. M.; Wang, J. W.; McKee, W. C.; Xu, Y.; Peng, Z. Q. Potential-Dependent Generation of O₂⁻ and LiO₂ and Their Critical Roles in O₂ Reduction to Li₂O₂ in Aprotic Li-O₂ Batteries. *J. Phys. Chem. C* **2016**, *120*, 3690-3698.

List of Publications

SCI publications (first or co-first author) [†: equal contribution]

1. **Gwan Yeong Jung†**, Eunhye Shin†, Ju Hyun Park, Byoung-Young Choi, Seung-Woo Lee, and Sang Kyu Kwak*, "Thermodynamic Control of Amorphous Precursor Phases for Calcium Carbonate via Additive Ions"
Chemistry of Materials, 2019, 31, 559-565.
2. Taejung Lim†, **Gwan Yeong Jung†**, Jae Hyung Kim, Sung O Park, Yong-Tae Kim, Hu Young Jeong, Sang Kyu Kwak* and Sang Hoon Joo*, "Atomically dispersed Pt–N₄ sites as efficient and selective electrocatalysts for the chlorine evolution reaction"
Nature Communications, 2020, accepted
3. Bora Seo†, **Gwan Yeong Jung†**, Se Jeong Lee†, Du San Baek, Young Jin Sa, Hyeong Woo Ban, Jae Sung Son, Kiyoung Park*, Sang Kyu Kwak*, and Sang Hoon Joo* , "Monomeric MoS₄²⁻-Derived Polymeric Chains with Active Molecular Units for Efficient Hydrogen Evolution Reaction"
ACS Catalysis, 2020, 10, 652-662
4. Chihyun Hwang†, JongTae Yoo†, **Gwan Yeong Jung†**, Se Hun Joo, Jonghak Kim, Aming Cha, Jung-Gu Han, Nam-Soon Choi, Seok Ju Kang, Sang-Young Lee, Sang Kyu Kwak*, and Hyun-Kon Song*, "A Biomimetic Superoxide Disproportionation Catalyst for Anti-Aging Lithium-Oxygen Batteries"
ACS Nano, 2019, 13, 9190-9197. [[News Broadcasting](#)]
5. Seok-Kyu Cho†, **Gwan Yeong Jung†**, Keun-Ho Choi, Jiyun Lee, JongTae Yoo*, Sang Kyu Kwak*, and Sang-Young Lee*, "Anti-oxidative lithium reservoir based on interstitial channels of carbon nanotube bundles"
Nano Letters, 2019, 19, 5879-5884. [[News Broadcasting, Back Cover](#)]
6. Du San Baek†, **Gwan Yeong Jung†**, Bora Seo, Jin Chul Kim, Tae Joo Shin, Hu Young Jeong, Sang Kyu Kwak*, and Sang Hoon Joo*, "Ordered Mesoporous Metastable α -MoC_{1-x} with Enhanced Water Dissociation Capability for Boosting Alkaline Hydrogen Evolution Activity"
Advanced Functional Materials, 2019, 29, 1901217.
7. Sung-Ju Cho†, **Gwan Yeong Jung†**, Su Hwan Kim, Minchul Jang, Doo-Kyung Yang, Sang Kyu Kwak*, and Sang-Young Lee*, "Monolithic heterojunction quasi-solid-state battery electrolytes based on thermodynamically immiscible dual phases"
Energy & Environmental Science, 2019, 12, 559-565. [[Front Cover](#)]
8. Bora Seo†, **Gwan Yeong Jung†**, Jae Hyung Kim, Tae Joo Shin, Hu Young Jeong, Sang Kyu Kwak*, and Sang Hoon Joo*, "Preferential horizontal growth of tungsten sulfide on carbon and insight into active sulfur sites for the hydrogen evolution reaction"
Nanoscale, 2018, 10, 3838-3848.

9. **Gwan Yeong Jung**[†], Woo Cheol Jeon[†], Sukbin Lee, Sang-Hyun Jung, Soo Gyeong Cho, and Sang Kyu Kwak*, "Reaction Characteristics of Ni-Al Nanolayers by Molecular Dynamics Simulation"
Journal of Industrial and Engineering Chemistry, **2018**, *57*, 290-296.
10. Jeong-Hoon Kim[†], **Gwan Yeong Jung**[†], Yong-Hyeok Lee[†], Jung-Hwan Kim, Sun-Young Lee*, Sang Kyu Kwak*, and Sang-Young Lee*, "Polysulfide-Breathing/Dual-Conductive, Heterolayered Battery Separator Membranes Based on 0D/1D Mingled Nanomaterial Composite Mats"
Nano Letters, **2017**, *17*, 2220–2228.
11. JongTae Yoo[†], Sung-Ju Cho[†], **Gwan Yeong Jung**[†], Su Hwan Kim, Keun-Ho Choi, Jeong-Hoon Kim, Chang Kee Lee, Sang Kyu Kwak*, and Sang-Young Lee*, "COF-Net on CNT-Net as a Molecularly Designed, Hierarchical Porous Chemical Trap for Polysulfides in Lithium–Sulfur Batteries"
Nano Letters, **2016**, *16*, 3292-3300.
12. Bora Seo[†], **Gwan Yeong Jung**[†], Young Jin Sa, Hu Young Jeong, Jae Yeong Cheon, Jeong Hyeon Lee, Ho Young Kim, Jin Chul Kim, Hyeon Suk Shin, Sang Kyu Kwak*, and Sang Hoon Joo*, "Monolayer-Precision Synthesis of Molybdenum Sulfide Nanoparticles and Their Nanoscale Size Effects in the Hydrogen Evolution Reaction"
ACS Nano, **2015**, *9*, 3728–3739.

SCI publications (co-author)

13. Xiaobo Shang[†], Inho Song[†], Jeong Hyeon Lee, Wanuk Choi, Hiroyoshi Ohtsu, **Gwan Yeong Jung**, Jaeyong Ahn, Myeonggeun Han, Jin Young Koo, Masaki Kawano, Sang Kyu Kwak*, and Joon Hak Oh*, "Heterochiral Doped Supramolecular Coordination Networks for High-Performance Optoelectronics"
ACS Applied Materials & Interfaces, **2019**, *11*, 20174-20182.
14. Nam Khen Oh[†], Changmin Kim[†], Junghyun Lee, Ohhun Kwon, Yunseong Choi, **Gwan Yeong Jung**, Hyeong Yong Lim, Sang Kyu Kwak*, Guntae Kim*, and Hyesung Park*, "In-situ Local Phase-Transitioned MoSe₂ in La_{0.5}Sr_{0.5}CoO_{3-δ} Heterostructure and Stable Overall Water Electrolysis over 1000 hours"
Nature Communications, **2019**, *10*, 1723. [[News Broadcasting](#)]
15. Kihun Jeong[†], Sodam Park[†], **Gwan Yeong Jung**, Su Hwan Kim, Yong-Hyeok Lee, Sang Kyu Kwak*, and Sang-Young Lee*, "Solvent-Free, Single Lithium-Ion Conducting Covalent Organic Frameworks"
Journal of the American Chemical Society, **2019**, *141*, 5880-5885. [[News Broadcasting](#)]
16. Kihun Jeong[†], Ju-Myung Kim[†], Su Hwan Kim, **Gwan Yeong Jung**, JongTae Yoo, Seung-Hyeok Kim, Sang Kyu Kwak*, and Sang-Young Lee*, "Carbon Nanotube-Cored Cobalt Porphyrin as A One-Dimensional Nanohybrid for Lithium-Ion Battery Anodes"
Advanced Functional Materials, **2019**, *29*, 1806937. [[Front Cover](#)]

17. Young Jin Sa†, Sung O Park†, **Gwan Yeong Jung**, Tae Joo Shin, Hu Young Jeong, Sang Kyu Kwak*, and Sang Hoon Joo*, "Heterogeneous Co–N/C Electrocatalysts with Controlled Cobalt Site Densities for the Hydrogen Evolution Reaction: Structure–Activity Correlations and Kinetic Insights"
ACS Catalysis, **2019**, *9*, 83–97.
18. Xiaobo Shang†, Inho Song†, **Gwan Yeong Jung**, Wanuk Choi, Hiroyoshi Ohtsu, Jeong Hyeon Lee, Jin Young Koo, Bo Liu, Jaeyong Ahn, Masaki Kawano, **Sang Kyu Kwak***, and Joon Hak Oh*, "Chiral Self-Sorted Multifunctional Supramolecular Biocoordination Polymers and Their Applications in Sensors"
Nature Communications, **2018**, *9*, 3933. [[News Broadcasting](#)]
19. Joohyuk Park, Manabu Shirai, **Gwan Yeong Jung**, Sung O Park, Minjoon Park, Jaechan Ryu, Sang Kyu Kwak*, and Jaephil Cho*, "Correlation of Low-Index Facets to Active Sites in Micrometer-Sized Polyhedral Pyrochlore Electrocatalyst"
ACS Catalysis, **2018**, *8*, 9647-9655.
20. Xiaobo Shang†, Cheol Hee Park†, **Gwan Yeong Jung**, Sang Kyu Kwak*, and Joon Hak Oh*, "Highly Enantioselective Graphene-Based Chemical Sensors Prepared by Chiral Noncovalent Functionalization",
ACS Applied Materials & Interfaces, **2018**, *10*, 36194-36201.
21. Dong Young Chung, Ji Mun Yoo, Subin Park, **Gwan Yeong Jung**, Jin Soo Kang, Chi-Yeong Ahn, Sang Kyu Kwak, and Yung-Eun Sung*, "Edge-Terminated MoS₂ Nanoassembled Electrocatalyst via In Situ Hybridization with 3D Carbon Network"
Small, **2018**, *14*, 1802191.
22. Chihyun Hwang, Shinho Choi, **Gwan Yeong Jung**, Juchan Yang, Sang Kyu Kwak, Soojin Park*, and Hyun-Kon Song*, "Graphene-wrapped Porous Sb Anodes for Sodium-Ion Batteries by Mechanochemical Compositing and Metallomechanical Reduction of Sb₂O₃"
Electrochimica Acta, **2017**, *252*, 25-32.
23. Woo-Jin Song†, Se Hun Joo†, Do Hyeong Kim†, Chihyun Hwang, **Gwan Yeong Jung**, Sohyeon Bae, Yeonguk Son, Jaephil Cho, Hyun-Kon Song, Sang Kyu Kwak*, Soojin Park*, and Seok Ju Kang*, "Significance of ferroelectric polarization in poly (vinylidene difluoride) binder for high-rate Li-ion diffusion"
Nano Energy, **2017**, *32*, 255-262.
24. Yeon-Su Oh, **Gwan Yeong Jung**, Jeong-Hoon Kim, Jung-Hwan Kim, Su Hwan Kim, Sang Kyu Kwak*, and Sang-Young Lee*, "Janus-Faced, Dual-Conductive/Chemically Active Battery Separator Membranes"
Advanced Functional Materials, **2016**, *26*, 7074-7083. [[Inside Back Cover](#)]
25. Sung-min Hyun, Jae Hwa Lee, **Gwan Yeong Jung**, Yun Kyeong Kim, Tae Kyung Kim, Sungeun Jeong, Sang Kyu Kwak*, Dohyun Moon*, and Hoi Ri Moon*, "Exploration of Gate-Opening and Breathing Phenomena in a Tailored Flexible Metal–Organic Framework"
Inorganic Chemistry, **2016**, *55*, 1920-1925.

26. Jinseon Kim†, Sanghyuk Kwon†, Dae-Hyun Cho, Byunggil Kang, Hyukjoon Kwon, Youngchan Kim, Sung O. Park, **Gwan Yeong Jung**, Eunhye Shin, Wan-Gu Kim, Hyungdong Lee, Gyeong Hee Ryu, Minseok Choi, Tae Hyeong Kim, Junghoon Oh, Sungjin Park, Sang Kyu Kwak, Suk Wang Yoon, Doyoung Byun, Zonghoon Lee, and Changgu Lee*, “Direct exfoliation and dispersion of two-dimensional materials in pure water via temperature control” *Nature Communications*, **2015**, 6, 8294.
27. Moo Yeol Lee, Hyeong Jun Kim, **Gwan Yeong Jung**, A-Reum Han, Sang Kyu Kwak, Bumjoon J. Kim*, and Joon Hak Oh*, “Highly Sensitive and Selective Liquid-Phase Sensors Based on a Solvent-Resistant Organic-Transistor Platform” *Advanced Materials*, **2015**, 27, 1540-1546. [[Inside Front Cover](#)]

Non-SCI publications

28. **Gwan Yeong Jung**, Woo Chul Jeon, Eun Hye Shin, and Sang Kyu Kwak*, “Application of Multiscale Molecular Modeling and Simulation Methods” *News & Information for Chemical Engineers*, **2014**, 32, 775-779 (Magazine)

